Scientific performance analysis for a novel science mission to characterise Enceladus' interior

Mattia Contarini

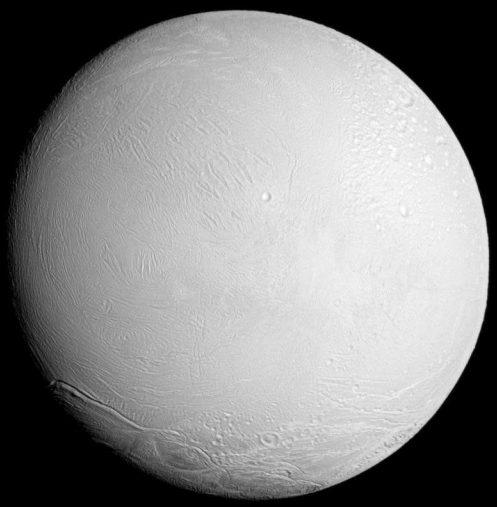

Delft University of Technology

TU Delft

Scientific performance analysis for a novel science mission to characterise Enceladus' interior

by

Mattia Contarini

to obtain the degree of Master of Science
at the Delft University of Technology,
to be defended publicly on October 28, 2025.

Student number:	5950104	
Project duration:	March 3, 2025 – October 28, 2025	
Thesis supervisor:	Dr. ir. D. Dirkx,	TU Delft
Committee chair:	Dr. ir. J. De Teixeira da Encarnação,	TU Delft
Committee external:	Prof. dr. B. L. Vermeersen,	TU Delft
Committee advisor:	Dr. ir. M. Rovira-Navarro,	TU Delft

Cover: https://science.nasa.gov/resource/brilliant-enceladus/

An electronic version of this thesis is available at https://repository.tudelft.nl/
The code developed for this work is available at https://github.com/mattiacontarini/EnceladusOrbiter

TU Delft

Preface

Here I am, thinking how to best describe in a couple of paragraphs the work of 8 months, which are the built up of two years of studies. The truth is that I could write a lot on the small moments shared with others that made my journey as it has been. Here it is a summary of it: the summary of a little story that I am sure is similar to the stories of many other students of TU Delft, which nonetheless are all unique.

I still remember the day in which I received the admission letter to the MSc Spaceflight Dynamics profile at the Aerospace Engineering faculty of TU Delft. It was March 8, 2023. I was studying for a turbomachinery course in the library of the Mechanical Engineering department of the University of Padua, Italy. While I was on my lecture notes, I took a look at the emails, and saw the admission letter. My heart started beating fast. I was hoping for the admission. And admission it was. When I finished reading the letter I was so happy that I could not keep all of it only to me. So I took my phone and called my mother. I could not continue studying that afternoon.

On September 4, 2023, I was here, in Delft, as a MSc Aerospace Engineering student. I did not know what I would have been through. Since then, I have had to work hard. I had to learn to manage anxiety, expectations, failures. I had to understand how to meddle with error codes that would frequently upset me and how to organise the mole of work that was thrown at me each and every week. My experience at TU Delft has been very different compared to my Bachelor's. In a short time, I had to adapt to a new system that played with different rules. But after the many weekends spent with my friends working on assignments, after nights in which I would go to sleep with my mind still running on the interpretation of some results, after a one-year long cycle of assignments and exams, and after 8 months of thesis research, here I am, sitting in my room writing this page that is supposed to be the first of the thesis, but is actually the last. I am happy for this journey, for the friends I met, and for what I learned. Most importantly, I am happy for that choice I made more than two years ago to apply to TU Delft. At the end of this Master's, I am more passionate on spaceflight than when I started, and I understood many things about me I had no clue about when I started.

I will conclude this page with a simple thank you to those that were in the first line with me through this journey. A thank you to my fellow TU friends, with whom I spent many hours sitting at a desk, working together to solve assignments and to bear the load. Without them, I would not have learned and overcome the problems as I did. A thank you to Dominic and Marc, because in different ways and on different research areas they guided me through this thesis, often pointing out potential issues while supporting and guiding my reasoning on how to solve them. A thank you also to all those friends whom I met outside of the TU environment. I spent good convivial moments with them, and they made me feel more attached to Delft. A special thank you to Fr. Richard, for helping me see what I was blind to. And of course, a thank you to my family and friends back home, whom I missed, especially during the hardest moments. The last thank you is for my mother, who bore the weight of my absence being conscious of what it meant for me to be here.

Mattia Contarini
Delft, October 14, 2025

Summary

Context Enceladus has been assessed as the prime target for the science theme *Moon of the Giant Planets* of the ESA Voyage 2050 scientific programme. Investigation of its interior is of interest to study its habitability. This work proposes a mission composed of an orbiter tracked by the ESA Estrack ground stations and by surface lander(s).

Aim The purpose of this work is to explore the potential contribution of the proposed mission to obtain accurate estimates for geophysical parameters of Enceladus, and to quantify how the accuracy of the estimates translates to uncertainty values for its interior properties, assessing which parameters can be best constrained with the selected observables.

Method The uncertainty associated to the geophysical parameters of interest is estimated through a covariance analysis approach. Given a set of mission design and science input parameters, the gravity field up to D/O 30, tidal Love numbers, libration amplitude, pole position, and pole rate are estimated for different mission scenarios. For the set of computed results, reference nominal values are proposed. They are used to study which interior properties can be constrained by the libration amplitude and the real component of the tidal Love numbers, through a Monte Carlo analysis. The formal error associated to the geophysical measurements is mapped to uncertainty values for the interior properties of Enceladus.

Results The addition of at least one surface lander improves the uncertainty of the libration amplitude and pole position of about two orders of magnitude with respect to the estimates based only on radio science data. Moreover, the landers enable the estimation of the radial displacement Love number. The static gravity coefficients do not show a significant improvement when the surface radio beacons are included in the mission architecture. The results suggest that planning of a future Enceladus mission should be based primarily on the number and location of the landers, and secondarily on the mission duration and length of the tracking arcs from the Earth Ground Station (GS)s. With respect to the investigation of the interior, the results show that the real component of the tidal Love numbers contributes mostly to knowledge on the density and thickness of the core and ocean, the shell shear modulus, and the shell bulk modulus. The ice shell thickness is best constrained through the libration amplitude, which appears to be a highly constraining observable on the interior model. The results suggest that the mechanical properties of the core, the viscosity of the shell, and the shell density are not well constrained by the selected observables.

Conclusions A mission of one month with one radio beacon and 8-hours long tracking arcs from Earth provides a significant improvement of the estimates compared to a purely radio science mission, and appears to be technically feasible with respect to longer radio science missions, due to the highly perturbed dynamical environment of Enceladus. The proposed mission allows to estimate the Love numbers and libration amplitude with a small uncertainty, leading to a significant improvement of the knowledge on the interior structure of Enceladus and on the rigidity and bulk modulus of the shell.

Contents

List of Abbreviations

CIRS Composite Infrared Spectrometer

DE Declination

DORIS Doppler Orbitography and Radiopositioning Integrated by Satellite

DSN Deep Space Network

DST Deep Space Transponder

DTE Direct-To-Earth

EoM Equations of Motion

ESA European Space Agency

FOV Field of view

GS Ground Station

INMS Ion Neutral Mass Spectrometer

ISS Imaging Science Subsystem

LOS Line-of-sight

MC Monte Carlo

MCMC Markov Chain Monte Carlo

MCS Media Calibration System

MH Metropolis-Hastings

MoI Moment of Inertia

NAC Imaging Science Subsystem Narrow Angle Camera

OMMs Orbit Maintenance Manoeuvres

RA Right Ascension

RK Runge-Kutta

RKDP Dormand-Prince

RKF Runge-Kutta-Fehlberg

RMS Root Mean Square

RTG Radioisotope thermoelectric generator

S/C Spacecraft

SEP Sun-Earth-probe

SH Spherical harmonics

SOI Sphere of Influence

SRP Solar radiation pressure

TEC Total Electron Content

Tudat TU Delft Astrodynamics Toolbox

WP Work Package(s)

List of Symbols

Notation	Description	Unit
g	Gravitational acceleration	$\mathrm{m\,s^{-2}}$
C	Moment of inertia	$\mathrm{kg\,m^2}$
M^*	Mass of secondary body	kg
M	Mass of primary body	kg
R	Average planetary radius, reference radius	m
$\overline{C}$	Moment of inertia factor	–
$\dot{\Omega}$	Angular velocity	$\mathrm{rad\,s^{-1}}$
$\overline{a}$	Equatorial radius	m
$\overline{b}$	Polar radius	m
f	Flattening	–
J_2	Zonal component of gravity field of degree 2	–
H_{lm}	Topography spherical harmonic coefficients	–
Z_{lm}	Spectral admittance	$\mathrm{mGal\,km^{-1}}$
l	Degree of spherical harmonics	–
U	Potential	$\mathrm{m^2 s^{-2}}$
m	Order of spherical harmonics	–
ρ	Density	$\mathrm{kg\,m^{-3}}$
$\overline{\rho}$	Mean density	$\mathrm{kg\,m^{-3}}$
a	First semi-axis of a triaxial ellipsoid / Orbital semi-major axis	m
b	Second semi-axis of a triaxial ellipsoid	m
c	Third semi-axis of a triaxial ellipsoid	m
e	Eccentricity	–
C'	Degree of compensation	–
d	Depth of compensation	m
f_{lm}	Compensation factor	–
ϕ	Libration amplitude	m
K_1	Coupling strength of the libration forcing	–
K_3	Effective strength of the total diurnal forcing	–
n	Mean motion	$\mathrm{rad\,s^{-1}}$
k_2	Full degree 2 Love number	–
k_{lm}	Degree and order varying gravity Love number	–
E	Energy	J
$\mathbf{p}$	Estimated parameters vector	NA
$\mathbf{x}$	State vector	NA
t	Epoch	s
$\mathbf{z}$	Observations vector	NA
$\mathbf{h}$	Observations model	NA
H_p	Matrix of the partials of the observations w.r.t. the parameters	NA
H_c	Matrix of the partials of the observations w.r.t. the consider parameters	NA
h_i	Single observation model	NA

Notation	Description	Unit
Φ	State transition matrix	NA
S	Sensitivity matrix	NA
n_{p_e}	Number of environmental parameters	–
n_b	Number of integrated bodies	–
W	Weight matrix	–
σ	Expected measurement error	NA
P	Covariance matrix	NA
$\mathbf{c}$	Covariance parameters	–
C^c	Assumed covariance matrix of the consider parameters	–
τ	Travel time	s
r	Range, radius	m
r^*	Pseudorange	m
$\Delta\phi$	Phase shift	rad
f_0	Carrier frequency	Hz
$\mathbf{r}$	Position vector	m
f	Frequency	Hz
λ	Wavelength	m
n^*	Refractivity	–
Δl	Optical path	m
P^*	Plasma parameter	$\mathrm{m\,s^{-2}}$
Q	Quality factor	–
W	Libration angle	rad
l	Mean anomaly	rad
ω_2	Orbital libration argument of the resonance Dione-Enceladus	rad
ϕ_4	Proper pericentre of Dione	rad
I	Identity matrix	NA
n	Size of the state vector	–
ϑ	Layer thickness	m
h_2	Full degree 2 radial Love number	–
θ	Co-latitude	rad
d^*	Distance between the centers of the primary and secondary body	m
ψ	Angle between the position vectors centred at the secondary and pointing respectively to the reference point on the secondary and to the centre of the primary	rad
ν	True anomaly	rad
ω	Argument of pericentre	rad
φ	Longitude	rad
i	Inclination	rad
ς	Latitude	rad
γ	Longitude of the ascending node	rad
$\overline{n}$	Mean motion	$\mathrm{rad\,s^{-1}}$
u	Tidal displacement	m
ϵ	Tidal lag	rad
α	Right ascension	rad
δ	Declination	rad
$\overline{\phi}$	Phase lag	rad
$\mathbf{v}$	Velocity	$\mathrm{m\,s^{-1}}$
μ	Gravitational parameter	$\mathrm{m^3\,s^{-2}}$
n_L	Number of landers	–
ω	Frequency of libration periodicities	Hz

Notation	Description	Unit
γ	Phase of libration periodicities	rad
M	Magnitude of libration periodicities	rad
$\mathbf{a}$	Acceleration	$\mathrm{m\,s^{-2}}$
h	Altitude	m
C_D	Drag coefficient	–
S	Cross-section area	$\mathrm{m^2}$
T_c	Doppler count time	s
ζ	Elevation	rad
A	Spin-pole right ascension nutation amplitude	rad
B	Spin-pole declination nutation amplitude	rad
Ω	Phase	rad
$\bar{P}_{lm}$	Normalized Legendre functions	–
R	Rotation matrix	–
C_SRP	Solar radiation pressure coefficient	–
l_2	Degree 2 Shida number	–
μ	Shear modulus	Pa
η	Shear modulus	Pas
K	Bulk density	Pa
$\bar{\nu}$	Poisson ratio	–
D	Bending rigidity	$\mathrm{Pam^{-3}}$
$\bar{\epsilon}$	Obliquity	rad
J_3	Zonal component of gravity field of degree 3	–
C_{lm}	Unnormalized gravity spherical harmonic cosine coefficients	–
S_{lm}	Unnormalized gravity spherical harmonic sine coefficients	–
$\bar{C}_{lm}$	Normalized gravity spherical harmonic cosine coefficients	–
$\bar{S}_{lm}$	Normalized gravity spherical harmonic sine coefficients	–
T	Final epoch/orbital period	s

List of Constants

Notation	Description	Quantity
G	Universal gravitational constant	$6.6743 \times 10^{-11}\,\mathrm{m^3\,kg^{-1}\,s^{-2}}$
c	Speed of light in vacuum	$2.99792458 \times 10^{5}\,\mathrm{km\,s^{-1}}$

List of Subscripts & Superscripts

Notation	Description
E	Enceladus
0	Initial/Reference
obs	Observation
hyd	Hydrostatic
nh	Non-hydrostatic
tot	Total
q	Equatorial
p	Polar
c	Core
s	Ice shell
e	Environmental
apr	A priori
r	Receiver
t	Transmitter
nd	Non-dispersive
u	Uplink
d	Downlink
o	Ocean
T	Tidal
s-a	Spin axis
V	Vehicle
L	Lander
rep	Repetition
D	Drag
emp	Empirical
z	Zenith
e	End
BF	Body frame
IF	Inertial frame

1. Introduction

1.1. Scientific rationale

The European Space Agency (ESA)'s Voyage 2050 scientific programme for the time-frame 2035-2050[1] will focus on the moons of the planets in the outer Solar System, on temperate exoplanets, and will investigate the early Universe. With respect to the science theme *Moons of the Giant Planets*, their exploration will address the habitability and workings of the Solar System (Sulaiman et al., 2022). Saturn's moon Enceladus has been assessed as the optimum candidate for a Large-class (L4) mission on this theme (Bunce et al., 2024).

With a mean radius of about 252 km (Spencer et al., 2009), Enceladus orbits Saturn in the E ring, between Mimas and Tethys (Porco et al., 2006). Enceladus' orbit has a semi-major axis of 238.02×10^3 km, leading to one revolution around Saturn in about 1.37 days (Porco et al., 2004). Furthermore, it has a 2:1 mean motion resonance with Dione, that excites its orbital eccentricity of 0.0047 (Porco et al., 2006).

From 2004 to 2017, the Cassini spacecraft executed 28 flybys of Enceladus (Bellerose et al., 2018). The flybys allowed to improve Enceladus' ephemeris, and refine the knowledge on its shape and size (Thomas, 2010), and on its mass (Rappaport et al., 2007). Additionally, the Cassini spacecraft allowed to acquire high-resolution images of the south polar terrain, revealing the presence of icy ridges, boulders, tectonic features, and four 130-km-long fractures named *tiger stripes* (Figure 1.1.1). Cassini's Composite Infrared Spectrometer (CIRS) found the south polar region to be warm, between 114 and 157 K (Porco et al., 2006). In correspondence of such surface patterns at the south pole, water vapour plumes and icy particles emanating from the ridges and fractures in the ice shell were observed. The attitude control data of Cassini on 6 fly-bys were used to study the plumes density (Lorenz & Burk, 2018). Tidal heating caused by dissipation of the body's orbital energy is considered the source of the geothermal activity on Enceladus (e. g., Spencer and Nimmo (2013), Sulaiman et al. (2022)) producing the plumes. The tidal heating is maintained over long timescales by Enceladus' 2:1 mean motion with Dione, as it is observed for other moons of the Solar System, like Io (Murray & Dermott, 2000).

Sampling of Enceladus' plumes ejecta and laboratory experiments have concluded that present-day hydrothermal activity at Enceladus might resemble what is observed in the deep ocean on the Earth (Sulaiman et al., 2022). The plumes contain sodium-salt-rich ice grains, meaning that the water droplets that later solidified were from a water reservoir that had been in contact with rocks (Postberg et al., 2009), reinforcing the idea of a subsurface ocean in contact with the core. Furthermore, Cassini's Ion Neutral Mass Spectrometer (INMS) sampled Enceladus' plumes and found ammonia, along with other various organic compounds. Molecular hydrogen was also found in the plumes: hydrothermal reactions of rock containing organic materials and reduced minerals have been considered the most plausible source of this hydrogen (Sulaiman et al., 2022).

Accessible salty ocean, organic compounds, and hydrothermal activity make Enceladus a prime target for exploring habitability outside the Earth's biosphere. The ESA Expert Committee for the Large-class mission on the theme *Moons of the Giant Planets* (Bunce et al., 2024) determined the following three areas of scientific investigation:

1. *The issue of habitability of ocean worlds and the interaction between the surface and the interior.*
2. *The issue of habitability of ocean worlds and the interaction with the external environments.*

[1] Voyage 2050 sets sail: ESA chooses future science mission themes

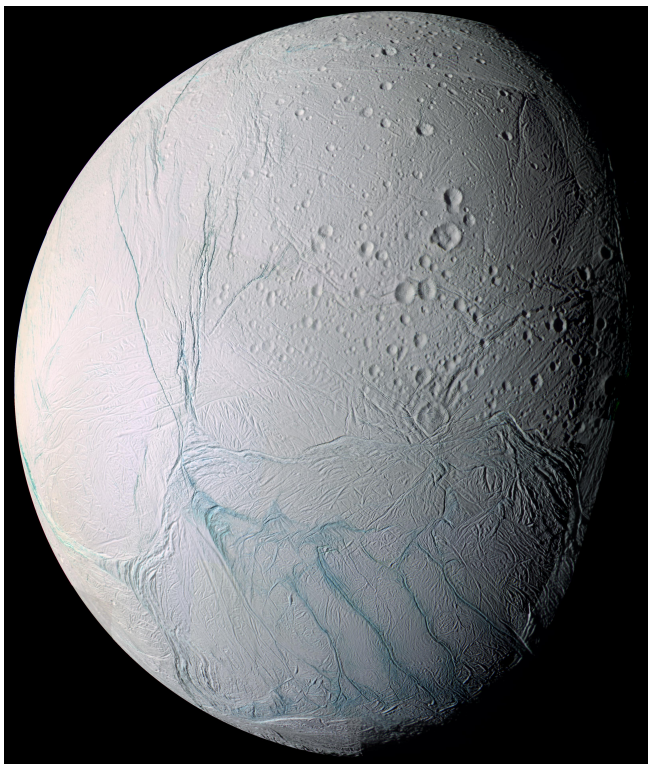

Figure 1.1.1.: Global false-color view of Enceladus taken by the Imaging Science Subsystem (ISS) onboard Cassini on July 14, 2005. The four active "tiger stripe" fractures appear as prominent blue-green lines surrounding the south pole. From Cassini Press Release PIA06254. Credits: NASA/JPL/Space Science Institute.

3. *The identification of prebiotic chemistry and the search for biosignatures on ocean worlds.*

Following the scientific interest of ESA towards Enceladus and other icy moons including Titan, Europa, Ganymede, and Callisto, various studies have been carried out with the objective of constructing a complete model of the interior structure of these bodies (e. g., Rambaux et al. (2011), Hussmann et al. (2016), Thomas et al. (2016), Van Hoolst et al. (2024), Park et al. (2024), Bagheri et al. (2025)). As highlighted by Bagheri et al. (2025) and Hemingway and Mittal (2019), the study of the interior structure is strictly associated to the study of the heat dissipation mechanisms, allowing to shed light on the tidal heating of Enceladus and the energy source of the plumes.

With the purpose of assessing Enceladus' astrobiological potential, Ermakov et al. (2021) identified the following science questions that should be addressed by future geophysical observations of the moon:

1. *What is the internal structure of Enceladus?*
2. *Where is the heat generated and how is it transported?*
3. *Is Enceladus currently in a steady state?*
4. *What are the feedbacks between volcanism and tectonics that regulate Enceladus' cryovolcanism?*

Enceladus is composed of a porous rocky core, a subsurface ocean, and an icy shell. An overview of the studies of the last decade on the interior structure of Enceladus is provided in Table 1.1.1. Ermakov et al. (2021) explored different types of measurements that could help improving our knowledge of the interior and internal dynamics of the moon:

1. Gravity
2. Libration amplitude
3. Shape

Table 1.1.1.: Last decade's studies on the interior structure of Enceladus. The table reports the thickness of the core, ocean, and ice shell.

Study	Core [km]	Ocean [km]	Ice shell [km]	Geophysical measurements
Iess, Stevenson, et al. (2014b)	~ 190	$10 - 30$	$30 - 40$	Gravity and shape
Mckinnon (2015)	$190 - 195$	~ 10	~ 50	Gravity and shape
Thomas et al. (2016)	~ 200	$26 - 31$	$21 - 26$	Physical libration amplitude
Čadek et al. (2016)	$180 - 185$	~ 50	$18 - 22$	Gravity, shape, and libration
Hoolst et al. (2016)	$170 - 205$	$21 - 67$	$14 - 26$	Physical libration amplitude
Beuthe et al. (2016)	$190 - 194$	$34 - 42$	$19 - 27$	Gravity and shape
Hemingway et al. (2018)	~ 190	$20 - 50$	$20 - 30$	Gravity and libration
Genova et al. (2024)	$194 - 198$	$35 - 39$	~ 20	Libration
Park et al. (2024)	$197 - 200$	$21 - 26$	$27 - 33$	Gravity, shape, and libration
Bagheri et al. (2025)	$183 - 213$	$5 - 47$	$22 - 34$	Gravity, shape, libration, heat budget

4. Heat dissipation
5. Magnetic induction

As shown in Table 1.1.1, all studies carried out in the last decade are based on these observables. In Table 1.1.1, it can be observed that the studies are in agreement, with quite a variable range width for the thickness of the different layers. Furthermore, all studies are based on the science data retrieved by Cassini, except for Genova et al. (2024), who combine the amplitude of physical libration measurements by Cassini with gravity data from a simulated radio science New Frontiers-class mission.

1.2. Research question

Based on the past studies and on the science questions proposed by Ermakov et al. (2021), in line with the interest of ESA in the astrobiological potential of Enceladus, this work has the aim of assessing how a novel orbiter mission to Enceladus could contribute to the science return for the investigation of the interior structure of Saturn's second innermost moon. The mission concept includes an orbiter tracked through a two-way radio link by a GS of the ESA Estrack network. Additionally, the mission expects a set of radio beacons to be deployed on the surface of the moon. The radio beacons track the spacecraft (S/C) through a two-way radio link. They allow to directly measure the surface displacement due to tides and improve the measurement of ice shell librations, enhancing the science return of the mission. Additionally, the data provided by the radio beacons are expected to be directly sensitive to the position of the rotation pole. The number of radio beacons (nine at maximum) has been determined to ensure a feasible and realistic mission architecture that could be implemented in future operations. Their position is determined based on the latitudinal spread of the orbital ground track.

Given the current knowledge of the interior structure of Enceladus (Table 1.1.1), this work assesses how the combination of gravity, surface displacements, and librations, retrieved through the described science mission, can improve the uncertainty on the constraints of geophysical parameters of interest of the moon, with the final goal of refining our knowledge of its interior.

In this perspective, this work aims to answer the following research question:

How can a novel orbiter mission to Enceladus coupled with surface radio beacons enhance the current knowledge of its interior structure?

The research question can be answered by addressing the following sub-questions:

1. *To which level of uncertainty can radio tracking data of the orbiter and radio beacons constrain geophysical measurements of Enceladus?*
2. *What are the prospects in terms of science return on the interior structure of Enceladus, given by the constrained geophysical measurements and parameters of interest?*

Answering the first sub-question will enable to assess how the presented radio science mission can contribute to inferring physical parameters of interest of Enceladus, e. g., spherical harmonics (SH) gravity coefficients, k_2 and h_2 Love numbers, and libration amplitude. These parameters, as described in Chapter 2, can be used to infer physical properties of the interior. Hence, constraining the uncertainty associated to the geophysical parameters of interest allows to assess how much such a mission scenario would improve the knowledge of Enceladus' interior. For answering the first sub-question, a set of stable science orbits for the S/C starting from a given initial condition will be considered (Section 3.1). Afterwards, the covariance analysis given the observations, solve-for and consider parameters (Section 2.2) will be performed. The covariance analysis of the geophysical measurements is performed through the TU Delft Astrodynamics Toolbox (Tudat)[2], which enables to simulate observations and perform the covariance analysis for selected solve-for and consider parameters. Following the procedure described by Dirkx et al. (2014), the observations are simulated using the result of the numerical integration of the Equations of Motion (EoM) and the rotation and deformation model of Enceladus.

In order to provide a comprehensive overview of how the mission design parameters (e. g., number and location of landers included, mission duration, tracking arc length, etc.) and the science parameters (e. g., a priori knowledge on the rotation pole position and velocity, Kaula constraint coefficient, etc.) affect the estimation results, the analysis of a wide set of tuning variables is performed, out of which considerations for the mission architecture and nominal reference values are proposed.

Finally, once the uncertainty of the geophysical parameters of interest is retrieved, considerations on the interior structure of Enceladus can be made. Answering the second sub-question will enable to determine how the formal error of the estimated geophysical parameters translates to uncertainty on the interior model of the moon. The sub-question is addressed through a Monte Carlo (MC) analysis in order to relate the interior parameters of Enceladus (e. g., layers' thickness, density, and mechanical properties) to the observables estimated through the covariance analysis algorithm. Through this approach, it will be possible to determine which parameters are most sensitive to the observables and can be best constrained. Additionally, this work will provide reference values for an indication of the level of accuracy that the mission scenario allows to reach in determining the interior structure of Enceladus. Considering the literature on the topic (e. g., Ermakov et al. (2021), Genova et al. (2024), Bagheri et al. (2025)), the uncertainty of the interior parameters can be mapped to uncertainty values for the geophysical observables through a Markov Chain Monte Carlo (MCMC) inversion. This method was considered when the interior investigation problem was first approached. However, it was not followed up on for time-management reasons, since it was decided to dedicate more time to the core of the work for the first research sub-question, and a robust setup of the MCMC analysis required more time than the available one. The results provided by the MC approach can thus be

[2] https://docs.tudat.space/en/latest/

considered indicative and of reference but are not the result of an interior model inversion (described in Section 2.3). However, they still provide an answer to the second research sub-question, assessing the benefits of the small formal errors associated to the geophysical parameters of interest on placing constraints on the interior.

In conclusion, addressing the above sub-questions allows to answer the research question and evaluate the impact of the proposed mission scenario on the improvement of the knowledge of Enceladus' interior, which might enhance considerably our understanding of the moon's heating mechanism and its predisposition to host life. A description of the structure of the thesis is given in the following section.

1.3. Structure of the thesis

This work is structured as follows. Chapter 2 provides the theoretical basis necessary to develop and understand the content of the work. It provides a study of the models and methods available in literature concerning both covariance analysis and investigation of planetary interiors.

Chapter 3 presents a detailed overview of the mission and the setup for the rotation and gravity models for Enceladus, necessary to perform the study as outlined in Section 1.2. Additionally, Chapter 3 describes the methodology followed to answer the research question presented in Section 1.2. The covariance analysis methodology followed to answer the first research sub-question is developed in Section 3.3. The second sub-question is answered through the methodology presented in Section 3.4, which describes the parameters of interest and the applied investigation approach.

Chapter 4 provides the verification for some choices and implementation inherent to the code setup, and for the adjustment of the rotation and tide models of Enceladus. Finally, some orbit-related aspects are verified.

The results and associated discussion are provided in Chapter 5. The chapter presents first the series of results aimed to answer the first research sub-question, while the investigation of the interior model is discussed in Section 5.4 and following. The results are organized according to the different methodology sections proposed in Chapter 3.

The thesis is closed by Section 5.7 on the validation of the results, Chapter 6 for the conclusions, and Chapter 7 on the possible future work that can be built on this thesis.

Finally, the project plan and the discussion of the work rearrangements for answering the research question within the given time limits are proposed in Appendix A. It follows a presentation of complementary theory/results on the gravity field, topography, and on the choice of the acceleration and integrator settings. Additionally, some results not shown in Chapter 5 because not immediately necessary and useful are provided in the appendix for the interested reader.

It should be noted that Appendix E.2.1 provides a verification paragraph that was not included in Chapter 4 since it follows closely the discussion in Appendix E.

2. Theoretical framework

This section gives the theoretical basis necessary for developing the problem. First, an overview of the physical parameters of interest for constraining the interior of Enceladus is given in Section 2.1. Section 2.1 is followed by a discussion on how the interior of a planetary body can be constrained through geophysical measurements.

The theoretical sections on the study of planetary interiors is followed by a presentation in Section 2.2 of the estimation framework for the assessment of the uncertainty associated to the geophysical measurements of interest given the available observables.

Furthermore, Section 2.3 gives an overview of the Bayesian inversion method used to retrieve constraints on the interior of a planetary body from the inferred geophysical properties. Finally, some fundamental aspects of orbit design for a science mission at Enceladus are presented in Section 2.4.

2.1. Physical parameters of interest

This section gives an overview of the physical quantities and parameters of interest for the characterisation of Enceladus' interior.

2.1.1. Average radius

The average radius allows to constrain the interior, given that it imposes a condition on the body's dimension. Enceladus can be modelled as a triaxial ellipsoid (e. g., Porco et al. (2004), Thomas (2010), Hemingway et al. (2018), Genova et al. (2024), Park et al. (2024)). When modelling Enceladus as a triaxial ellipsoid, the average radius can be used to put a constraint on the semi-major axis of the outermost layer. Following the model by Genova et al. (2024):

$$a_3 = R_{\mathrm{E}} \tag{2.1.1}$$

where a_3 is the first semi-major axis of the ice shell and R_{E} the average moon's radius. Even if the moon is assumed to be spherically symmetric as in Bagheri et al. (2025), the average radius can still be used to put a constraint on its size. A discussion of the effects of modelling Enceladus as a triaxial ellipsoid instead of a spherically symmetric body is proposed in Section 2.1.6.

Enceladus' radius was estimated to be $252.1 \pm 0.2\,\mathrm{km}$ (Porco et al., 2006). The radius was estimated through ISS imagery.

2.1.2. Mass

Together with the average radius, the mass puts a constraint on the layers thickness and density. In case of a three-layer triaxial ellipsoid model, the mass of Enceladus can be computed with the following equation (Genova et al., 2024):

$$M_{\mathrm{E}} = \frac{4}{3}\pi \sum_{i=0}^{2} \rho_i \left(a_{i+1} b_{i+1} c_{i+1} - a_i b_i c_i\right) \tag{2.1.2}$$

where ρ_i is the mean density of the ith layer and a, b, c denote the semi-axes of the triaxial ellipsoid, with $c < b < a$. The semimajor axes can be defined as (Genova et al., 2024)

$$\begin{aligned} a_1 &= r_\mathrm{c} \\ a_2 &= r_\mathrm{c} + \vartheta_\mathrm{o} \\ a_3 &= R_\mathrm{E} \end{aligned} \tag{2.1.3}$$

where ϑ_o is the thickness of the ocean and r_c is the core radius. As a result, the mass defines a constraint on the semi-axes and the average density of the various layers of the ellipsoid. On the other hand, in case Enceladus is assumed to be spherically symmetrical, Equation 2.1.2 is simplified to

$$M_\mathrm{E} = \frac{4}{3}\pi \sum_{i=0}^{2} \rho_i \left(r_{i+1}^3 - r_i^3\right) \tag{2.1.4}$$

Enceladus's mass inferred from the Cassini radio tracking data during the moon flybys was estimated to be $(1.0798 \pm 0.0016) \times 10^{20}\,\mathrm{kg}$ (Rappaport et al., 2007).

2.1.3. Mass moment of inertia

The mass Moment of Inertia (MoI) provides information on the distribution of mass within the body: a moment of inertia larger than the one for a sphere of uniform density suggests a body whose density increases with depth (Rovira-Navarro, 2022, Chapter 1). Additionally, the MoI allows to impose a constraint on the interior structure of the moon (e. g., Bagheri et al. (2025), Genova et al. (2024), Rovira-Navarro (2022), Porco et al. (2004)). Assuming a three-layer triaxial ellipsoid model, the moment of inertia C can be computed as (Genova et al., 2024)

$$C = \frac{4}{15}\pi \sum_{i=0}^{2} \rho_i \left(a_{i+1}b_{i+1}c_{i+1}\left(a_{i+1}^2 + b_{i+1}^2\right) - a_i b_i c_i \left(a_i^2 + b_i^2\right)\right) \tag{2.1.5}$$

For a three-layer sphere, the moment of inertia reads

$$C = \frac{4}{15}\pi \sum_{i=0}^{2} \rho_i \left(r_{i+1}^5 - r_i^5\right) \tag{2.1.6}$$

The moment of inertia can be determined through gravity measurements, as discussed in Section 2.1.5. Enceladus' moment of inertia was estimated to be equal to $0.335MR^2$ (Iess, Stevenson, et al., 2014b).

2.1.4. Gravity coefficients

Gravity field measurements are key to study the interior of a planetary body (e. g., Wieczorek (2015), Ermakov et al. (2021), Gomez Casajus et al. (2022)). As presented in Appendix B, the gravity field can be expressed in terms of a spherical harmonics expansion. Both the static and dynamic information entailed by the gravity field provides insights on the interior properties of a planetary body. For instance, the $C_{2,0}$ and $C_{2,2}$ coefficients provide information on the long-term fluid behaviour of the moon in response to the centrifugal and tidal perturbing potentials (Appendix B). On the other hand, the gravitational response of the moon to a periodic forcing, as described by the k_2 Love number (see Section 2.1.6), leads to insights in the dynamical and energy dissipation mechanisms within the moon (e. g., Rovira-Navarro (2022)).

With respect to Enceladus, it ought to be noted that it is a body in non-hydrostatic equilibrium, as determined by Iess, Stevenson, et al. (2014b) through the SH degree 2 cosine gravity coefficients ratio $C_{2,0}/C_{2,2} \neq \frac{10}{3}$, a value expected for bodies in hydrostatic equilibrium. The fact that Enceladus is non-hydrostatic implies that its topography, defined as $r_3 - h_3$, where h_3 is the equipotential surface

with mean radius r_3, is non-zero, and therefore it must be maintained either by elastic support, isostasy, and/or dynamical processes in the ice shell (Čadek et al., 2016). Isostatic variations in the thickness of the ice shell may contribute to the support of Enceladus' non-hydrostatic interior structure (McKinnon, 2013). Additionally, the cold and rigid exterior contributes to the support of a non-hydrostatic equilibrium of gravity and pressure (Hemingway et al., 2018).

The gravity field harmonic coefficients are of interest for constraining the degree of differentiation of the interior (e. g., Scheeres et al. (2001)). In particular, the degree-2 harmonic coefficients can be used to determine the MoI for a non-hydrostatic body, as presented in Section 2.1.5. Additionally, the zonal component of degree three of the gravity field (J_3) allows to impose a further constraint on the triaxial ellipsoid model for a non-hydrostatic body (Genova et al., 2024):

$$J_3 = \frac{1}{4} Z_T \frac{R_\mathrm{E}^2}{GM} H_{30}^\mathrm{nh} \tag{2.1.7}$$

where

$$Z_T(l) = 4\pi G \left(\frac{l+1}{2l+1}\right) \rho_\mathrm{s} \left[1 - \left(1 - \frac{\vartheta_\mathrm{s}}{R_\mathrm{E}}\right)^{l+2} \left(\frac{g_\mathrm{top}}{g_\mathrm{bottom}}\right) f_{l0}\right] \tag{2.1.8}$$

is the gravity/topography admittance. In (2.1.7), H_{30}^nh is the zonal non-hydrostatic component of the degree 3 for the topography spherical harmonics expansion (further details on the hydrostatic and non-hydrostatic terms are given in Section 2.1.5). Additionally, in (2.1.8), ϑ_s is the mean shell thickness, while g_top and g_bottom are the point mass gravity accelerations at the top and bottom of the shell, respectively:

$$\begin{aligned} g_\mathrm{top} &= \frac{GM}{R_\mathrm{E}^2} \\ g_\mathrm{bottom} &= \frac{GM}{\left(r + \vartheta_\mathrm{o}\right)^2} - \frac{4}{3}\pi G \rho_\mathrm{s} \frac{R_\mathrm{E}^3 - \left(r_\mathrm{c} + \vartheta_\mathrm{o}\right)^3}{\left(r_\mathrm{c} + \vartheta_\mathrm{o}\right)^2} \end{aligned} \tag{2.1.9}$$

The investigation of the higher degree gravity coefficients can be used to correlate topographic features to gravity (e. g., Goossens et al. (2020)). Additionally, the inclusion of the higher degree gravity coefficients avoids an overoptimistic estimate of the lower degree terms, since the same observational information is used to estimate a higher number of parameters (a more complete discussion on the estimation framework is provided in Section 2.2).

2.1.5. Topography

Similarly to the gravity field quadrupole, also the topography spherical harmonics expansion, presented in Appendix C, is necessary for the determination of the MoI for a body in non-hydrostatic equilibrium, as discussed below. Furthermore, the non-hydrostatic term of the degree-3 zonal harmonic component feeds into (2.1.7). The topography data can be retrieved via an on-board altimeter, through reconstruction of a global network of control points, based on the selected orbit and on the sampling frequency of the altimeter (e. g., Durante et al. (2024)).

From gravity and topography measurements to moment of inertia

As already mentioned, one of the physical quantities allowing the determination of the level of differentiation of a celestial body is the mass MoI (e. g., Schubert et al. (2007)).

For bodies in hydrostatic equilibrium, the Darwin-Radau relation (Murray & Dermott, 2000) for the MoI factor holds:

$$\overline{C} = \frac{C}{M^* R^2} = \frac{2}{3}\left[1 - \frac{2}{5}\left(\frac{5}{2}\frac{q}{f} - 1\right)^{1/2}\right] \tag{2.1.10}$$

where

$$q = \frac{\dot{\Omega}^2 a^3}{GM} \tag{2.1.11}$$

is the ratio of the centrifugal acceleration at the equator to the gravitational acceleration and

$$f = \frac{\overline{a} - \overline{b}}{\overline{a}} \tag{2.1.12}$$

is the flattening of the body. However, as already mentioned in Section 2.1.4, Iess, Stevenson, et al. (2014b) showed that the value of J_2/C_{22} for Enceladus differs from the value required for hydrostatic equilibrium $\left(\frac{10}{3}\right)$ of about 5%. Hence, the non-hydrostatic behaviour of the moon ought to be taken into account when studying its interior.

Gravity measurements have proved to be relevant in order to study the internal structure of Enceladus (Table 1.1.1). Considering that it is non-hydrostatic (Iess, Stevenson, et al., 2014b), in order to retrieve its MoI, the gravitational quadrupole can be used. The observed degree-2 coefficients for gravity $\left({J_2}^{\text{obs}}, C_{22}^{\text{obs}}\right)$ and topography $\left(H_{20}^{\text{obs}}, H_{22}^{\text{obs}}\right)$ can be computed through the linear sum of the hydrostatic and non-hydrostatic parts, with the assumption that the non-hydrostatic parts are small with respect to the hydrostatic ones (Genova et al., 2024, Section 3.1). Hence

$$\begin{aligned} {J_2}^{\text{obs}} &= {J_2}^{\text{hyd}} + {J_2}^{\text{nh}} \\ C_{22}^{\text{obs}} &= C_{22}^{\text{hyd}} + C_{22}^{\text{nh}} \\ H_{20}^{\text{obs}} &= H_{20}^{\text{hyd}} + H_{20}^{\text{nh}} \\ H_{22}^{\text{obs}} &= H_{22}^{\text{hyd}} + H_{22}^{\text{nh}} \end{aligned} \tag{2.1.13}$$

For the gravitational quadrupole, in order to separate the hydrostatic terms from the non-hydrostatic ones, Genova et al. (2024) and Mckinnon (2015) assume a two-layer ellipsoid model for Enceladus and compute the hydrostatic terms through a numerical approach introduced by Tricarico (2014). The iterative approach is presented for completeness in Appendix D.

For the topography quadrupole, the harmonic hydrostatic coefficients are obtained through the following formulation (Genova et al., 2024):

$$\begin{aligned} H_{20,i}^{\text{hyd}} &= -a_i \left(\frac{2}{3}\alpha_i + \frac{1}{7}\alpha_i^2 - \frac{1}{3}\alpha_{1_i} - \frac{1}{7}\alpha_i \alpha_{1_i} - \frac{1}{3.7}\alpha_i^3 \right) \\ H_{22,i}^{\text{hyd}} &= \frac{1}{6} a_i \left(\alpha_{1_i} - \frac{3}{7}\alpha_i \alpha_{1_i} \right) \end{aligned} \tag{2.1.14}$$

where α_{1_i} is the equatorial flattening, and α_i is the flattening of the meridional section of the triaxial ellipsoid in whose plane lies the semi-major axis of the ith layer (Genova et al., 2024):

$$\begin{aligned} \alpha_{1_i} &= \frac{a_i - b_i}{a_i} \\ \alpha_i &= \frac{a_i - c_i}{a_i} \end{aligned} \tag{2.1.15}$$

Once the hydrostatic components have been determined through the iterative numerical procedure proposed by Tricarico (2014) (refer to Appendix D), the non-hydrostatic parts can be computed through Equation 2.1.13 by subtracting the hydrostatic terms from the measured coefficients.

The ratio between the gravity and topography harmonic coefficients of the same degree and order leads to the components of the spectral admittance (presented in Appendix C):

$$\begin{aligned} Z_{20} &= -\frac{J_2^{\text{nh}}}{H_{20}^{\text{nh}}} \\ Z_{22} &= \frac{C_{22}^{\text{nh}}}{H_{22}^{\text{nh}}} \end{aligned} \tag{2.1.16}$$

If the shell is assumed to have no significant lateral variations of the mechanical properties, then the non-hydrostatic topography is expected to influence equally the zonal and sectoral gravity coefficients (Hemingway et al., 2018). Hence, the condition $Z_{20} = Z_{22}$ is expected under the assumption of negligible lateral variations of the mechanical properties of Enceladus' shell. Thus, given the simplified two-layer model, by keeping fixed the density of the ice shell $\left(\rho_s = 925 \text{ kg m}^{-3}\right)$ and varying the density of the core between $2000 - 3000 \text{ kg m}^{-3}$ (Genova et al., 2024), the intersection of the admittances gives the expected value of MoI (see Figure 2.1.1).

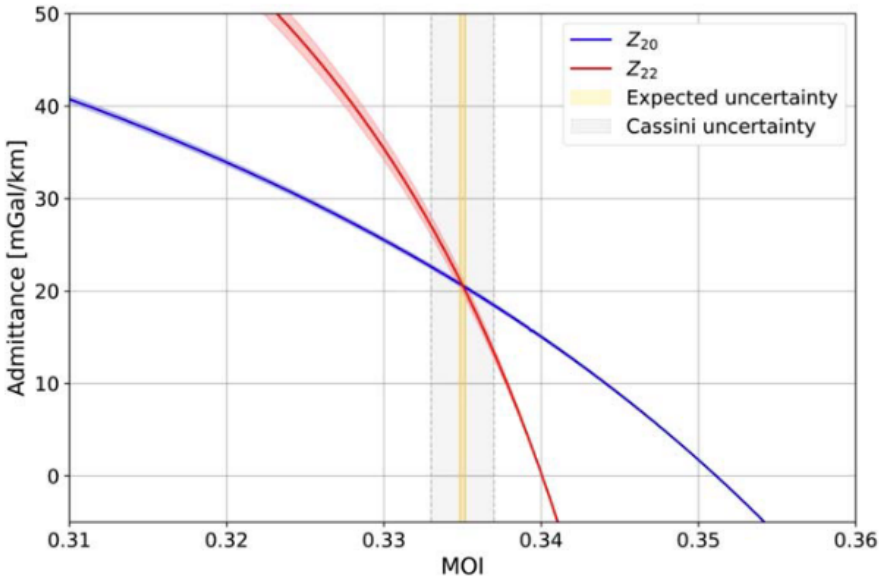

Figure 2.1.1.: Degree-2 admittances as a function of the MoI factor. The plot is retrieved from Genova et al. (2024) and was produced with a two-layer model by accounting for the fourth-order expression for equilibrium figures (Tricarico, 2014). Ice density is considered fixed, and only the density of the rocky core is varied. The intersection of the admittances leads to the expected MoI.
Image credits: Genova et al. (2024).

Furthermore, the admittance gives an indication of the degree to which topography is compensated and the depth at which compensation occurs (Iess, Stevenson, et al., 2014a). Compensation factors indicate to what extent the gravity due to excess surface topography is compensated at depth by a mass deficit or excess. Such factors depend on the harmonic degree (Mckinnon, 2015). To determine the degree and depth of Airy isostatic compensation, the formula for the admittance Z_{lm} presented by Iess, Stevenson, et al. (2014a) for the case of surface loading can be considered:

$$Z_{lm} = \frac{3\rho_s}{(2l+1)\,R\overline{\rho}} \left[1 - C' \left(1 - \frac{d}{R}\right)^l\right] \tag{2.1.17}$$

In the equation, the degree of compensation C' is zero when the topography loading is uncompensated, while is equal to one when the topography is fully compensated (Iess, Stevenson, et al., 2014a). Equation 2.1.17 can be rewritten as a function of the compensation factor f_{lm}, which entails both the degree of compensation and the compensation depth:

$$Z_{lm} = \frac{3\rho_s}{(2l+1)\,R\overline{\rho}} f_{lm} \tag{2.1.18}$$

If complete Airy compensation is assumed, then $f_{lm} = 1 - (1 - d/R)^l$. Since, as explained above, $Z_{20} = Z_{22}$ when isotropic admittance is assumed, given the negligible lateral variations of the mechanical properties of the shell, then in this situation $f_{20} = f_{22}$.

To check *a posteriori* the assumption of isotropic admittance, the $(3, 0)$ terms of gravity and topography can be used (Iess, Stevenson, et al., 2014a) to compute the spectral admittance Z_{30} (Equation C.0.4). Assuming a fully isostatic ice shell, the ratio Z_{20}/Z_{30} should be approximately 0.991, if the properties

given in Iess, Stevenson, et al. (2014a, Table S6) are assumed. Hence, if the measured value of Z_{30} is corrected by this factor to obtain the equivalent degree-2 value, in case of intersection with Z_{20} and Z_{22}, it provides an *a posteriori* check on the assumption of isotropic admittance (see Figure 2.1.2).

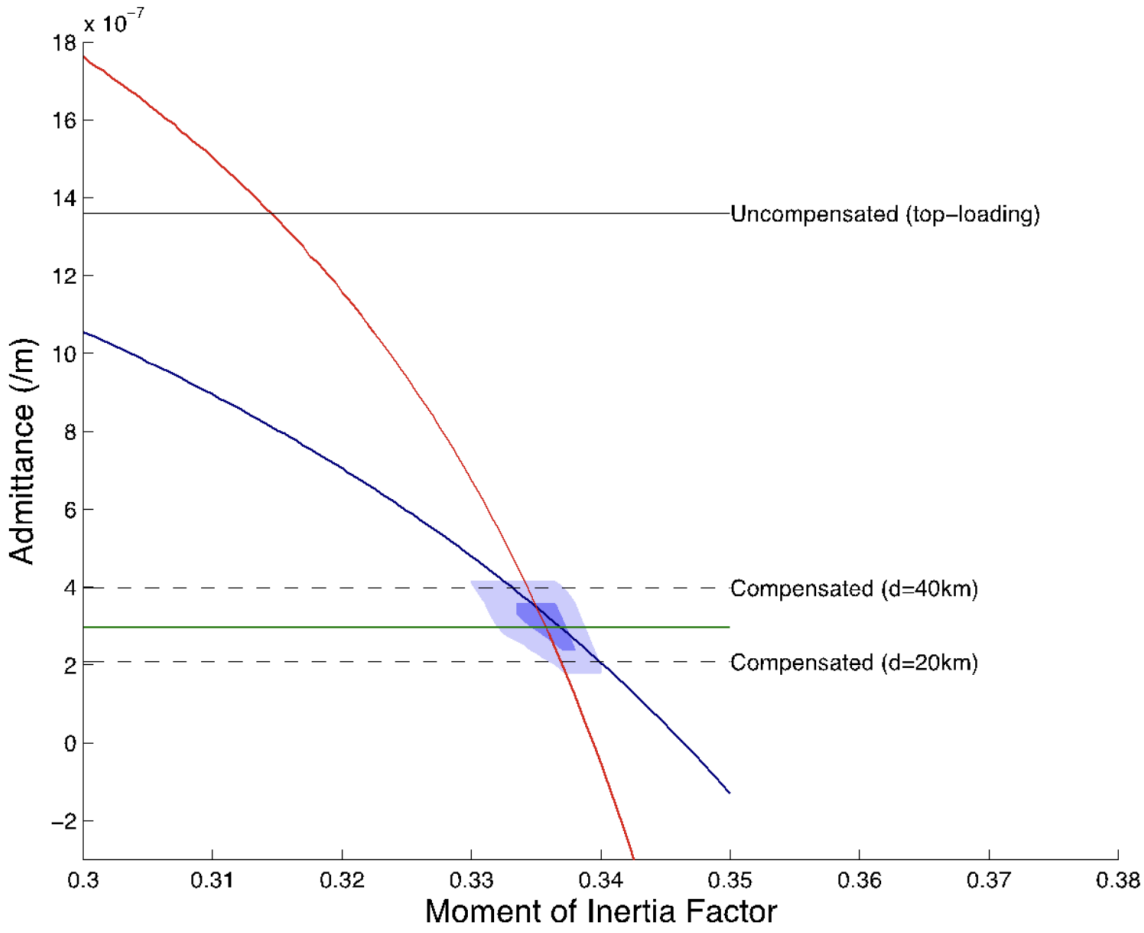

Figure 2.1.2.: Degree-2 and 3 admittances as a function of the MoI. The plot shows the region of 1-σ (dark blue) and 2-σ (pale blue) agreement between the admittances estimated separately from the $(2,0)$ (blue line), $(2,2)$ (red line), and $(3,0)$ (green line) gravity and topography terms. The $(3,0)$ term was multiplied by 0.991 to obtain the equivalent degree-2 value. The solid line at $\sim 14 \times 10^{-7}$ m^{-1} represents the admittance expected for uncompensated topography. The dashed horizontal lines represent the admittances for fully compensated topography.
Image credits: Iess, Stevenson, et al. (2014a).

The region of agreement of the admittances can also be obtained by performing a MC analysis by varying the gravity and topography coefficients normally distributed according to their formal uncertainties.

As mentioned already in Section 2.1.3, Iess, Stevenson, et al. (2014b) determined a MoI of $0.335MR^2$, equal to the value found by Genova et al. (2024).

2.1.6. Love numbers

The gravitational and radial Love numbers of degree 2, k_2 and h_2, describe respectively the response of the gravity field and radial shape of the body to the perturbing rotational, tidal, and surface loading potential (e. g., Sabadini et al. (2016), Hussmann et al. (2016)). The Love numbers depend on the internal properties of the body (Rovira-Navarro, 2022). As described by Sabadini et al. (2016), the Love numbers are a function of the material stratification and of the harmonic degree l.

The tidal potential due to the gradient of the gravitational force that a body experiences because of a perturbing object can be described as (Rovira-Navarro, 2022):

$$U^{\mathrm{T}} = -\frac{GM^*}{d^*}\sum_{l=2}^{\infty}\left(\frac{r}{d^*}\right)^l P_l\left(\cos\psi\right) \tag{2.1.19}$$

In (2.1.19), d^* is the distance between the centres of the perturbed and perturbing body, r is the distance from the point at which the potential is computed to the centre of the perturbed, and finally ψ is the angle between $\mathbf{r}$ and $\mathbf{d}^*$. P_l is a Legendre polynomial of degree l.

If the perturbing body is orbiting around the perturbed one, considering a reference frame fixed on the latter, the geometrical parameters d^* and ψ can be expressed in terms of the orbital parameters of the perturbing object:

$$\begin{aligned} d^* &= f\left(a^*, e^*, \nu^*\right) \\ \psi &= f\left(\theta, \varphi, i^*, \gamma^*, \omega^*, \nu^*\right) \end{aligned} \tag{2.1.20}$$

where a^* is the semi-major axis of the perturbing object, e^* is its eccentricity, and ν^* is the true anomaly. Furthermore, θ is the co-latitude, φ is the longitude in the rotating frame rotating with the object, i^* is the angle between the rotational axis and the normal to the orbital plane. By substituting the expressions in (2.1.20), a more physically intuitive expression for the tidal potential is obtained (Rovira-Navarro, 2022, Equation 2.3). Considering only the leading lower order terms, the following expression for the tidal potential can be derived:

$$U^{\mathrm{T}} = -\left(\overline{n}R\right)^2\left(\frac{r}{R}\right)^2\left(U_0^{\mathrm{T}} + U_e^{\mathrm{T}} + U_i^{\mathrm{T}}\right) \tag{2.1.21}$$

with

$$\begin{aligned} U_0^{\mathrm{T}} &= -\frac{1}{2}P_{20}\left(\cos\theta\right) + \frac{1}{4}P_{22}\left(\cos\theta\right)\cos\varphi \\ U_e^{\mathrm{T}} &= e^*\left(-\frac{3}{2}P_{20}\left(\cos\theta\right)\cos\left(\overline{n}^* t\right) + \frac{3}{4}P_{22}\left(\cos\theta\right)\cos 2\varphi\cos\left(n^* t\right) + P_{22}\left(\cos\theta\right)\sin\left(2\varphi\right)\sin\left(\overline{n}^* t\right)\right) + O\left(e^{*2}\right) \\ U_i^{\mathrm{T}} &= \sin i^* P_{21}\left(\cos\theta\right)\cos\varphi\sin\left(\omega^* + \overline{n}^* t\right) + O\left(\sin^2 i^*\right) \end{aligned} \tag{2.1.22}$$

The first component, U_0^{T}, is the tide that the moon would experience for a circular equatorial orbit, leading to a frozen bulge. As discussed by Murray and Dermott (2000), since the line connecting the moon to the empty focus of the orbit moves with the same velocity as the mean motion of the moon, the frozen bulge points towards the empty focus. As a result, the body is characterised by a permanent gravity field and surface variation, as it will be discussed later in this section. The other two components have diurnal frequency and are respectively the eccentricity term $\left(U_e^{\mathrm{T}}\right)$, which is caused by the eccentric orbit, and the obliquity term $\left(U_i^{\mathrm{T}}\right)$, that arises when the orbit is not equatorial. The eccentricity tide is generated due to the fact that the distance between the moon and the planet varies along the orbit, leading to a variable amplitude of the tide. Furthermore, because of the variable velocity of the moon between the pericentre and apocentre, the tidal bulge librates with respect to the reference meridian of the frozen bulge (see Figure 2.1.3). The librating component of the eccentricity tide is given by the terms of U_e^{T} in (2.1.22) dependent on the longitude of the planet in the moon's fixed reference frame. On the other hand, the obliquity tide is dependent on the angle between the orbital plane of the moon and the rotation axis of the planet, produced by the latitudinal libration of the planet (see Figure 2.1.3). The eccentricity and obliquity tides lead to a time-dependent tidal potential (see Equation 2.1.22) and gravity field variations (discussed later in this section).

As presented in Efroimsky and Makarov (2013), the Love numbers k_l are used to describe the change $\Delta U\left(\mathbf{r}\right)$ of the moon's potential at a certain surface location $\mathbf{R} = (R, \varsigma, \varphi)$, with R being the body's radius, ς the latitude and φ the longitude, as a function of the perturber's potential $U^{\mathrm{perturber}}$:

$$\Delta U\left(\mathbf{r}^{\mathrm{perturber}}\right) = \sum_{l=2}^{\infty} k_l\left(\frac{R}{r}\right)^{l+1} U^{\mathrm{perturber}}\left(\mathbf{R}, \mathbf{r}^{\mathrm{perturber}}\right) \tag{2.1.23}$$

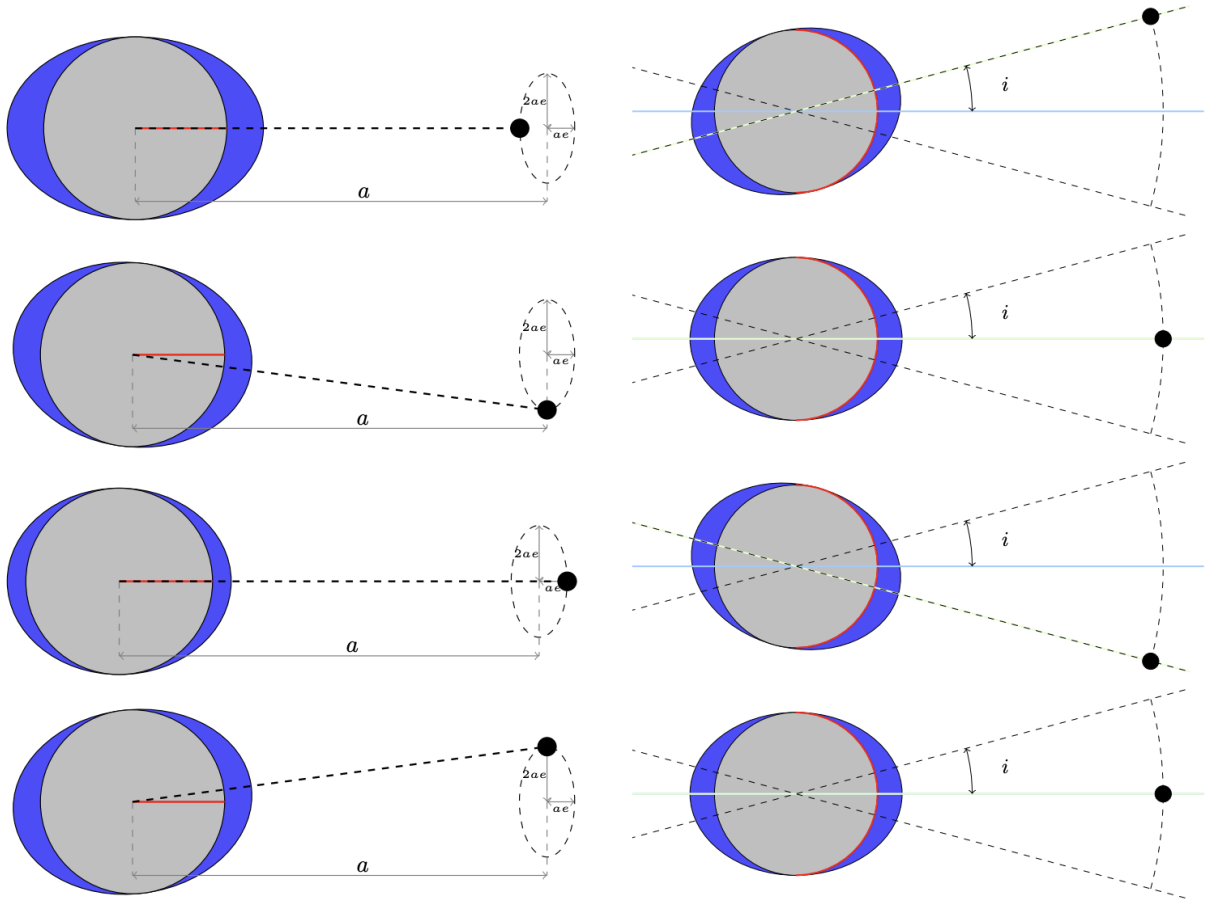

(a) Eccentricity tide. **(b)** Obliquity tide.

Figure 2.1.3.: Dynamic tides for a tidally locked moon in the moon-fixed reference frame. The red line corresponds to the reference meridian, which is directed towards the point that the planet would occupy if the orbit of the moon was circular.
Image credits: Rovira-Navarro (2022).

where $\mathbf{r}^{\text{perturber}}$ is the location of the perturber in the reference frame fixed on the tidally perturbed body. Since planetary bodies possess a viscoelastic behaviour, their response to an external forcing is not instantaneous but is characterized by a time delay. Hence, the planet's response lags behind with respect to the one of an elastic body. Considering the lagging tidal potential, the radial and lateral displacements of the moon due to tides can be described through the Love numbers (Rovira-Navarro, 2022):

$$\begin{aligned} u_r\left(r,\theta,\varphi,t\right) &= \Re\left\{\frac{h\left(r,\theta,\varphi\right)}{g_0}U^{\mathrm{T}}\left(R,\theta,\varphi,t\right)\right\} = -\frac{|h|}{g_0}\left[U^{\mathrm{T}}\right]_{\mathrm{lag}} \\ \mathbf{u}_{\theta,\varphi}\left(r,\theta,\varphi,t\right) &= \Re\left\{\frac{l\left(r,\theta,\varphi\right)}{g_0}\nabla_{\theta,\varphi}U^{\mathrm{T}}\left(R,\theta,\varphi,t\right)\right\} = -\frac{|l|}{g_0}\left[\nabla_{\theta,\varphi}U^{\mathrm{T}}\right]_{\mathrm{lag}} \\ U\left(r,\theta,\varphi,t\right) &= \Re\left\{\left[\left(\frac{r}{R}\right)^l + k\left(r,\theta,\varphi\right)\right]U^{\mathrm{T}}\left(R,\theta,\varphi,t\right)\right\} = \left(\frac{r}{R}\right)^l U^{\mathrm{T}} + |k|\left[U^{\mathrm{T}}\right]_{\mathrm{lag}} \end{aligned} \tag{2.1.24}$$

where

$$\nabla_{\theta,\varphi} = \left(\frac{\partial}{\partial\theta}, \frac{1}{\sin\theta}\frac{\partial}{\partial\varphi}\right) \tag{2.1.25}$$

In (2.1.24), u_r is the radial surface displacement, $\mathbf{u}_{\theta,\varphi}$ is the lateral surface displacement, while U describes the gravitational tidal response of the body. Hence, the h and l Love numbers relate the tidal perturbation to the radial and lateral displacement, while the k tidal Love number indicates how the gravity field is affected by the tidal potential. The tidal gravity response of the body is described

by the variation of the normalized gravity field coefficients $\Delta\bar{C}_{lm}$ and $\Delta\bar{S}_{lm}$, computed according to (2.1.26) (Petit & Luzum, 2010):

$$\Delta\bar{C}_{lm} - i\Delta\bar{S}_{lm} = \frac{k_{lm}}{2l+1}\frac{GM_j}{GM^*}\left(\frac{R}{r_j}\right)^{l+1}\bar{P}_{lm}\left(\cos\theta\right)e^{-im\varphi} \tag{2.1.26}$$

with M_j and M^* being the masses of the tide-raising and deforming body respectively, and R and r_j are respectively the deforming body radius and the distance between the two bodies. In terms of real spherical harmonics, the variation of the normalized spherical harmonic coefficients translates to

$$\Delta\bar{C}_{lm} = \frac{k_{lm}}{2l+1}\frac{GM_j}{GM^*}\left(\frac{R}{r_j}\right)^{l+1}\bar{P}_{lm}\left(\cos\theta\right)\cos\left(m\varphi\right) \tag{2.1.27a}$$

$$\Delta\bar{S}_{lm} = \frac{k_{lm}}{2l+1}\frac{GM_j}{GM^*}\left(\frac{R}{r_j}\right)^{l+1}\bar{P}_{lm}\left(\cos\theta\right)\sin\left(m\varphi\right) \tag{2.1.27b}$$

As for the surface displacement, the position displacement of a point on the surface of a tidally deformed body can be computed according to Equation 2.1.28 (Petit & Luzum, 2010):

$$\Delta\mathbf{r} = \frac{GM_jR}{GM^*r_j}\left\{h_2\hat{\mathbf{r}}\left(\frac{3\left(\hat{\mathbf{r}}_j\cdot\hat{\mathbf{r}}\right)^2-1}{2}\right)+3l_2\left(\hat{\mathbf{r}}_j\cdot\hat{\mathbf{r}}\right)\left[\hat{\mathbf{r}}_j-\left(\hat{\mathbf{r}}_j\cdot\hat{\mathbf{r}}\right)\hat{\mathbf{r}}\right]\right\} \tag{2.1.28}$$

It should be noted that modelling Enceladus as a triaxial ellipsoid allows to take into account the shape effect of the permanent equatorial bulge produced by the tides raised by Saturn on Enceladus. Deviation of a body from spherical symmetry can affect its tidal response (e. g., Berne et al. (2023)). Bagheri et al. (2025) performed a sensitivity study of the impact of lateral variations in the shell, deviating from the assumption of spherical symmetry. They observed larger surface displacements with respect to the symmetrical case, leading to conservative estimates for the Love numbers.

For viscoelastic bodies, the Love numbers are complex numbers, while for perfectly elastic bodies they are real numbers. The imaginary term of the number relates to the energy dissipation due to tides. For a synchronous satellite (Rovira-Navarro, 2022):

$$\dot{E} = -\Im\left(k_2\right)\frac{\left(\overline{n}^*R\right)^5}{G}\left(\frac{21}{2}e^{*2}+\frac{3}{2}\sin^2 i^*\right) \tag{2.1.29}$$

If the inclination of the moon's orbit about the central planet is assumed negligible, (2.1.29) becomes (Segatz et al., 1988):

$$\dot{E} = -\frac{21}{2}\Im\left(k_2\right)\frac{\left(\overline{n}^*R\right)^5}{G}e^{*2} \tag{2.1.30}$$

It can be observed that for an equatorial circular orbit, (2.1.29) leads to an energy dissipation equal to zero, since the tidal bulge is frozen and there is no external forcing that causes the tides to librate with respect to the reference meridian.

The imaginary part of the k_2 Love number is related to the quality factor Q, which is related to the interior properties of the moon (Segatz et al., 1988):

$$\left|\Im\left(k_2\right)\right| = \frac{\left|k_2\right|}{Q} \tag{2.1.31}$$

The quality factor is proportional to the ratio of energy stored in tidal motion to the energy dissipated over one tidal cycle. It can be expressed as a function of the tidal lag ϵ (Y. Wu, 2005):

$$Q = \frac{1}{\tan 2\epsilon} \approx \frac{1}{2\epsilon} \tag{2.1.32}$$

Another useful piece of information which is provided by the gravitational and radial displacement Love number is the phase lag difference (Hussmann et al., 2016). The phase lag difference $\Delta\overline{\phi}$ is the difference between the phase lag of k_2 and the phase lag associated to h_2:

$$\Delta\overline{\phi} = \overline{\phi}_{k_2} - \overline{\phi}_{h_2} \tag{2.1.33}$$

where

$$\begin{aligned} \overline{\phi}_{k_2} &= \arctan \frac{\Im(k_2)}{\Re(k_2)} \\ \overline{\phi}_{h_2} &= \arctan \frac{\Im(h_2)}{\Re(h_2)} \end{aligned} \tag{2.1.34}$$

are the phase lags of k_2 and h_2 respectively. The phase lags are produced by a delay of the moon's response to the periodic forcing due to the viscosity of the ice and silicate rock. In case of tidal friction, a satellite's response to the periodic forcing has a time-lag due to relaxation times related to the viscosity of the planetary material (ice or silicate rock). The time-lag causes a geometrical lag, meaning that the tidal bulge of Enceladus is slightly offset with respect to the direction to Saturn (Hussmann et al., 2016).

As already mentioned in Section 1.1, Enceladus is constituted by a rocky core, on top of which a subsurface ocean lies, covered by an outer ice shell layer. The ocean mechanically decouples the ice shell from the core (e. g., Hussmann et al. (2016), Matsuyama et al. (2018)), hence the phase lag of Enceladus' surface displacement is mostly dependent on the viscosity of the ice shell, even if the two layers are still gravitationally coupled. On the other hand, the phase lag of the moon's gravity field depends on both the viscosity of the core and ice shell, because both have a gravity signal contributing to the gravity field of the body. In particular, a low-viscosity core leads to a large gravity phase lag but has a smaller effect on the surface-displacement phase lag due to the mechanical decoupling of the core and shell. On the contrary, a low-viscosity ice shell produces phase lags in the gravity field and surface displacements of similar magnitude (Rovira-Navarro, 2022). The phase-lag difference becomes large if the outer shell is mechanically decoupled from the deep interior by a liquid layer (Hussmann et al., 2016). As a result, the difference between gravity and surface displacement phase-lags allows to distinguish between a low-viscosity and high-viscosity core and brings information on the interior of the moon.

A tidal phase lag would affect the orbit of the spacecraft, since the geometrical lag of the shell and of the core affect the potential of the body, according to (2.1.24). Thus, the measured response would lag the one expected from the perturbing potential. Hence, $\Im(k_2)$ can be derived through radio tracking of the S/C (Ermakov et al., 2021). On the other hand, the surface displacements phase lag, dependent on $\Im(h_2)$, can be derived through satellite altimetry (Steinbrügge et al., 2018) or through knowledge of the deformation of the shape of the moon through a network of radio beacons as included in the considered mission scenario (Section 1.2).

2.1.7. Longitudinal libration amplitude

Physical librations are periodic variations in the rotation rate of a body. Given the torque that produces the librations, the measurement of the amplitude of the moon's response can bring information on its interior (e. g., Comstock and Bills (2003)), such as ocean and ice shell thickness (Thomas et al., 2016).

The libration of Enceladus is caused by its non-spherical dynamical figure. The equatorial bulge due to the moon's rotation and the deformation because of the tides lead to a gravitational torque generated by Saturn, which affects the rotational motion of the body, (e. g., Rambaux et al. (2010), Hoolst et al. (2016)). As described by Murray and Dermott (2000), for a synchronously rotating satellite on an eccentric orbit, the line joining the orbiting mass to the empty focus of its orbit rotates at the same rate as the mean motion of the orbiting mass. Hence, a synchronously rotating moon rotates with

the frozen tidal bulge pointed towards the empty focus, where the planet would lie if the orbit of the moon was circular. Now, since the orbit of Enceladus is elliptical with an eccentricity of 0.0047 (Porco et al., 2006), the planet moves on an ellipse in a reference frame fixed to the moon and rotating with it. As a result, in addition to the frozen bulge, an elastic bulge librating with respect to the direction to the empty focus is to be considered. Hence, the moon is characterized by a tidal bulge oscillating with respect to the reference direction (Murray & Dermott, 2000, Chapter 4). The body's librational response to the gravitational forcing of the planet is dependent on the inertia of the body.

The equation for the libration angle of a moon in synchronous spin-orbit resonance, after linearization to the first order of the non-linear differential equation for the libration angle, is given by Rambaux et al. (2010, Equation 6). The equation is composed of an oscillatory term and a damping term accounting for the moon's viscoelastic properties. The dissipating term has the effect of introducing a negative shift in the moon's librational phase, which is not equal to the phase of the forcing, as it would be in case of no internal dissipation.

Rambaux et al. (2010) report three main longitudinal librational oscillations for Enceladus, based on Vienne A. and Duriez L. (1995), reported in Table 2.1.1. Enceladus is in a 1:1 spin-orbit resonance with Saturn (e. g., Hemingway et al. (2018), Oberst et al. (2017), Mckinnon (2015)), to which is associated the short-period libration, related to the mean anomaly l (Rambaux et al., 2010). The long-period libration of 11 years is due to the 2:1 orbital resonance with Dione, while the 3.7 years long libration is caused by the proper pericentre ϕ_4 of Dione. The resonance with Dione, other than exciting Enceladus' orbital eccentricity, produces a torque on the moon, due to its non-spherical figure. This leads to a libration mode associated to the resonant forcing.

The rotation model of Enceladus for the orientation of the spin axis and the rotation of the prime meridian around the spin axis is described by Park et al. (2024, Equations 4, 5, and 6). The model is a least-squares fit of the SAT441 ephemeris for the Saturnian system (Jacobson, 2022) and is a function of the epoch expressed both in centuries and days since J2000. The general formulation for the rotation model elaborated by Park et al. (2024) for the right ascension (α) and declination (δ) of the spin-axis pole, and the longitude of the prime meridian (W) is defined as:

$$\alpha^{\text{s-a}}(t) = \alpha_0^{\text{s-a}} + \dot{\alpha}_0^{\text{s-a}} t + \sum_{j=1}^{q} A_j \sin\left(\dot{\Omega}_j(t) + \Omega_j\right) \tag{2.1.35}$$

$$\delta^{\text{s-a}}(t) = \delta_0^{\text{s-a}} + \dot{\delta}_0^{\text{s-a}} t + \sum_{j=1}^{q} B_j \cos\left(\dot{\Omega}_j t + \Omega_j\right) \tag{2.1.36}$$

$$W(t) = W_0 + \dot{W}_0 t + \sum_{j=1}^{q} W_j \cos\left(\omega_j d + \gamma_j\right) \tag{2.1.37}$$

where $(\alpha_0, \delta_0, W_0)$ are constant terms; $\left(\dot{\alpha}_0, \dot{\delta}_0, \dot{W}_0\right)$ are rate terms; q is the number of terms in the nutation series; (A_j, B_j, W_j) are respectively the nutation amplitudes of α and δ, and the libration amplitude; $\left(\dot{\Omega}_j, \omega_j\right)$ are respectively the nutation frequency of α and δ and the libration frequency; (Ω_j, γ_j) are the respective phases; t is the time in seconds since J2000 and d is the time in days since J2000. The notation was retrieved by Archinal et al. (2018). The complete expressions for the rotation angles are given in Park et al. (2024, Equations 4, 5, 6). As it can be observed in (2.1.35) to (2.1.37), the formulation includes constant, linear, and librations terms. In their formulation, Park et al. (2024) accounted for the observed forced longitudinal libration of Enceladus.

Enceladus' libration periodicities listed in Table 2.1.1 were retrieved by Rambaux et al. (2010) by considering the following equation to describe the longitudinal libration motion:

$$\phi = M_d \sin\left(\omega_d t + \beta_d\right) e^{-\lambda_d t} + \sum_i B_i \sin\left(\omega_i t + \gamma_i + \beta_i\right) \tag{2.1.38}$$

Table 2.1.1.: Main physical librations of Enceladus for $(c-b)/a = 0.0168$, corresponding to a shell thickness of 82 km, a shell density of 1000 kg/m^3, and a rock density of 3000 kg/m^3. A global subsurface ocean was not accounted for. By varying the mass distribution, values for the short-period libration in the range $112 - 139$ m where found. Retrieved from Rambaux et al. (2010). The notation from Vienne A. and Duriez L. (1995) is applied: l is Enceladus' mean anomaly; ω_2 is the libration argument of the Enceladus-Dione resonance; ϕ_4 is the proper pericentre of Dione.

i	Argument	Period, $(2\pi/\omega_i)$ [days]	Magnitude, (M_i) [m]	Phase, (γ_i) [deg]
1	l	1.37	127	27.83
2	ω_2	4035.64	1.14×10^3	-83.26
3	ϕ_4	1418.93	827	128.68

(2.1.38) is composed of a damping term and an exciting term. The damping term is proportional to $e^{-\lambda_d t}$, where λ_d is the damping coefficient at the resonant frequency and its resonant frequency is $\lambda_d = \sqrt{\omega_0^2 - \gamma_d^2}$. Furthermore, M_d is the amplitude of the damping term, while β_d is its phase. The damping term accounts for the heat dissipation that occurs due to the libration of tides. Furthermore, ω_i is the frequency of the considered libration periodicity and γ_i their relative phase. The terms B_i and β_i are

$$B_i = \sqrt{\frac{M^2\left(4\lambda_i^2\omega_i^2 + \omega_0\right)}{\left(\omega_0^2 - \omega_i^2\right)^2 + 4\lambda_i^2\omega_i^2}} \tag{2.1.39}$$

$$\beta_i = \arctan\left(\frac{-2\lambda_i\omega_i^3}{\left(\omega_0^2 - \omega_i^2\right)^2 + 4\lambda_i\omega_i^2}\right) \tag{2.1.40}$$

Finally, the coefficients λ_i are frequency-dependent damping coefficients defined by

$$\lambda_i = \frac{3}{2}\frac{k_2 R^3}{C}\frac{\overline{n}^4}{GM}\delta t_i \tag{2.1.41}$$

where δt_i is the time delay, which is a function of the moon's interior viscoelastic properties and $\overline{n}$ is Enceladus' mean motion (Rambaux et al., 2010).

The longitudinal libration depends on the forcing and on the degree-2 shape of the moon's layers (Hoolst et al., 2016). As already considered in Section 2.1, the interfaces between the layers can be described by triaxial ellipsoids. Hoolst et al. (2016) present the libration amplitude for the shell of a small icy moon with a subsurface ocean:

$$\phi_\mathrm{s} \approx \frac{4eK_3}{C_\mathrm{s}\left(n^2 - K_1/C_\mathrm{s}\right)} \tag{2.1.42}$$

The parameters K_1 and K_3 are defined in Van Hoolst et al. (2013). The libration amplitude strongly depends on the thickness of the ice shell and is affected by a non-hydrostatic shape of the outer surface and the interfaces. In fact, different principal MoIs associated to each layer affect the torques exerted on the shell (Hoolst et al., 2016). Hoolst et al. (2016) report that in the case of compensation, by assuming that only the ocean-shell interface of the three-layer triaxial ellipsoid model is not an equipotential surface, the following equations hold:

$$\frac{2}{3}\alpha_\mathrm{c} r_\mathrm{c}^0 g_\mathrm{c} = \frac{5}{6}n^2\left(r_\mathrm{c}^0\right)^2 + \frac{8\pi G}{15}\left[\alpha_\mathrm{s}\rho_\mathrm{s} + \alpha_0\left(\rho_0 - \rho_\mathrm{s}\right) + \alpha_\mathrm{c}\left(\rho_\mathrm{c} - \rho_0\right)\right]\left(r_\mathrm{c}^0\right)^2 \tag{2.1.43}$$

$$\frac{1}{6}\beta_\mathrm{c} r_\mathrm{c}^0 g_\mathrm{c} = \frac{1}{4}n^2\left(r_\mathrm{c}^0\right)^2 + \frac{2\pi G}{15}\left[\beta_\mathrm{s}\rho_\mathrm{s} + \beta_0\left(\rho_0 - \rho_\mathrm{s}\right) + \beta_\mathrm{c}\left(\rho_\mathrm{c} - \rho_0\right)\right]\left(r_\mathrm{c}^0\right)^2 \tag{2.1.44}$$

where g_c is the local gravity at the core interface and α_c and β_c are respectively the polar and equatorial flattening:

$$\alpha_\mathrm{c} = \frac{\left(a_\mathrm{c} + b_\mathrm{c}\right) - c_\mathrm{c}}{\left(a_\mathrm{c} + b_\mathrm{c}\right)/2} \tag{2.1.45}$$

$$\beta_{\mathrm{c}} = \frac{a_{\mathrm{c}} - b_{\mathrm{c}}}{a_{\mathrm{c}}} \tag{2.1.46}$$

Finally, r_{c}^0 is the mean radius of the core interface:

$$r_{\mathrm{c}}^0 = a_{\mathrm{c}} \left(1 - \frac{\alpha_{\mathrm{c}}}{3} - \frac{\beta_{\mathrm{c}}}{2}\right) \tag{2.1.47}$$

Thus, as performed by Hoolst et al. (2016), if a large set of interior structure models is constructed, with constraints given by the radius and mass of the moon, and the MoI as determined from the gravity field (see Section 2.1.5), it is possible to compute the libration amplitude of the shell via (2.1.42). The set of interior models is built by varying the thickness of the core, ocean, and ice shell, and their respective densities. Hoolst et al. (2016, Table 1) report the ranges for thickness and densities for different modeling hypothesis that match the observed libration amplitude of the shell.

Hence, if the uncertainty of the libration amplitude measurements is known, it is then possible to put a constraint on the interior model. Measurements of physical libration amplitudes can be performed through photogrammetry using spacecraft imagery (Hemingway et al., 2018). Photogrammetry is based on the use of control points, which are surface features, such as craters, whose locations are digitized and used to reconstruct a 3D model of the body's shape (Thomas et al., 2016). In particular, image coordinates of four or more points on crater rims are used to fit an ellipse, whose centre is recorded as the control point's image coordinates. By performing a rotation of the coordinates with the camera's inertial orientation matrix, the coordinates of the control points are obtained in the body-centered reference frame. This measurement technique was applied for the Cassini mission: the spacecraft's Imaging Science Subsystem Narrow Angle Camera (NAC) located 488 control points and tracked them through 340 images. The coordinates of the control points were adjusted in order to minimize the square of the residuals between the observed and predicted positions of the control points, based on the assumed rotational model for the satellite. When the model does not describe the satellite's rotation accurately, larger errors will result in the reconstructed control point network. Hence, the libration amplitudes must be varied in order to minimize the reconstruction error (Hemingway et al., 2018). In the study by Thomas et al. (2016), the computed longitudinal physical libration amplitude of the shell is about $0.120 \pm 0.014\,\mathrm{deg}$ (2σ). The measurements analysis provided by Thomas et al. (2016) was used by Hoolst et al. (2016) to infer the interior model of the moon including a global subsurface ocean, as already showed by Thomas et al. (2016).

2.1.8. Spin axis orientation

As discussed by Genova et al. (2024) and Park et al. (2024), the orientation parameters of the spin axis, i. e., Right Ascension (RA) ($\alpha^{\mathrm{s\text{-}a}}$) and Declination (DE) ($\delta^{\mathrm{s\text{-}a}}$), which are tied to the obliquity ($\bar{\epsilon}$), give an independent constraint on the MoI, with the assumption that Enceladus is in a Cassini state. It is possible to derive the MoI from the obliquity through the following equation (e. g., Baland et al. (2016)):

$$\bar{\epsilon} = \frac{2iC\dot{\Omega}}{3M_{\mathrm{E}}R_{\mathrm{E}}^2\left(-C_{2,0} + 2C_{2,2}\right)n + 2C\dot{\Omega}} \tag{2.1.48}$$

where $\dot{\Omega}$ is the constant orbital precession rate, i is the orbital inclination, and n is the mean motion.

The Cassini state is an equilibrium state of the spin axis in which the precession of the spin axis follows the precession of the orbit, meaning that the spin axis is fixed with respect to a reference frame fixed in the orbital plane that precesses with the orbit (Correia, 2015). The Cassini state results from the coplanarity between the spin axis, orbit plane normal, and the ecliptic normal remaining coplanar (Peale & Cassen, 1978). The Cassini state can be reached over time through dissipation due to tidal heating. Hence, assuming that Enceladus is in a Cassini state, the moment of inertia of the moon can be computed as described in Baland et al. (2016, Section 3), in which the projection of the unit vectors aligned with the rotation axis of the core and shell is put in relation to the moment of inertia

of the respective layers. The obliquity of the core and shell feeds into the unit vector associated to the rotation axis. Furthermore, Baland et al. (2016) showed that the non-hydrostatic behaviour of the shell has a small effect on its obliquity, which is in the range $[1.06;\ 1.35] \times 10^{-4}$ deg.

As described in Genova et al. (2024), the obliquity approach provides a cross-check of the MoI measured through the gravity measurements (refer to Section 2.1.5).

2.2. Estimation framework

Given the purpose of this work to assess the uncertainty level to which geophysical parameters of interest of Enceladus can be estimated with the described mission setup, this section gives an overview of the estimation method used to study the problem.

The problem of determining the geophysical measurements introduced in Chapter 2 can be solved through a weighted batch least-squares parameters estimation, (*e.g.* Montenbruck et al. (2000), Dirkx et al. (2014)).

2.2.1. Variational equations formulation

The variational equations are used to describe the influence of the parameters of interest on the dynamics of the system. Given a state vector $\mathbf{x}$ for any type of dynamics (translation and/or rotational) and for any considered body, and given a vector of environmental parameters of interest $\mathbf{p}_\mathrm{e}$, the EoM that describe the system can be written as

$$\dot{\mathbf{x}} = \mathbf{f}\left(\mathbf{x}, \mathbf{p}_\mathrm{e}, t\right) \tag{2.2.1}$$

where $\mathbf{f}$ represents the dynamical model. The estimation parameters of interest for this work are described in Section 3.3.1.

Before presenting the variational equations, it is necessary to introduce the state transition matrix $\Phi\left(t, t_0\right)$ and sensitivity matrix $S(t)$:

$$\Phi\left(t, t_0\right) \coloneqq \frac{\partial \mathbf{x}(t)}{\partial \mathbf{x}\left(t_0\right)} \tag{2.2.2}$$

$$S(t) \coloneqq \frac{\partial \mathbf{x}(t)}{\partial \mathbf{p}_\mathrm{e}} \tag{2.2.3}$$

The variational equations are the differential equations used to solve for the state transition matrix and sensitivity matrix (e. g., Montenbruck et al. (2000)):

$$\begin{aligned} \frac{d}{dt}\Phi(t; t_0) &= \frac{\partial \mathbf{f}\left(\mathbf{x}, \mathbf{p}_\mathrm{e}, t\right)}{\partial \mathbf{x}(t)}\Phi(t; t_0) \\ \frac{d}{dt}S(t) &= \frac{\partial \mathbf{f}\left(\mathbf{x}, \mathbf{p}_\mathrm{e}, t\right)}{\partial \mathbf{x}(t)}S(t) + \frac{\partial \mathbf{f}\left(\mathbf{x}, \mathbf{p}_\mathrm{e}, t\right)}{\partial \mathbf{p}} \end{aligned} \tag{2.2.4}$$

The initial conditions for the variational equations are the following:

$$\begin{aligned} \Phi\left(t_0, t_0\right) &= I_{n\times n} \\ S\left(t_0\right) &= 0_{n\times n_{p_e}} \end{aligned} \tag{2.2.5}$$

where n is the size of the state vector, while n_{p_e} is the number of environmental parameters of interest.

2.2.2. Covariance analysis

When mission data are not available, the observations needed to model the problem can be simulated (Dirkx et al., 2014). The observations are produced by integrating the EoM (2.2.1) and variational equations (2.2.4)-(2.2.5) for the bodies of interest. The integration of the variational equations allows to compute the partial derivatives of the observations with respect to the estimated parameters. As proposed by Dirkx et al. (2014), the same model can be used for both the generation of the observations and the estimation. To mitigate the fact that the observations and estimation model are equal, without accounting for systematic errors that would affect the real tracking data, a strategy based on consider parameters can be applied. The consider parameters allow to avoid the assumption that the estimation model can perfectly capture the observation model.

Let $\mathbf{p}$ denote the vector of estimated parameters, following the notation by Dirkx et al. (2014):

$$\mathbf{p} = \begin{pmatrix} \mathbf{x}_0 \\ \mathbf{p}_\mathrm{e} \end{pmatrix} \tag{2.2.6}$$

where $\mathbf{x}_0$ is the initial state vector for the bodies of interest.

For the mission concept considered in this research (Chapter 1), the observations consist in the range and range-rate of the S/C with respect to the ESA's Estrack antennas, which track the orbiter through a two-way radio link, as mentioned in Section 1.2. Furthermore, each radio beacon in the field of view (FOV) of the orbiter provides two-way Doppler measurements between the landers and the S/C.

Direct-To-Earth (DTE) radiometric Doppler measurements between a lander and a GS on the Earth's surface have already been considered for constraining the libration and tidal deformation of Phobos (Le Maistre et al., 2013), and for determining the orientation and rotation parameters of Mars (Le Maistre et al., 2012). The parameters were estimated using the Doppler shift on a radio signal due to the relative motion of the lander with respect to the GS.

Let us consider the observation vector

$$\mathbf{z} = \begin{pmatrix} z_1 \\ \dots \\ z_T \end{pmatrix} \tag{2.2.7}$$

of measurements taken at time $t_1, \dots, T$. It is possible to model the observations as

$$z_i(t_i) = h_i\left(t_i, \mathbf{p}\right) + \epsilon_i \tag{2.2.8}$$

or in vector form

$$\mathbf{z} = \mathbf{h}\left(T, \mathbf{p}\right) + \boldsymbol{\epsilon} \tag{2.2.9}$$

In (2.2.8), h_i is the observation model as a function of the solve-for parameters and of the time at which the observation is taken. Furthermore, ϵ_i accounts for the difference between the measurements and the modelled observations. ϵ_i includes measurement errors, which generally are assumed to be randomly distributed with zero-mean value (Montenbruck et al., 2000, Section 8.1).

The design matrix H_p associated to the observations is given by the partial derivatives of the observations with respect to the parameters to be estimated:

$$H_p\left(T,\, \mathbf{p}\right) = \frac{\partial \mathbf{h}\left(T,\, \mathbf{p}\right)}{\partial \mathbf{p}} \tag{2.2.10}$$

Considering a single observation h_i, the partial derivatives of the observations with respect to the parameter vector are calculated through the state transition and sensitivity matrices (Dirkx et al., 2014):

$$\frac{\partial h_i}{\partial \mathbf{p}} = \sum_j \left(\frac{\partial h_i}{\partial \mathbf{x}}\left(t_j\right) \Big|_{\mathbf{p}=\text{const.}} \frac{\partial \mathbf{x}}{\partial \mathbf{p}}\left(t_j\right) \right) + \frac{\partial h_i}{\partial \mathbf{p}} \Big|_{\mathbf{x}=\text{const.}} \tag{2.2.11}$$

$$\frac{\partial \mathbf{x}(t)}{\partial \mathbf{p}} = \begin{pmatrix} \Phi(t, t_0) & S(t) \\ 0_{n_{pe} \times 6n_b} & I_{n_{pe} \times n_{pe}} \end{pmatrix} \tag{2.2.12}$$

In (2.2.12), n_b is the number of bodies for which the initial state is estimated.

Information on the probability distribution of the estimated parameters is described by the covariance matrix P. When *a priori* information on the accuracy of the initial guess is available, the *a priori* covariance matrix $P^{(\text{apr})}$ can be used to penalize those initial solutions that deviate from the *a priori* guess (Montenbruck et al., 2000, Section 8.1.5). The a priori information typically derives from existing estimates or measurements. $P^{(\text{apr})}$ can be included in the covariance matrix of the solution as

$$P(T) = \left(\left(P^{(\text{apr})} \right)^{-1} + \left(P^{(0)}(T) \right)^{-1} \right)^{-1} \tag{2.2.13}$$

where

$$P^{(0)}(T) = \left({H_p}^T(T) W(T) H_p(T) \right)^{-1} \tag{2.2.14}$$

In (2.2.14), $W(T)$ is the weight matrix that contains the weights associated to all observations up to the final time T. If the measurement errors are assumed to be uncorrelated, W is diagonal and is computed through the reciprocal of the expected measurement error σ_i squared (e. g., Montenbruck et al. (2000)):

$$W(T) = \begin{pmatrix} \sigma_1^{-2} & & 0 \\ & \ddots & \\ 0 & & \sigma_n^{-2} \end{pmatrix} \tag{2.2.15}$$

Given its definition of (2.2.15), the weight matrix is used to make the algorithm rely more on the observations with smaller uncertainty, since such observations have a larger σ_i^{-2}.

As described by e. g., Dirkx et al. (2014), to account for the impact of unmodelled systematic errors, such range biases or time biases, which limit the attainable orbit determination accuracy, it is possible to include their effect in the covariance computation. A number of extra parameters is added to the estimation procedure. Such parameters are not estimated, but their uncertainty is included when determining the covariance matrix. The consider covariance matrix is thus obtained. The consider parameters $\mathbf{c}$ are included as a parameter in the estimation model. The vector $\mathbf{c}$ includes those force and measurement model parameters that are not modelled or are uncertain and are not adjusted as part of the estimation procedure; however, they are considered nonetheless (Bierman, 1977). The consider parameters are assumed to be small quantities with an expected value of zero, independent of the measurement information. Since the $\mathbf{c}$ parameters are not estimated, the $\mathbf{c}$ vector retains its *a priori* covariance matrix, which appears as an error source degrading the filter covariance P. An example of the application of the consider parameters is given by Jacobson (2010), who includes observation biases as consider parameters. Dirkx et al. (2014) use range bias and the position of the Earth GSs (in terms of deviations from the known position) as consider parameters for their DTE Phobos laser ranging investigation. The covariance matrix including the consider parameters, and without the *a priori* contribution, is calculated as (Montenbruck et al., 2000):

$$P^{(0,c)}(T) = P^{(0)}(T) + \left(P^{(0)}(T) {H_p}^T(T) W(T) \right) \left(H_c(T) C^c {H_c(T)}^T \right) \left(P^{(0)}(T) {H_p}^T(T) W(T) \right)^T \tag{2.2.16}$$

where H_c is the matrix of partials of the observations with respect to the consider parameters and C^c is the assumed covariance matrix of the consider parameters. Including the *a priori* covariance matrix into the consider covariance matrix $P^{(0,c)}$ through (2.2.13) leads to

$$P^{(c)}(T) = \left(\left(P^{(\text{apr})} \right)^{-1} + \left(P^{(0,c)}(T) \right)^{-1} \right)^{-1} \tag{2.2.17}$$

The covariance $P^{(c)}(T)$ can be used to compute the propagated covariance of the state at any later epoch t (S. Fayolle, 2025):

$$P_{\mathbf{x}}^{(c)}(t, T) = \left[\Phi(t, t_0) ; S(t) \right] P^{(c)}(T) \left[\Phi(t, t_0) ; S(t) \right]^T \tag{2.2.18}$$

The formal error for parameters and state estimate is obtained from the square root of the diagonal elements of $P^{(c)}(T)$ and $P_{\mathbf{x}}^{(c)}(t,T)$, which represents the variance associated to the solve-for parameters.

2.2.3. Observations

For the considered mission scenario, radiometric observations are expected to be provided through a radio link between the radio beacons and the S/C, and between the S/C and one of the GSs of the Estrack network (Chapter 1). Table 2.2.1 reports the uplink and downlink frequencies for deep-space communications.

Table 2.2.1.: Uplink and downlink frequencies for deep-space communications. Retrieved from Thornton and Border (2005).

Band	Uplink frequency [MHz]	Downlink frequency [MHz]
S	$2110 - 2120$	$2290 - 2300$
X	$7145 - 7190$	$8400 - 8450$
Ka	$34,200 - 34,700$	$31,800 - 32,300$

For the two-way radio link between the GS and the S/C, the following observations are normally available for interplanetary missions (e. g., Genova and Petricca (2021), S. Fayolle (2025), Srinivasan et al. (2025)):

1. The slant range from the S/C and the GS, computed from the round-trip light time of a radio signal emitted from the GS to the S/C and transmitted back to the GS.
2. The range rate of the S/C relative to the GS, computed from the Doppler shift of the two-way radio wave.
3. Delta-differential one-way ranging (delta-DOR), that measures the delay in the time of arrival of a signal transmitted by the probe and received by two widely separated ground stations. The delta-DOR measurement provides the angular position of the spacecraft.

For this work, the slant range and range-rate observations are considered. The delta-DOR measurement is generally used during the interplanetary cruise phase, so it will not be considered further for the orbiter phase. In addition to the observation by the Earth GSs, the radio tracking data of the S/C from the Enceladus landers provide range-rate observations. These are included in the covariance analysis, for obtaining information on how the landers can help constrain the study of the time-variable behaviour of the moon, in relation to geophysical parameters such as the radial displacement Love number and libration amplitude (Section 2.1.6 and Section 2.1.7).

Slant range

A two-way range observable can be defined as (Moyer, 1981)

$$r^* = c\,(t_4 - t_1) \tag{2.2.19}$$

where t_1 and t_4 are the signal initial transmission and final reception times at the GS. In this section, it will be assumed that the uplink signal is transmitted at the epoch t_1 and received by the S/C at t_2; the downlink signal is then transmitted back to the GS at the epoch t_3, and is finally received by the GS at t_4.

A deep-space range measurement is fundamentally a measurement of phase delay $\Delta\phi$ between the transmitted and received signal at the GS (Thornton & Border, 2005). From the phase delay, the round-tripe travel time is inferred, from which the range can be computed. The signal round-trip

travel time can be computed through common tone-ranging systems, which measure the phase shift between the outgoing and incoming signal (e. g., Montenbruck et al. (2000), Asmar (2022)):

$$\tau = \frac{\Delta\phi}{2\pi f_0} \tag{2.2.20}$$

where f_0 is the frequency of the carrier.

Given the measured phase delay, the pseudorange r^* between the GS and the S/C can be computed as (Montenbruck et al., 2000)

$$r^* = \frac{1}{2}c\tau \tag{2.2.21}$$

The pseudorange is not the proper measure of the slant range r, since the signal experiences delays due to the onboard S/C transponder and to the propagation through the atmosphere and interplanetary media (Thornton & Border, 2005). Hence, a model for the range r can be inferred from the measured phase delay as (e. g., Moyer (1981), S. Fayolle (2025)):

$$r^* = r + c\sum_i \delta t_i \tag{2.2.22}$$

In (2.2.22), the terms δt_i are corrections for the signal delays caused by the S/C on-board transponder and media delays. Media delays include the refraction of the signal due to the troposphere and interplanetary media. A model for the delay of the signal due to refraction is given in Section 2.2.4. On the other hand, the correction for the delay due to the onboard transponder can be modelled as (S. Fayolle, 2025)

$$\delta t_{\text{transponder}} = t_3 - t_2 \tag{2.2.23}$$

where t_2 is the epoch at which the uplink signal is received by the S/C, while t_3 is the epoch at which the downlink signal is transmitted back to the GS, according to the link transmit and receive epochs introduced above. Bertone et al. (2018, Table 1) summarises the transponder delay for some missions. They are reported in Table 2.2.2.

Table 2.2.2.: Transponder delay for various launched spacecrafts. Retrieved from Bertone et al. (2018, Table 1).

Spacecraft	Launch	Transponder delay [μs]
BepiColombo Mercury Planetary Orbiter	2018	$4.8 - 6$
Herschel	2009	5.2
Planck	2009	5.2
Mars Reconnaissance Orbiter	2005	1.4149
Venus Express	2005	2.085
Messenger	2004	1.371
Rosetta	2004	$4.8 - 6$
Mars Express	2003	2.076
Mars Odissey	2001	1.4266
Cassini	1997	$4.8 - 6$
Mars Global Surveyor	1996	0.7797

The ranging instrumentation for deep space missions can measure the signal phase shift with a typical accuracy of 1 m (1 σ) at X-band (Asmar, 2022).

When setting up the observation model in Tudat[1], the two-way range observations are modelled as a series of one-way range observations $h^{\text{1-way}}$, defined as:

$$h_{\text{1-way}}(t_\text{r}, t_\text{t}) = |\mathbf{r}_\text{r}(t_\text{r}) - \mathbf{r}_\text{t}(t_\text{t})| \tag{2.2.24}$$

[1] Tudat observation models

where $\mathbf{r}_\mathrm{r}$, $\mathbf{r}_\mathrm{t}$, t_r, t_t are the position function of the receiver and transmitter, and the evaluation epoch of receiver and transmitter for the one-way range observable. The series for the uplink and downlink produces the two-way range observable:

$$h_{\text{2-way}}\left(t_1, t_2, t_4\right) = \left|\mathbf{r}_{\mathrm{S/C}}\left(t_2\right) - \mathbf{r}_{\mathrm{GS}}\left(t_1\right)\right| + \left|\mathbf{r}_{\mathrm{GS}}\left(t_4\right) - \mathbf{r}_{\mathrm{S/C}}\left(t_2\right)\right| \tag{2.2.25}$$

where the S/C and the GS are respectively the receiver and transmitter in the uplink, while they are the transmitter and receiver in the downlink. The reception time of the first one-way range is set as transmission time of the second one-way range ($t_3 = t_2$) [2].

Range rate

The range rate is defined as the velocity of the S/C in the GS − S/C Line-of-sight (LOS) direction:

$$\dot{r} = \frac{\left(\mathbf{r}_{S/C} - \mathbf{r}_{GS}\right) \cdot \dot{\mathbf{r}}_{S/C}}{\left\|\mathbf{r}_{S/C} - \mathbf{r}_{GS}\right\|} \tag{2.2.26}$$

Due to the relative motion between the S/C and the GS, the Doppler effect produces a frequency shift of the signal. Hence, the measurement of the range-rate is based on the Doppler shift of the two-way signal. Generally, the measurement of the Doppler shift is an average quantity evaluated over a count time T_c (Moyer, 2000). A typical value for the count time is 60 s (e. g., Thornton and Border (2005), Genova and Petricca (2021)). Such averaged Doppler measurement will be used to model the observations in the simulation. In Tudat, the two-way averaged Doppler observation is modelled as

$$h_{\text{2-doppler}} = \frac{h_{\text{2-way}}\left(t_1, t_2, t_4 = t + \Delta t\right) - h_{\text{2-way}}\left(t_1, t_2, t_4 = t\right)}{\Delta t} \tag{2.2.27}$$

2.2.4. Error sources

The errors affecting the radio science measurements derive from the combination of the following errors (e. g., Moyer (2000), Asmar et al. (2005), Iess, Di Benedetto, et al. (2014), S. Fayolle (2025)):

- media propagation delays (troposphere, ionosphere, plasma);
- instrumental noise (thermal noise, mechanical noise, noise in the frequency transponder);
- numerical noise.

With respect to the observation model, two noise sources are to be considered:

- uncertainties and biases in the Earth orientation parameters and Earth GS;
- dynamical model noise.

In this section, an overview of the different error sources is given.

[2] Tudat observation models settings

Troposphere

One of the corrections that should be accounted for is related to the influence of the troposphere on the delay of the uplink and downlink signals between the GS and the S/C.

Due to its refractive index, the troposphere bends the waves traversing it and changes their speed of propagation. As discussed in Montenbruck et al. (2000), it is necessary to distinguish the refraction due to water vapor (wet effect) from the one caused by dry air (dry effect).

The delay of the radio signal introduced by the wet and dry tropospheric effects can be described according to the Hopfield model, for which the tropospheric range correction is given by (Montenbruck et al., 2000):

$$\Delta r_{\text{troposphere}} = k_\lambda \sum_{j=1}^{2} \frac{{n^*}_j}{10^6} \sum_{i=1}^{9} \frac{\alpha_{ij} r_j^i}{i} \tag{2.2.28}$$

In (2.2.28), k_λ is a constant close to 1 for radio frequencies and whose formulation is given in Montenbruck et al. (2000, Section 6.3.2). Furthermore, n^* is the refractivity associated to the dry (${n^*}_1$) and wet (${n^*}_2$) effect. α_{ij} are polynomial coefficients that are dependent on the reference dry and wet troposphere height and on the elevation. The dry and wet troposphere heights are a function of atmospheric pressure, temperature, and partial pressure of water vapour. Finally, r_j is the distance to the top of the dry and wet troposphere.

For the Deep Space Network (DSN) tracking stations, Moyer (2000) describes the total tropospheric zenith dry and wet range corrections:

$$r_{\text{z,dry}} = \left(r_{\text{z,dry}}\right)_{\text{model}} + \Delta r_{\text{z,dry}} \tag{2.2.29}$$

$$r_{\text{z,wet}} = \left(r_{\text{z,wet}}\right)_{\text{model}} + \Delta r_{\text{z,wet}} \tag{2.2.30}$$

where the first terms are the modelled corrections according to Estefan and Sovers (1994), while the second terms are the solved-for constant corrections at the tracking station. The modelled corrections relate to the tropospheric range correction via the following equation:

$$\Delta r_{\text{troposphere}} = r_{\text{z,dry}} R_{\text{dry}}\left(\zeta\right) + r_{\text{z,wet}} R_{\text{wet}}\left(\zeta\right) \tag{2.2.31}$$

In (2.2.30), $\left(r_{\text{z,dry}}\right)_{\text{model}}$ and $\left(r_{\text{z,wet}}\right)_{\text{model}}$ can be expressed as power or Fourier series, given by Estefan and Sovers (1994, Equations 3 and 4). As an example, the power series formulation for the modelled wet and dry zenith range corrections is given by:

$$\left(r_{\text{z},i}\right)_{\text{model}} = \sum_{k=0}^{n} C_k X^k \tag{2.2.32}$$

where the coefficients of the series can be found in Estefan and Sovers (1994, Figure 3a), while the argument X of the series is a normalized function of the time tag associated to the signal (Moyer, 2000, Section 10.2.3.3). The series were obtained by fitting the model provided by Estefan and Sovers (1994, Equations 1 and 2). Such corrections are applied by the Regres editor used for the DSN (Moyer, 2000).

The troposphere affects also the Doppler measurements, for which generally the dry effect is dominant with respect to the wet effect, but it can be more easily predicted and corrected, based on the elevation of the S/C (Bertotti et al., 2003). With respect to the wet effect, the variability of the distribution of water vapour in the Earth's atmosphere causes the fluctuation of the wet tropospheric refractivity (Iess, Di Benedetto, et al., 2014). The wet tropospheric delay can be estimated through a Media Calibration System (MCS) installed close to the deep space antenna. The radiometer measures the wet path delay along the probe-GS LOS. The wet tropospheric noise was found to be higher in summer daytime and lower in winter nighttime (e. g., Lasagni Manghi et al. (2023), Iess, Di Benedetto, et al. (2014)). For their investigation, Iess, Di Benedetto, et al. (2014) considered a sinusoidal trend with annual periodicity and an average level of $1.95 \times 10^{-5}\,\mathrm{m\,s^{-1}}$ with an upper bound of $3.00 \times 10^{-5}\,\mathrm{m\,s^{-1}}$, for an integration time of 60 s.

Ionosphere

The ionospheric refraction is caused by the presence of charged particles in the high atmosphere, generated by the absorption of solar UV radiation.

The ionospheric correction is given by (Montenbruck et al., 2000, Section 6.3.3):

$$\Delta r^{\text{ionosphere}} = \frac{\alpha}{f^2} \tag{2.2.33}$$

where α is a ionospheric parameter, dependent on the Total Electron Content (TEC), which is the integral of the electron number density over the path followed by the radio signal. The ionospheric parameter can be determined by measuring the delay in the signal at two different frequency bands, since it is frequency dependent, as shown in (2.2.33):

$$\begin{aligned} \Delta r_1^{\text{ionosphere}} &= \frac{\alpha}{f_1^2} \\ \Delta r_2^{\text{ionosphere}} &= \frac{\alpha}{f_2^2} \end{aligned} \tag{2.2.34}$$

The dual frequency correction method for the ionospheric refraction is applied by Doppler Orbitography and Radiopositioning Integrated by Satellite (DORIS), on frequencies of 2036 MHz and 401 MHz (Montenbruck et al., 2000, Section 6.3.3).

Plasma

As discussed by Iess, Di Benedetto, et al. (2014) and Parisi et al. (2014), the plasma environment affects the Doppler measurements by inducing a frequency change. The plasma has a dispersive effect. As shown in Iess, Di Benedetto, et al. (2014, Figure 2), the plasma has the most influential effect on Doppler measurements for interplanetary spacecrafts, such as Cassini. The plasma effect is particularly sensitive to the Sun-Earth-probe (SEP) angle: for values close to zero, the plasma delay tends to be maximum.

This noise source can be calibrated and corrected by using a multi-frequency link of type X/X, X/Ka, Ka/Ka, where the first band refers to the uplink signal, while the second band refers to the downlink signal. Bertotti et al. (1992) describe the frequency shift induced by the plasma effect in terms of the optical path change $d\Delta l$:

$$\frac{f(t) - f_0}{f_0} = \frac{d\Delta l(t)}{c\,dt} \tag{2.2.35}$$

The optical path is then given by the phase change due to the plasma effect:

$$\Delta l(t) = \frac{c\Delta\phi}{2\pi f_0} \tag{2.2.36}$$

which can be rearranged (Bertotti et al., 1992) as

$$\Delta l(t) = \Delta l_{\text{nd}} + \frac{P^*}{f^2} \tag{2.2.37}$$

where the first term is the non-dispersive term, while the second one is the dispersive term and is proportional to the plasma-dependent parameter P. The non dispersive contribution can be measured with two different carrier frequencies, given that P^* is unchanged:

$$\Delta l_{\text{nd}} = \frac{f_1^2\Delta l_1 - f_2^2\Delta l_2}{f_1^2 - f_2^2} \tag{2.2.38}$$

This allows also to determine the plasma parameter P^*.

For a round-trip loop, (2.2.36) can be rewritten as (Lasagni Manghi et al., 2023)

$$\Delta l(t) = \Delta l_{\mathrm{nd}} + \frac{{P^*}_{\mathrm{u}}}{f_{1\mathrm{u}}^2} + \frac{{P^*}_{\mathrm{d}}}{f_{2\mathrm{d}}^2} \tag{2.2.39}$$

In this case, three terms are to be determined: the non-dispersive term, and the uplink and downlink plasma parameter. Given that with only two observables the problem cannot be solved, it is necessary to add a third observable. The third observable can be achieved with a mixed signal given by the redistribution of the uplink X signal to a downlink X and nearby Ka signal (Bertotti et al., 1992). In such a way, the combinations X/X, X/Ka, Ka/Ka allow to correct for the plasma effect (e. g., De Tiberis et al. (2011), Lasagni Manghi et al. (2023)). As reported by Iess, Di Benedetto, et al. (2014), such a three-link system allowed to remove the plasma effect, achieving an accuracy of Doppler residuals of about $4.50 \times 10^{-6}\,\mathrm{m\,s^{-1}}$ for an integration time of 1000 s during the solar conjunction of Cassini, with a SEP angle smaller than 10 deg.

The plasma environment has an effect on the range measurements as well, due to the change in optical path. Iess, Di Benedetto, et al. (2014) reported the range noise due to interplanetary plasma, equal to 800 cm for a SEP angle of 15 deg and 350 cm for a SEP angle of 30 deg.

Transponder noise

The on-board transponder is used to lock the uplink frequency to the downlink frequency to avoid interference between the two radio signals, according to pre-defined frequency ratios (Moyer, 2000). As described in the previous section, it also serves to generate the three-way link for calibrating the plasma noise.

As described in Iess, Di Benedetto, et al. (2014), the white noise of the transponder affects the Doppler measurements of an interplanetary S/C at frequencies larger than $10^{-4} - 10^{-3}$ Hz. As an example, the Deep Space Transponder (DST) of the Cassini spacecraft introduced a noise of about $0.006\,\mathrm{mm\,s^{-1}}$ for an integration time of 60 s. For the Rosetta spacecraft, the Doppler transponder noise amounted to $0.015\,\mathrm{mm\,s^{-1}}$, for the same integration time (Iess, Di Benedetto, et al., 2014).

The DST represents a source of error also for the range measurements, due to the delay introduced in the light time, i. e., the processing time between reception and re-emission of a two-way link at the S/C (Bertone et al., 2018). As suggested by Bertone et al. (2018), the DST time delay can be estimated together with the rest of the parameters of interest.

Mechanical noise

Due to wind, gravitational loading, and thermal gradients, the GS antenna introduces a mechanical noise. For the ESA's antennas, it is estimated at the level of ≈ 0.005 mm/s at an integration time of 60 s. Iess, Di Benedetto, et al. (2014) assumed the same value of noise for the antennas of the DSN.

As for the range measurements, Moyer (2000) provides a correction formula to account for the misalignment of the antenna's axes due to wind, gravity, and thermal loading of the antenna, so that the tracking point of the antenna is corrected to account for the movement of the phase center. Additionally, the mechanical noise is not considered in Iess, Di Benedetto, et al. (2014). Furthermore, also Armstrong et al. (2008), who consider antenna mechanical noise in precision spacecraft tracking due to the time-dependent unmodeled motion of the ground antenna's phase center, only report the effect of mechanical noise on Doppler tracking. As a result, the mechanical noise for range measurements can be assumed to be calibrated.

Ground station bias

The GS bias includes different systematic effects that occur at the GS end of the link. Such systematic effects include the uncertainty in the GS location, and the effect of Earth tides and ephemeris. For the Cassini spacecraft, the bias was shown by Iess, Di Benedetto, et al. (2014) to be at the level of 1.5 m, while Thornton and Border (2005) reported a bias of 2 m.

The bias does not affect the Doppler measurements, as these are differential measurements.

Numerical noise

Iess, Di Benedetto, et al. (2014) mentioned that numerical noise due to round-off errors caused by finite number representation had an impact for the Rosetta and Cassini missions. The influence of numerical noise is particularly relevant for Doppler measurements, since it is inversely proportional to the Doppler count time.

For the Rosetta spacecraft, the numerical noise amounts to $\approx 1.92 \times 10^{-5}\,\mathrm{m\,s^{-1}}$ for a count time of 60 s. Furthermore, for a double precision representation of a number, the numerical noise introduces an error of about 0.15 mm at 10 AU (Saturn's semimajor axis is 9.573 AU[3]). The numerical noise can be reduced with adequate software implementations (Zannoni & Tortora, 2013).

Thermal noise

The thermal noise at the GS causes range and Doppler jitter. Such noise source is a random source, whose variance is given by (Kinman & Berner, 2003):

$$\sigma = \frac{c}{16 f_0 \sqrt{\frac{P_r}{N_0} T}} \tag{2.2.40}$$

where f_0 is the frequency of the range signal, $\frac{P_r}{N_0}$ is the signal-to-noise density ratio, and T is the integration time.

Typical values for the random thermal noise in the X band are given by Thornton and Border (2005) and are equal to $0.03\,\mathrm{mm\,s^{-1}}$ for the Doppler measurements and about 60 cm for the range measurements.

Dynamical model noise

The noise in the dynamical model is caused by accelerations that are not modeled but that ought to be accounted for. Examples of accelerations that might represent a source of dynamical noise are the radiative forcing due to thermal emission and reflection of the S/C, caused both by the heat generated by the on-board radioisotope thermoelectric generator (RTG), instruments, and by the incident solar radiation. Additional sources of dynamical noise can be the drag caused by the S/C traversing Enceladus' plumes or the specular and diffuse reflectivity of the high-gain antenna (Bertotti et al., 2003). These noise sources can be estimated from Doppler measurements in combination with attitude data. Another parameter that could introduce noise is the effect of relativity on the light-time of the signal.

Such noise sources cannot be directly associated to the observations in the covariance analysis, but their degrading effect on the solution of the estimator can be obtained by adding such acceleration terms to the parameters to be estimated. In fact, if the same observations set is used for estimating more parameters, a worse quality of the results is expected.

[3] NASA Saturn fact sheet

For a mission to the outer Solar System, typical values for the total range and Doppler noise affecting the Earth GSs are for instance those generally assumed for the radio tracking of the Juice spacecraft: 0.2 m and $1.2 \times 10^{-5}\,\mathrm{m\,s^{-1}}$ (e. g., Di Benedetto et al. (2021), M. Fayolle et al. (2023), Magnanini et al. (2024)). These are the values considered in this work.

2.3. Interior model inversion

The geophysical constraints given by the collected measurements can be used to constrain the properties of the internal structure of Enceladus through a MCMC algorithm, based on the probabilistic framework of Bayesian inference (e. g., Genova et al. (2024), Genova et al. (2019), Petricca et al. (2023), Drilleau et al. (2021), Filice et al. (2025)). The MCMC algorithm allows to estimate the properties of the interior by generating models that are consistent with the observations.

A Markov chain is a sequence of random variables $\mathbf{X}_1, \ldots, \mathbf{X}_n$ such that the future state is dependent only on the present state, not on the past ones (Sharma, 2017). Formally, it is written as

$$p\left(\mathbf{X}_{n+1} = \mathbf{x} | \mathbf{X}_1 = \mathbf{x}_1, \mathbf{X}_2 = \mathbf{x}_2, \ldots, \mathbf{X}_n = \mathbf{x}_n\right) = p\left(\mathbf{X}_{n+1} = \mathbf{x} | \mathbf{X}_n = \mathbf{x}_n\right) \tag{2.3.1}$$

For the considered application, examples of a set of variables $\mathbf{X}$ are the thickness and density of the three interior layers of Enceladus.

The purpose of the algorithm is the exploration of the parameter space for converging to a stable distribution. The most general MCMC algorithm is the Metropolis-Hastings (MH) algorithm (e. g., Chib (2001), Sharma (2017), Petricca et al. (2023)). For the problem at hand, the distributions of the internal properties are assumed to be Gaussian. To allow the algorithm to consider a sufficient number of samples, multiple chains are generated and run in parallel. Petricca et al. (2023) considered 30 distinct chains, while Drilleau et al. (2021) considered 96 independent chains in parallel, and Genova et al. (2024) generated 20 chains. Every chain is composed of multiple items that evolve at every iteration of the algorithm. The parameters distribution is used to supply a proposal value together with an associated probability of move, which is used to determine if the proposal value should be taken as the next item of the chain (Chib, 2001). Since the starting model for each chain is randomly chosen within the initial distribution, each chain follows a distinct and independent path with respect to the other chains.

At each iteration, the synthetic data generated by the considered model are compared to the real observations, and the misfit is computed. The data $\mathbf{d}$ are related to the parameters $\mathbf{X}$ through the equation

$$\mathbf{d} = A\left(\mathbf{X}\right) \tag{2.3.2}$$

where the non linear operator A represents the forwards problem (Drilleau et al., 2021). An example of the data vector $\mathbf{d}$ for the problem at hand is the set of geophysical parameters of interest, such as mass MoI, longitudinal libration amplitude, mass, mean radius, J_2 harmonic coefficient. The misfit $\Delta\left(\mathbf{d}^*, A\left(\mathbf{X}\right)\right)$ is determined by the difference between the observed data $\mathbf{d}^*$ and the computed data $A\left(\mathbf{X}\right)$. Minimizing the misfit function is equivalent to maximizing the likelihood function $p\left(\mathbf{d}^*, \mathbf{X}\right)$. In their analysis, Drilleau et al. (2021) defined the misfit function as the ratio between the difference of the observed and synthetic data over the standard deviation associated to the observations.

The best fitting models are then selected for each chain, and the best models from the different chains are sorted in ascending order. The best models can be selected based on the probability of the model given the data or on the predictive accuracy of the model for the future data (Sharma, 2017).

The convergence of a Markov chain is driven by its property of irreducibility: a Markov chain is irreducible if it can go from any state $\mathbf{x}$ of a discrete state space to any other state $\mathbf{y}$ in a finite number of steps, i. e., if there exists an integer n such that

$$p\left(\mathbf{X}_{n+1} = \mathbf{y} | \mathbf{X}_n = \mathbf{x}\right) > 0 \tag{2.3.3}$$

For an irreducible Markov chain with a unique stationary distribution π, the expectation of a function $g(\mathbf{x})$ over π approaches the average taken over the output of a Markov chain,

$$E_\pi [g(\mathbf{x})] = \int g(\mathbf{x}) \pi(\mathbf{x}) d\mathbf{x} = \lim_{n\to\infty} \frac{1}{n} \sum_{i=1}^{n} g(\mathbf{x}_i) \tag{2.3.4}$$

This property allows to compute MC estimates of the quantities of interest from a Markov chain.

As already mentioned, the most general MCMC algorithm is the Metropolis-Hastings algorithm. Supposing that we are interested in sampling a distribution $f(\mathbf{x})$ on a space E, with $\mathbf{x} \in E$, we want to construct a transition model $K(\mathbf{x}, \mathbf{y})$ to go from $\mathbf{x}$ to $\mathbf{y}$. The MH algorithm is composed of a two-step process:

1. Specify a proposal distribution $q(\mathbf{y}|\mathbf{x})$
2. Accept items from $q(\mathbf{y}|\mathbf{x})$ with acceptance ratio $\alpha(\mathbf{x}, \mathbf{y}) = \min\left[1, \frac{f(\mathbf{y})q(\mathbf{x}|\mathbf{y})}{f(\mathbf{x})q(\mathbf{y}|\mathbf{x})}\right]$

Hence, the transition model is given by

$$K(\mathbf{x}, \mathbf{y}) = q(\mathbf{y}|\mathbf{x}) \alpha(\mathbf{x}, \mathbf{y}) \tag{2.3.5}$$

A pseudocode of the full algorithm can be found in Sharma (2017, Section 3.2).

When a chain converges, the misfit is expected to decrease significantly, and the model parameters reach a stable value. When the best chains are selected, they are run in parallel for further iterations in a second step, starting from the models of the found chains. In the second step, the sampling of the parameter space is performed with narrower Gaussian proposal distributions. As pointed out by Drilleau et al. (2021), applying a narrower Gaussian distribution to the parameters to be explored allows to maintain the solution close to the one found in the first step, which led to a good fit of the data.

Generally, in order to avoid biases in the final distributions, at each step, a selected number of models at the beginning of each chain is discarded (Ermakov et al., 2021).

Genova et al. (2024) applied the MCMC algorithm to develop a model for the interior structure of Enceladus. A three-layer model with a core, ocean, and ice-shell is assumed. The reference data used to compute the misfit are the mass, MoI, J_3, and the gravitational Love number k_2, computed by using the radio-tracking data of Cassini and topography data. Furthermore, the free parameters investigated in the MCMC algorithm are the density, thickness, and rigidity of the core and ocean, and the ice shell thickness. To each free parameter, Genova et al. (2024) assigned a step size for the random walkers, and a range within which the interior parameters were sampled. With the given geophysical measurements, the MCMC algorithm allowed to constrain the core radius and density, the ocean thickness and density, and the viscosity and shear modulus of the ice shell.

Petricca et al. (2023) applied the interior model inversion through the MCMC algorithm to generate a model for the interior of the icy moons of the Solar System, using gravity and magnetic field measurements. The method was then applied to the specific case of Europa, considering a four-layer model with a metallic core, rocky mantle, an ocean, and an ice shell. The considered free parameters include the density and thickness of each layer, except for the density of the ice shell, assumed to be equal to pure water ice. The geophysical measurements used by Petricca et al. (2023) are the mass, MoI, and magnetic induction amplitude. Each free parameter is sampled whithin an initial range preventing the generation of physically inconsistent models. Furthermore, the authors present the results in terms of the mode of the resulting output distribution and the 68% credible intervals. The credible intervals were determined based on the shortest possible interval in which the parameter falls within a certain probability (e. g., $\sim 68\%$ or $1\,\sigma$).

Compared to a MC analysis, the MCMC algorithms allow to map the uncertainty on the observables to those on the parameters by updating the chains at every iteration and by exploring the design space towards the areas with higher probability, i. e., the areas of lower mismatch between the modelled and

measured observations. Such functionality is not present in an MC analysis, because the algorithm does not converge towards the areas with higher probability. However, the MC algorithm retains the capability of exploring the relationship between the observations and the parameters. Hence, through an MC run, it is still possible to determine the areas of higher probability for a given value of the observables, and thus study how the uncertainty of the observations relates to the uncertainty on the parameters. The analysis however lacks a mapping of one to the other, which instead is provided by the MCMC approach.

2.4. Orbit design for a science mission at Enceladus

In this section, a few considerations on orbit design for an orbiter mission at Enceladus are presented.

Considering, e. g., Genova et al. (2024) and Ermakov et al. (2021), near-circular near-polar orbits with altitudes between 100 and 150 km are the most suited for a gravity exploration mission at Enceladus. These orbits allow to reach a uniform coverage of the gravity field of the moon, with a reasonably good measurement resolution, thanks to the low altitude and steady precession of the orbital plane. However, such orbits are highly unstable, and they tend to be stable only at low inclination values. The instability of the orbit is caused by the third-body perturbation of Saturn (e. g., Scheeres et al. (2001), Benedikter et al. (2022)). Scheeres et al. (2001) derived that for an orbiter around a planetary satellite, low-altitude near-circular orbits experience an exponential growth of their eccentricity for a range of inclinations centred around 90 deg.

Benedikter et al. (2022) conducted a grid search of initial conditions for stable orbits with repeating ground tracks. The orbits were considered stable if they did not impact the moon or escaped its Sphere of Influence (SOI), and were propagated with the relevant accelerations, without relying on a purely analytical model, which was used by Scheeres et al. (2001). Additionally, Benedikter et al. (2022) accounted for the non-circular orbit of Enceladus and the non-spherical gravity fields of Enceladus and Saturn, including perturbations by the other bodies, such as the Sun and Jupiter. The grid search was performed in a search space centred around the solutions provided by Russell and Lara (2009), for a semi-major axis $a_0 = [400, 550]$ km, inclination $i_0 = [50, 65]$ deg, and eccentricity $e_0 = [0, 0.1]$. Three initial states were found, each one leading to a different number of revolutions N_{rep} after which the orbit is repeated. The properties of the three solutions are reported in Table 2.4.1. Such solutions were found with the gravity settings for Enceladus and Saturn provided by Iess, Stevenson, et al. (2014b) and Iess et al. (2019).

As it can be observed, all the found solutions have a mean inclination close to 60 deg and an altitude comprised in between $169.8 - 283.0$ km, to allow a reasonably good coverage of Enceladus' surface, especially of the south polar region, which is of particular scientific interest for the mission considered by Benedikter et al. (2022). All three orbits keep their general shape over 200 days, and they remain stable (i. e., no impact on the surface and no escape) in long-term propagations beyond 15 years, considering all accelerations listed in Table 2.4.2. Generally, it was observed that solutions with a lower altitude tend to be less stable, due to the larger influence of Enceladus' non-spherical gravity field. Additionally, also the perturbation induced by the drag caused by the plumes was assessed by Benedikter et al. (2022). A peak density of 47×10^{-12} kg m^{-3} at an altitude of 99 km and a latitude of -90 deg as reported by Lee et al. (2013) was considered for a worst-case scenario. The drag was modelled as given in (2.4.1):

$$\|\mathbf{a}_{\text{D}}\| = \frac{\rho \|\mathbf{v}\|^2 C_D S}{2 M_{\text{S/C}}} \tag{2.4.1}$$

where $\mathbf{v}$ is the relative velocity of the S/C with respect to the ejecta. For a Cassini-like spacecraft with $S = 18.6$ m^2, $C_D = 2.2$, and $M_{\text{S/C}} = 2150$ kg, and the maximum velocity of the three orbits of $\|\mathbf{v}\| = 139$ m s^{-1}, a drag acceleration $\|\mathbf{a}_{\text{D}}\| = 8.6 \times 10^{-12}$ km s^{-2} was obtained, comparable to the gravitational accelerations by the Saturnian moons (Benedikter et al., 2022).

Table 2.4.1.: Orbit solutions with repeating ground track for an Enceladus science mission. Retrieved from Benedikter et al. (2022). The solutions were determined with the gravity settings for Enceladus and Saturn provided by Iess, Stevenson, et al. (2014b) and Iess et al. (2019). The following symbols are considered: semi-major axis (a); eccentricity (e); inclination (i); altitude (h); number of revolutions after which the orbits are repeated (N_{rep}), and associated period of repetition (T_{rep}).

Parameter	Unit	K_1	K_2	K_3
a_0	km	0.45362×10^3	0.49041×10^3	0.47752×10^3
e_0	–	0.7594×10^{-1}	0.7594×10^{-1}	0.7594×10^{-1}
i_0	deg	0.5517×10^2	0.5625×10^2	0.5648×10^2
N_{rep}	–	5	9	14
T_{rep}	days	1.2919	2.5788	3.8744
mean i	deg	56.4	57.7	57.8
max. i	deg	59.5	61.0	61.1
mean h	km	200.6	234.1	222.5
max. h	km	234.3	283.0	264.0
min. h	km	169.8	191.2	185.7

Starting from the solutions by Benedikter et al. (2022), Auer Wilkins et al. (2025) performed a new grid search considering the updated gravity field model by Park et al. (2024) for Enceladus, obtained by fitting the SAT441 ephemerides (Jacobson et al., 2022) with the revised orientation model by Park et al. (2024). The solutions computed by Auer Wilkins et al. (2025) are still repeating with the same repeating properties of those by Benedikter et al. (2022), showed in Table 2.4.1. The solutions by Auer Wilkins et al. (2025) are provided in Section 3.1.

Alternatively to the solutions found by Benedikter et al. (2022) and Auer Wilkins et al. (2025), a near-circular near-polar orbit can be designed in order to maximize the coverage of Enceladus. However, due to its high instability, such orbit would need multiple Orbit Maintenance Manoeuvres (OMMs) per day, without which the S/C would impact or escape within as little as one day (Russell & Lara, 2009). Genova et al. (2024) performed a preliminary trajectory analysis to obtain a uniform spatial coverage and a minimum number of OMMs.

Table 2.4.2.: Accelerations considered by Benedikter et al. (2022) for the long-term propagation of the stable orbit solutions provided in Table 2.4.1.

Body	Acceleration
Enceladus	GM+ Higher Terms
Saturn	GM+ Higher Terms
Sun	GM
Jupiter Barycentre	GM
Mimas	GM
Tethys	GM
Dione	GM
Rhea	GM
Titan	GM
Hyperion	GM

3. Methodology

With the purpose of providing the models and methods applied to produce the results needed to answer the research question presented in Section 1.2, this chapter describes the mission architecture (Section 3.1) and models setup (Section 3.2), followed by a presentation of the covariance analysis method used to study the uncertainty of geophysical parameters of interest (Section 3.3). The section terminates with the method used for the investigation of the interior (Section 3.4).

The flow chart in Figure 3.0.1 provides an overview of the process executed to produce the results needed to answer the research question. It can be observed that the covariance analysis work (FC3) provides the answer to the first research sub-question, while the interior investigation (FC4) leads to an answer to the second sub-question. The flow chart shows how the reference values for the formal errors of the geophysical parameters of interest produced in the nominal representative cases study (FC3.2) feed into the interior investigation. The chart is to be used by the reader as a reference through this chapter. A complete explanation of the method followed in each step of Figure 3.0.1 is provided in the following sections.

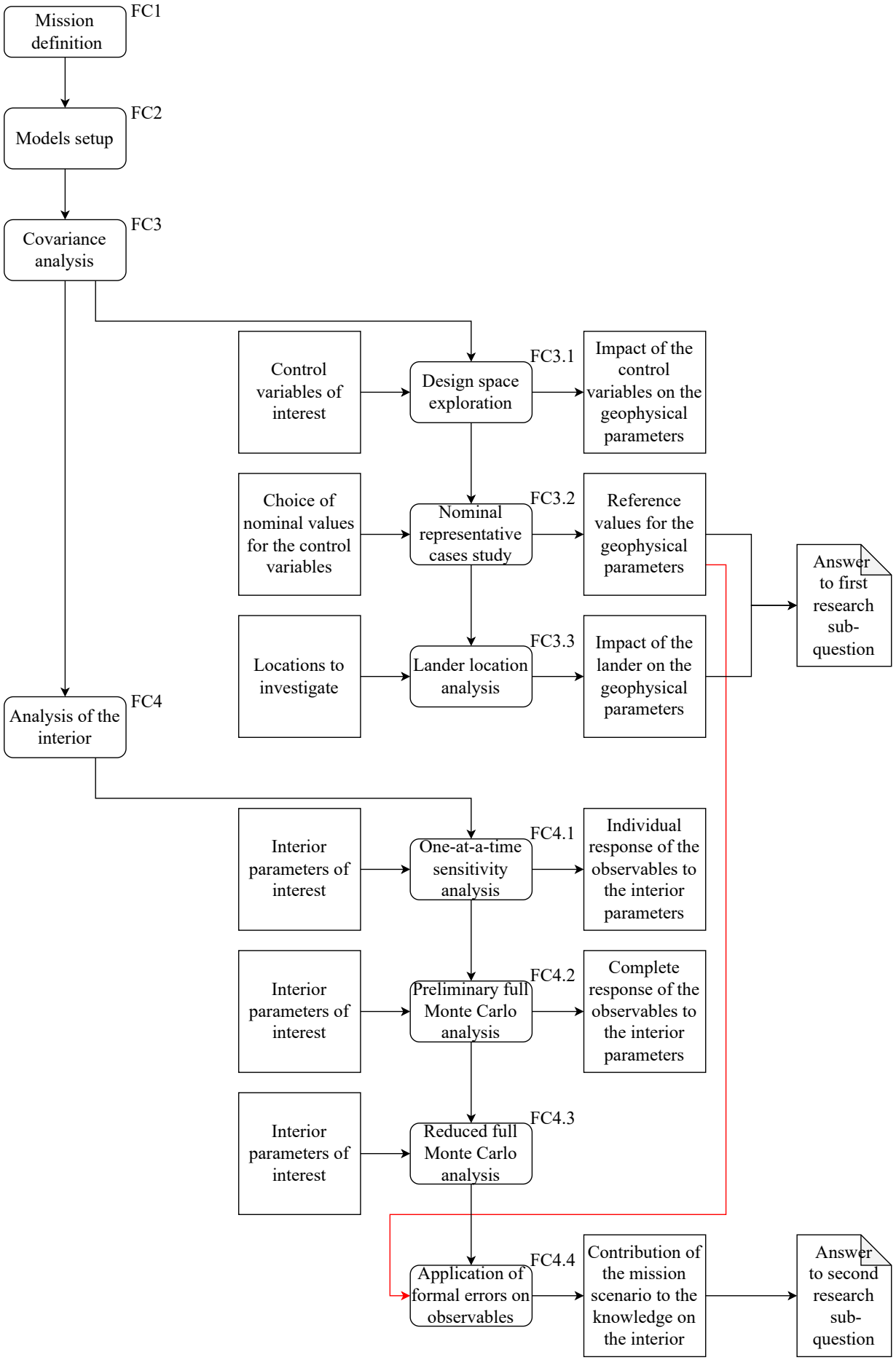

Figure 3.0.1.: Methodology flow chart. The labels FCn refer to the flow chart step. The red line shows how the results produced in the covariance analysis are used to study the interior.

3.1. Mission architecture overview

As already introduced in Section 1.2, the mission concept is composed of an orbiter around Enceladus, tracked through a two-way link by the Estrack GSs, and through a two-way link by a set of radio beacons located at selected locations. The noise level of the two sets of links is reported in Table 3.1.1.

Table 3.1.1.: Doppler and range noise for the radio links with the Earth GSs and the Enceladus landers.

Link	Doppler noise level [$\mathrm{m\,s^{-1}}$] (Integration time of 60 s)	Range noise level [m]	Notes
Estrack GSs	1.2×10^{-5}	0.2	Values generally assumed for the Juice mission (e. g., Di Benedetto et al. (2021), M. Fayolle et al. (2023))
Enceladus landers	1.0×10^{-4}	1.0	

An overview of the relevant vehicle parameters is given in Table 3.1.2, while the distribution of the radio beacons is detailed in Table 3.1.3 and shown in Figure 3.1.1. The coordinates of the radio beacons are selected so that they may provide a uniform coverage of the longitude and latitude range of interest. As shown by Figure 3.1.1, since the latitude of the ground tracks is bounded in the region $\sim [-60; 60]$ deg, the radio beacons are homogenously deployed in this latitude range. Furthermore, a minimum elevation angle of 15 deg is set as condition for a viable observation, for the Earth GS (as in e. g., Di Benedetto et al. (2021), Magnanini et al. (2024)). Additionally, even though the link between the S/C and the surface landers is not affected by atmospheric effects (except for the noise introduced by the possible refraction of the signal due to the water particles expelled by the Tiger Stripes at the South Pole), the minimum elevation of 15 deg is adopted also for the link with the landers, to avoid possible multipath effects due to the reflection on the icy surface and to consider the mechanical setup and disposition of the antenna within the lander, which might limit its FOV.

Table 3.1.2.: Relevant vehicle parameters.

Parameter	Unit	Value
Mass	kg	2150
Reference surface area	$\mathrm{m^2}$	100
Radiation pressure coefficient	–	1.2

Table 3.1.3.: Geodetic coordinates of the landers on the surface of Enceladus.

Lander	Altitude [m]	Latitude [deg]	Longitude [deg]
L_1	0.0	−60.0	0.0
L_2	0.0	−30.0	40.0
L_3	0.0	0.0	80.0
L_4	0.0	30.0	120.0
L_5	0.0	60.0	160.0
L_6	0.0	−60.0	200.0
L_7	0.0	−30.0	240.0
L_8	0.0	0.0	280.0
L_9	0.0	30.0	320.0

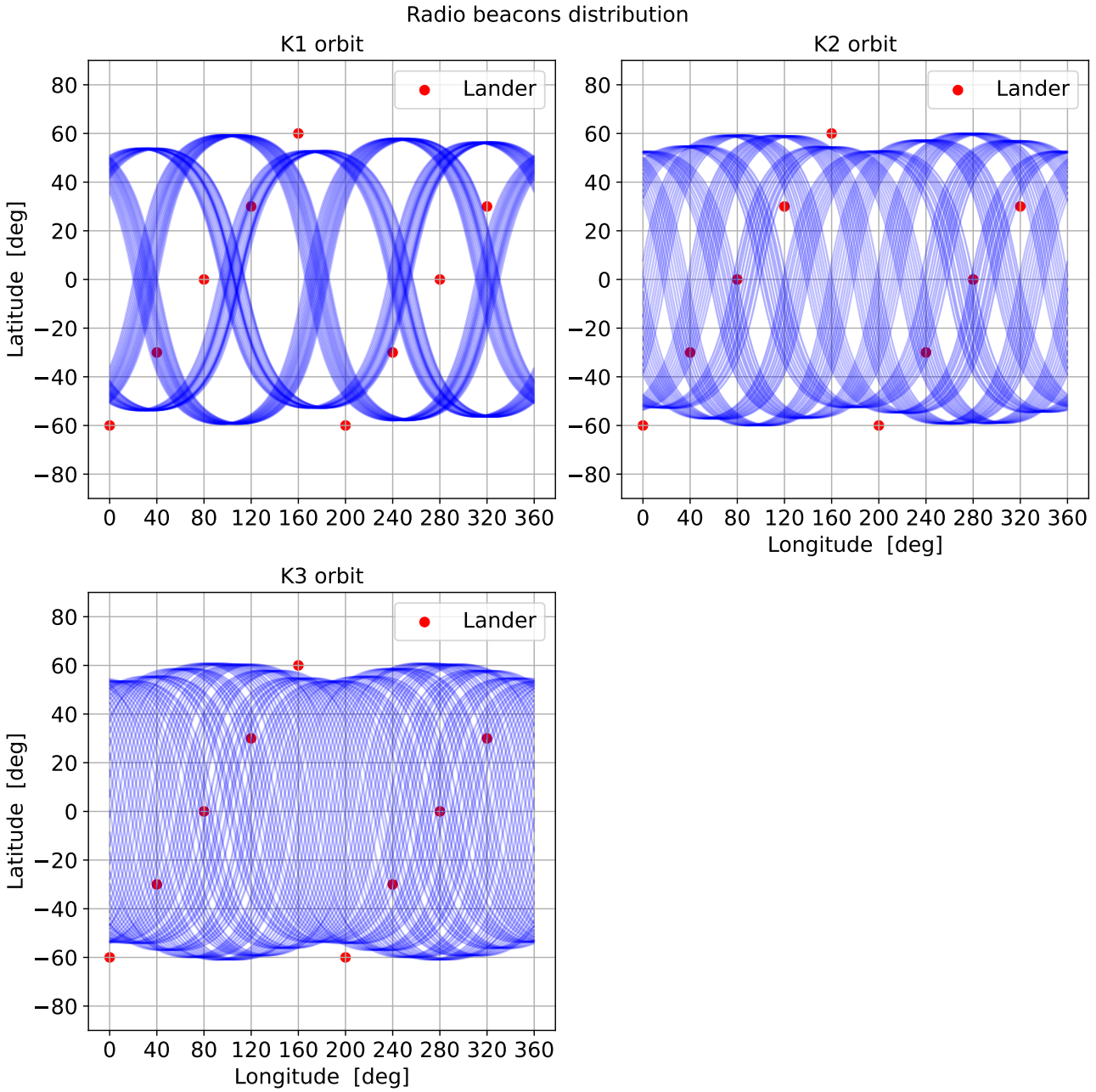

Figure 3.1.1.: Distribution of the radio beacons on the surface of Enceladus, as described in Table 3.1.3, showing their coverage by the different orbit solutions. The orbits are propagated for a period of 28 days with the dynamical model detailed in Table 3.1.4.

In terms of the S/C orbit, three stable orbits retrieved from Auer Wilkins et al. (2025) are available, as mentioned in Section 2.4. The initial state solutions were computed by Auer Wilkins et al. (2025) considering the gravity field coefficients for Enceladus and Saturn provided respectively by Park et al. (2024) and Iess et al. (2019). The solutions provided by Auer Wilkins et al. (2025) are repeating with the same repeating properties as of those in Table 2.4.1 by Benedikter et al. (2022), and are reported in Table 3.1.5. This work is based on the solutions provided in Table 3.1.5. The dynamical model considered by Auer Wilkins et al. (2025) to obtain the solutions is reported in Table 3.1.4.

Table 3.1.4.: Dynamical model considered by Auer Wilkins et al. (2025) to obtain the initial states solutions reported in Table 3.1.5.

Body	Acceleration
Enceladus	SH $(3, 3)$ grav. acceleration
Saturn	SH $(8, 0)$ grav. acceleration

Table 3.1.5.: Refined orbit solutions with repeating ground track for an Enceladus science mission. Retrieved from Auer Wilkins et al. (2025). The dynamical model presented in Table 3.1.4 was used to compute these solutions. The initial states are provided both in Keplerian and Cartesian elements. The Keplerian elements are the following: semi-major axis (a); eccentricity (e); inclination (i); argument of pericentre (ω); longitude of the ascending node (γ); true anomaly (ν). The Cartesian elements are referred to the Enceladus-centred inertial frame. The gravity field settings used to obtain these solutions are retrieved from Iess et al. (2019) for Saturn and Park et al. (2024) for Enceladus. The table provides also the number of revolutions after which the orbits are repeated (N_{rep}), the associated period of repetition (T_{rep}), and the mean altitude of the orbits.

Parameter	Unit	K1	K2	K3
a_0	m	4.50999999×10^5	4.87000000×10^5	4.75000000×10^5
e_0	–	$5.99999999 \times 10^{-2}$	$8.00000004 \times 10^{-2}$	$7.00000000 \times 10^{-2}$
i_0	deg	5.23895829×10^1	5.26376142×10^1	5.36298676×10^1
ω_0	deg	2.60938356×10^2	2.60962372×10^2	2.61055539×10^2
γ_0	deg	1.64440308×10^1	1.65993162×10^1	1.64440308×10^1
ν_0	deg	9.18538771×10^1	9.18538761×10^1	9.18538761×10^1
x_0	m	4.37860747×10^5	4.71789124×10^5	4.60709175×10^5
y_0	m	9.48716723×10^4	1.02222980×10^5	9.98223410×10^4
z_0	m	-4.47516654×10^4	-4.82193361×10^4	-4.70869558×10^4
$v_{x,0}$	$\mathrm{m\,s^{-1}}$	$6.67354927 \times 10^{-1}$	3.14085658	2.46463058
$v_{y,0}$	$\mathrm{m\,s^{-1}}$	7.94830037×10^1	7.66580975×10^1	7.56765950×10^1
$v_{z,0}$	$\mathrm{m\,s^{-1}}$	9.86040217×10^1	9.50418662×10^1	9.76068794×10^1
N_{rep}	–	5	9	14
T_{rep}	days	1.2919	2.5788	3.8744
mean h	km	197.0	230.4	219.0

3.2. Propagation, estimation, and environment models setup

As shown in the flow chart displayed in Figure 3.0.1, the definition of the mission architecture is followed by the setup of the models (FC2). This section provides the presentation of the implemented acceleration, propagation, environment, and estimation models.

3.2.1. Acceleration, environment, and integrator setup

The setup to simulate the observations for the different link ends requires the definition of an environment model, a dynamical model, and propagator settings.

The selected propagator settings are reported in Table 3.2.1. The integrator settings are selected so that they lead to a small integration error, with a smooth and reliable behaviour, in order for it to be considered negligible with respect to the error caused by the dynamical model. Additionally, the selected settings avoid excessive computational time. The method and associated results used for

the choice of the integrator settings are presented in Appendix E.1. With the selected propagator settings and the dynamical model reported in Table 3.1.4, an integration error of the order of $\sim 10^{-4}$ m is achieved. The verification in Appendix E.2.1 shows that with the acceleration model selected in Table 3.2.2, the integrator settings lead to an integrator error of $\sim 10^{-2}$ m. Nonetheless, Appendix E.2.1 shows that the selected settings are still the optimal solution when considering computational time, and they still allow to answer the research question, as discussed in Section 4.1.

Table 3.2.1.: Considered propagator settings.

Parameter	Value
Propagator model	Cowell
Integrator	Fixed step RKF5(6)
Integration time step	15 s

The considered bodies, with the acceleration they apply on the orbiter and the relative environment models are reported in Table 3.2.2. A description of the method used to choose the bodies included in the dynamical model is given in Appendix E.2. It should be noted that the dynamical model selected for this work presents additional perturbations with respect to the model used by Auer Wilkins et al. (2025) and reported in Table 3.1.4. The additional accelerations are considered in order to minimize the physical model error and to account for the most relevant bodies from which an hypothetical Enceladus orbiter would be affected. The analysis in support of this choice is provided in Appendix E.2.

The integration of the orbit solutions (reported in Table 3.1.5) with the considered acceleration and environment models is performed in a multi-arc fashion. Thus, the entire integration arc is split up in shorter sub-arcs, whose initial state is taken at the same epoch on the nominal solutions produced integrating the initial states of Table 3.1.5 with the dynamical model of Table 3.1.4. Dividing the mission in multiple arcs is an established approach for estimation applications (e. g., Magnanini et al. (2024), M. Fayolle et al. (2022), Gomez Casajus et al. (2022), Durante et al. (2020), Iess et al. (2019), Dirkx et al. (2019), Zannoni et al. (2018)). It allows to process smaller batches of data collected during non-contiguous orbital segments. The division of the arcs may be due to orbital manoeuvres that require the S/C to exit its nominal science mode, interrupting the nominal acquisition of data. Section 4.1 provides a verification that the orbit solutions propagated with the dynamical model from Table 3.2.2 in a multi-arc fashion are still representative of a science orbit at Enceladus and are stable.

As presented in Table 3.2.2, the gravity settings of Saturn and Enceladus are retrieved from Auer Wilkins et al. (2025), Iess et al. (2019) and Park et al. (2024), following the environment model setup used by Auer Wilkins et al. (2025). The applied gravity settings are reported in Table 3.2.3 and Table 3.2.4. Finally, the rotational model of Enceladus is presented separately in Section 3.2.2.

3.2.2. Enceladus' rotation model

As mentioned in Section 3.2.1, this section provides a discussion of the rotation model of Enceladus. In Section 2.1.7 it was pointed out how measurements of the libration of a body can provide information on its interior, such as the mean thickness of the ice shell, as pointed out by Ermakov et al. (2021). Additionally, libration measurements provide a constraint that must be met by the developed interior models, as considered by Hoolst et al. (2016). In order to include the libration as a solve-for parameter for the covariance analysis algorithm, according to Table 3.3.1, it is necessary to assign to Enceladus a rotation model that includes the libration terms. Similarly, as discussed in Section 2.1.8, the orientation of the spin-axis allows to compute the obliquity, which gives an independent constraint on the MoI, which is related to the degree of differentiation of the interior (e. g., Rovira-Navarro (2022)). Hence, in order to include the rotation pole position, the rotation model of Enceladus must include at least

Table 3.2.2.: Acceleration settings and environment settings for the bodies included in the dynamical model. The environment settings refer to the ephemeris model, gravity field, shape, rotation, atmosphere, and radiation source model. Only the relevant and needed environment settings are presented.

Body	Acceleration settings	Environment settings/kernels of interest
Sun	*GM* grav. acc.; cannonball SRP	Ephemeris from inpop19a_TDB_m100_p100_spice.bsp. Isotropic point source with a luminosity of 3.828×1026 W (Dirkx et al., 2022).
Saturn	SH (8,0) grav. acceleration.	Gravity settings from Auer Wilkins et al. (2025) and Iess et al. (2019) (reported in Table 3.2.4). Ephemeris from NOE-6-2018-MAIN-v2.bsp.
Enceladus	SH (3,3) grav. acc.	Gravity settings from Park et al. (2024) (reported in Table 3.2.3). Rotation model from Park et al. (2024) (discussed in Section 3.2.2). Ephemeris from NOE-6-2018-MAIN-v2.bsp. Spherical shape from pck00010.tpc.
Tethys	*GM* grav. acc.	*GM* from NOE-6-2018-MAIN-v2.tpc. Ephemeris from NOE-6-2018-MAIN-v2.bsp.
Dione	*GM* grav. acc.	*GM* from NOE-6-2018-MAIN-v2.tpc. Ephemeris from NOE-6-2018-MAIN-v2.bsp.
Mimas	*GM* grav. acc.	*GM* from NOE-6-2018-MAIN-v2.tpc. Ephemeris from NOE-6-2018-MAIN-v2.bsp.
Rhea	*GM* grav. acc.	*GM* from NOE-6-2018-MAIN-v2.tpc. Ephemeris from NOE-6-2018-MAIN-v2.bsp.
Titan	*GM* grav. acc.	*GM* from NOE-6-2018-MAIN-v2.tpc. Ephemeris from NOE-6-2018-MAIN-v2.bsp.

Table 3.2.3.: Enceladus gravity field settings. Retrieved from Park et al. (2024).

Parameter	Unit	Value
GM	$\mathrm{m^3\,s^{-2}}$	$7.210366688598896 \times 10^9$
R	m	2.566000×10^5
$C_{2,0}$	–	-5477.45×10^{-6}
$C_{2,1}$	–	7.86×10^{-6}
$C_{2,2}$	–	1517.90×10^{-6}
$C_{2,3}$	–	177.82×10^{-6}
$S_{2,1}$	–	7.60×10^{-6}
$S_{2,2}$	–	-275.31×10^{-6}

Table 3.2.4.: Saturn gravity field settings. Retrieved from Auer Wilkins et al. (2025) and Iess et al. (2019).

Parameter	Unit	Value
GM	$m^3\,s^{-2}$	$3.793120749865224 \times 10^{16}$
R	m	6.03300000×10^{7}
$C_{2,0}$	-	$-1.629061510215236 \times 10^{-2}$
$C_{3,0}$	-	$-9.519974025353707 \times 10^{-8}$
$C_{4,0}$	-	$9.351185734877162 \times 10-4$
$C_{5,0}$	-	$5.984128286091720 \times 10^{-8}$
$C_{6,0}$	-	$-8.676367491774778 \times 10^{-5}$
$C_{7,0}$	-	$-4.808382695890572 \times 10^{-7}$
$C_{8,0}$	-	$1.393087926846997 \times 10^{-5}$
$C_{9,0}$	-	$-8.921515415583946 \times 10^{-7}$
$C_{10,0}$	-	$-5.425691388908470 \times 10^{-6}$

the constant terms for the rotation pole right-ascension and declination. The model presented in Section 2.1.7 retrieved from Park et al. (2024) accounts for both the libration terms and the constants terms for the pole position, according to the general formulation reported in (2.1.35) to (2.1.37).

As discussed in Section 2.1.7, Enceladus is characterized by a 1:1 spin-orbit resonance, thus it is necessary to ensure that with the selected rotation model, the frozen bulge is directed towards the tide-raising body (Murray & Dermott, 2000), for the purpose of estimating the libration amplitude (as selected in Table 3.3.1). Hence, the rotation model of Enceladus is investigated, to ensure that the prime meridian is aligned with the Enceladus-Saturn direction. The Enceladus-fixed spherical coordinates of Saturn and the orbital eccentricity of Enceladus are plotted in Figure 3.2.1. The results are generated using the rotation model by Park et al. (2024) and the associated DE440 (Park et al., 2021) and SAT441 (Jacobson et al., 2022) ephemerides. In Figure 3.2.1, it is possible to observe that when the model by Park et al. (2024) is implemented with no correction on the longitude of the prime meridian, the Enceladus-fixed longitude of Saturn is characterized by a sinusoidal trend about an average of about -6.0 deg. Hence, the prime meridian presents a constant offset with respect to the Enceladus-Saturn direction. The presence of the offset might be caused by the choice of Park et al. (2024) of defining the longitude of the prime meridian so that the centre of the Salih crater is located at -5 deg longitude. Thus, for the purpose of this work, a correction of the constant prime meridian offset W_0 is necessary to ensure that the mean Enceladus-fixed longitude of Saturn is equal to zero. The correction to W_0 is applied by adding the offset of Saturn's Enceladus-fixed longitude to the original W_0. The verification of the correct implementation of Enceladus' rotation model is reported in Section 4.3.1.

As already noted, the rotation model presented by Park et al. (2024) was generated with the DE440 (Park et al., 2021) and SAT441 (Jacobson et al., 2022) ephemerides, different with respect to the DE438[1] and SAT427[2] ephemerides used by Auer Wilkins et al. (2025) to generate the orbit solutions presented in Table 3.1.5. Hence, given the necessity of using coherent rotation and ephemerides models, the covariance analysis shall be performed with the DE440 and SAT441 planetary ephemerides. An assessment of the impact of switching the ephemerides on the covariance analysis setup and the verification that the orbits are still stable, allowing to answer the research question, is given in Section 4.6.

Finally, within the estimation framework of the observation partials, given that the constant terms of the declination ($\delta_0^{\text{s-a}}$) and right-ascension ($\alpha_0^{\text{s-a}}$) and the diurnal libration amplitude (W_T) are to be estimated (see Table 3.3.1), Tudat requires the partial derivatives of the rotation matrix from the Enceladus-fixed frame to the inertial frame with respect to the rotation parameters. Indicating with

[1] https://naif.jpl.nasa.gov/pub/naif/generic_kernels/spk/planets/
[2] https://naif.jpl.nasa.gov/pub/naif/pds/wgc/kernels/spk/

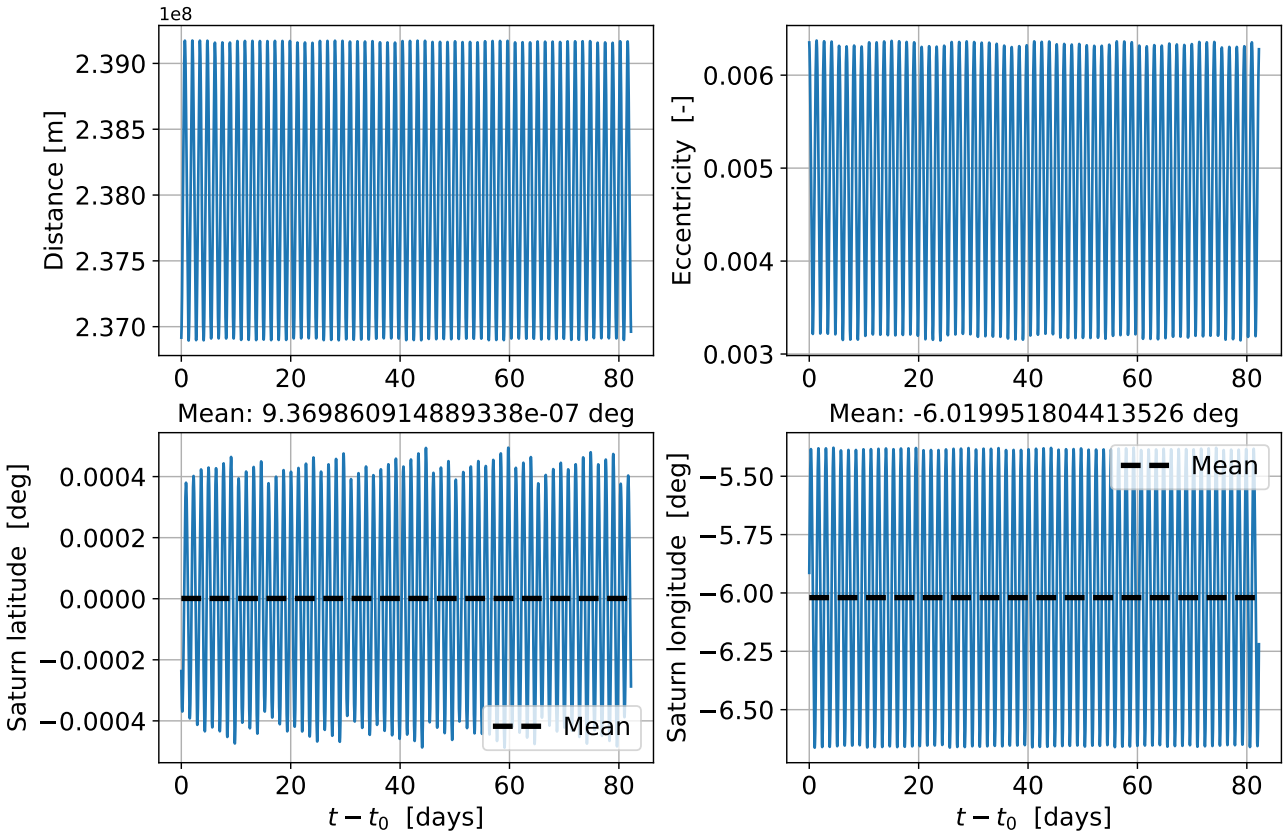

Figure 3.2.1.: Enceladus-fixed coordinates of Saturn and orbital eccentricity of Enceladus. The rotation model from Park et al. (2024) is considered, with a correction of W_0. The mean values are computed over 60 orbits.

$R^{\mathrm{IF/BF}}$ the rotation matrix from the body-fixed to the inertial frame, the following partial derivatives ought to be computed:

$$\frac{\partial R^{\mathrm{IF/BF}}}{\partial \alpha_0^{\mathrm{s\text{-}a}}}; \frac{\partial R^{\mathrm{IF/BF}}}{\partial \delta_0^{\mathrm{s\text{-}a}}}; \frac{\partial R^{\mathrm{IF/BF}}}{\partial \dot{\alpha}_0^{\mathrm{s\text{-}a}}}; \frac{\partial R^{\mathrm{IF/BF}}}{\partial \dot{\delta}_0^{\mathrm{s\text{-}a}}}; \frac{\partial R^{\mathrm{IF/BF}}}{\partial W_T}$$

The rotation matrix from body-fixed to inertial frame can be computed as (Bills & Scott, 2022):

$$R^{\mathrm{IF/BF}} = R_3\left(\alpha + \pi/2\right) R_1\left(\pi/2 - \delta\right) R_3\left(W\right) \tag{3.2.1}$$

where α is the right-ascension, δ is the declination, and W is the longitude of the prime meridian. The equations for the right-ascension, declination, and longitude of the prime meridian are reported in Section 2.1.7. In Tudat, the $\partial R^{\mathrm{IF/BF}}/\partial \alpha_0^{\mathrm{s\text{-}a}}; \partial R^{\mathrm{IF/BF}}/\partial \delta_0^{\mathrm{s\text{-}a}}; \partial R^{\mathrm{IF/BF}}/\partial \dot{\alpha}_0^{\mathrm{s\text{-}a}}; \partial R^{\mathrm{IF/BF}}/\partial \dot{\delta}_0^{\mathrm{s\text{-}a}}$ partials are already implemented. Thus, it has been necessary to implement only the $\partial R^{\mathrm{IF/BF}}/\partial W_T$ partials. Given the previously defined expressions, the following equation for $\partial R^{\mathrm{IF/BF}}/\partial W_T$ can be derived:

$$\frac{\partial R^{\mathrm{IF/BF}}}{\partial W_T} = R_3\left(\left(\alpha^{\mathrm{s\text{-}a}} + \pi/2\right)\right) R_1\left(\left(\pi/2 - \delta^{\mathrm{s\text{-}a}}\right)\right) \begin{pmatrix} -\sin W & -\cos W & 0 \\ \cos W & -\sin W & 0 \\ 0 & 0 & 0 \end{pmatrix} \sin\left(\omega_T t + \gamma_T\right) \tag{3.2.2}$$

In Equation 3.2.2, ω_T and γ_T refer to the frequency and phase associated to the diurnal libration amplitude W_T. The verification of the analytical formulation for the partial derivatives of the rotation matrix is reported in Section 4.2.

Furthermore, it should be noted that for the purpose of the estimation problem, it is not necessary to include all of the nutation terms in the rotation model of Enceladus, but only those that make the model sensitive to the parameters to estimate. However, when deleting the unnecessary nutation terms,

some long period trends might affect the evolution of the Enceladus-fixed coordinates of Saturn and result in long-period trends in the tidal forcing. In such scenario, the correction of the rotation model is required. For the purpose of this thesis, in order to avoid the generation of long period trends, and for keeping the ephemeris and rotation model consistent, all of the nutation terms are kept. Consistency between the rotation and ephemeris models is necessary because, as pointed out by Park et al. (2024), the coefficients for the rotation model in (2.1.35) to (2.1.37) were found through a least-squares fit of the SAT441 ephemerides (Jacobson, 2022), used in this work for the orbit propagation. Still, the analysis of the tidal forcing is carried out, to ensure that Enceladus is effectively tidally locked, with the prime meridian aligned with Saturn. The verification to ensure that Enceladus is tidally locked with Saturn is performed in Section 4.3.1.

3.2.3. Removal of the permanent tide

As presented in Section 2.1.6, the effect produced by the tidal forcing on the gravity field and surface displacement of the body is described through the Love numbers, which connect the tidal response of the body to the tidal forcing from which it is affected. Given that Enceladus is in a 1:1 spin-orbit resonance around Saturn, as mentioned in Section 2.1.7, the gravitational pull by Saturn produces a frozen equatorial bulge, on top of which the time-varying tidal response of the moon is summed. Thus, if the permanent tidal bulge is not removed, the time-varying effect on the gravitational and surface displacement is masked, leading to an overly optimistic estimate of the Love numbers. Below, the process for removing the effect of the permanent tide on the gravity field and shape of Enceladus is outlined.

Gravity field variations

Given that the full degree 2 tidal Love number is of interest (see Table 3.3.1), the analysis of the tidal forcing is carried out on the $(2,0)$, $(2,1)$, and $(2,2)$ gravity terms. The quantities $\Delta\bar{C}_{lm}/k_{lm}$ and $\Delta\bar{S}_{lm}/k_{lm}$, already presented in Section 2.1.6 in the form of the tidal response, are computed according to Equation 3.2.3:

$$\frac{\Delta\bar{C}_{lm}}{k_{lm}} = \frac{1}{2l+1}\frac{GM_j}{GM^*}\left(\frac{R}{r_j}\right)^{l+1}\bar{P}_{lm}\left(\cos\theta\right)\cos\left(m\varphi\right) \tag{3.2.3a}$$

$$\frac{\Delta\bar{S}_{lm}}{k_{lm}} = \frac{1}{2l+1}\frac{GM_j}{GM^*}\left(\frac{R}{r_j}\right)^{l+1}\bar{P}_{lm}\left(\cos\theta\right)\sin\left(m\varphi\right) \tag{3.2.3b}$$

The tidal forcing terms of degree 2 are plotted over 60 orbits in Figure 3.2.2. It is possible to observe that the variations of the $(2,0)$ and $(2,2)$ components are about two orders of magnitude smaller with respect to the mean, which is shifted from the zero value. For instance, $\Delta\bar{C}_{2,0}/k_{2,0}$ has an average value of -1.47×10^{-3}, while the amplitude of its oscillations are of the order of $\sim10^{-5}$. The offset from the zero average value is due to the permanent tide. Hence, by removing the effect of the frozen bulge on the gravity field within the estimation framework, the time-varying component of the tidal forcing is not masked by the permanent tide. As a result, within the covariance analysis algorithm, the k_2 Love number is effectively sensitive only to the time-varying tides raised by Saturn on Enceladus, and a possible overoptimistic estimation of k_2 is avoided.

The removal of the effect of the permanent tide on the gravity field variation of Enceladus is performed by computing the mean of $\frac{\Delta\bar{C}_{lm}}{k_{lm}}$ and $\frac{\Delta\bar{S}_{lm}}{k_{lm}}$ and subtracting it from the quantities computed through (3.2.3):

$$\left(\frac{\Delta\bar{C}_{lm}}{k_{lm}}\right)^* = \frac{\Delta\bar{C}_{lm}}{k_{lm}} - \text{mean}\left(\frac{\Delta\bar{C}_{lm}}{k_{lm}}\right) \tag{3.2.4a}$$

$$\left(\frac{\Delta\bar{S}_{lm}}{k_{lm}}\right)^* = \frac{\Delta\bar{S}_{lm}}{k_{lm}} - \text{mean}\left(\frac{\Delta\bar{S}_{lm}}{k_{lm}}\right) \tag{3.2.4b}$$

The verification of the removal of the effect of the permanent tide on the gravity field is proposed in Section 4.3.2.

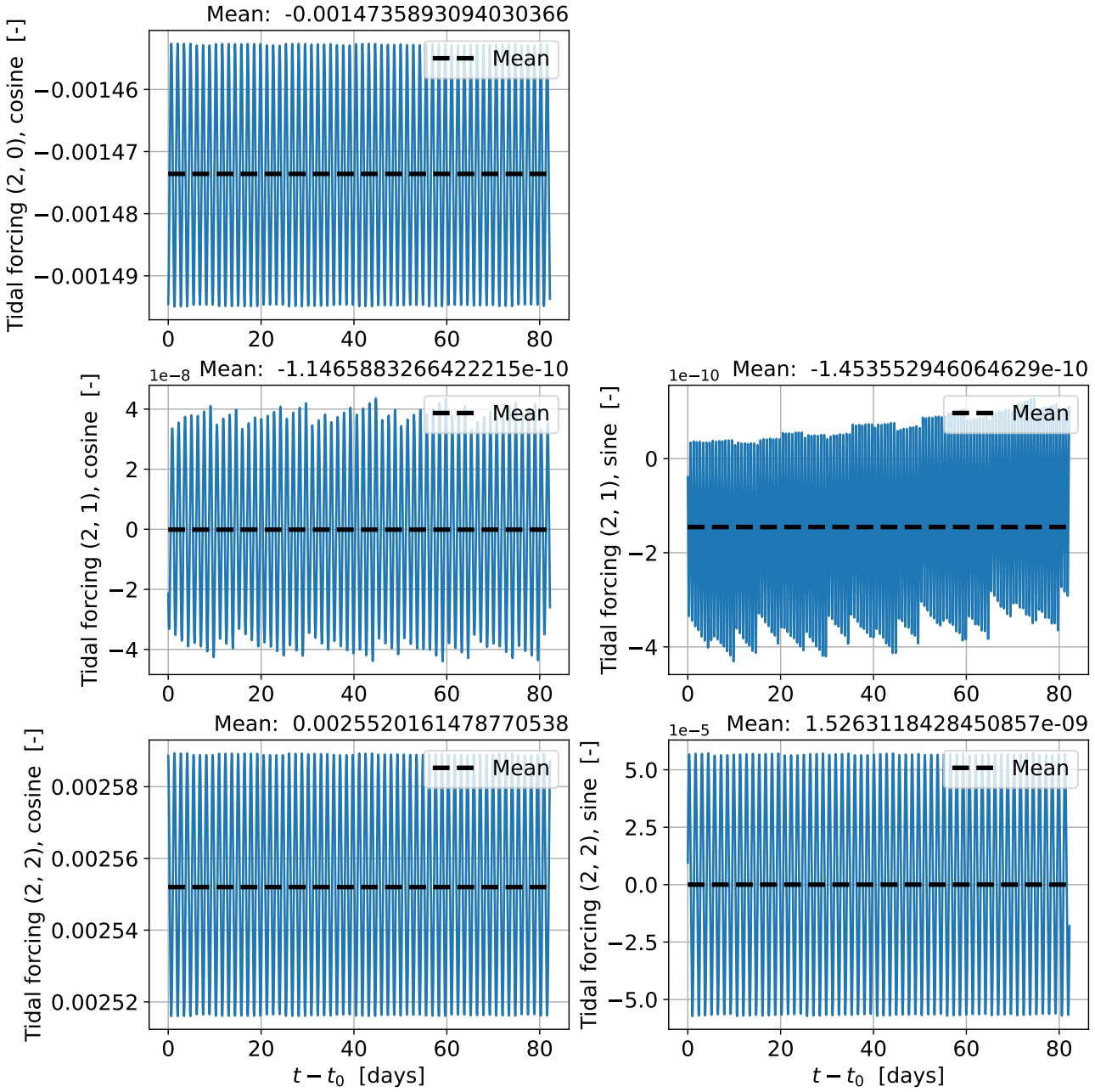

Figure 3.2.2.: Tidal forcing analysis for the cosine and sine terms of degree 2. The forcing is computed from the right-hand side side of Equation 3.2.3.

Surface displacement

Similarly to the gravity field deformation, also the effect of the permanent tide on the surface displacement must be corrected, so that the estimated radial displacement Love number is sensitive exclusively to the time-varying surface tidal displacements, avoiding an excessively optimistic estimation resulting from the static tidal bulge signal. Figure 3.2.3 shows the position displacement of each lander from Table 3.1.3 including the effect of the permanent tide. It can be observed that the variation of $\Delta\mathbf{r}$ is significantly smaller than the average value for most landers. In many, the variations are barely visible due to the large permanent displacement. As mentioned above, this may lead to an overly optimistic estimate of h_2, given the strong signal of the permanent tide. Thus, a correction must be performed.

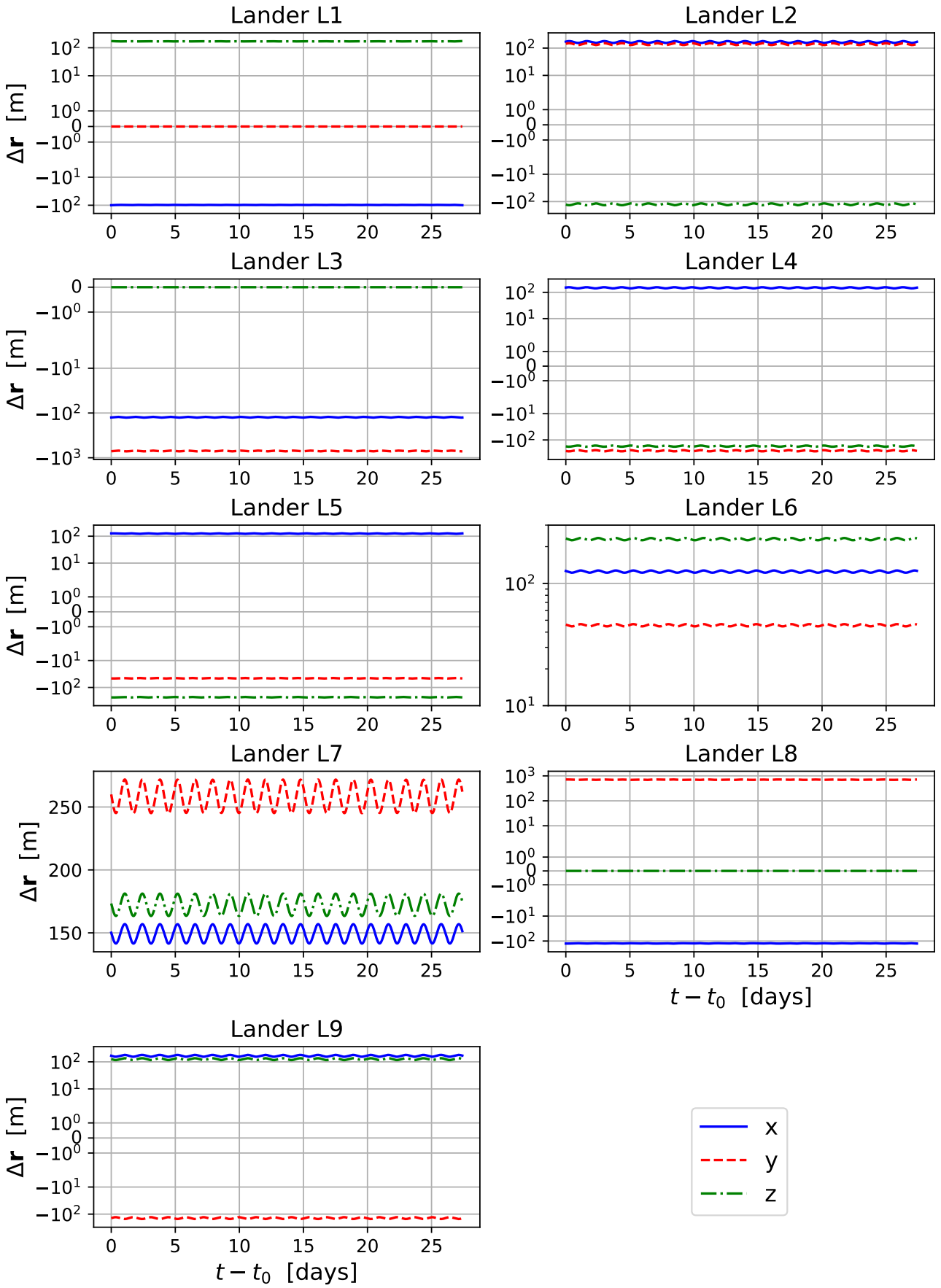

Figure 3.2.3.: Component-wise position displacement of the landers listed in Table 3.1.3, including the effect of the permanent tide. The plots show how large is the effect of the static tidal bulge with respect to the time-dependent variations.

The correction is performed for every lander listed in Table 3.1.3. As presented in Section 2.1.6, the position displacement of the lander due to the tidal deformation of Enceladus is computed according to Equation 2.1.28. Assuming that there is not lateral surface displacement, the landers position displacement is computed with a Shida number $l_2 = 0$. Furthermore, likewise to the gravitational tidal forcing, the correction of the surface displacement that is required for the estimation of the h_2 Love number is computed per unit of h_2. Also in this case, the average radial surface displacement due to tides at every lander location is computed over an integer number of orbits. The average value is then subtracted from the lander position displacement per unit of h_2. Recalling (2.1.28) for the surface displacement $\Delta\mathbf{r}$, the corrected tidal displacement is computed as

$$\left(\frac{\Delta\mathbf{r}}{h_2}\right)^* = \left(\frac{\Delta\mathbf{r}}{h_2} - \text{mean}\left(\frac{\Delta\mathbf{r}}{h_2}\right)\right)\Bigg|_{l_2=0} \tag{3.2.5}$$

The verification of the removal of the effect of the permanent tide on the surface displacement is reported in Section 4.3.3.

3.2.4. Radial displacement Love number observation partials

As for now, the partial derivatives of the observations with respect to the radial displacement Love number are not available in Tudat. Hence, in order to include h_2 among the estimation parameters, it is necessary to compute manually the partial derivatives, according to the following equation:

$$\frac{\partial\mathbf{h}}{\partial h_2} = \sum_{j=1,4} \frac{\partial\mathbf{h}}{\partial\mathbf{r}_{L_k}}(t_j)\,\frac{\partial\mathbf{r}_{L_k}}{\partial h_2}(t_j) \tag{3.2.6}$$

where $\mathbf{r}_{L_k}$ is the position of the k-th lander tracking the spacecraft at the epoch t_j. The sum is taken for the epochs of transmission t_1 of the signal and the epoch t_4 at which the signal is received back at the lander, assuming the definition adopted in Section 2.2.3.

Given the reduced round-trip light-time from the lander to the S/C and back to the lander, in the order of $\sim 7\times10^{-4}$ s for a 200-km orbit, including a nominal transponder delay of 6×10^{-6} s as the one of Cassini (see Section 2.2.4), it can be assumed that the surface tidal response of Enceladus changes negligibly given its orbital period of 1.37 days ($\approx 1.2\times10^5$ s), about 9 orders of magnitude higher. Hence, Equation 3.2.6 can be simplified as follows:

$$\frac{\partial\mathbf{h}}{\partial h_2} = \left(\sum_{j=1,4} \frac{\partial\mathbf{h}}{\partial\mathbf{r}_{L_k}}(t_j)\right)\frac{\partial\mathbf{r}_{L_k}}{\partial h_2}(t_4) \tag{3.2.7}$$

thus using the partial derivative of the lander position at the receive time.

$\frac{\partial\mathbf{r}_{L_k}}{\partial h_2}(t_4)$ describes the variation of the position of a surface point with respect to the h_2 Love number at the epoch t_4. The relation between the position displacement of a surface point and the h_2 Love number was already presented in Section 2.1.6. Recalling (2.1.28), (3.2.7) can be written as

$$\frac{\partial\mathbf{h}}{\partial h_2} = \left(\sum_{j}^{1,4} \frac{\partial\mathbf{h}}{\partial\mathbf{r}_{L_k}}(t_j)\right)\left(\Delta\mathbf{r}_{L_k}(t_4)\right)\Big|_{h_2=1,l_2=0} \tag{3.2.8}$$

As a result, given the output design matrix as produced by Tudat, it is possible for every observation to compute the h_2 partial, by taking the already available partial derivatives of the observation with respect to the landers position, and computing the landers position displacement with $h_2 = 1$ and $l_2 = 0$, keeping in consideration the correction values computed beforehand (Section 3.2.3). The position displacement of the landers due to the gravitational tidal forcing of degree 2, i. e., the quantity

$$\left(\Delta\mathbf{r}_{L_k}(t_4)\right)\Big|_{h_2=1,l_2=0}$$

is computed through the available Tudat functionality[3]. The following equation is then implemented for every observation:

$$\frac{\partial h_i}{\partial h_2} = \left(\sum_{j}^{1,4} \frac{\partial h_i}{\partial \mathbf{r}_{L_k}} (t_j) \right) \left(\left(\Delta \mathbf{r}_{L_k} (t_4) \right) \Big|_{h_2=1, l_2=0} - \overline{\Delta \mathbf{r}}_{L_k} \Big|_{h_2=1, l_2=0} \right) \tag{3.2.9}$$

3.3. Covariance analysis

As outlined in the flow chart in Figure 3.0.1, the setup of the propagation, acceleration, and environment models is followed by the execution of the covariance analysis (FC3). With the covariance analysis, this work aims to answer the first research sub-question (Section 1.2), by providing reference values for the level of uncertainty for geophysical parameters of interest that the described mission setup (Section 3.1) can achieve. The covariance analysis work is divided in three steps: the exploration of the design space (FC3.1, Section 3.3.2), the study of nominal representative scenarios (FC3.2, Section 3.3.3), and the investigation of the impact of the location of a single lander on the uncertainty associated to the geophysical parameters of interest (FC3.3, Section 3.3.4). Before presenting the followed methodology for the covariance analysis, the estimation parameters are provided in Section 3.3.1.

3.3.1. Estimation parameters

This section presents and discusses the set of solve-for parameters considered in this work for the covariance analysis. The list of parameters is summarized in Table 3.3.1, which reports also the consider parameters, as described in Section 2.2.2.

Firstly, the initial state (position and velocity) of the orbiter around Enceladus is estimated, so that the orbit can be propagated through the state transition matrix (see Section 2.2.1). Additionally, given that the landers provide information on the local surface displacement, their position is a relevant piece of information for the measurement of the surface deformation of the moon. As a result, their position is estimated.

Furthermore, in terms of geophysical quantities, the spherical harmonic gravity coefficients up to degree and order 30 and the gravitational parameter of Enceladus are estimated. The choice of estimating the gravity field expansion up to degree and order 30 follows from Genova et al. (2024), who simulate a gravity mapping phase to Enceladus through a New Frontiers-class orbiter mission, estimating the uncertainty for the harmonic gravity coefficients up to $l, m = 30$. For the coefficients of degree 2, the a priori uncertainty is retrieved from Park et al. (2024), while for the rest, the Kaula rule is applied, according to Equation 3.3.1 (Lemoine et al., 2013):

$$\sigma = \frac{\kappa}{l^2} \tag{3.3.1}$$

In (3.3.1), κ is the Kaula coefficient used to tune the a priori constraint. It ought to be pointed out that the Kaula rule is inconsistent with uncompensated topography (Ermakov et al., 2021). For this reason, the κ coefficient will be investigated further in the next section, following the procedure laid out in Figure 3.0.1 (FC3.1).

Of particular scientific interest are the gravity quadrupole harmonic coefficients and the degree 3 zonal harmonic coefficient: they provide information on the MoI and the long-period fluid behaviour of the moon (refer to Section 2.1.4). Finally, estimating such a large number of parameters allows to infer a more realistic estimate of the standard deviation associated to the gravity harmonic coefficients, since the information provided by the radio tracking data is used for numerous solve-for parameters instead of just a few ones. Moreover, to study the interior dynamic response, as described in Section 2.1.6,

[3] basicTidalBodyDeformation.cpp

Table 3.3.1.: Estimated and consider parameters with the associated nominal a priori uncertainty.

Estimated parameter	Unit	Symbol	Par. size	Nominal a priori uncertainty
Arc-wise S/C initial position	m	$\mathbf{r}^i_{0,\mathrm{V}}$	$3n_{\mathrm{arcs}}$	5×10^3
Arc-wise S/C initial velocity	$\mathrm{m\,s^{-1}}$	$\mathbf{v}^i_{0,\mathrm{V}}$	$3n_{\mathrm{arcs}}$	0.5
Landers position in Enceladus-fixed frame	m	$\mathbf{r}^{\mathrm{E}}_{\mathrm{L},i}$	$3\,n_{\mathrm{L}}$	1×10^2
Enceladus gravitational parameter	$\mathrm{m^3\,s^{-2}}$	μ_{E}	1	3×10^7
Enceladus spherical harmonic cosine and sine coefficients from $(l,m) = (1,0)$ up to $(l,m) = (30,30)$	–	${C_{lm}}^{\mathrm{E}}$; ${S_{lm}}^{\mathrm{E}}$	$495 + 465$	Kaula constraint with $\kappa = 1 \times 10^{-3}$; for the degree 2 coefficients, the a priori values are given in Table 3.3.3.
Enceladus degree 2 gravity deformation Love number	–	$\Re\left(k_2\right); \Im\left(k_2\right)$	2	1×10^{-2}; 1×10^{-2}
Enceladus degree 2 surface displacement Love number	–	h_2	1	∞
Enceladus diurnal libration amplitude	deg	W_T	1	3×10^{-4}
Enceladus rotation pole position (constant terms)	deg	$\alpha_0^{\text{s-a}}$; $\delta_0^{\text{s-a}}$	2	∞
Enceladus rotation pole rate	deg	$\dot{\alpha}_0^{\text{s-a}}$; $\dot{\delta}_0^{\text{s-a}}$	2	∞
SRP coefficient	–	C_{SRP}	1	1×10^{-10}
Arc-wise empirical acceleration	$\mathrm{m\,s^{-2}}$	$\mathbf{a}^i_{\mathrm{emp}}$	$3n_{\mathrm{arcs}}$	1×10^{-9}
Consider parameter	**Unit**	**Symbol**	**Par. size**	**Nominal a priori uncertainty**
Earth GS position	m	$\Delta\mathbf{r}_{\mathrm{GS}}$	3	5×10^{-3}

both the real and imaginary part of the gravitational (k_2) and radial displacement (h_2) Love number are estimated. The imaginary component of k_2 allows to compute the tidal phase lag difference, from which information on the tidal dissipation can be inferred (refer to Section 2.1.6). As pointed out in Section 2.1.6, the h_2 Love number can be included as a solve-for parameter by integrating the radio tracking measurements provided by the landers.

The dynamic response of the interior to the external forcings is studied also through the libration modes, which are related to the interior properties of the moon, as described in Section 2.1.7. The libration modes of Enceladus are reported in Table 2.1.1, which shows that the moon is characterized by a short-period diurnal libration and two long-period librations due to the 2:1 resonance with Dione. Given that the period of the non-diurnal librations (about 3 and 11 years respectively) is much longer than the expected duration of the science phase (a few months), the most useful libration mode for studying the interior response of Enceladus is the diurnal one, even if its amplitude is the smallest. Furthermore, since for the diurnal libration the ratio of the resonant frequency ($\approx 1.03\,\mathrm{rad\,day^{-1}}$, corresponding to a period of ≈ 6.1 days) to the diurnal frequency ($\approx 4.58\,\mathrm{rad\,day^{-1}}$ corresponding to a period of $\approx$ 1.37 days) is smaller than one (Rambaux et al., 2010), the diurnal libration is particularly sensitive to the interior of the moon, given that the libration amplitude is more easily damped by the ratio smaller than one. On the other hand, for the librations due to the orbital resonance with Dione, $\omega_0/\omega_i >> 1$, hence considering Rambaux et al. (2010, Equations 3 and 6), the libration amplitude is nearly equal to the magnitude of the coupling (reported by Vienne A. and Duriez L. (1995)). Such long-period modes are at first order independent of the internal structure of the moon (Rambaux

et al., 2011). As also discussed by Van Hoolst et al. (2024) for the cases of Callisto and Ganymede, the most promising librations for studying the internal structure of a moon are those close to the resonant frequency.

Finally, in order to include the effect of the noise introduced by the thermal radiative acceleration due to the RTGs and for including other possible dynamical noise sources not accounted for, empirical accelerations are added to the solve-for parameters, as discussed in Section 2.2.4. The empirical accelerations are estimated anew at every arc. The effect of the empirical accelerations is of introducing a dynamical model uncertainty in the estimation model. Along the same line, also the SRP coefficient, associated to the SRP acceleration, is estimated.

Similarly, effects such as the range bias due to the DST and GS time delay (Bertone et al., 2018) and the uncertainty associated to the position of the Earth GS are included as consider parameter, as already mentioned in Section 2.2.2. The need for precise knowledge of the considered station position was discussed by Zumberge et al. (2009). The deviation of the position of the considered GS with respect to the known value is assumed to be small, with zero mean and a standard deviation of 5 mm. The selected value is in agreement with the 3D position accuracy estimate for the ESA stations by Leinen et al. (2007).

Other parameters, such as the orbital elements of Enceladus and the Earth ephemeris, are not included among the estimated parameters, since their inclusion is out of the scope of this work, as data from past and present missions would be required (e. g., Dirkx et al. (2014), Verma (2014)).

3.3.2. Covariance design space exploration

As shown in Figure 3.0.1, the design space exploration (FC3.1) has the aim of assessing the impact of selected control variables on the geophysical parameters. This allows to assess how the solve-for parameters are affected by the mission design and by a set of science parameters, eventually leading to the choice of settings that can be representative for a future orbiter mission to Enceladus and that lead to tight constraints on the geophysical parameters that describe the moon.

Hence, in order to study how the mission architecture and science parameters affect the formal error of the solve-for parameters, a number of design variables is selected and their individual influence on the solution is assessed. This design space exploration is performed with the aim of selecting a few combinations of settings that may lead to optimal and realistic solutions, to be used in the next step (FC3.2 in Figure 3.0.1).

The parameters to be estimated were already introduced in Table 3.3.1. The design parameters with their associated values are reported in Table 3.3.2. The covariance analysis is performed with a base configuration on top of which the control parameters are tuned. The base configuration is presented in Table 3.3.3. The control parameters are divided on mission design and science-related parameters, given that some variables are related to the mission architecture, for instance the length of the tracking arcs, the number of landers deployed on Enceladus' surface, and the mission duration. The science parameters are related to the geophysical measurements of interest and have a direct influence on the results, including the Kaula coefficient used to compute the a priori constraint on the SH gravity field coefficients, according to (3.3.1). As already mentioned in Section 3.3.1, the generally considered rule of (3.3.1) is inconsistent with uncompensated topography (Ermakov et al., 2018). For this reason, its investigation must be included in the covariance design space exploration. It should be noted that the Kaula constraint is not applied to those gravity terms for which knowledge of the uncertainty is already available in literature. Such terms are the following: $C_{2,0}$, $C_{2,1}$, $C_{2,2}$, $C_{3,0}$, $S_{2,0}$, $S_{2,0}$. For these terms, the adopted a priori uncertainty is indicated in Table 3.3.3.

For every included landers case as shown in Table 3.3.2, the listed tuning parameters were varied. In such a way, both the effect of adding a number of landers and varying one of the tuning parameters can be considered. For every run, a few science-related parameters of interest are saved and plotted, including:

Table 3.3.2.: Design space explored in the preliminary covariance analysis study.

Mission design parameter	Unit	Values	Notes
Landers to include	–	None; L_3; (L_1, L_3); ($L_1, L_2, L_3, L_4, L_5, L_6, L_7, L_8, L_9$)	Reported in Table 3.1.3
Initial state solution	–	$K_1; K_2; K_3$	Reported in Table 3.1.5
Arc duration	days	$1; 2; 7$	M. Fayolle et al. (2022), Magnanini et al. (2024)
Simulation duration	days	$28; 60; 90$	
Inclusion of lander range observable	–	Yes; No	
Duration of tracking arc from Earth GSs	hrs	$4; 6; 8$	Based on the nominal values by S. Fayolle (2025) and Genova et al. (2024).
A priori σ on lander position	m	$1 \times 10^2; 1 \times 10^3$	
A priori σ on SRP coefficient	–	$\infty; 1 \times 10^{-1}; 1 \times 10^{-10}$	Large range of values chosen to include both the case in which the SRP is known from the design and tests on the S/C and the case in which the SRP is unconstrained.
Science parameter	**Unit**	**Values**	
Kaula constraint coefficient	–	$1 \times 10^{-6}; 1 \times 10^{-5}; 1 \times 10^{-4}; 4 \times 10^{-4}; 1 \times 10^{-3}$	Multiple orders of magnitude considered due to an inconsistency with of the Kaula rule (Equation 3.3.1) with uncompensated topography (Ermakov et al., 2018). The central value (4×10^{-4}) is taken from Genova et al. (2024) for partially compensated topography.
A priori σ on empirical acc.	$\mathrm{m\,s^{-2}}$	$1 \times 10^{-9}; 1 \times 10^{-8}; 1 \times 10^{-7}; 1 \times 10^{-6}; 1 \times 10^{-5}$	Large range of empirical accelerations, to account for a wide set of unmodelled accelerations scenarios. The considered upper boundary value is two orders of magnitude smaller than the magnitude of the perturbation by Saturn (see Figure E.2.1a).
Duration of empirical accelerations arc	hrs	$12; 24$	
A priori σ on rotation pole position	deg	(∞, ∞); $(1 \times 10^{-1}, 1 \times 10^{-1})$; $(1 \times 10^{-2}, 1 \times 10^{-2})$	
A priori σ on rotation pole rate	$\mathrm{deg\ s^{-1}}$	(∞, ∞); $(1 \times 10^{-1}, 1 \times 10^{-1})$; $(1 \times 10^{-2}, 1 \times 10^{-2})$	

Table 3.3.3.: Base configuration used for the design space exploration.

Mission design parameter	Unit	Value	Notes
Landers to include	–	$L_1, L_2, L_3, L_4, L_5, L_6, L_7, L_8, L_9$	
Initial state solution	–	K_1	
Arc duration	days	1	Genova et al. (2024)
Duration of tracking arc from Earth GSs	hrs	8	S. Fayolle (2025), Genova et al. (2024)
Arc-wise tracking delay from Earth GSs	hrs	2	
Simulation duration	days	28	Benedikter et al. (2022)
Inclusion of lander range observable	–	No	
A priori constraint (σ) on lander position	m	1×10^{2}	
A priori constraint (σ) on SRP coefficient	–	1×10^{-10}	Considered close to zero because no significant variations are expected to happen. Variations due to a geometry change of the S/C can be absorbed by the empirical accelerations.
Science parameter	**Unit**	**Value**	**Notes**
Kaula constraint coefficient	–	1×10^{-3}	Zannoni et al. (2020)
A priori constraint (σ) on $C_{2,0}$	–	36.99×10^{-6}	Park et al. (2024)
A priori constraint (σ) on $C_{2,1}$	–	13.66×10^{-6}	Park et al. (2024)
A priori constraint (σ) on $C_{2,2}$	–	14.70×10^{-6}	Park et al. (2024)
A priori constraint (σ) on $C_{3,0}$	–	33.42×10^{-6}	Park et al. (2024)
A priori constraint (σ) on $S_{2,1}$	–	9.19×10^{-6}	Park et al. (2024)
A priori constraint (σ) on $S_{2,2}$	–	10.87×10^{-6}	Park et al. (2024)
A priori constraint (σ) on empirical acc.	$\mathrm{m\,s^{-2}}$	1×10^{-9}	
Duration of empirical accelerations arc	days	1	
A priori constraint (σ) on rotation pole position	deg	$(\infty; \infty)$	Unconstrained because Archinal et al. (2018) do not report the associated uncertainty.
A priori constraint (σ) on rotation pole rate	$\mathrm{deg\,s^{-1}}$	$(\infty; \infty)$	Unconstrained because Archinal et al. (2018) do not report the associated uncertainty.
A priori constraint (σ) on gravitational Love number $(\Re(k_2); \Im(k_2))$	–	$\left(1 \times 10^{-2}; 1 \times 10^{-2}\right)$	Bagheri et al. (2025)
A priori constraint (σ) on libration amplitude	deg	3×10^{-4}	Park et al. (2024)
A priori constraint (σ) on Earth GSs position	m	5×10^{-3}	Dirkx et al. (2014)

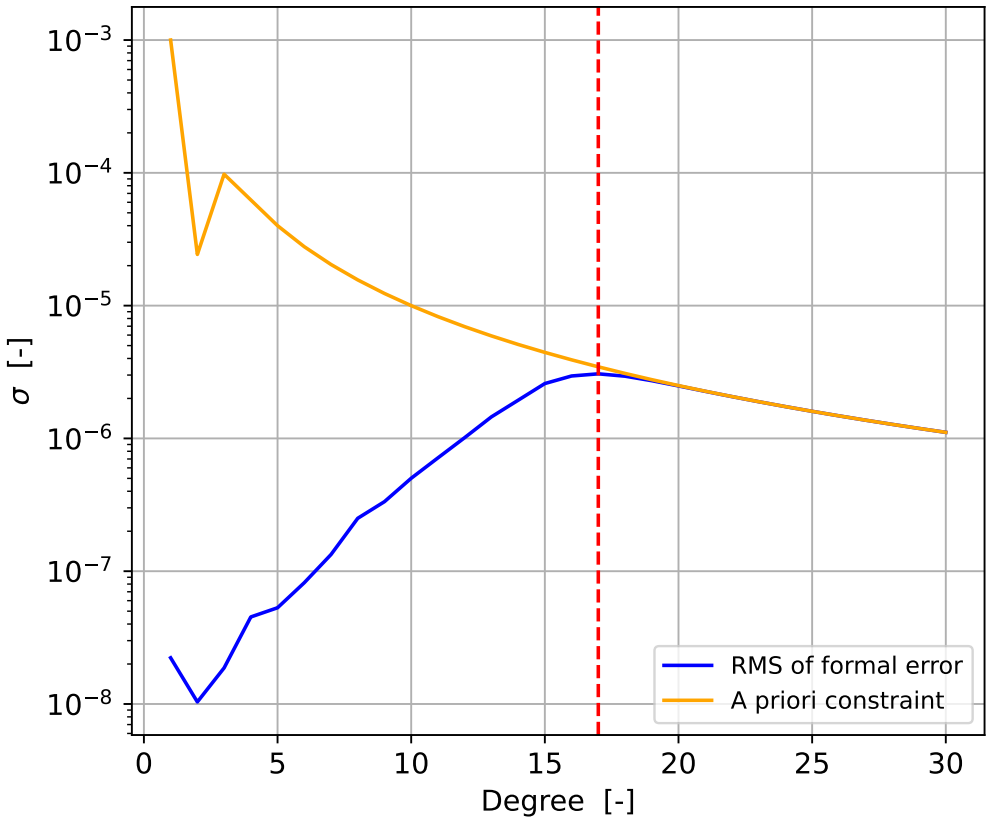

Figure 3.3.1.: Gravity degree strength associated to the cosine terms. The plot shows the RMS of the formal errors for the cosine terms (blue line), and the a priori constraint set by the Kaula rule (orange line), according to Equation 3.3.1. The dashed red line highlights the degree 17, at which the RMS is within 10% of the Kaula constraint. The analysis is performed with the base settings reported in Table 3.3.3. The irregular behaviour for a degree $l \leq 3$ is due to the a priori constraint set on the cosine terms according to Table 3.3.3. These constraints were retrieved by Park et al. (2024) as indicated in Table 3.3.3.

- Formal error for the diurnal libration amplitude: $\sigma\,(W)$.
- Formal error for the k_2 Love number: $\sigma\,(k_2)$.
- Formal error for the h_2 Love number: $\sigma\,(k_2)$.
- Formal error for the pole right-ascension and declination: $\sigma\,(\alpha_0)$, $\sigma\,(\delta_0)$.
- Formal error for the pole rate $\sigma\,(\dot{\alpha})$, $\sigma\left(\dot{\delta}\right)$.
- Maximum estimatable degree of the gravity field.
- Root Mean Square (RMS) of the formal errors of the gravity degree 2 coefficients.
- RMS of the formal errors of the landers position.

The maximum estimatable degree of the gravity field is computed as the degree for which the RMS of the formal error of the cosine coefficients at that degree is 90% of the a priori constraint set by the Kaula rule, i.e. the difference between the RMS and the a priori σ is within 10% of σ, computed through Equation 3.3.1. Figure 3.3.1 shows the degree strength and the maximum degree that can be estimated when the above presented definition of maximum degree is applied.

With respect to the estimation of the libration amplitude, it should be noted that at the moment there is no distinction in Tudat between the libration of the core and the libration of the shell. Thus, for the study cases in which no landers are included in the mission architecture in accordance with Table 3.3.2, it is expected that most of the signal contributing to the estimated formal error comes from the gravity signal of the core affecting the S/C orbit, which is the strongest compared to the signal of the ice shell. Hence, the estimated formal error of the libration amplitude is associated to the diurnal libration of the whole body, not only of the shell. Thus, the estimated libration amplitude with no landers in the mission architecture cannot be considered the expected estimate of the libration of the shell, since it absorbs the contribution of the core and is thus overoptimistic. On the other hand, when radio beacons are included in the mission architecture (in accordance with Table 3.3.2), given that they are most sensible to the libration of the ice shell on which they stand, the effect of the core is masked, and the estimated formal error is associated to the shell.

The results of the covariance design space exploration are presented in Section 5.1.

3.3.3. Study of nominal representative cases

Given the results produced in the design space exploration as described in Section 3.3.2, a second analysis according to Figure 3.0.1 (FC3.2) is performed on a reduced number of scenarios with the aim of producing nominal reference values. The design space exploration produced results for every setting indicated in Table 3.3.2. Given the analysis of the results proposed in Section 5.1, this section collects a few nominal values for the control variables detailed in Table 3.3.2. A few representative settings are thus selected for the production of nominal cases that can serve as reference for a few mission scenarios. Eighteen configurations are run, given three orbit solutions, two arc lengths, and three landers scenarios. For an orbit solution, the cases with no landers, only L_3, and all of the available landers are considered, for both a 1-day and 7-day arc. The settings applied for the tuning parameters shown in Table 3.3.2 are described in Table 3.3.4.

The displayed settings are selected given that, as determined in Section 5.1, the number of surface radio beacons is a leading control parameter, hence a set of multiple representative cases ought to be considered. Additionally, the arc length has an impact both on the design of the orbit manoeuvres and on the formal errors of the estimation parameters, as discussed in Section 5.1. An arc length of 1 day allows for more frequent orbit manoeuvres, while it allows for less observations in a single arc, with respect to an arc duration of 7 days, as mentioned by M. Fayolle et al. (2022). A longer arc length leads to lower formal errors on the S/C initial state uncertainty and on parameters such as the formal errors of the Love numbers, the SH gravity field coefficients, the libration amplitude, and the pole position. Such results are discussed in Section 5.1. However, it should be considered that a 7 days-arc might lead to a more challenging orbit control, given that an orbiter at Enceladus experiences Saturn's strong dynamical perturbation, as discussed in Section 2.4 and further developed Appendix E.2. Hence, it might not be possible to obtain a 7-days arc from the point of view of orbit control, due to the need of executing orbit manoeuvres, which would require the S/C to exit its nominal science mode. Thus, the representative results are computed also for an arc length of 1 day.

The results are provided in Section 5.2.

Table 3.3.4.: Values of the tuning parameters shown in Table 3.3.2 used for the production of nominal reference results for the formal errors of the estimated parameters.

Parameter	Unit	Value(s)
Lander to include	–	None; L_3; (L_1, L_2, L_3, L_4, L_5, L_6, L_7, L_8, L_9)
Initial state solution	–	K_1; K_2; K_3
Arc duration	days	1; 7
Duration of tracking arc from Earth GSs	hrs	8
Arc-wise tracking delay from Earth GSs	hrs	2
Simulation duration	days	28
Inclusion of lander range observable	–	No
A priori σ on SRP coefficient	–	1×10^{-10}
Kaula constraint coefficient	–	4×10^{-4}
A priori σ on empirical acc.	$\mathrm{m\,s^{-2}}$	1×10^{-9}
A priori σ on lander position	m	1×10^{2}
Duration of empirical accelerations arc	days	1
A priori σ on rotation pole position	deg	(∞, ∞)
A priori σ on rotation pole rate	$\mathrm{deg\ s^{-1}}$	(∞, ∞)

3.3.4. Single lander location analysis

As presented in Section 3.2.1, the landers are assigned to predetermined homogeneously distributed locations on the surface of Enceladus. In this section, as highlighted in Figure 3.0.1 (FC3.3), a preliminary sensitivity study is performed in order to assess the impact of the location of a single surface radio beacon on the covariance analysis results. The combined results of Section 3.3.3 (FC3.2) and Section 3.3.4 (FC3.3) will allow to determine how the considered mission architecture can help constrain geophysical parameters of interest, answering the first research sub-question (Section 1.2).

The investigated latitudes and longitudes are presented in Figure 3.3.2. The analysis is performed for each of the three orbit solutions provided in Table 3.1.5. At every location, the covariance analysis is carried out, and the figures of merit listed in Section 3.3.2 are saved. It should be noted that the distribution of the h_2 Love number is not provided, since the correction for the surface displacement due to the tidal bulge is required for every location, meaning that the average radial displacement per unit of h_2 as in Equation 3.2.5 had to be computed for every location over an integer number of orbits. Due to time constraints, it was chosen not to include this figure of merit. A trend associated to the longitude of the lander is expected for this parameter. In particular, since Enceladus is tidally locked to Saturn and thus shows always the same face to it, it is expected that better estimates of h_2 are performed when the lander is located closer to the Saturn-Enceladus axis, hence at longitudes closer to 0 deg or 180 deg, in correspondence of the corrected frozen bulge, where the tidal forcing is expected to be higher.

By showing the distribution of the parameters of interest based on the considered locations, it is possible to investigate which surface coordinates provide the most suitable locations for a possible future single-lander Enceladus science mission. Additionally, by executing the sensitivity analysis for each orbit solution, it is possible to study the effect of the selected orbit on the parameters distribution, inferring insights on the effect of orbit design on the science return. The analysis is carried out with the nominal base configuration presented in Table 3.3.3. The results are provided in Section 5.3.

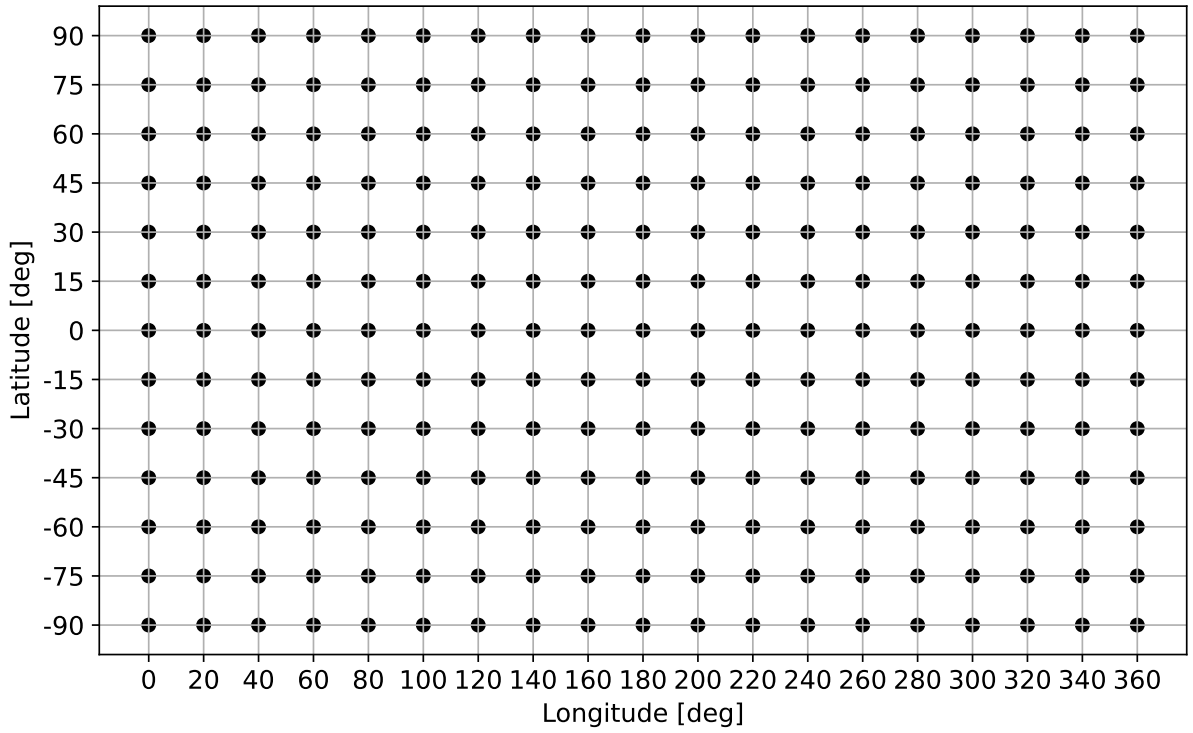

Figure 3.3.2.: Investigated locations for the single lander location analysis.

3.4. Analysis of the interior

This section aims to present the methodology followed to answer the second sub-question introduced in Section 1.2. Thus, the method discussed here has the purpose to produce results for studying which interior parameters are most sensitive to the observables and inferring how the formal error associated to the estimated geophysical measurements translates to the uncertainty on the interior parameters.

The investigated interior parameters are presented in Table 3.4.1, while the observables considered for this analysis are listed in Table 3.4.2. It should be noted that the mechanical properties of the ocean are not included among the parameters of interest, since the ocean is assumed to be an incompressible inviscid layer (Rovira-Navarro et al., 2024). For the core and shell, the mechanical properties are taken into consideration, given that they contribute to the tidal behaviour of the moon and recognised to be of interest from the science literature (e. g., Bagheri et al. (2025), Genova et al. (2024), Rovira-Navarro et al. (2024), Ermakov et al. (2021), Nimmo et al. (2007)).

Given an interior model, the observables associated to the tidal response of Enceladus (i. e., the Love numbers) are computed through the code provided by Rovira-Navarro et al. (2024). The model assumes a three-layer body, with a non-deformable solid core, surrounded by an incompressible liquid layer and a solid shell. The properties of each layer are assumed constant with radius. Additionally, the model neglects the gravitational coupling between the inner core and the outer shell, which are expected to have a small effect on the tidal response of the body. Dynamic liquid tides in the liquid layer are neglected as well. The model determines the tidal response of the body by solving the mass, momentum, and Poisson's equation, with a constitutive expression relating stress and displacements (Rovira-Navarro et al., 2024, Equations 1 and 2). On the other hand, the libration amplitude is computed using the formulation of Van Hoolst et al. (2013, Equations 45 and 46) for the case of an icy satellite with a global subsurface ocean. Van Hoolst et al. (2013) use the torque on the tidal bulge of a given layer to compute the associated libration amplitude. The implementation of the equations was provided by Rovira-Navarro et al. (2024).

Table 3.4.1.: Interior parameters of interest investigated in the interior model analysis.

Layer	Parameter	Symbol
Core	Radius	R_c
	Density	ρ_c
	Shear modulus	σ_c
	Viscosity	η_c
	Bulk modulus	K_c
Ocean	Thickness	d_o
	Density	ρ_o
Ice shell	Thickness	d_s
	Density	ρ_s
	Shear modulus	σ_s
	Viscosity	η_s
	Bulk modulus	K_s

Table 3.4.2.: Observables considered for the interior structure analysis.

Parameter	Symbol
Diurnal libration amplitude of the shell	W_s
Real part of the gravitational Love number	$\Re(k_2)$
Real part of the radial displacement Love number	$\Re(h_2)$

In order to understand which interior parameters can be best constrained with the available measurements and to provide reference results on how the constraints on the observables translate to uncertainties in the interior properties, the following analyses are performed, as indicated in Figure 3.0.1 (FC4):

1. Preliminary one-at-a-time sensitivity analysis (FC4.1), performed by varying one single interior parameter at a time with uniform distribution within a given range of interest.
2. Preliminary full MC analysis (FC4.2), performed by varying every interior parameter simultaneously, and by assuming uniform distribution within a given range of interest.
3. Reduced full MC analysis (FC4.3), performed by varying every interior parameter simultaneously, within specific restricted ranges of interest, derived from the previous analysis (FC4.2).

As pointed out in Figure 3.0.1 (FC4.4), the interior models produced in the reduced full MC analysis are used to constraint the interior with the formal errors on the observables estimated in the covariance nominal cases analysis (FC3.2, methodology outlined in Section 3.3.3 and results shown in Section 5.2). In the following sections, an overview of the method applied in each analysis step is provided.

3.4.1. Preliminary one-at-a-time sensitivity analysis

The preliminary sensitivity analysis is performed through a one-at-a-time MC analysis, by varying one single parameter at each run, assuming uniform distribution on logarithmic scale within the ranges of interest, detailed in Table 3.4.3. This allows to have a reference for the expected trends in the full MC analysis.

Table 3.4.3.: Interior parameters and range of interest for the preliminary one-at-a-time sensitivity analysis (FC4.1 in Figure 3.0.1).

Layer	Parameter	Unit	Variability range	Notes
Core	R_c	km	$120 - 210$	Based on the range provided by Bagheri et al. (2025).
	ρ_c	$kg\,m^{-3}$	$2000 - 3000$	Genova et al. (2024)
	μ_c	Pa	$1 \times 10^9 - 80 \times 10^9$	Based on the range provided by Bagheri et al. (2025).
	η_c	Pa s	$1 \times 10^{15} - 1 \times 10^{20}$	Based on the range provided by Bagheri et al. (2025, Table 6) for the case of tidal activity in the shell.
	K_c	Pa	$1 \times 10^9 - 1 \times 10^{11}$	Based on the nominal value by Rovira-Navarro et al. (2022).
Ocean	R_o	km	$201 - 240$	Based on the thickness ranges provided by Park et al. (2024, Table 9), Thomas et al. (2016), and Beuthe et al. (2016).
	ρ_o	$kg\,m^{-3}$	$1000 - 1300$	Genova et al. (2024)
Ice shell	R_s	km	$210 - 260$	Based on the thickness ranges provided by Park et al. (2024, Table 9), Thomas et al. (2016), and Beuthe et al. (2016).
	ρ_s	$kg\,m^{-3}$	$800 - 1000$	Bagheri et al. (2025)
	μ_s	Pa	$1 \times 10^9 - 5 \times 10^9$	Based on Genova et al. (2024) and Bagheri et al. (2025)
	η_s	Pa s	$1 \times 10^{12} - 1 \times 10^{20}$	Based on Bagheri et al. (2025)
	K_s	Pa	$1 \times 10^9 - 1 \times 10^{11}$	Based on the nominal value by Rovira-Navarro et al. (2022)

It should be noted that when varying the interior model parameters, the constraints on mass, MoI, and radius are not implemented. Thus, the variation of parameters such as the layers thickness and density leads to a body with different mass, MoI, and radius with respect to the nominal model for Enceladus (Table 3.4.5). This choice has been made with the purpose of avoiding the degeneracy between the thickness and density of each layer that otherwise would arise and would cause the impossibility to distinguish between the effects of the two parameters. A more rigorous approach is applied in the following analysis in Section 3.4.2. The interior parameters investigated in this phase are those described in Table 3.4.1.

The preliminary results obtained from this analysis, presented in Section 5.4, allow to have a first understanding of the influence of the mechanical and physical properties of Enceladus' interior on the observables.

3.4.2. Preliminary full Monte Carlo analysis

The preliminary full Monte Carlo analysis (FC4.2 in Figure 3.0.1) is performed by varying all control variables at every run and storing the resulting geophysical observables (detailed in Table 3.4.2). The control variables and the associated ranges of interest considered in the analysis are listed in Table 3.4.4. It can be noted that for the ice shell, instead of sampling the bulk modulus, which is among the

parameters of interest according to Table 3.4.1, the Poisson ratio $\bar{\nu}_\mathrm{s}$ is sampled. The Poisson ratio is related to the bulk modulus K through the following equation (Mott et al., 2008):

$$\frac{\mu}{K} = \frac{3\,(1-2\bar{\nu})}{2\,(1+\bar{\nu})} \tag{3.4.1}$$

(3.4.1) can be rearranged as

$$\bar{\nu} = \frac{1}{2}\frac{3K-2\mu}{3K+\mu} \tag{3.4.2}$$

The Poisson ratio is sampled because it ensures that the bulk modulus obtained through (3.4.1) is in agreement with feasible values for the Poisson ratio, namely in the interval $0.3-0.5$. The value of 0.3 is retrieved from Gammon et al. (1983) for polycrystalline ice, while the upper boundary value 0.5 is imposed by the mathematical formulation of $\bar{\nu}$. As it can be observed in (3.4.2), the following statement holds for a given sampled value of rigidity μ:

$$\lim_{K\to\infty}\left(\frac{1}{2}\frac{3K-2\mu}{3K+\mu}\right) = \frac{1}{2}$$

Hence, the upper limit of 0.5 is considered for sampling the Poisson ratio of the shell. The bulk modulus K_s, which is used for the computation of the observables as presented in Section 3.4, is then computed from (3.4.1).

Table 3.4.4.: Interior parameters and range of interest for the preliminary full Monte Carlo analysis (FC4.2 in Figure 3.0.1).

Layer	Parameter	Unit	Variability range	Notes
	R_c	km	$120-210$	Based on the range provided by Bagheri et al. (2025).
Core	μ_c	Pa	$1\times10^{9}-80\times10^{9}$	Based on the range provided by Bagheri et al. (2025).
	η_c	Pa s	$1\times10^{16}-1\times10^{20}$	Based on the range provided by Bagheri et al. (2025, Table 6) for the case of tidal activity in the shell.
	K_c	Pa	$1\times10^{9}-1\times10^{11}$	Based on the nominal value by Rovira-Navarro et al. (2022).
Ocean	ϑ_o	km	$1-40$	Based on the ranges provided by Park et al. (2024, Table 9), Thomas et al. (2016), and Beuthe et al. (2016).
	ρ_s	$\mathrm{kg\,m^{-3}}$	$800-1000$	Bagheri et al. (2025)
	μ_s	Pa	$1\times10^{9}-5\times10^{9}$	Based on Genova et al. (2024) and Bagheri et al. (2025)
Ice shell	η_s	Pa s	$1\times10^{12}-1\times10^{20}$	Based on Bagheri et al. (2025)
	$\bar{\nu}_\mathrm{s}$	$-$	$0.3-0.5$	Based on the value for polycrystalline ice by Gammon et al. (1983) and on the upper limit imposed by its formulation (Equation 3.4.2).

Given a set of sampled parameters, the core density, ocean density, and shell thickness are computed by applying the constraints on mass, MoI, and radius, shown in Equation 3.4.3.

$$M = \frac{4}{3}\pi\left(\rho_\mathrm{c}R_\mathrm{c}^3 + \rho_\mathrm{o}\left(R_\mathrm{o}^3-R_\mathrm{c}^3\right) + \rho_\mathrm{s}\left(R_\mathrm{s}^3-R_\mathrm{o}^3\right)\right) \tag{3.4.3a}$$

$$R = R_s \tag{3.4.3b}$$

$$C = \frac{8}{15}\pi\left(\rho_c R_c^5 + \rho_o\left(R_o^5 - R_c^5\right) + \rho_s\left(R_s^5 - R_o^5\right)\right) \tag{3.4.3c}$$

The value for the constraints are reported in Table 3.4.5. It should be noted that they are not implemented with an associated uncertainty range. This choice was taken, for time constraints reasons, to avoid the effect of their uncertainty on the trends between the observables and interior properties. Including the uncertainty associated to the constraints would lead to a more complete set of results, including a source of uncertainty that would actually be present for a science mission. However, the trends for the interior properties are expected to still be representative, and the major conclusion points are expected to still hold, allowing to answer the research question.

Table 3.4.5.: Constraints imposed to the interior models for the computation of the ocean and core density, and the shell thickness.

Parameter	Unit	Value	Notes
M	kg	1.08×10^{20}	Flandes et al. (2024), in agreement with the value by Rappaport et al. (2007) reported in Section 2.1.2
R	km	252.1	Porco et al. (2006)
C	$\mathrm{kg\,m^2}$	$0.338MR^2$	Park et al. (2024)

Given the constraints and a sampled interior model, the ocean and core density, and the shell thickness are computed. Hence, the shell libration amplitude, and the k_2 and h_2 Love numbers are computed for the considered model, applying the method by Rovira-Navarro et al. (2024) and Van Hoolst et al. (2013), implemented by Rovira-Navarro et al. (2024), as already introduced in Section 3.4. It should be noted that not all models are going to result in reasonable values for ρ_o, ρ_s, and d_s. The ranges of interest for these parameters are shown in Table 3.4.6. Those samples that have a value for such parameters outside of these nominal ranges are discarded.

Table 3.4.6.: Range of interest for the core and ocean density applied as constraints for a physically viable model.

Parameter	Unit	Range	Notes
ρ_c	$\mathrm{kg\,m^{-3}}$	$2000 - 3000$	Genova et al. (2024)
ρ_o	$\mathrm{kg\,m^{-3}}$	$1000 - 1300$	Genova et al. (2024)
d_s	km	≥ 1	Genova et al. (2024)

The selection of the viable models based on the ranges provided in Table 3.4.6 is followed by a second process of filtering, based on the measured shell libration amplitude. Thomas et al. (2016) report a shell libration amplitude of $0.12 \pm 0.021\,\mathrm{deg}$ (3σ), measured through surface control-points tracking of the images taken by the Cassini ISS, as already presented in Section 2.1.7. Given that the interior models that do not yield to a shell libration amplitude within the $\pm 3\sigma$ range are not possible, they are discarded. The remaining models are then considered for the analysis of Enceladus' interior properties. The process described in this section is outlined in Figure 3.4.1.

The full MC allows to determine the interior parameters to which the selected observables are most sensitive to, hence those parameters that can be constrained. Additionally, it accounts for the interactions between the different interior parameters in producing the observables, leading to an improved understanding of the relationship between the geophysical observables and the interior properties. The next step consists in translating the formal errors associated to the observables into reference uncertainty values for the parameters that can be constrained (FC4.3 and FC4.4 in the flow chart of Figure 3.0.1). This investigation is carried out in Section 3.4.3.

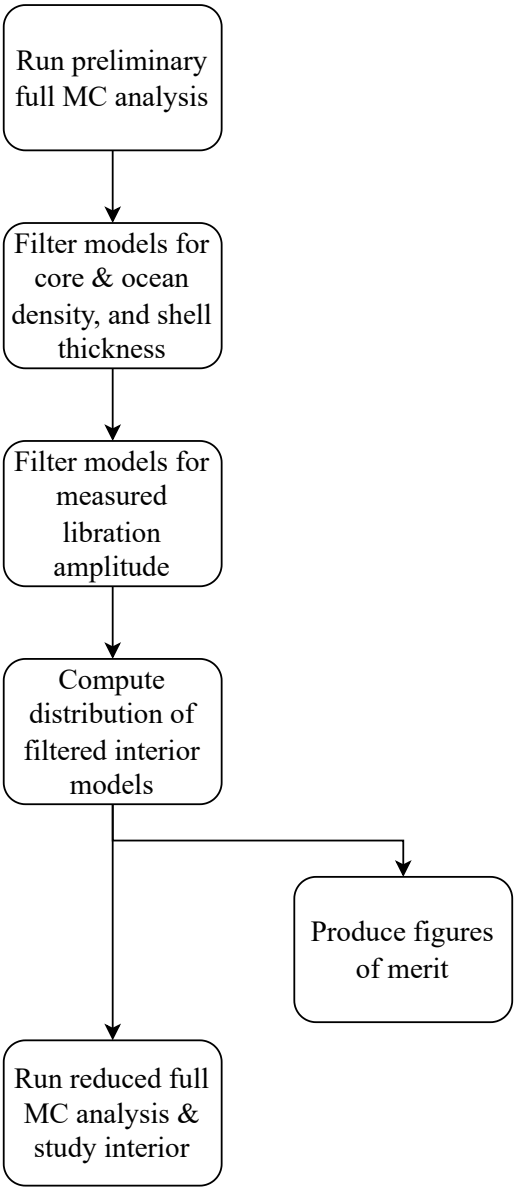

Figure 3.4.1.: Flow chart for the process followed in the preliminary full MC analysis (within the FC4.2 step in Figure 3.0.1).

3.4.3. Constraining the interior with the available estimated uncertainties

After the preliminary full MC analysis (FC4.2 in the flow chart of Figure 3.0.1), laid out in Section 3.4.2, a second refined full MC is run (FC4.3). The purpose of this second MC is to generate enough acceptable samples for studying how the formal errors of the selected observables constrain the interior. The interior parameters sampled in this analysis are the same as those considered in Table 3.4.1. The considered associated ranges are obtained by considering the mean $\pm\, 2\sigma$ interval, where σ is the standard deviation of the interior properties distribution produced in the preliminary full MC analysis (FC4.2) after the non-physically feasible models are discarded as outlined in Section 3.4.2. The reduced ranges are given in Table 3.4.7. The second full MC is thus run, and the results are once again filtered based on the core and ocean density, on the shell thickness, and on the libration amplitude (refer to Section 3.4.2).

Table 3.4.7.: Interior parameters and range of interest for the reduced full Monte Carlo analysis (FC4.3 in Figure 3.0.1).

Layer	Parameter	Unit	Variability range
Core	R_c	km	$180.37 - 203.69$
	μ_c	Pa	$1 \times 10^9 - 80 \times 10^9$
	η_c	Pa s	$1 \times 10^{16} - 1 \times 10^{20}$
	K_c	Pa	$1 \times 10^9 - 1 \times 10^{11}$
Ocean	ϑ_o	km	$25.09 - 52.13$
Ice shell	ρ_s	$\mathrm{kg\,m^{-3}}$	$800 - 1000$
	μ_s	Pa	$1 \times 10^9 - 5 \times 10^9$
	η_s	Pa s	$1 \times 10^{12} - 1 \times 10^{20}$
	$\bar{\nu}_s$	$-$	$0.3 - 0.5$

Given the filtered dataset, the interior of Enceladus can be constrained by applying the estimated formal error associated to the geophysical parameters as a constraint on the interior models. By filtering those models that do not match the estimated uncertainty for the geophysical observables, it is possible to study how the accuracy associated to the measurements can help constrain the interior properties. For the mean value of the observables, the mean value of the distribution of the filtered dataset is considered. The constraints given by the formal errors of the selected observables (Table 3.4.2) are then applied as a $\pm 3\sigma$ range centred about the mean value. The constraints are applied to the dataset filtered for the non-physically viable interior models. It is thus possible to compute the distribution of the resulting interior parameters distribution, and study how the mission architecture can help constrain Enceladus' interior, answering the second research sub-question (Section 1.2), as outlined in Figure 3.0.1.

By applying the formal errors as constraints for the interior, it is possible to consider a set of different scenarios. In a first step, only the real component of the Love numbers is used to constrain the interior. The addition of the libration amplitude follows in a second step. When the filtered dataset according to the considered scenario is obtained, it is possible to plot the distribution of the interior parameters after the constraint is applied. This allows to study how the estimated formal errors contribute to the knowledge of the interior. The results are reported in Section 5.6.

4. Verification

4.1. Feasibility and stability of the propagated orbit solutions

To verify that the orbits obtained with the dynamical model from Table 3.2.2 are still representative of a science orbit around Enceladus, the selected accelerations of Table 3.2.2 are added to the propagator settings of the dynamics simulator, and are used to propagate a multi-arc orbit over a time-span of 28 days, with an arc duration of 1 day. The division of the observation data in multiple arcs was discussed in Section 3.2.1. The arc duration is selected based on S. Fayolle (2025) and Magnanini et al. (2024), who divide the entire span of the observations in multiple arcs of 1 day, respectively for the flybys of JUICE around the Galilean moons, and for the 500 km-altitude circular orbit phase of JUICE around Ganymede (GCO500). The multi-arc difference, introduced by the physical model with respect to the nominal orbit solutions provided in Table 3.1.5, and propagated with the dynamical model described in Table 3.1.4, is assessed. In a second step, the stability of the orbits over the considered propagation time span is investigated.

To perform the comparison between the two different sets of orbit solutions in a multi-arc fashion, the initial state of each arc is taken on the nominal base-case orbit at the respective epoch. Every arc is thus integrated for 1 day, and the norm of the position and acceleration difference is computed for every integrated epoch of the arc. The arc-wise results are shown in Figure 4.1.1. Furthermore, for each arc, the variational equations are integrated, and the state transition matrix from the start to the end of the arc, as defined in (2.2.2), is used to compute the velocity correction needed to adjust the final state of the arc, so that it coincides with the state at the same epoch on the nominal base-case trajectory. Thus, given the final position difference at the end of the arcs, the state transition matrix is used to compute the $\Delta\mathbf{v}_i\left(t_{0,i}\right)$ at the start of each arc, according to:

$$\Delta\mathbf{v}_i\left(t_{0,i}\right) = -\left(\frac{\partial\mathbf{r}_i\left(t_\mathrm{e},i\right)}{\partial\mathbf{v}_i\left(t_0,i\right)}\right)^{-1}\left(\mathbf{r}_i\left(t_{0,i}\right) - \mathbf{r}_i^*\left(t_{\mathrm{e},i}\right)\right) \tag{4.1.1}$$

where $\left(\frac{\partial\mathbf{r}_i(t_\mathrm{e},i)}{\partial\mathbf{v}_i(t_0,i)}\right)$ is the upper right sub-matrix of the state transition matrix:

$$\Phi_i\left(t_{\mathrm{e},i},t_{0,i}\right) = \begin{pmatrix} \frac{\partial\mathbf{r}_i(t_\mathrm{e},i)}{\partial\mathbf{r}_i(t_0,i)} & \frac{\partial\mathbf{r}_i(t_\mathrm{e},i)}{\partial\mathbf{v}_i(t_0,i)} \\ \frac{\partial\mathbf{v}_i(t_\mathrm{e},i)}{\partial\mathbf{r}_i(t_0,i)} & \frac{\partial\mathbf{v}_i(t_\mathrm{e},i)}{\partial\mathbf{v}_i(t_0,i)} \end{pmatrix} \tag{4.1.2}$$

The arc-wise position and acceleration difference between the propagated multi-arc orbits and nominal base case solutions by Auer Wilkins et al. (2025) (Table 3.1.5) are showed in Figure 4.1.1. It can be observed that the perturbing accelerations introduced in Section 3.2.1 and reported Table 3.2.2 lead to a maximum position difference of the order of $\sim 50\,\mathrm{m}$, with a maximum acceleration difference of $\sim 4\times10^{-6}\,\mathrm{m\,s^{-2}}$, about three orders of magnitude smaller than the perturbing acceleration by Saturn, showed in Figure E.2.1a.

The $\Delta\mathbf{v}_i\left(t_{0,i}\right)$ at the start of each arc required to correct the position difference is plotted in Figure 4.1.2a as a function of arc index. It can be observed that for one day-long arcs, the required impulsive $||\Delta\mathbf{v}||$ to correct for the position deviation from the base-case orbit at the end of the arc is quite small, of the order of magnitude between $\sim 10^{-5} - 10^{-3}\,\mathrm{m\,s^{-1}}$. As shown by Figure 4.1.2b, the impulsive velocity corrections allow to reach a final position deviation smaller than 10^{-3} m at the end of the arc. In conclusion, given the small arc-wise position difference introduced by the perturbations (Figure 4.1.1),

and given the small initial impulsive manoeuvres required to correct for the final position deviation at the end of the arc (Figure 4.1.2a), the perturbed multi-arc orbit can be considered quite close to the base-case one and it is still possible to use the initial state solutions provided in Table 3.1.5. Hence, the multi-arc orbit accounts for the main perturbing terms (Table 3.2.2) which affect the state of the vehicle and is still well representative for a science orbit around Enceladus.

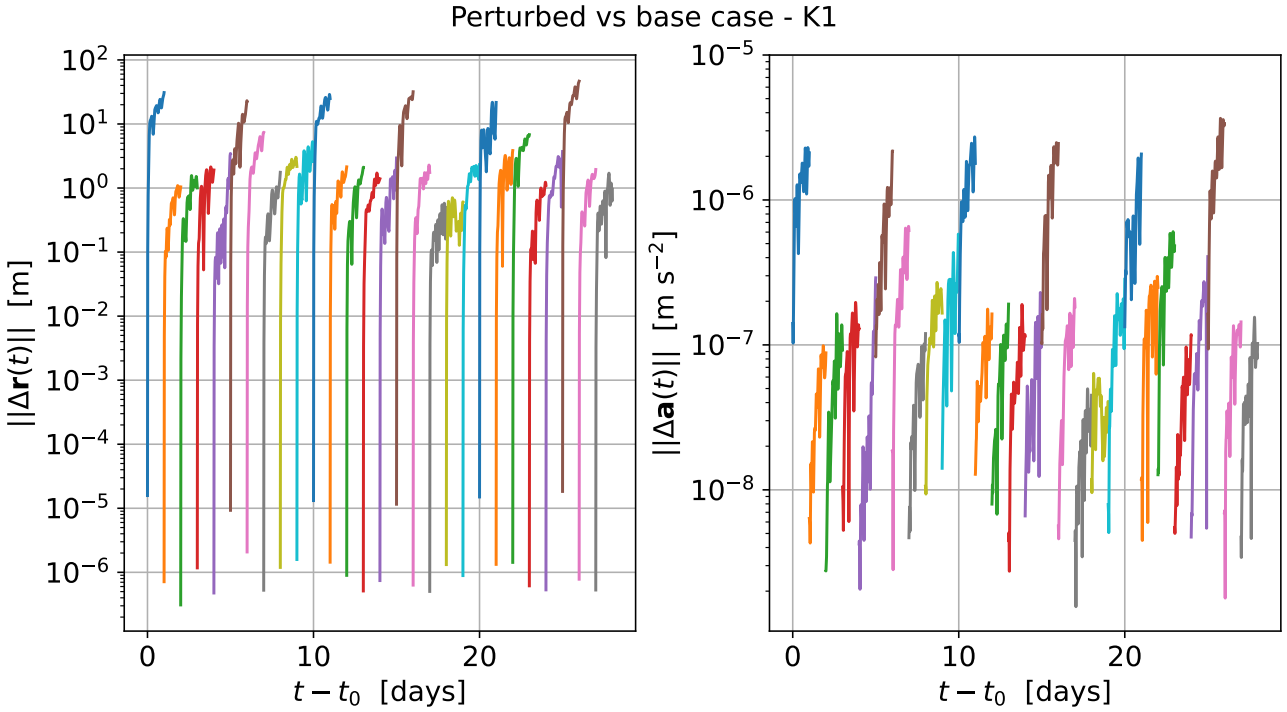

Figure 4.1.1.: Arc-wise position and acceleration difference between the perturbed case with the additional acceleration settings from Table 3.2.2 and the nominal orbits propagated with the dynamical model described in Table 3.1.4. Considered initial state: K_1.

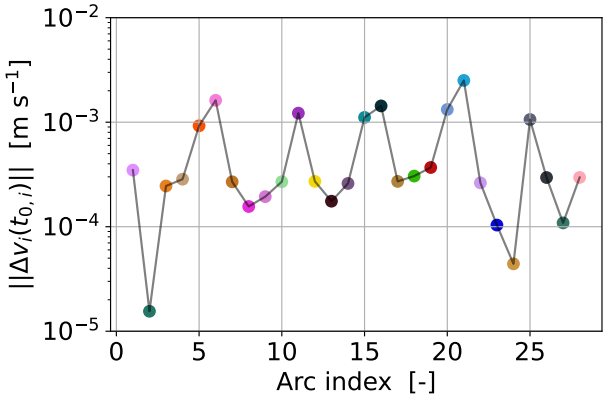

(a) Norm of initial velocity correction at the start of each single arc.

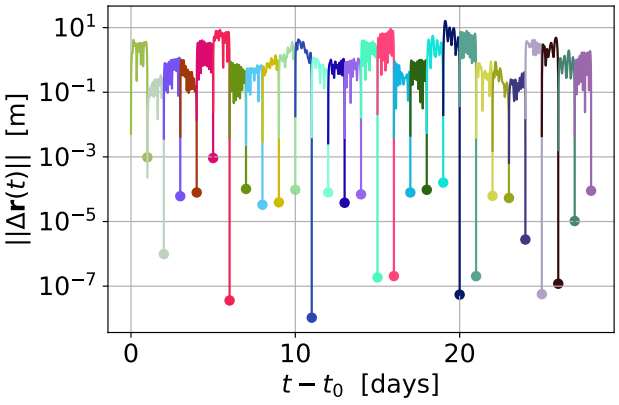

(b) Norm of position difference for multi-arc initial velocity correction. The markers point out the final position difference at the end of every arc, whose allowed upper limit was set to 10^{-3} m.

Figure 4.1.2.: Multi-arc initial velocity correction. The correction is applied so that the final state of the arc matches the nominal base-case state at the same epoch computed with the dynamical model detailed in Table 3.1.4. Considered initial state: K_1.

To show that the selection of the dynamical model is valid also for the K_2 and K_3 solutions, which have similar Keplerian elements to K_1 (see Table 3.1.5), the multi-arc analysis is performed also for these solutions. The results are comparable to those for K_1 and are reported in Appendix F. Similarly to K_1, they show that the K_2 and K_3 solutions are still representative of a science orbit around Enceladus allowing to answer to the first research sub-question.

Finally, to show that the orbits remain stable around Enceladus without crashing on its surface or escaping its SOI, the altitude history of the single-arc perturbed orbit is computed. The altitude history for the perturbed K_1 orbit is reported in Figure 4.1.3, which shows that it is stable over the entire considered time span and does not collapse on the surface of Enceladus, nor escape. As a reference, the 3D view of the perturbed K_1 orbit is shown in Figure 4.1.4. The results for the K_2 and K_3 orbits are analogous and are displayed in Appendix F.

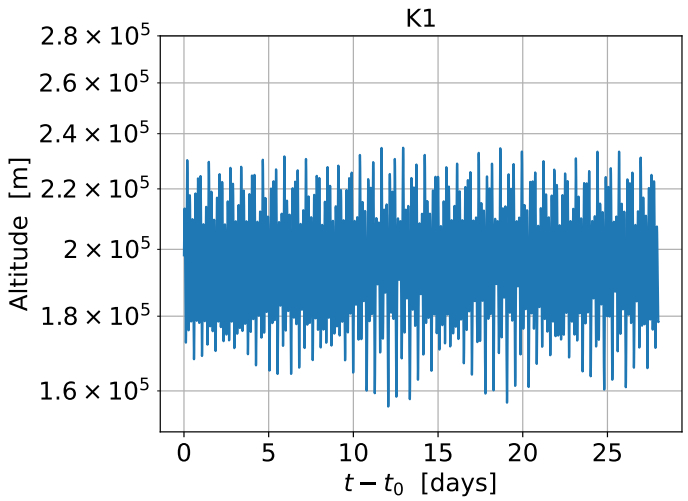

Figure 4.1.3.: Altitude history for the perturbed K_1 science orbit. The acceleration settings from Table 3.2.2 are applied.

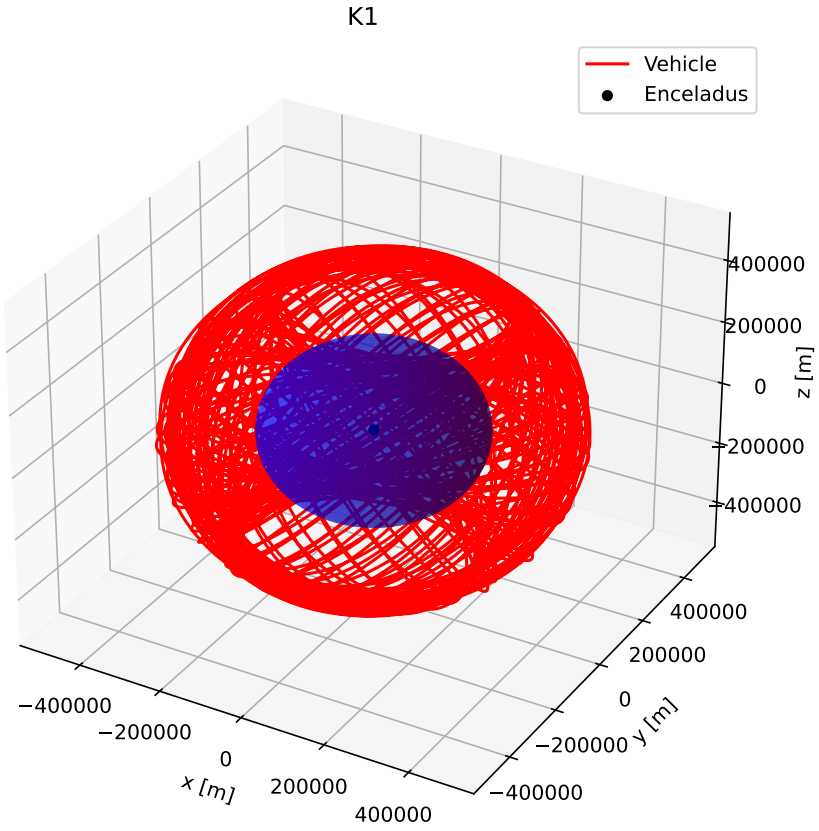

Figure 4.1.4.: 3D view of the perturbed science orbit propagated for 28 days, including the acceleration settings reported in Table 3.2.2. Considered initial state: K_1.

4.2. Partial derivatives of the rotation matrix associated to the body-fixed frame with respect to the libration amplitude

As presented in Section 2.1.7, the shell libration amplitude is dependent on the interior properties of the moon, such as the shell thickness. Thus, as proposed in Table 3.3.1, the diurnal libration amplitude of Enceladus is included among the solve-for parameters. Section 3.2.2 discussed that for the purpose of including the libration amplitude as a solve-for parameter, it was necessary to implement the partial derivatives of the rotation matrix from the Enceladus-fixed frame to the inertial frame with respect to the libration amplitude, since they were not already available in Tudat. Equation 3.2.2 describes the analytical formulation of the partial derivatives derived in Section 3.2.2.

The verification is performed via the numerical finite differences method, by computing the values of both the analytical partial derivatives and the derivatives obtained by finite differences, for a sweep of libration frequencies. Given that the finite differences method refers to the definition of derivative for a derivable function, the comparison between the analytical and numerical results is expected to yield to similar results. The numerical partial derivative of the rotation matrix with respect to the libration amplitude W_j, produced by a tidal forcing with frequency ω_j and phase γ_j is computed as follows:

$$\begin{aligned}\frac{\partial R^{\mathrm{IF/BF}}}{\partial W_j} &= \lim_{w\to 0} \frac{R^{\mathrm{IF/BF}}\left(W_j + w\right) - R^{\mathrm{IF/BF}}\left(W_j - w\right)}{2w} \\ &\approx \left(\frac{R^{\mathrm{IF/BF}}\left(W_j + w\right) - R^{\mathrm{IF/BF}}\left(W_j - w\right)}{2w} \right) \Bigg|_{w \ll 1}\end{aligned} \tag{4.2.1}$$

The numerical partial derivative is computed through Equation 4.2.1, using the dedicated unit test in Tudat[1]. It should be noted that in Tudat, when performing the rotation of a vector from an initial frame to a final one, the Tudat software executes the active rotation of the vector instead of the passive rotation of the frame. This means that in order to compute the transformed coordinates of the vector, the software keeps the frame fixed and rotates the vector of an opposite angle with the respect to the nominal transformation that converts the coordinates of the vector in the old frame to the new frame. In this way, instead of "passively" seeing the frame rotate, the software "actively" changes the coordinates of the vector in the same frame. Thus, the active rotation is obtained through a rotation with opposite angle with respect to the passive one. As a result, given the model of (3.2.1), the implemented rotation matrix is as follows:

$$R^{\mathrm{IF/BF}} = R_3\left(-\left(\alpha + \pi/2\right)\right) R_1\left(-\left(\pi/2 - \delta\right)\right) R_3\left(-W\right) \tag{4.2.2}$$

The implemented partials are thus

$$\frac{\partial R^{\mathrm{IF/BF}}}{\partial W_T} = R_3\left(-\left(\alpha^{\text{s-a}} + \pi/2\right)\right) R_1\left(-\left(\pi/2 - \delta^{\text{s-a}}\right)\right) \begin{pmatrix} -\sin W & \cos W & 0 \\ -\cos W & -\sin W & 0 \\ 0 & 0 & 0 \end{pmatrix} \sin\left(\omega_T t + \gamma_T\right) \tag{4.2.3}$$

The comparison of the numerical and analytical partials computed respectively with Equation 4.2.1 and Equation 4.2.3 is provided in Table 4.2.1. The test is carried out considering the rotation matrix from the Jupiter-fixed frame to the inertial frame, and the already implemented libration terms associated to Jupiter, whose frequencies are indicated in the first column of Table 4.2.1. Table 4.2.1 shows that the absolute difference between the analytical and numerical partials is at least five orders of magnitude smaller than the value of the derivatives. Considering for simplicity of reasoning the formulation of the covariance matrix without consider parameters, as provided in (2.2.13), a variation of 1×10^{-5} in the h_2 partials transfers to a variation with the same order to the formal error of h_2. This is due to the product ${H_p}^T(T)W(T)H_p(T)$ of which the inverse is taken three times, considering (2.2.13) and (2.2.14). Given that the inverse does not change the number of digits of accuracy, an error of the level 1×10^{-10} is transferred to the covariance matrix. Since the formal errors are computed with the square root of the diagonal elements of the covariance matrix, an error of the order of 1×10^{-5} is mapped to the estimated uncertainty for the h_2 Love number. Given that an uncertainty of 10^{-5} on the formal errors is sufficiently small, the implementation of the partial derivatives of the rotation matrix from the body-fixed frame to the inertial frame can be considered verified.

[1] unitTestRotationMatrixPartials.cpp

Table 4.2.1.: Partial derivatives of the rotation matrix from the inertial frame to the Jupiter-fixed frame with respect to the libration amplitude for different forcing frequencies. The verification was performed through the IAU rotation matrix partials unit test available in Tudat.

Meridian frequency [deg yrs^{-1}]	Numerical partials			Analytical partials			Absolute difference $(\times 10^{-6})$		
60.70	-0.268	-0.088	-1.388×10^{-11}	-0.268	-0.088	0	-9.545	-3.138	1.388×10^{-5}
	0.081	-0.241	-2.776×10^{-11}	0.081	-0.241	0	2.893	-8.597	2.776×10^{-5}
	0.034	-0.116	0	0.034	-0.116	0	1.225	-4.150	0
48.50	0.892	0.293	-4.163×10^{-11}	0.892	0.293	0	-5.828	-1.916	4.163×10^{-5}
	-0.270	0.803	2.776×10^{-11}	-0.270	0.803	0	1.766	-5.249	-2.776×10^{-5}
	-0.114	0.388	5.551×10^{-11}	-0.114	0.388	0	0.748	-2.534	-5.551×10^{-11}
11.92	0.379	0.125	2.776×10^{-11}	0.379	0.125	0	2.941	0.967	-2.776×10^{-5}
	-0.115	0.341	5.551×10^{-11}	-0.115	0.341	0	-0.891	2.648	-5.551×10^{-5}
	-0.049	0.165	0	-0.049	0.165	0	-0.377	1.278	0
2.626	-0.223	-0.073	-1.388×10^{-11}	-0.223	-0.074	0	-7.012	-2.305	1.388×10^{-5}
	0.068	-0.201	5.551×10^{-11}	0.068	-0.201	0	-2.125	-6.315	-5.551×10^{-5}
	0.029	-0.097	5.551×10^{-11}	0.029	-0.097	0	0.899	-3.048	-5.551×10^{-5}
0.643	-0.802	-0.264	5.551×10^{-11}	-0.802	-0.264	0	5.948	1.955	-5.551×10^{-5}
	0.243	-0.722	-2.776×10^{-11}	0.243	-0.722	0	-1.803	5.357	2.776×10^{-5}
	0.102	-0.349	-5.551×10^{-11}	0.103	-0.349	0	-0.763	2.586	5.551×10^{-5}

4.3. Rotational and tidal model consistency

4.3.1. Tidally locked rotation model of Enceladus

As discussed in Section 3.2.2, due to the 1:1 spin-orbit resonance that characterises Enceladus rotation (Section 2.1.7), it is necessary to ensure that in the implemented rotation model of Enceladus, the prime meridian points towards Saturn. In Section 3.2.2, the rotation model by Park et al. (2024) was adopted, according to the formulation of (2.1.35) to (2.1.37). To the implemented model was added a correction for W_0. The figures of merit for the rotation model, already shown in Section 3.2.2 with no correction, are proposed in Figure 4.3.1 after the addition of a correction term to W_0, as explained in Section 3.2.2.

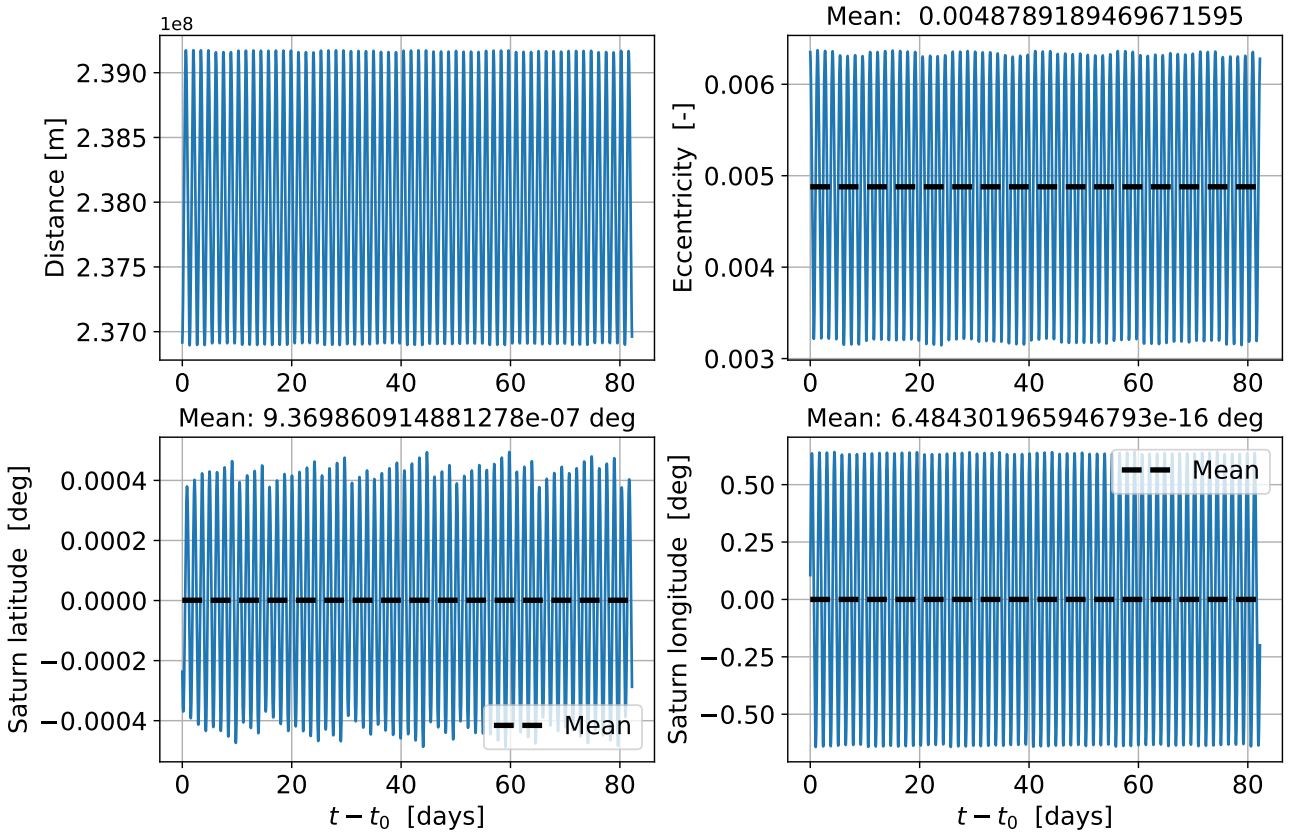

Figure 4.3.1.: Enceladus-fixed coordinates of Saturn and orbital eccentricity of Enceladus. The rotation model from Park et al. (2024) is considered, with a correction of W_0. The mean values are computed over 60 orbits.

It is possible to observe a small amplitude oscillation of Saturn's latitude about a zero-mean value, and a libration in longitude about the fixed bulge pointing towards Saturn, as expected after the correction. Thus, the rotation model can be considered verified. Furthermore, Figure 4.3.1 shows an oscillating eccentricity, with an average value in agreement with literature (e. g., Porco et al. (2006), Rhoden et al. (2020)). The eccentric orbit is maintained over time by the 2:1 resonance with Dione which excites the orbit, and by the tidal heating which tends to circularize it.

4.3.2. Removal of the effect of the permanent tide on the gravity field variations

Section 3.2.3 describes the removal of the effect of the permanent tide on the gravity field variation. As discussed in Section 3.2.3, the removal is performed to avoid the time-varying gravity field variations to be masked by the frozen bulge due to the permanent tide raised by Saturn on Enceladus.

After the removal of the permanent tide, the effect of the frozen bulge on the gravity field variations is absent, as shown in Figure 4.3.2. The plots show that after the correction, the gravity field coefficient variations of degree 2 oscillate about the zero-mean value, thus capturing the gravity tidal response as a consequence of only the tidal bulge variation about the frozen shape.

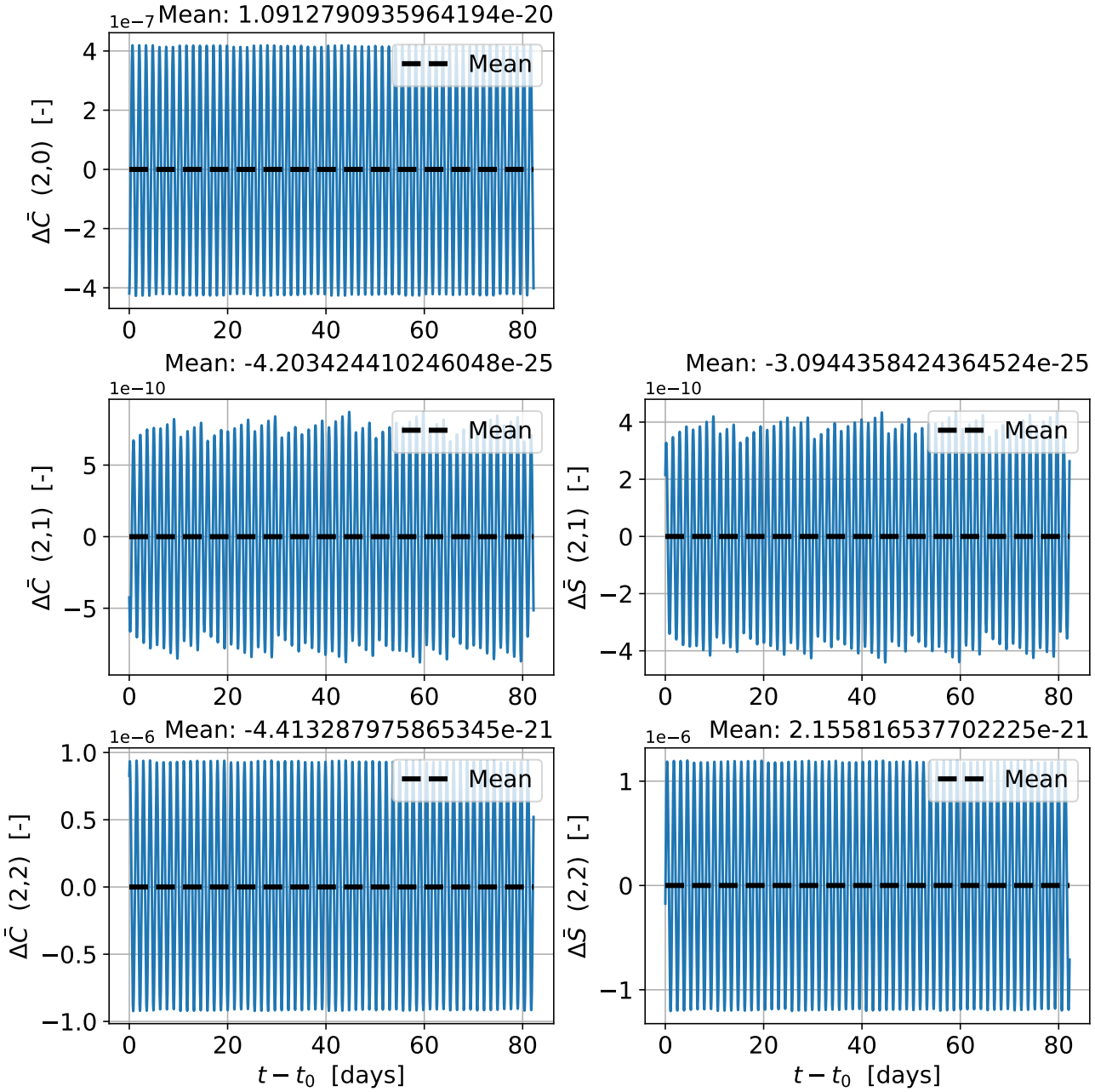

Figure 4.3.2.: Tidal response analysis for the cosine and sine terms of degree 2. The forcing is computed from the right-hand side side of Equation 2.1.27. The following value for the complex k_2 Love number is used: $k_2 = 0.02 + j0.01$ (Genova et al., 2024).

4.3.3. Removal of the effect of the permanent tide on the surface displacement

As discussed in Section 3.2.3, the correction for the effect of the permanent tidal bulge on Enceladus applies also to its shape. To avoid an overoptimistic estimate of the h_2 Love number, it is necessary to correct the permanent position displacement of the landers due to the frozen bulge. The discussion on the correction is given in Section 3.2.3.

After the removal of the effect of the permanent tide, the landers' surface displacement shows an oscillatory behaviour about a zero-mean value, as displayed in Figure 4.3.3. The detailed average values of the landers' corrected radial displacement are reported in Table 4.3.1. Additionally, in terms of the tidal displacement amplitude, the order of magnitude of the computed position displacements is in agreement with the results provided by Ermakov et al. (2021), who show that the expected tidal displacement in Enceladus is of the order of a few meters, with a maximum radial displacement in the interval $0.5 - 6.5\,\mathrm{m}$ in the equatorial region.

Table 4.3.1.: Average tidal position displacement of the Enceladus landers, after correction of the static tidal bulge.

Lander	Position displacement component	Average value [m]
L_1	x	$-3.773932567175805 \times 10^{-15}$
	y	0.0
	z	$-1.935940981024535 \times 10^{-15}$
L_2	x	$-4.759188245018649 \times 10^{-15}$
	y	$9.483806115376144 \times 10^{-15}$
	z	$-1.8449056610835004 \times 10^{-14}$
L_3	x	$5.122177178960749 \times 10^{-15}$
	y	$7.46028685187669 \times 10^{-14}$
	z	$-6.65779393603561 \times 10^{-30}$
L_4	x	$1.2583616376659478 \times 10^{-14}$
	y	$-1.5303152516670135 \times 10^{-14}$
	z	$-1.2940843581491387 \times 10^{-14}$
L_5	x	$-1.8106233728778574 \times 10^{-14}$
	y	$-9.845354617040698 \times 10^{-16}$
	z	$-2.1005823903482734 \times -14$
L_6	x	$-2.590473407942354 \times 10^{-14}$
	y	$1.0153607124435973 \times 10^{-14}$
	z	$3.9848118526088346 \times 10^{-14}$
L_7	x	$-1.625959954896202 \times 10^{-14}$
	y	$-2.0027770387027632 \times 10^{-14}$
	z	$-2.2182657074239464 \times 10^{-14}$
L_8	x	$1.187060239927321 \times 10^{-14}$
	y	$-1.3914575801113845 \times 10^{-14}$
	z	$1.118801075530965 \times 10^{-30}$
L_9	x	$9.126578910544237 \times 10^{-15}$
	y	$5.20860311561363 \times 10^{-15}$
	z	$-1.1062519891568771 \times 10^{-14}$

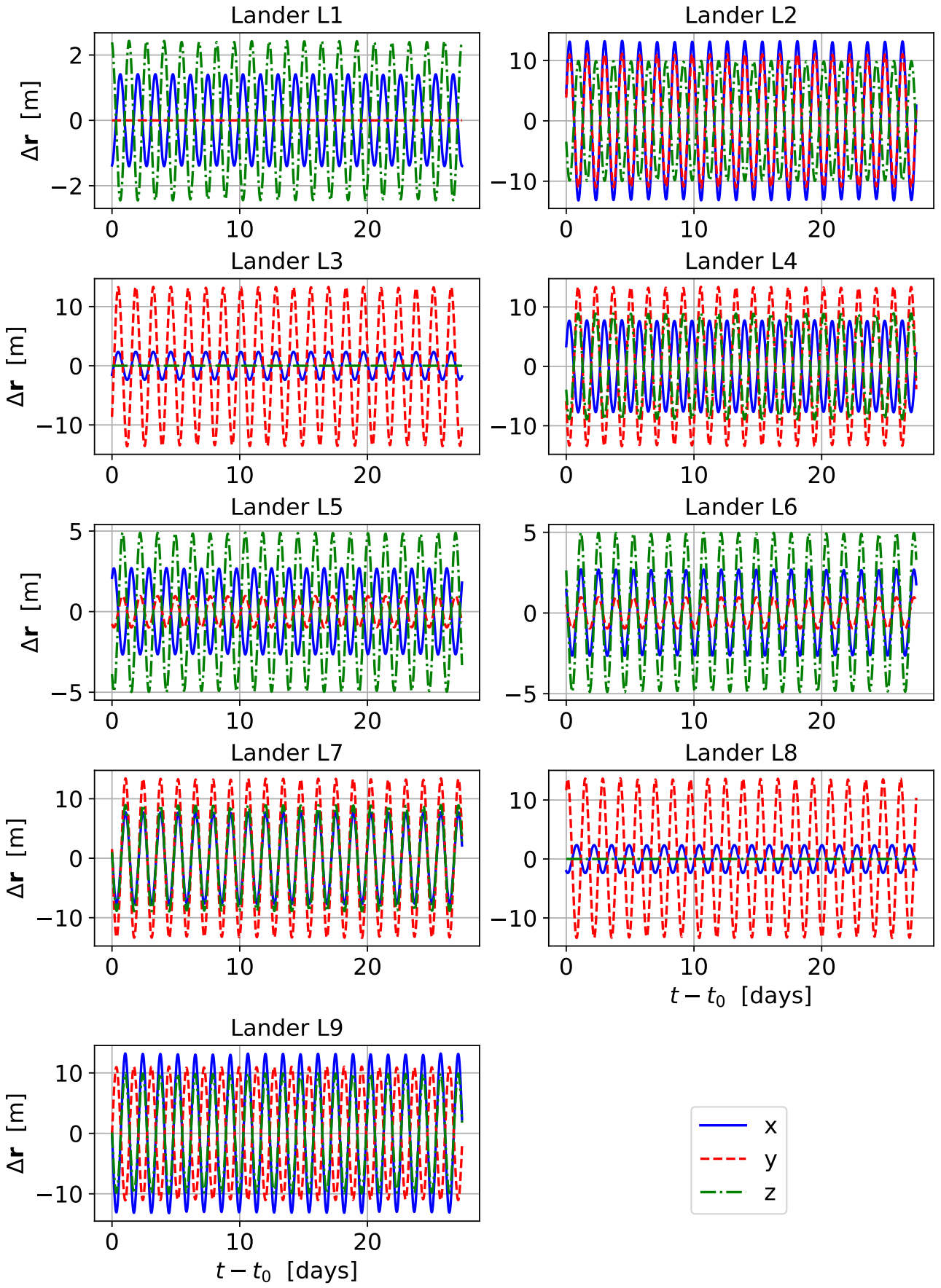

Figure 4.3.3.: Corrected position tidal displacement of Enceladus' surface landers. The displacement components oscillate around a zero-mean value due to the removal of the effect of the frozen bulge.

4.4. Radial displacement Love number observation partials

Section 3.2.4 describes how the partial derivative of the observations with respect to the h_2 Love number is computed, given the available partials of the observations with respect to the landers position and the available surface tidal displacement. As mentioned in Section 3.2.4, both these quantities are retrieved from Tudat. Thus, given the formulation of Equation 3.2.9 and the behaviour of the landers position displacement as shown in Figure 4.3.3, the partials of the observations with respect to the h_2 Love number are expected to show an oscillating behaviour about a zero-mean value, as displayed in Figure 4.4.1. The implementation of Equation 3.2.9 can thus be considered verified, given the available partials of the observations with respect to the landers position and the available surface tidal displacement.

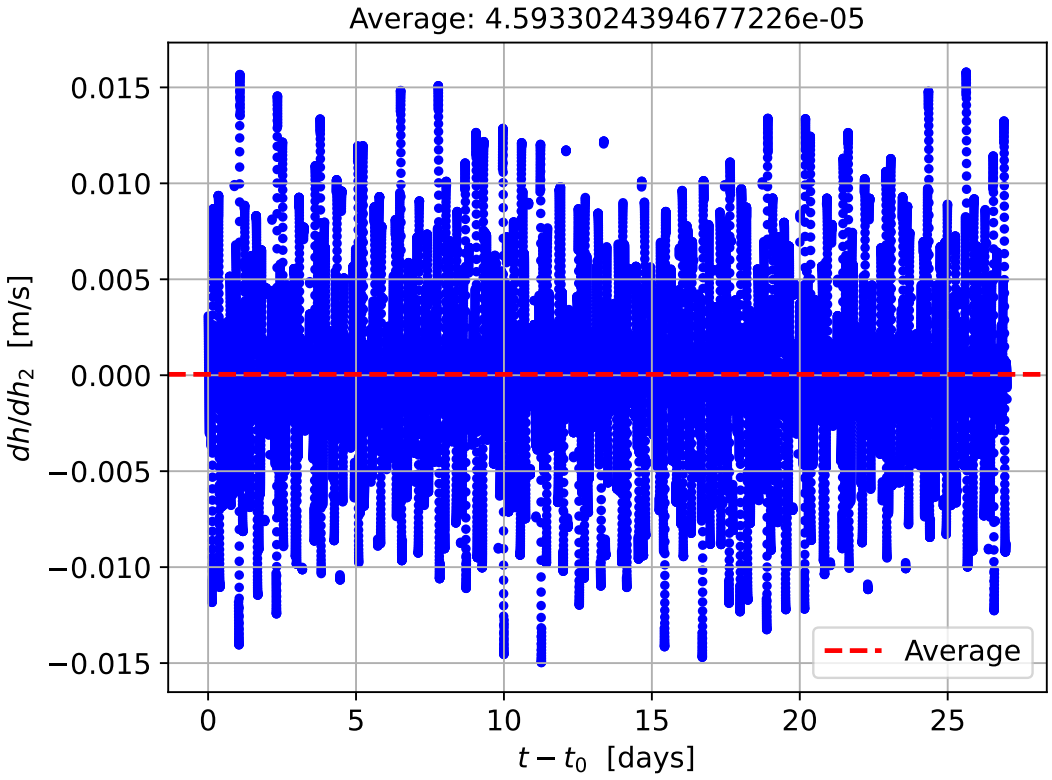

Figure 4.4.1.: Observation partials with respect to the h_2 Love number.

4.5. Spacecraft visibility conditions from the surface landers

As presented in Section 3.1, a minimum elevation angle of 15 deg is set for the condition of a viable lander observation, in order to avoid possible multipath effects.

The verification is performed by displaying the elevation angle of the S/C with respect to the landers at the observation epochs. Figure 4.5.1 shows that the elevation angle for all the landers is always higher than 15 deg. For the quantitative details, Table 4.5.1 reports the minimum elevation angle for each lander.

Table 4.5.1.: Minimum elevation angle of the S/C as seen by every surface lander.

Lander	L_1	L_2	L_3	L_4	L_5	L_6	L_7	L_8	L_9
Min. elevation [deg]	15.15	15.23	15.11	15.29	15.06	15.35	15.33	15.21	15.06

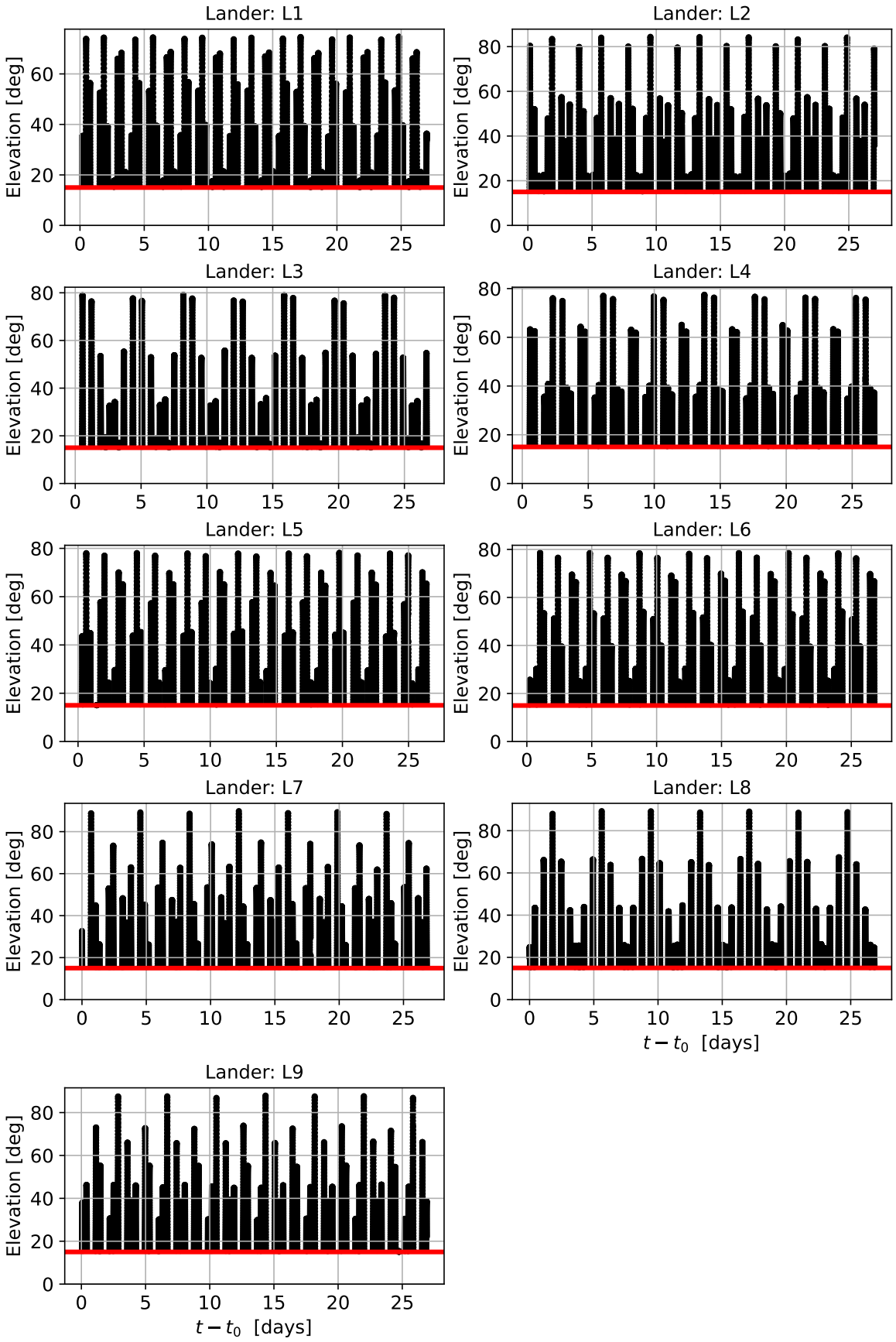

Figure 4.5.1.: Elevation angle of the S/C as seen by the surface landers at the observation epochs. The horizontal red line corresponds to the 15 deg limit for the viable observation condition. Orbit solution: K_1.

4.6. Stability of the orbit after change of the ephemeris models

The choice of the propagator settings proposed in Section 3.2.1 and the results presented in Appendix E.1 and Appendix E.2 for supporting it are produced with the DE438[2] and SAT427[3] kernels. However, as presented in Section 3.2.2, the rotation model of Enceladus from Park et al. (2024) was reconstructed using the DE440 (Park et al., 2021) and SAT441 (Jacobson et al., 2022) kernels. Hence, due to the need of having a coherent ephemeris and rotation model, the covariance analysis is performed with the DE440 and SAT441 kernels. Thus, the impact of using such ephemeris models on the orbit of the S/C, the integrator settings, and the dynamical model is assessed, to verify that these choices are still valid and that the change of ephemeris models still allows to answer the research question.

The DE440 ephemeris was generated by fitting planetary orbits to ground-based and space-based observations, using 7 years of new data with respect to the DE430 ephemeris, on which the DE438 is based (with respect to the DE430, the DE438 contains updated ephemeris for Mercuy, Mars, and Jupiter). Furthermore, the SAT427 kernel presents an improvement of the Saturnian system ephemeris, generated using a combination of data from Pioneer 11, Voyager 1, Voyager 2, and Cassini, together with Earth-based observations and data generated by the Hubble Space Telescope (Jacobson et al., 2022). The orbit model of the satellites accounts for the effects of the Saturnian rings, tidal effects, and a general relativistic correction.

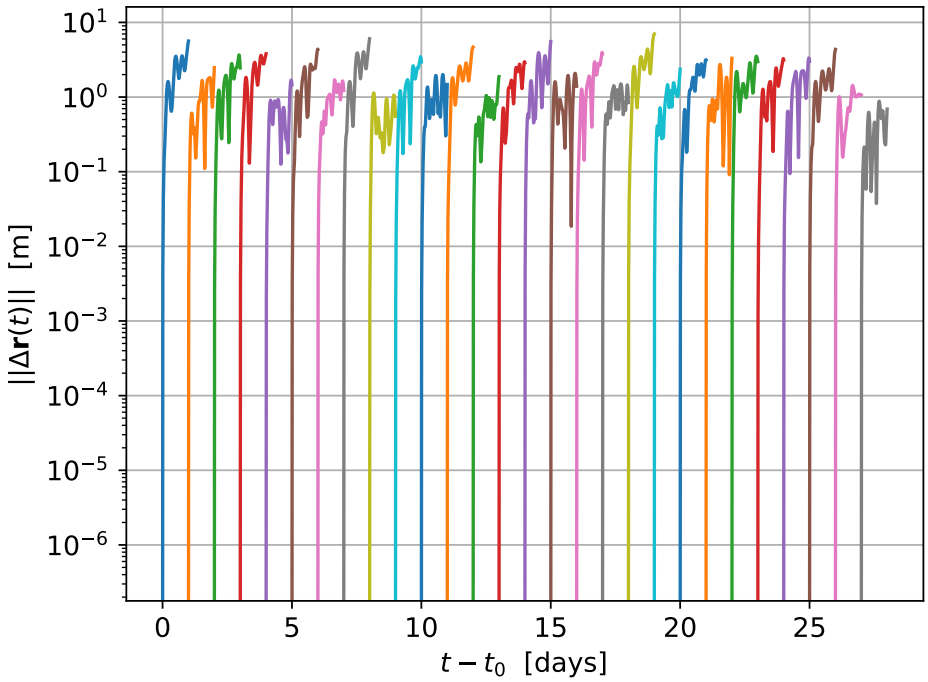

Figure 4.6.1.: Multi-arc position difference for the K_1 orbit solution propagated with the DE440 and SAT441 ephemeris kernels vs. the DE438 and SAT427 kernels.

Figure 4.6.1 shows the position difference for the K_1 initial state integrated with the two different ephemerides sets. As it is possible to observe, using the DE440 and SAT441 kernels instead of the DE438 and SAT427 kernels introduces an error below the 10 m level for an arc length of 1 day. Given the negligible position difference with respect to the orbit size (Table 3.1.5), the resulting orbits can still be considered representative for the analysed science mission scenario, and the relevant acceleration settings to be considered are expected to be the same.

[2] https://naif.jpl.nasa.gov/pub/naif/generic_kernels/spk/planets/
[3] https://naif.jpl.nasa.gov/pub/naif/pds/wgc/kernels/spk/

As for the integrator settings, with the DE440 and SAT441 ephemerides, the integrator has a very similar behaviour with respect to the case of the DE438 and SAT427 ephemerides. After 28 days, the Runge-Kutta-Fehlberg (RKF)5(6) integrator with a fixed time step of 15 s (as selected in Section 3.2.1) leads to a position error of 10^{-2} m, higher with respect to the previous case due to additional perturbing accelerations (refer to Appendix E.2.1 for the associated discussion). However, the integrator settings can still be considered acceptable for the scope of this work, since the integrated orbit is still representative of a science orbit around Enceladus (Appendix E.2.1). For details on the behaviour of the integrator, the reader is referred to Figure E.2.4.

Finally, to explicitly show that the integrated orbits with the updated planetary ephemerides still are bounded to Enceladus and resemble closely the orbits integrated with the original ephemeris kernels, the altitude difference with respect to the original orbits is plotted over time in Figure 4.6.2. A single one-month long arc is considered, for the purpose of discussing the stability of the orbit over a long integration time. As it can be observed, after 1 month of integration, the altitude difference is bounded in the region $[-20; 20]$ m for all three orbits. Hence, given that the original orbits are stable and bounded to Enceladus, as verified in Section 4.1, also the orbits with the DE440 and SAT441 ephemeris kernels are stable and bounded to the moon, i.e. the S/C does not escape nor crash on Enceladus. Thus, K_1, K_2, and K_3 integrated with the DE440 and SAT441 planetary ephemerides still allow to answer the first research sub-question.

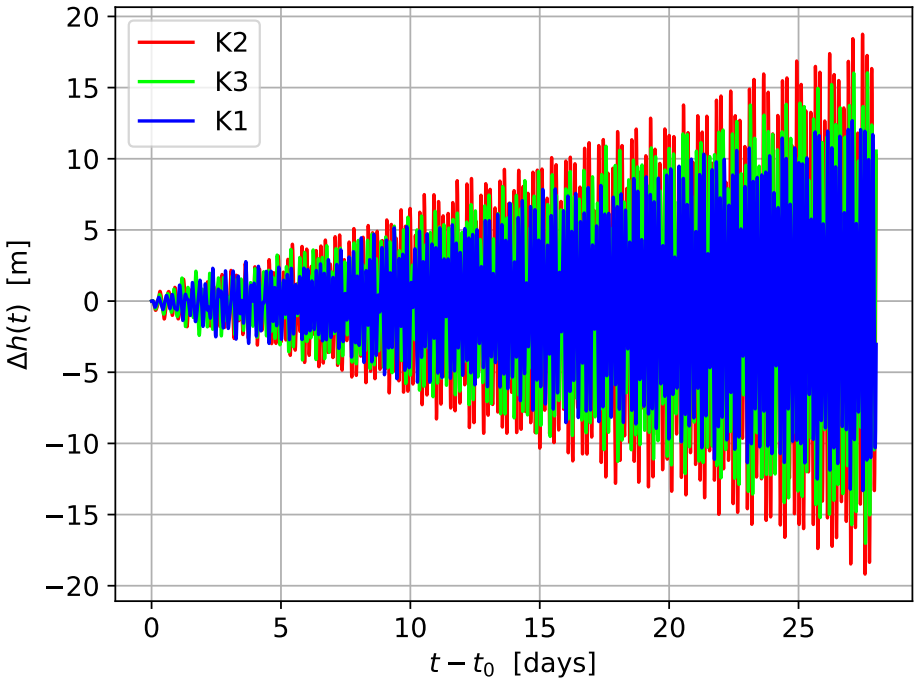

Figure 4.6.2.: Altitude difference between the orbits propagated with the DE440 and SAT441 ephemeris kernels vs. the DE438 and SAT427 kernels.

5. Results and discussion

5.1. Covariance design space exploration

As described in Section 3.3.2, for the exploration of the design space, the covariance analysis is performed on a series of configurations obtained by tuning one parameter at a time on top of a base configuration. The base configuration is reported in Table 3.3.3. The series of configurations is presented in Table 5.1.1. The parameters of interest considered for the covariance design space exploration are given in Section 3.3.2.

Table 5.1.1.: Configurations used for the covariance design space exploration. The first part of the table describes the tuned parameter for the given configuration and the given landers scenario (in accordance with the methodology presented in Section 3.3.2). N is referred to the list index of the considered tuning parameter, while X refers to the included landers scenario. In the second part of the table, the included landers scenarios are described. The coordinates of the landers are provided in Table 3.1.3.

Configurations	Tuning parameter	Unit	Values
$X.0.N$	Initial state solution	–	$[K_1; K_2; K_3]$
$X.1.N$	Arc duration	days	$[1; 2; 7]$
$X.2.N$	Simulation duration	days	$[28; 60; 90]$
$X.3.N$	Kaula constraint coefficient	–	$\left[10^{-6}; 10^{-5}; 10^{-4}; 4 \times 10^{-4}; 10^{-3}\right]$
$X.4.N$	A priori σ on emp. acc.	$\mathrm{m\,s^{-2}}$	$\left[10^{-9}; 10^{-8}; 10^{-7}; 10^{-6}; 10^{-5}\right]$
$X.5.N$	A priori σ on landers position	m	$\left[10^{2}; 10^{3}\right]$
$X.6.N$	Inclusion of landers range observable	–	[No; Yes]
$X.7.N$	Duration of empirical accelerations arc	hrs	$[12; 24]$
$X.8.N$	Earth GSs tracking arc	hrs	$[4; 6; 8]$
$X.9.N$	A priori σ on rotation pole position	deg	$\left[\infty; 10^{-1}; 10^{-2}\right]$
$X.10.N$	A priori σ on rotation pole rate	$\mathrm{deg\ s^{-1}}$	$\left[\infty; 10^{-1}; 10^{-2}\right]$
$X.11.N$	A priori σ on SRP	–	$\left[\infty; 10^{-1}; 10^{-10}\right]$
Configurations	Tuning parameter	Unit	Value
$0.Y.N$	Included landers	–	None
$1.Y.N$	Included landers	–	L_3
$2.Y.N$	Included landers	–	L_1; L_3
$3.Y.N$	Included landers	–	L_1; L_2; L_3; L_4; L_5; L_6; L_7; L_8; L_9

The produced figures of merit for the design space exploration are shown in Figure 5.1.1 to Figure 5.1.9. The largest driver for most figures of merit is the addition of radio beacons on Enceladus' surface. The plots show that when only the equatorial lander L_3 is added to the mission design (configurations $1.Y.N$), figures of merit such as the formal error associated to the libration amplitude (Figure 5.1.1), pole position (Figure 5.1.6) and pole rate (Figure 5.1.7) are characterized by a reduction of about two orders of magnitude with respect to the configurations with no lander (configurations $0.Y.N$).

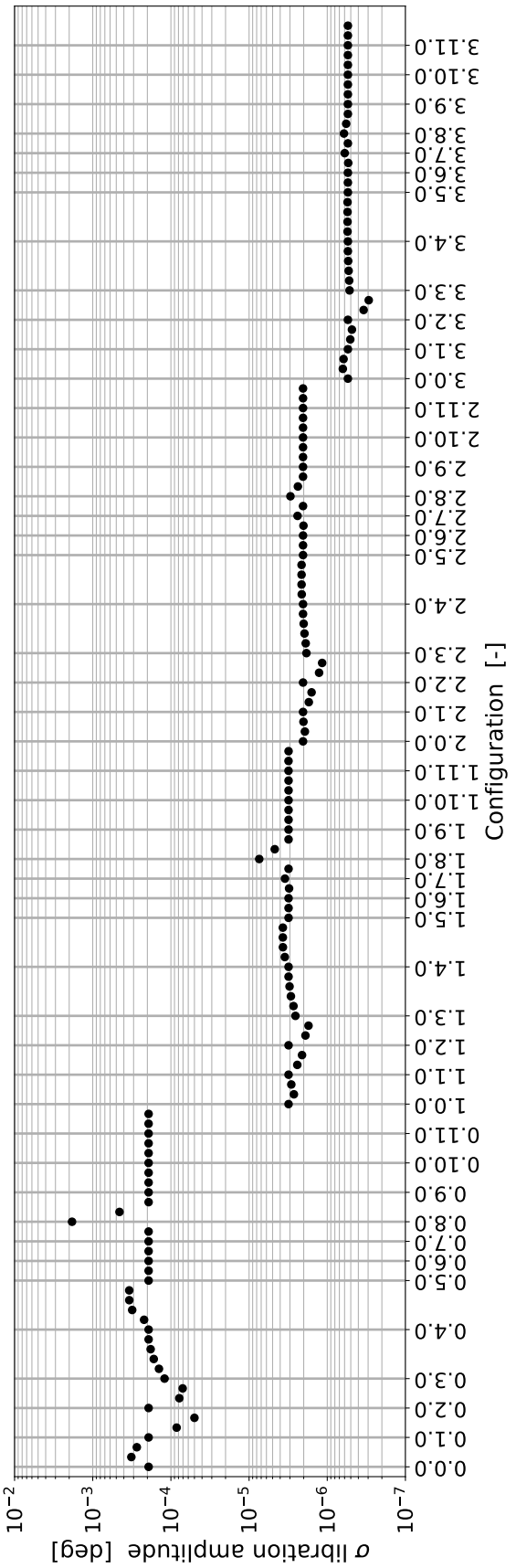

Figure 5.1.1.: Covariance design space exploration for the libration amplitude. Each tick on the axis of the configurations indicates the first value of the series $X.Y.N$, i. e., the configuration $X.Y.0$. The first index refers to the included landers scenario, while the second index refers to the considered tuning parameter, in accordance with Table 5.1.1.

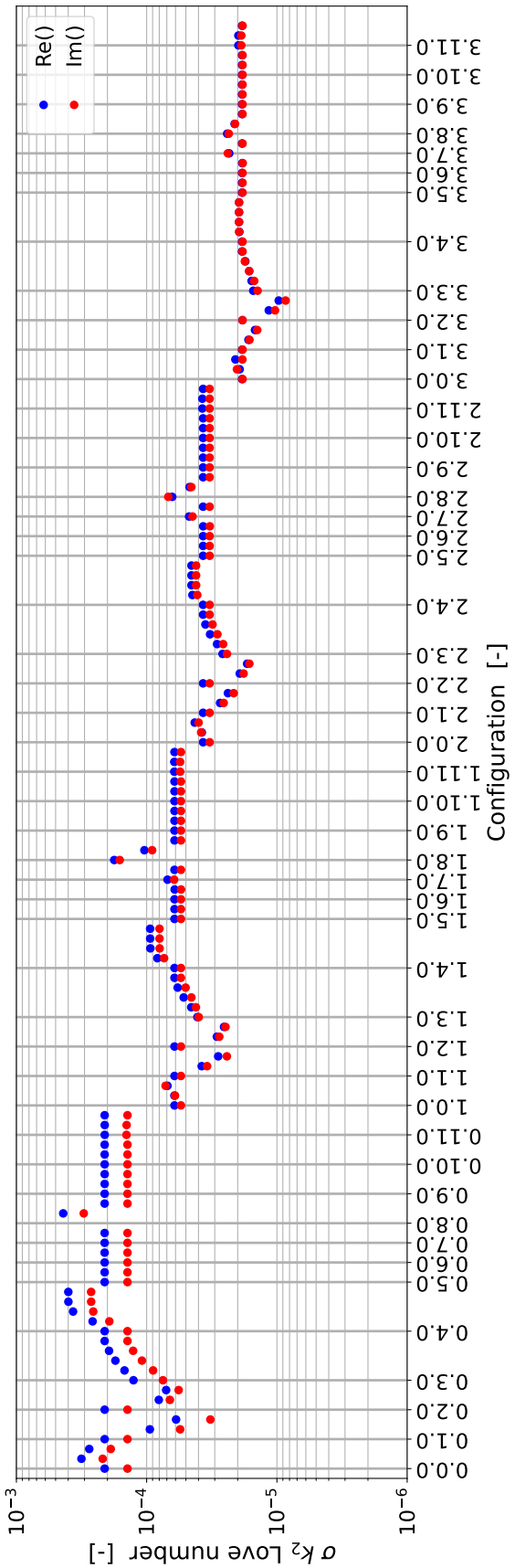

Figure 5.1.2.: Covariance design space exploration for the k_2 Love number. Each tick on the axis of the configurations indicates the first value of the series $X.Y.N$, i. e., the configuration $X.Y.0$. The first index refers to the included landers scenario, while the second index refers to the considered tuning parameter, in accordance with Table 5.1.1.

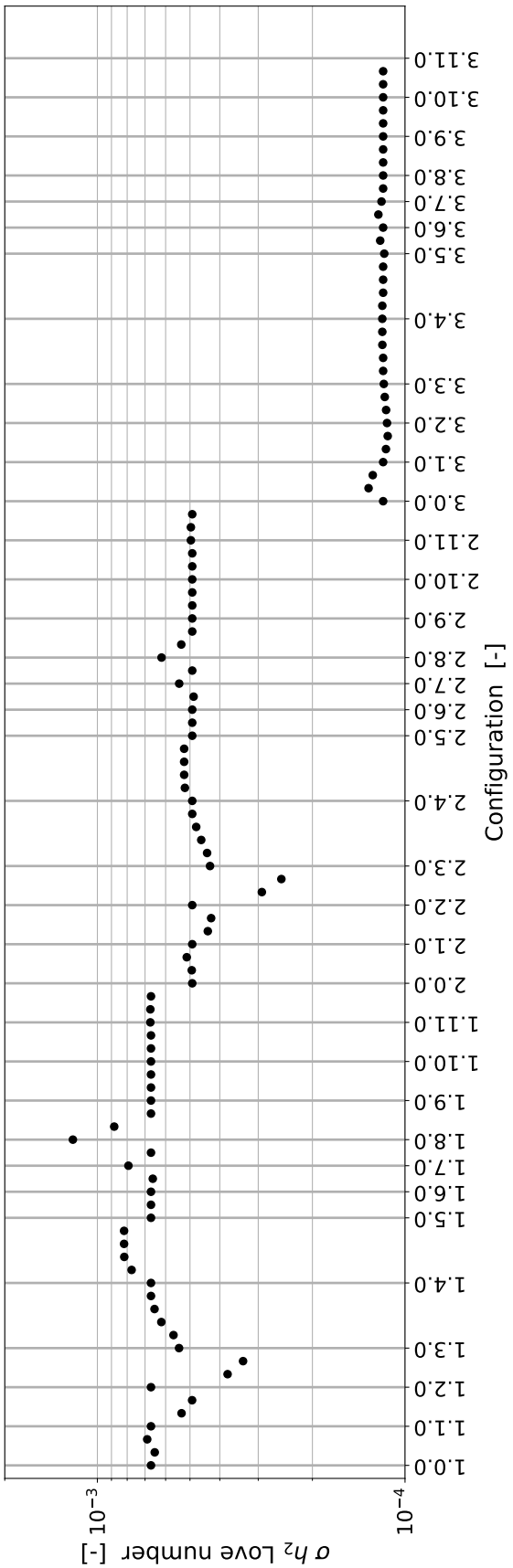

Figure 5.1.3.: Covariance design space exploration for the h_2 Love number. Each tick on the axis of the configurations indicates the first value of the series $X.Y.N$, i. e., the configuration $X.Y.0$. The first index refers to the included landers scenario, while the second index refers to the considered tuning parameter, in accordance with Table 5.1.1.

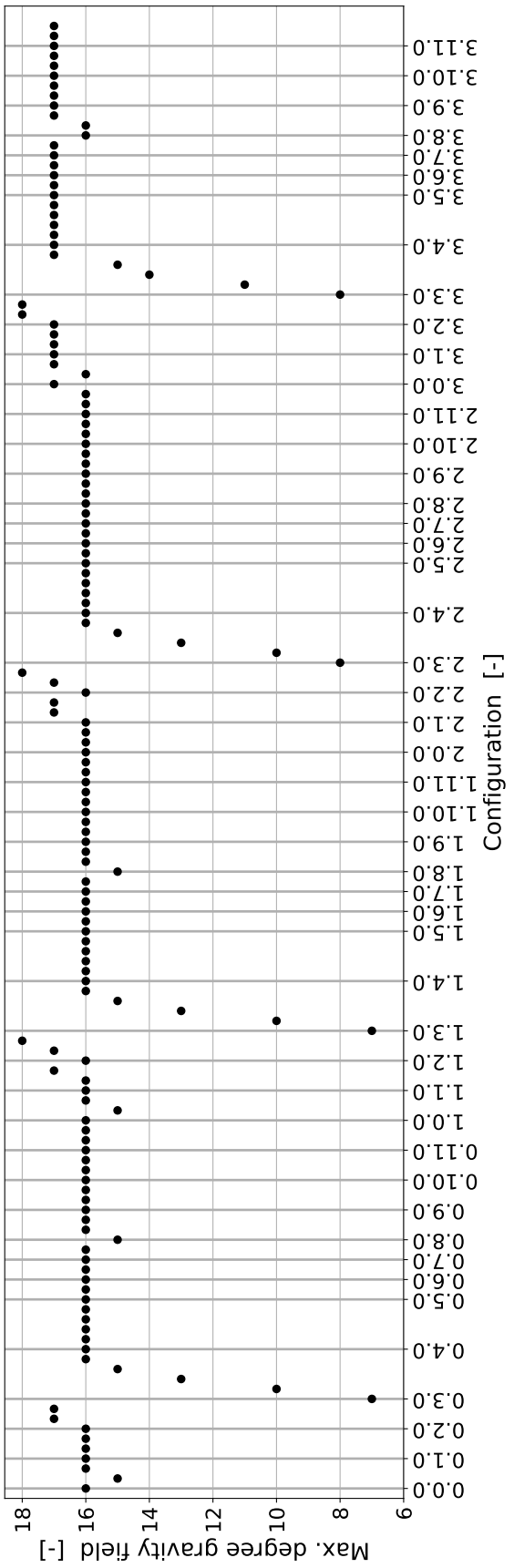

Figure 5.1.4.: Covariance design space exploration for the maximum estimatable gravity field degree. The maximum degree is defined at 90% of the Kaula constraint. Each tick on the axis of the configurations indicates the first value of the series $X.Y.N$, i. e., the configuration $X.Y.0$. The first index refers to the included landers scenario, while the second index refers to the considered tuning parameter, in accordance with Table 5.1.1.

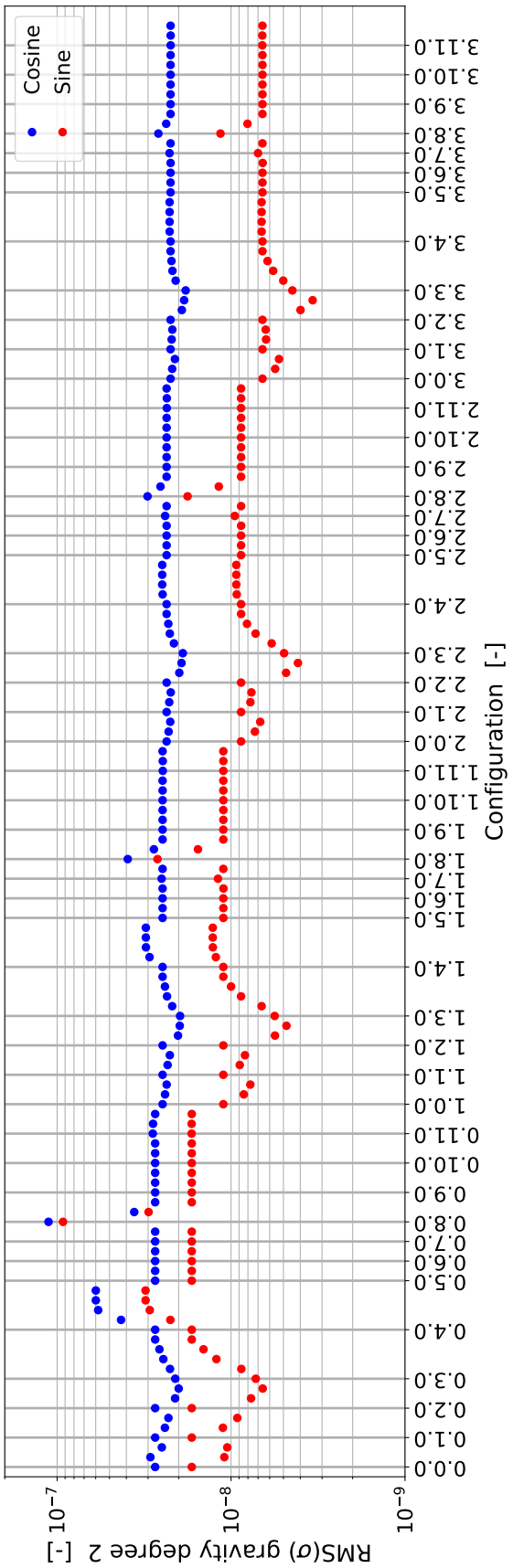

Figure 5.1.5.: Covariance design space exploration for the RMS of the formal errors of the cosine and sine coefficients of degree 2. Each tick on the axis of the configurations indicates the first value of the series $X.Y.N$, i. e., the configuration $X.Y.0$. The first index refers to the included landers scenario, while the second index refers to the considered tuning parameter, in accordance with Table 5.1.1.

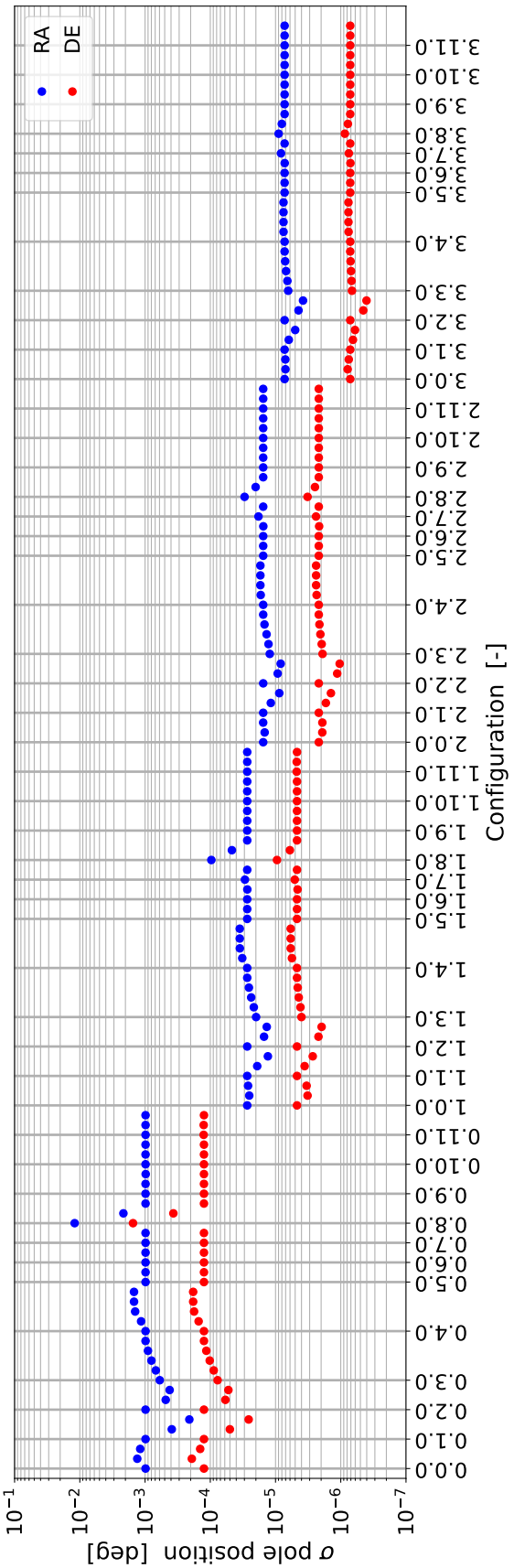

Figure 5.1.6.: Covariance design space exploration for the formal error of the pole right-ascension and declination. Each tick on the axis of the configurations indicates the first value of the series $X.Y.N$, i. e., the configuration $X.Y.0$. The first index refers to the included landers scenario, while the second index refers to the considered tuning parameter, in accordance with Table 5.1.1.

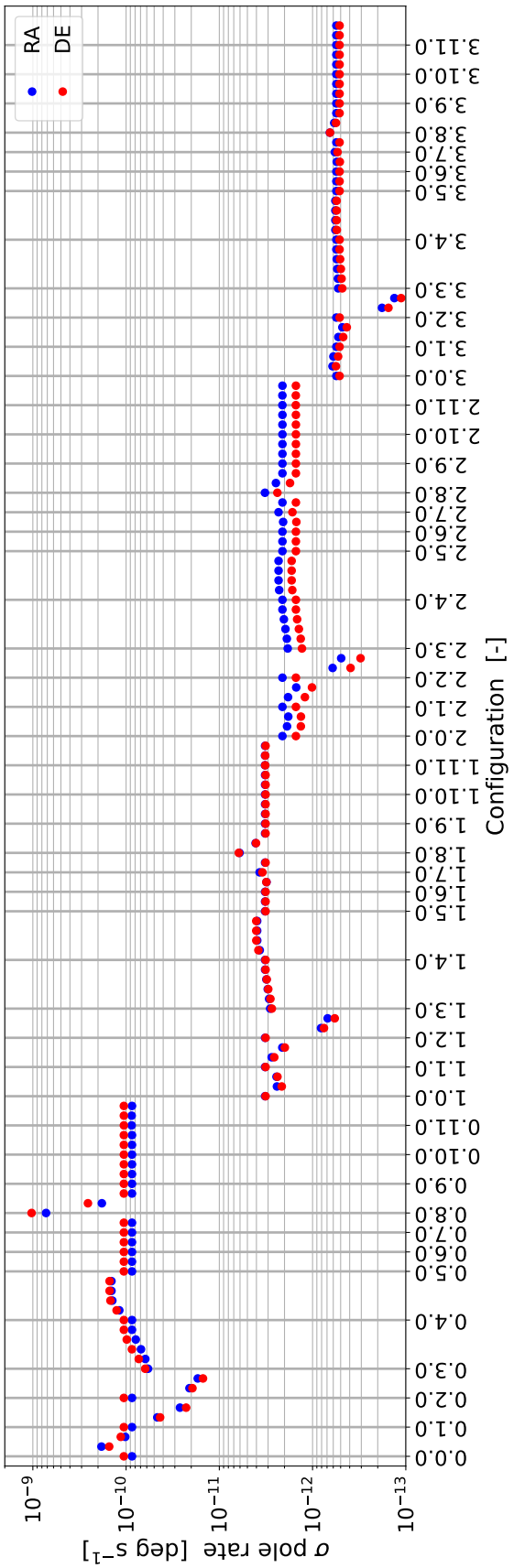

Figure 5.1.7.: Covariance design space exploration for the formal error of the pole rate. Each tick on the axis of the configurations indicates the first value of the series $X.Y.N$, i. e., the configuration $X.Y.0$. The first index refers to the included landers scenario, while the second index refers to the considered tuning parameter, in accordance with Table 5.1.1.

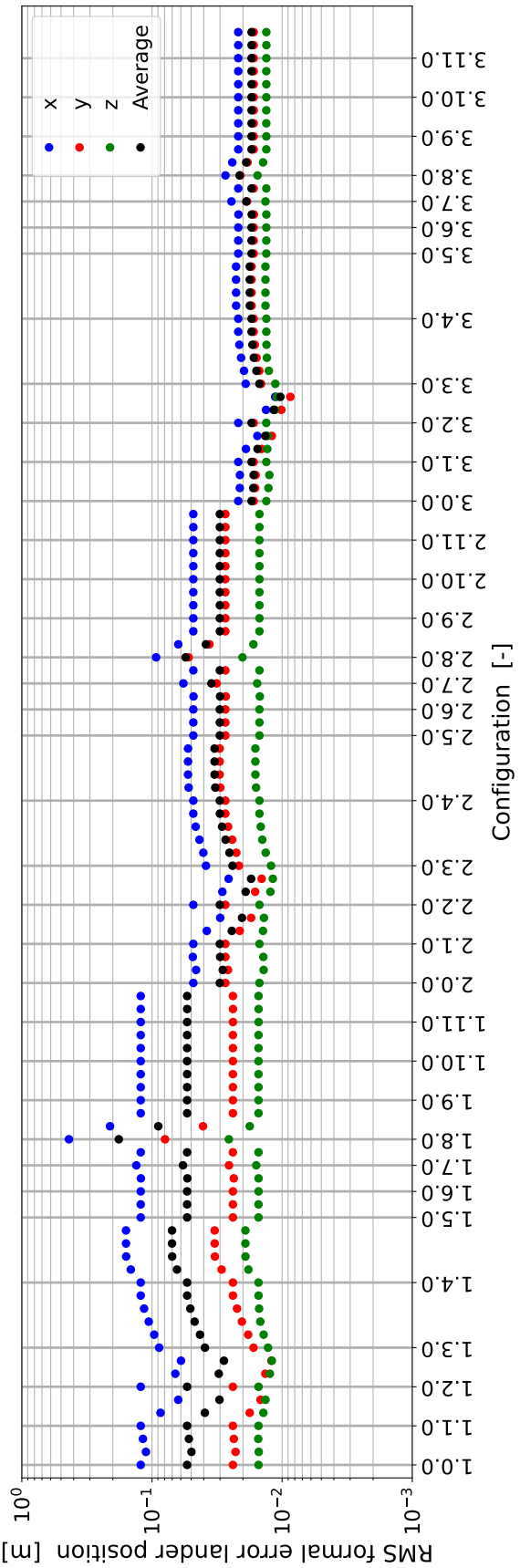

Figure 5.1.8.: Covariance design space exploration for the RMS of the formal error of the landers' position. Each tick on the axis of the configurations indicates the first value of the series $X.Y.N$, i. e., the configuration $X.Y.0$. The first index refers to the included landers scenario, while the second index refers to the considered tuning parameter, in accordance with Table 5.1.1.

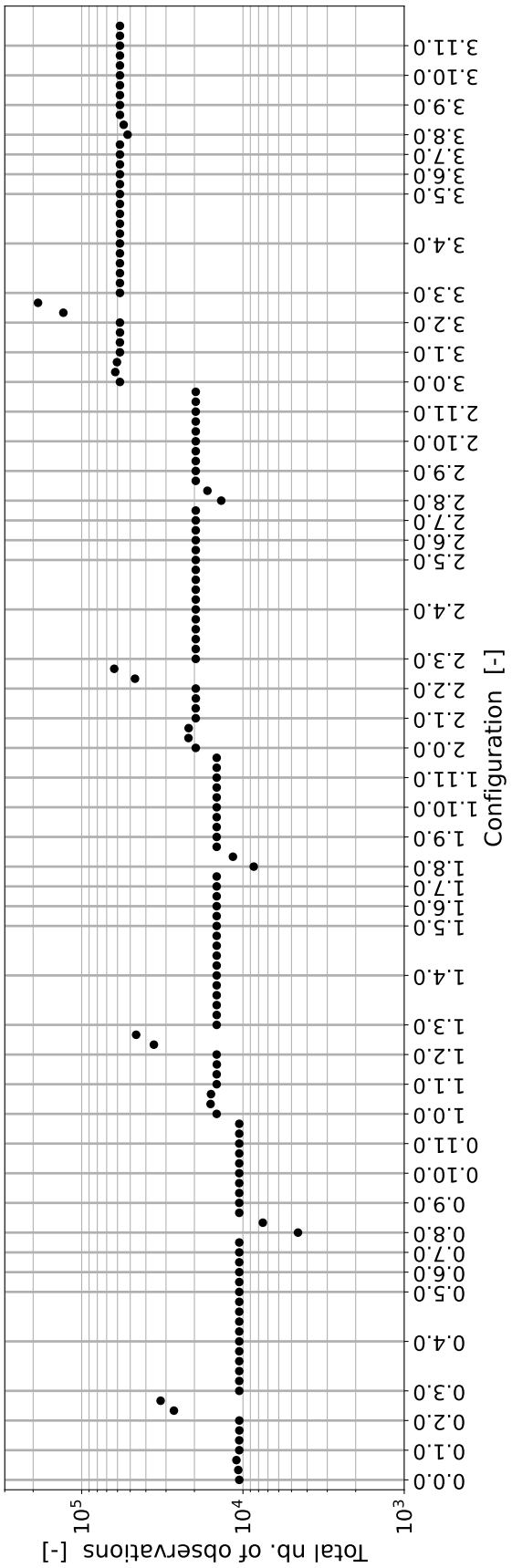

Figure 5.1.9.: Total number of observations produced in the covariance design space exploration. Each tick on the axis of the configurations indicates the first value of the series $X.Y.N$, i. e., the configuration $X.Y.0$. The first index refers to the included landers scenario, while the second index refers to the considered tuning parameter, in accordance with Table 5.1.1.

With respect to the libration amplitude, as mentioned in Section 3.3.2, it is not possible in Tudat to distinguish between the libration of the core and the one of the shell. Thus, when no radio beacons are placed on Enceladus, the estimated formal error of the libration amplitude is associated to the diurnal libration of the whole body, including the gravity signal of the core, considerably higher with respect to the one of the ice shell.

Furthermore, the k_2 Love number (Figure 5.1.2) is reduced of roughly 3 times, from around 2×10^{-4} to about 6×10^{-5} for many of the considered configurations, when one lander is included in the mission architecture, compared to none. On the other hand, there are some figures of merit for which adding the L_3 lander has not a major effect. They are the RMS of the formal error of the degree 2 gravity coefficients (Figure 5.1.5) and the maximum estimatable degree of the gravity field (Figure 5.1.4). There is no major trend in these static gravity-related figures of merit due to the fact that the landers, because of their sensitivity to the movements of the ice shell, allow to more accurately determine the time-varying dynamical response of Enceladus to the forcing by Saturn, both in terms of gravity and shape. However, they do not significantly contribute to knowledge on the static gravity, given that the links with the Earth GSs provide most of the gravity signal with a lower noise for the estimation of the static SH gravity field coefficients. The landers' data are in fact affected by a higher noise compared to the Earth radio tracking data, making them weight less according to the definition of the weight matrix of (2.2.15). Hence, while the addition of landers to the mission architecture enhances the estimation of dynamic parameters, such as the Love numbers, it does not provide a significant contribution to the static gravity, estimated mostly thanks to the links with the Earth GSs.

It should be observed that for the figures of merit for which the addition of landers has a significant effect on the results, the improvement of the formal error obtained when adding the L_3 lander to a configuration with no landers ($1.Y.N$ vs $0.Y.N$) is much larger than the effect of including additional landers when already one is present. The trend can be observed in Figure 5.1.1, Figure 5.1.2, Figure 5.1.6, and Figure 5.1.7. This is an interesting result, showing that a mission with an orbiter and one lander can already provide good results without deploying a set of multiple radio beacons, which would increase the complexity and costs of the mission with diminishing science returns.

Other than the trend related to the number of surface beacons, there are minor trends related to mission design parameters such as the mission duration, the length of the tracking arcs from the Earth GSs, the estimation arcs length, and science parameters like the a priori constraint on the empirical accelerations and the Kaula constraint.

As for the mission duration (configurations $X.2.N$), a longer simulation length leads to smaller formal errors and a higher gravity degree-strength. As an example, Figure 5.1.3 shows that when only the lander L_3 is included in the mission scenario, the formal error on the h_2 Love number decreases from about $\sim 7 \times 10^{-4}$ to $\sim 3 \times 10^{-4}$ for a simulation duration increasing from 28 days to 90 days (configurations 1.2.0, 1.2.1, 1.2.2). On the other hand, the gravity degree-strength (Figure 5.1.4) increases from 16 to 18 for the same configurations. The other figures of merit show similar trends. The improvement of the formal errors due to a longer mission is given by the higher amount of observations: for the configurations 1.2.0, 1.2.1, 1.2.2, the mission produces in total 14552, 35681, and 45958 observations respectively, as shown in Figure 5.1.9. The reduction of the formal error with higher number of observations is explained by the fact that due to the formulation of the covariance matrix as presented in Section 2.2.2, the formal errors have a behaviour inversely proportional to the square root of the number of observations n:

$$\sigma(p) \sim \frac{1}{\sqrt{n}} \tag{5.1.1}$$

Hence, the larger the number of observations, the better accuracy can be achieved by the science mission. However, for many parameters, such as the libration amplitude, h_2 Love number, pole position and rate, the effect of the mission duration is secondary to the number of landers. Figure 5.1.7 shows that with no landers, increasing the mission length (configurations 0.2.0, 0.2.1, 0.2.2) leads to a reduction of both the RA and DE of about one order of magnitude, from $\sim 1 \times 10^{-10}$ to $\sim 1.5 \times 10^{-11}$ deg s^{-1}; however, with only L_3, the numbers decrease of about 5 times, in the range $\sim 3.2 \times 10^{-12} - 6.9 \times 10^{-13}$ deg s^{-1} for the RA, with a very similar trend in DE. When adding a second lander, the range becomes

$\sim 2.1 \times 10^{-12} - 4.9 \times 10^{-13}$ deg s^{-1}, with a reduction of about 4 times. Finally, with nine landers, the reduction is from $\sim 5.6 \times 10^{-13}$ to $\sim 1.3 \times 10^{-13}$ deg s^{-1}, again about 4 times. Similar trends are observed in Figure 5.1.3, Figure 5.1.1, and Figure 5.1.6. Hence, it appears that the addition of multiple landers to the mission architecture tends to attenuate the influence of the mission length. This result can be explained by considering the noise affecting the landers link (Table 3.1.1) and the ratio between the number of landers data to Earth GSs data. As presented in Section 2.2.2, the noise level is used in the computation of the weight matrix, according to the definition presented in Equation 2.2.15. Thus, the higher the noise affecting the single observation, the lower the weight of the observation, as mentioned earlier. As for the ratio between the number of observations, when an increasing number of landers is added to the mission, the ratio between the number of landers observations and Earth GSs observations increases significantly, as reported in Table 5.1.2. Thus, the covariance algorithm relies on significantly more landers data which have a smaller weight with respect to the Earth GSs data. Hence, even though more observations are collected with about the same ratio between the 28-days case and the 90-days case, the proportion of observations with a larger noise is higher with respect to the case of no landers or just one lander. The result is a reduced improvement of the formal errors. A possible way to circumvent this issue for a future mission could be de-weighting the observations by a factor $\sqrt{n}$ (e. g., Lainey et al. (2019), S. Fayolle (2025)). In conclusion, given the strong gravity perturbations by Saturn, generally requiring orbit control manoeuvres as discussed in Section 2.4, it might be more beneficial for the mission costs and planning to design the mission architecture in terms of the number of landers, with a shorter mission length.

Table 5.1.2.: Ratio of number of landers observations over number of Estrack GSs observations for different landers scenario and mission length values.

Landers included	Mission length [days]	Ratio of nb. of landers data to Earth GSs data [−]
None	28	0
None	90	0
L_3	28	0.38
L_3	90	0.42
L_1; L_3	28	0.86
L_1; L_3	90	0.94
L_1; L_2; L_3; L_4; L_5; L_6; L_7; L_8; L_9	28	4.50
L_1; L_2; L_3; L_4; L_5; L_6; L_7; L_8; L_9	90	4.76

With respect to the length of the Earth GSs tracking arcs (configurations $X.8.N$), a longer tracking arc leads to reduced formal errors across most of the figures of merit. For instance, for the 0.8.0, 0.8.1, and 0.8.2 configurations, the RMS of the formal errors for the degree 2 cosine gravity coefficients (Figure 5.1.5) decreases of a factor 4 from 1.1×10^{-7} to 2.7×10^{-8} with a tracking arc length increasing from 4 to 8 hours. As anothe example, considering the formal error of the landers' position (Figure 5.1.8), when only L_3 is present on Enceladus, the average RMS varies from $\sim 2 \times 10^{-1}$ m to $\sim 5.5 \times 10^{-2}$ m when changing the length of the Earth GSs tracking arc (configurations 1.8.0 to 1.8.2). In this case, the range width is ~ 0.145 m. When L_1 is added (configurations 2.8.0 to 2.8.2), the amplitude decreases to ~ 0.025 m. Finally, when all nine landers are included in the mission architecture (configurations 3.8.0 to 3.8.2), then the variability range of the average RMS is ~ 0.005 m. The length of the tracking arc has also an effect on geophysical parameters to which the radio beacons are most sensitive, like the pole position (Figure 5.1.6), the h_2 Love number (Figure 5.1.3), and the libration amplitude (Figure 5.1.1). For the configurations 0.8.0, 0.8.1, and 0.8.2, the formal error associated to the declination (Figure 5.1.6), decreases from $\sim 1.5 \times 10^{-3}$ deg for a tracking arc 4 hours long to $\sim 1.3 \times 10^{-4}$ deg for 8 hours, about one order of magnitude smaller. As for the h_2 Love number, looking at the cases 1.8.0, 1.8.1, 1.8.2,

it is possible to notice that the formal error is reduced of about a factor 2 from $\sim 1.2 \times 10^{-3}$ to $\sim 6.7 \times 10^{-4}$. For the same configurations, the formal error of the libration amplitude (Figure 5.1.1) shows a decrease from $\sim 7.4 \times 10^{-6}$ deg to $\sim 3.1 \times 10^{-6}$ deg, again about a factor 2. The k_2 Love number (Figure 5.1.2) behaves similarly. The reason for which an increase of the tracking arc from 4 to 8 hours leads to a non-negligible improvement of the estimated formal errors is to be found in the number of observations, similarly to the case of the mission duration, and in the sensitivity of the solve-for parameters to exposure of the spacecraft to the gravitational environment around Enceladus. Considering for instance the configurations 0.8.0, 0.8.1, and 0.8.2, Figure 5.1.9 shows that the total number of observations, produced entirely by the Earth GSs, increases from 4558 to 10541, a factor 2.3, while for the the configurations 0.8.0, 0.8.1, and 0.8.2 it increases by a factor 1.7. Moreover, some parameters like the static gravity coefficients or the pole position seem to be more dependent on the tracking arc length compared the Love numbers and libration amplitude. This is due to the fact that longer tracking arcs allow to acquire more data along the ground track, as shown in Figure 5.1.10 for a 8 hrs vs. 4 hrs long tracking arc. For the static gravity coefficients, longer tracking arcs from Earth produce more observations sensitive to the static gravity signal. For the pole parameters, they are quite dependent on the length of the tracking arcs, since more observations are retrieved when the spacecraft is located at higher latitudes, as the comparison in Figure 5.1.10 highlights.

With respect to the length of the estimation arcs (configurations $X.1.N$), longer arcs allow to obtain a higher accuracy on the estimation parameters, given that more observations are available within the arc, similarly to the influence of the length of the tracking arc. Considering the example of the k_2 Love number (Figure 5.1.2), when only the L_3 lander is included in the mission architecture, the formal error of $\Re(k_2)$ decreases by a factor 2 from $\sim 6.1 \times 10^{-5}$ to $\sim 2.8 \times 10^{-5}$ for an increase of the arc length from 1 to 7 days. A similar trend is observed for the formal error associated to other estimation parameters of interest. For instance, the same configurations lead to a variation of h_2 (Figure 5.1.3) in the range $6.7 \times 10^{-4} - 4.9 \times 10^{-4}$, with a decrease of a factor ~ 1.4, and a variation of the libration amplitude (Figure 5.1.1) in the interval $\sim 3.1 \times 10^{-6} - 2.1 \times 10^{-6}$ deg, a decrease of a factor ~ 1.5. On the other hand, the arc length appears not to affect the maximum degree of the gravity field (Figure 5.1.4), and the RMS of the formal error of the degree 2 gravity coefficients (Figure 5.1.5) shows a negligible trend with the arc length, in agreement with the maximum gravity degree. In general, considering the produced figures of merit, even though the arc duration has a visible effect, it is quite small in magnitude, and is quite reduced with respect to the influence of the number of landers included. In light of the orbit design considerations exposed in Section 2.4, an arc length of 7 days appears to be too long for a mission in a highly perturbed dynamical environment. Thus, given that the improvement in the formal errors is quite marginal, it appears to be more likely that a possible future mission to Enceladus will rely on estimation arcs one or two-days long.

Aside from the mission parameters, also the Kaula constraint coefficient and the a priori constraint on the empirical accelerations have a visible but small impact on the figures of merit. The Kaula coefficient expresses the a priori knowledge on the gravity field coefficients according to Equation 3.3.1. As described in Table 3.3.2, the Kaula coefficient is varied in the range $1 \times 10^{-6} - 1 \times 10^{-3}$, spanning various orders of magnitude in order to have a comprehensive overview of its effect on the formal errors. In the displayed plots, it is possible to observe that the variation of the Kaula coefficient has a small effect on the figures of merit. For instance, when no lander is included in the mission architecture, the formal error of the libration amplitude (Figure 5.1.1) increases from $\sim 1.2 \times 10^{-4}$ to $\sim 1.9 \times 10^{-4}$ (configurations 0.3.0 to 0.3.4). For the same cases, the $RMS\,(\sigma)$ for the degree 2 gravity coefficients (Figure 5.1.5) varies in the interval $\sim 2.1 \times 10^{-8} - 2.7 \times 10^{-8}$ for the cosine terms, and in the interval $\sim 7.2 \times 10^{-9} - 1.7 \times 10^{-8}$ for the sine terms. The fact that the Kaula coefficient has no significant effect on the degree 2 terms can be explained by considering that the Kaula constraint is not applied to such terms, as mentioned in Section 3.3.2 and indicated in Table 3.3.3. The only parameter significantly affected by the Kaula constraint is the maximum estimatable gravity field degree, due to its definition, introduced in Section 3.3.2. When varying the Kaula coefficient κ (see Equation 3.3.1) in the range $1 \times 10^{-6} - 1 \times 10^{-3}$, the maximum estimatable gravity degree varies in between $7 - 16$. For the nominal

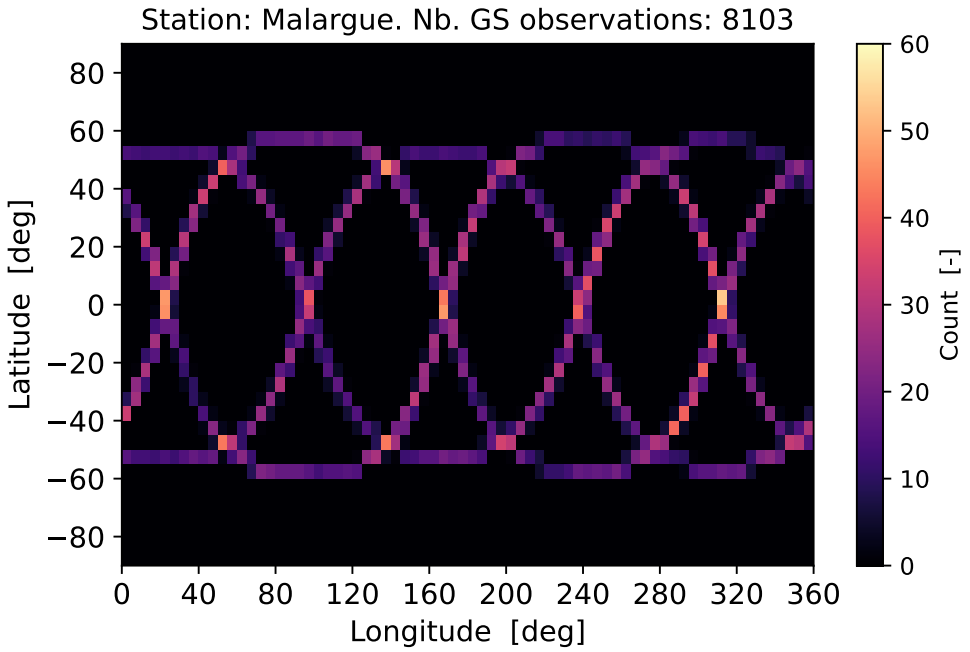

(a) Observations number density for a 8 hours long tracking arc.

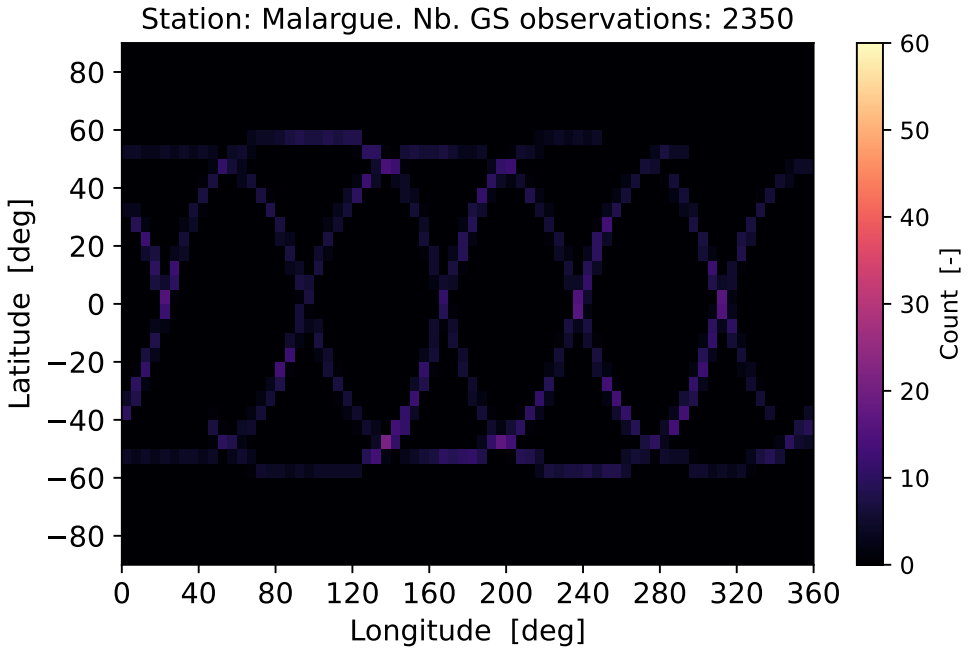

(b) Observations number density for a 4 hours long tracking arc.

Figure 5.1.10.: Observations number density along the ground track of the K_1 orbit (initial state provided in Table 3.1.5) for the Malargue GS (35 deg S, 69 deg W).

value of 4.0×10^{-4} assumed by Genova et al. (2024), consistent with gravity predicted by partially compensated topography, the gravity field can be estimated up to a maximum degree equal to 15 for all landers scenarios (see Figure 5.1.4).

Similarly, the figures of merit show that also the a priori uncertainty on the empirical accelerations leads to a small impact on the formal error of the estimation parameters. For example, Figure 5.1.1 shows a variation for the libration amplitude in the range $\sim 1.9 \times 10^{-4} - 3.4 \times 10^{-4}$ deg with no lander (configurations 0.4.0 to 0.4.4). For the same configurations, the RMS of the formal error for the gravity degree 2 varies in the range $2.7 \times 10^{-8} - 6.0 \times 10^{-8}$. The fact that the formal error shows a small increase with an increasing a priori σ is an expected trend, given that a higher a priori uncertainty on the empirical accelerations imposes less constraints on unmodelled accelerations, hence introducing a larger uncertainty in the dynamical model, which translates in a larger uncertainty on the rest of the estimation parameters.

In conclusion, the following main points of consideration can be summarised:

1. The number of landers included in the mission architecture is an important driver. The parameters related to the dynamical response of Enceladus to Saturn's forcing, such as the tidal k_2 (Figure 5.1.2) and h_2 (Figure 5.1.3) Love numbers, the diurnal libration amplitude (Figure 5.1.1), the pole position (Figure 5.1.6) and rate (Figure 5.1.7) heavily rely on the landers count. As mentioned earlier, this is mainly due to the sensitivity of the landers to movements of the ice shell. With respect to the static gravity field, its estimation relies more on the Estrack GSs data, affected by a lower noise (Table 3.1.1) and more sensitive to the gravity signal of the deep interior.

2. The number of landers affects the impact of other tuning parameters on the estimation results. It was observed that for an increasing number of landers, most figures of merit show a reduced variability of the formal error when varying the tuning parameters, including for example the mission length. The visible effect of the increasing number of landers on the reduction of the different configurations' variability is due to the significantly larger amount of available observations produced by the radio beacons. The larger number of observations would thus reduce the impact of one single control variable on the covariance results. With the nominal base case settings of a mission duration of 28 days, an 8 hrs tracking arc from Earth, and the K_1 orbit, the total number of observations increases from $10,541$ for zero landers to $57,924$ for nine landers, as shown in Figure 5.1.9, making the influence of the control variables negligible with respect to the contribution of the number of available observations. Thus, the variability range of the figures of merit caused by a single control parameter is reduced. It should be noted that the landers data are affected by a higher noise, making the algorithm reliant on many observations with more noise and lower weight, according to the definition of the weight matrix (Equation 2.2.15). A possible way to reduce the reliance of the algorithm on the landers data is to further de-weight them by a factor $\sqrt{n}$ (e. g., Lainey et al. (2019), S. Fayolle (2025)). The fact that the number of landers has a significant effects on the quality of the estimation results and on the effect of the other mission design parameters suggests that based on its mission objectives, an Enceladus mission comprising of a set of radio beacons should first be analysed in terms of the number and location of the beacons, following up with the analysis of mission design parameters such as the mission duration and the arcs length.

3. As for the mission duration, a longer mission leads to a general improvement of the static gravity coefficients, the dynamic parameters (Love numbers, libration amplitude), the pole position and rate, and the uncertainty associated to the landers position. Across the different landers scenarios, the number of observations triplicates when increasing the mission duration by a factor 3 from 28 to 90 days (see Figure 5.1.9). Since the formal errors follow Equation 5.1.1, the mission length is a relevant design parameter, as the estimated formal errors show. However, due to the complexity of orbit design at Enceladus, and given the reduction of its influence with multiple landers, long missions appear to be not necessary to achieve tight constraint on Enceladus' geophysical parameters.

4. The length of the Earth GSs tracking arcs affects particularly the static gravity coefficients and the pole parameters. A longer tracking from Earth allows to produce more observations along the ground tracks, both at low and higher latitudes (Figure 5.1.10), increasing the number of observations sensitive to the static gravity field and pole parameters.
5. With respect to the length of the estimation arcs, longer arcs allow to obtain a higher accuracy, with an improvement of the formal error for the tidal Love numbers and libration amplitude by a factor $1 - 2$. It appears to have a negligible effect on the estimation of the static gravity coefficients. The improvement of the formal errors due to the length of the estimation arcs is explained by considering that longer arcs allow to fit more data within the same arc, hence improving the resulting formal errors. However, the frequency of the orbit manoeuvres in the perturbed dynamical environment of Enceladus must be taken into account. Hence, 1-day arcs are expected to be considered in a future Enceladus mission.
6. Science parameters such as the Kaula coefficient (Equation 5.1.1) and the a priori constraint on the empirical accelerations have a visible but reduced influence on the solve-for parameter. The Kaula constraint has a relevant impact only on the maximum estimatable degree of the gravity field, due to its definition. As for the empirical accelerations, a larger a priori constraint leads to a higher uncertainty on the estimation parameters, since a larger uncertainty is introduced in the dynamical model. The effect of both parameters is however secondary.

5.2. Study of nominal representative cases

As indicated in the flow chart of Figure 3.0.1 (FC3.2), and described in Section 3.3.3, the design space exploration is followed by the study of reference scenarios, for the production of nominal results. The aim of the analysis is to answer the first research sub-question (Section 1.2) and to provide reference values for a future science mission to Enceladus. The results of this analysis are displayed in Figure 5.2.1.

The trend related to the number of surface radio beacons included in the mission analysis, already discussed in Section 5.1, is clearly visible. For parameters such as the pole RA and DE and the libration amplitude, adding the L_3 lander to the base configuration with no landers leads to an improvement of the formal error of about two orders of magnitude, as already observed in Figure 5.1.6 and Figure 5.1.1. Additionally, it is visible how using 9 homogeneously spread radio beacons improves the formal errors only marginally with respect to the case of 1 radio beacon. This result was observed also in the previous section.

For what concerns the arc length, as expected, a 1-day arc leads to higher formal errors than a 1-week arc. However, the improvement given by the latter is not significant. All parameters present a minor difference between the two sets of cases.

In terms of the orbit, there are minor differences in the resulting formal errors. The detailed values for each scenario are reported in Appendix G.

The results provided in this section can be used as a reference for study or comparison purposes with the literature. Section 5.7 shows that the results for the case with no radio beacons is in agreement with similar studies available in literature. Table 5.2.1 highlights the improvement given by adding one lander to the mission architecture for one selected scenario from the set of results shown in Figure 5.2.1 and provided in Appendix G.

Genova et al. (2024) reports the estimated uncertainty for some geophysical parameters, for a mission setup consisting of an orbiter carrying an onboard optical navigation camera. The camera is used to provide complementary measurements for a precise onboard localization of the S/C during periods not covered by radio tracking passes. The navigation camera is used during the science phase for refinement of the orientation parameters of Enceladus, including the librations. Table 5.2.2 shows a comparison between the results by Genova et al. (2024) and those of a reference single-lander mission scenario

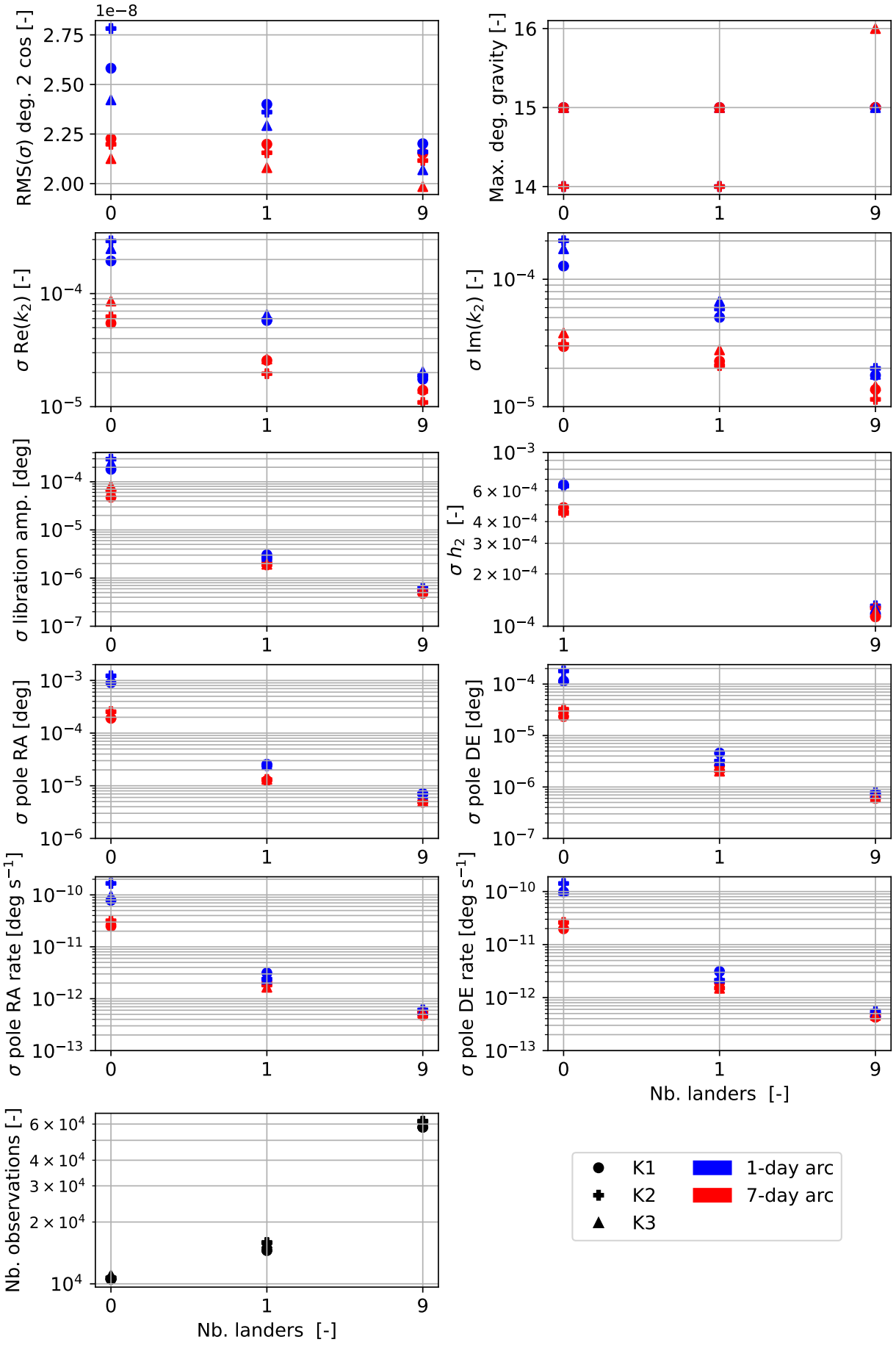

Figure 5.2.1.: Summary of the covariance analysis results for the representative cases described in Table 3.3.4.

Table 5.2.1.: Comparison of two selected nominal scenarios showing the improvement in the science return. The scenarios are obtained with the K_1 orbit and an arc length of 1 day. Scenario 1 has no radio beacons, while Scenario 2 includes one radio beacon (L_3) in the mission architecture.

Parameter	Unit	Scenario 1	Scenario 2
$RMS\,(\sigma)$ deg. 2 cos & sin	–	$(2.58; 1.44) \times 10^{-8}$	$(2.40; 1.00) \times 10^{-8}$
Max. deg. gravity	–	15	15
$\sigma\ (\Re(k_2); \Im(k_2))$	–	$(1.94; 1.27) \times 10^{-4}$	$(5.78; 5.02) \times 10^{-5}$
$\sigma\,(W_s)$	deg	1.82×10^{-4}	3.04×10^{-6}
$\sigma\,(h_2)$	–	–	6.52×10^{-4}
$\sigma\,(\alpha_0; \delta_0)$	deg	$(9.03; 1.15) \times 10^{-4}$	2.56×10^{-5}; 4.57×10^{-6}
$\sigma\left(\dot{\alpha}; \dot{\delta}\right)$	deg s^{-1}	$(7.88; 9.84) \times 10^{-11}$	$(3.13; 3.10) \times 10^{-12}$

from this work. By relating the mission parameters detailed in the second part of the table, it can be observed that the two considered mission scenarios are comparable. For instance, both missions have a duration of 1-month with the same tracking and estimation arcs length. They both have a comparable altitude, and both rely on a very similar minimum elevation angle for radio tracking purposes. Elements of difference are the eccentricity of the orbit, which is near-circular in the case of Genova et al. (2024) and more elliptical in this work, and the inclination. The orbit considered for the comparison in this work (K_1, from Table 3.1.5) has an inclination of $52 - 60$ deg, while the orbit considered by Genova et al. (2024) is near polar and reaches higher latitudes, as shown in Genova et al. (2024, Figure 1). Despite the differences, the orbits can still be considered comparable, because both are representative of a science orbit about Enceladus, and the differences in inclination and eccentricity are not such that the two missions are fundamentally different and answer to different mission objectives.

Comparing the formal errors for the solve-for parameters, Table 5.2.2 shows that the presence of one radio beacon on the surface of Enceladus leads to considerably better results for the orientation parameters (libration amplitude, pole right-ascension and declination), with a reduction of the formal error of about two orders of magnitude. With respect to the gravitational Love number, the improvement is marginal. However, the lander allows to estimate the radial displacement Love number, not provided by Genova et al. (2024). Finally, in terms of the static gravity field, the two missions lead to comparable values, given that the signal for the low degree static coefficients is produced by the deeper interior, to which the lander is not directly sensitive compared to the ice shell movements. Thus, given that most of the gravity signal from the deeper interior feeds into the low-noise Earth radio-tracking data of the orbiter, as mentioned already in Section 5.1, and given that the missions are comparable in terms of duration, tracking arc length, and altitude, the formal errors for the static gravity field coefficients are similar. In conclusion, a lander mission appears to be more suitable for obtaining tight constraints on the geophysical measurements, especially those related to the dynamic behaviour of the shell, i. e., radial displacement Love number and libration amplitude, and to the pole position, related to the obliquity (Section 2.1.8).

Table 5.2.2.: Comparison between the results for the orbiter mission by Genova et al. (2024) and the results produced in this work.

Estimated geophysical aram-eter	Unit	Orbiter + single lander (this work)	Orbiter + optical navigation camera (Genova et al., 2024)
$\sigma\left(C_{2,0}\right)$	–	8.93×10^{-9}	1.94×10^{-8}
$\sigma\left(C_{2,2}\right)$	–	6.53×10^{-9}	7.10×10^{-9}
$\sigma\left(C_{3,0}\right)$	–	1.38×10^{-8}	$2.35. \times 10^{-8}$
$\sigma\ (\Re(k_2); \Im(k_2))$	–	$(5.8; 5.0) \times 10^{-5}$	9×10^{-5}; 1.2×10^{-4}
$\sigma\left(W_{\mathrm{s}}\right)$	deg	3.0×10^{-6}	4.2×10^{-4}
$\sigma\left(h_2\right)$	–	6.52×10^{-4}	–
$\sigma\left(\alpha_0; \delta_0\right)$	deg	2.56×10^{-5}; 4.57×10^{-6}	1.2×10^{-3}; 1.1×10^{-4}
Mission parameter	Unit	Orbiter + single lander (this work)	Orbiter + optical navigation camera (Genova et al., 2024)
Mission length	days	28	30
Estimation arc length	days	1	1
Tracking arc length	hrs	8	8
Number of landers	–	1	0
Min. elevation angle	deg	15	10
Orbit eccentricity	–	0.06	Near-circular
Orbit inclination	deg	$52 - 60$	Near-polar
Orbit altitude	km	197	$100 - 150$
A priori constraint on empir-ical accelerations	$\mathrm{m\,s^{-2}}$	1×10^{-9}	1×10^{-10}

5.3. Single lander location analysis

Following the flow chart of Figure 3.0.1 (FC3.3), the work on the covariance analysis is concluded by the investigation of the effect of the location a single lander on the uncertainty for the geophysical parameters of interest (listed in Section 3.3.2). In the following sections, the results are presented based on the associated orbit solution (from Table 3.1.5). It should be noted that for the k_2 Love number, the following quantity is plotted in order to reduce the number of figures of merit and include the effect of both the real and imaginary parts:

$$\sqrt{\left(\sigma\left(\Re(k_2)\right)\right)^2 + \left(\sigma\left(\Im(k_2)\right)\right)^2}$$

5.3.1. Results associated to the K1 orbit

The distribution of the parameters of interest (provided in Section 3.3.2), based on the location of the radio beacon for the K_1 orbit, is provided in Figure 5.3.1 to Figure 5.3.6.

Comparing the dependency of the formal errors on the location of the lander, it is possible to observe that the lander coordinates have a variable impact on the science estimates. As it can be expected for the libration amplitude (Figure 5.3.1) and the gravitational Love number (Figure 5.3.2), the associated formal error is the highest when the lander is located at the poles, where it is less sensitive to the tidal response and the libration of the moon. This is a result observed also for the rotation pole RA (Figure 5.3.3).

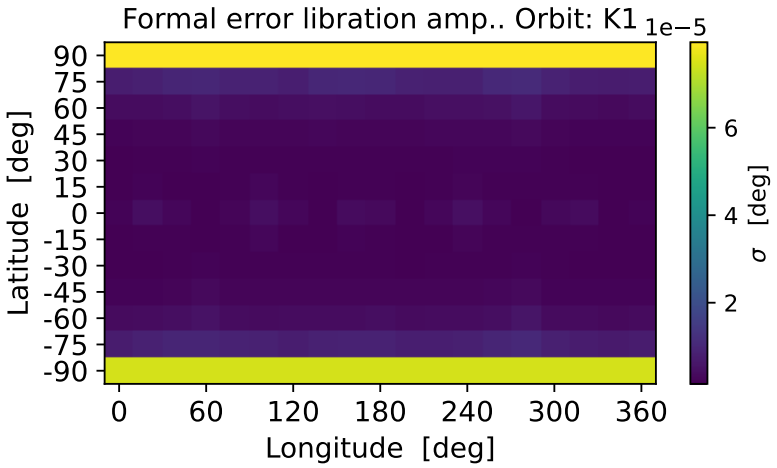

Figure 5.3.1.: Formal error for the libration amplitude as a function of the lander location. Orbit solution: K_1.

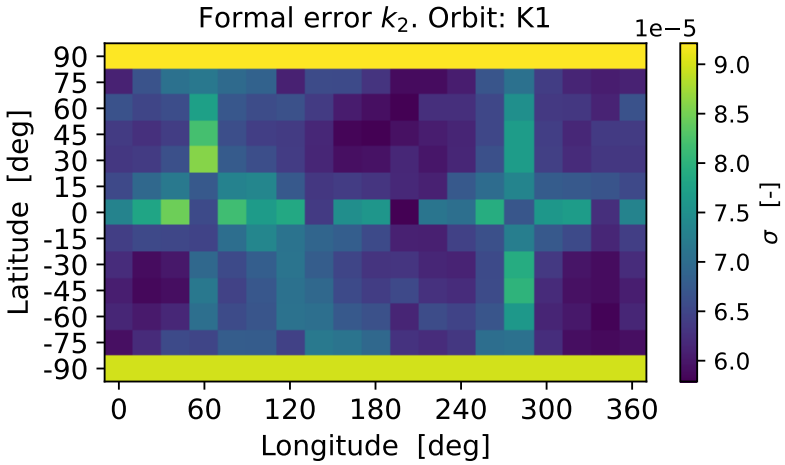

Figure 5.3.2.: Formal error for the k_2 Love number as a function of the lander location. The following quantity is plotted: $\sqrt{(\sigma(\Re(k_2)))^2 + (\sigma(\Im(k_2)))^2}$. Orbit solution: K_1.

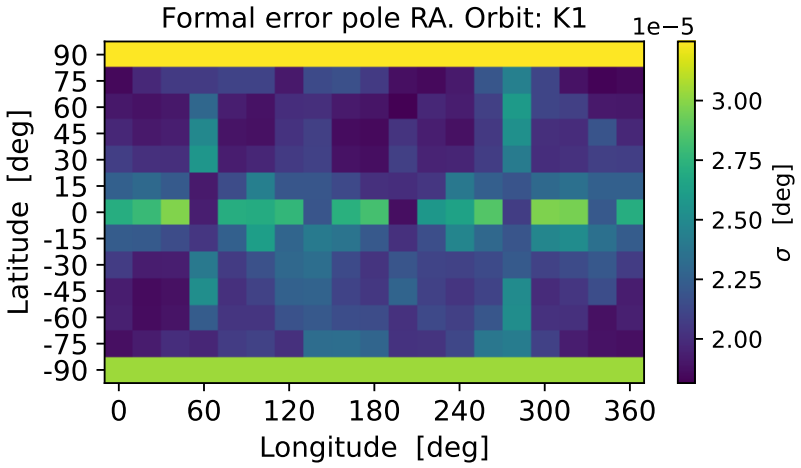

Figure 5.3.3.: Formal error for the rotation pole right ascension as a function of the lander location. Orbit solution: K_1.

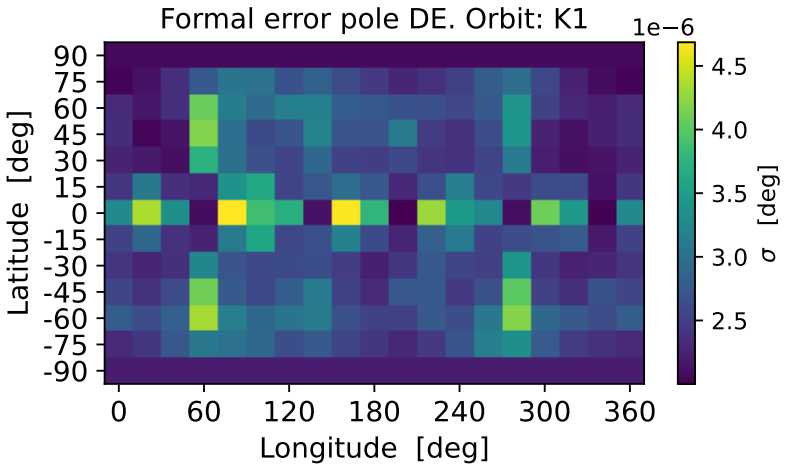

Figure 5.3.4.: Formal error for the rotation pole declination as a function of the lander location. Orbit solution: K_1.

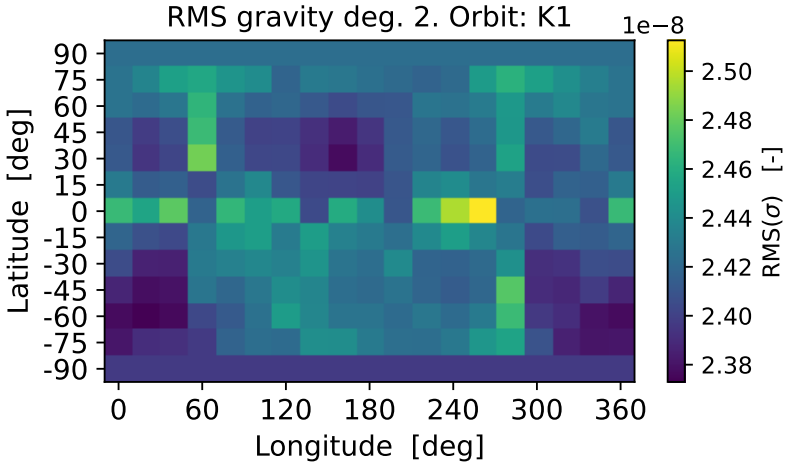

Figure 5.3.5.: RMS of the formal error for the degree 2 gravity coefficients as a function of the lander location. Orbit solution: K_1.

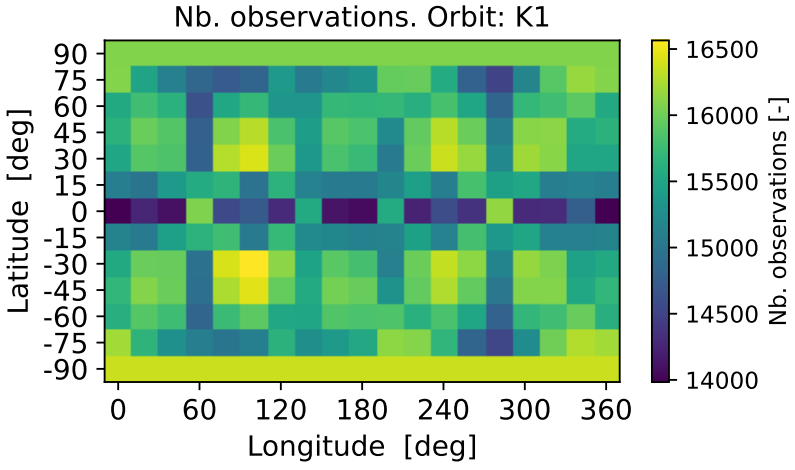

Figure 5.3.6.: Total number of observations as a function of the lander location. Orbit solution: K_1.

Furthermore, considering the formal error associated to the libration amplitude (Figure 5.3.1), it appears that there is no preferential location for the radio beacon away from the poles. On the other hand, the variability of the formal error for other parameters behaves differently. For example, for k_2 (Figure 5.3.2) the variability of the plotted quantity $\sqrt{(\sigma(\Re k_2))^2 + (\sigma(\Im k_2))^2}$ appears to be higher. Considering the number of observations reported in Figure 5.3.6, it is possible to infer that the variability pattern of the formal error for k_2 follows the pattern associated to the number of observations. Specifically, for those locations where less observations are available, like along the equator, the formal error on k_2 reasonably tends to be higher. This result suggests that in order to maximize the science return, study of the orbital and telecommunication geometry in relation to the location of the lander is necessary. The number of observations depends on the visibility of the S/C from the lander, both in terms of period of time in which the S/C is in the FOV of the radio beacon and in terms of the satisfaction of the condition of minimum elevation. However, it should be noted that such variability of the formal error is bounded to the range $\sim 6.0 \times 10^{-5} - 8.5 \times 10^{-5}$, and the effect is smaller in comparison to the improvement given by adding one radio beacon with respect to none, as shown in Figure 5.1.2, Figure 5.2.1, and highlighted in Table 5.2.1.

Considering the formal error for the rotation pole position, the poles appear to be a good location for estimating the declination (Figure 5.3.4), given that the lander position is directly sensitive to the inclination of Enceladus' rotation axis with respect to its orbital plane. Meanwhile, the right ascension (Figure 5.3.3) appears to better estimated at mid-latitudes, given that along the direction of right ascension, a variation in right ascension is expected to have larger effects on the position of the lander at mid-latitudes compared to the poles. This is due to the fact the obliquity of Enceladus with a global subsurface ocean is expected to be small, with an upper boundary of $3.96 - 3.98 \times 10^{-4}$ deg (Baland et al., 2016). Hence, with a small obliquity, Enceladus' spin axis is only slightly aligned from the orbital plane axis. Thus, the direction of right-ascension is closely aligned with the direction of spin, making the landers more sensitive to the RA at lower latitudes. This effect is then combined with the number of observations (Figure 5.3.6), lower at the equator and higher at mid-latitudes. It should be noted that for the RA, the results are also more sensitive to the spin, with a possible higher correlation with this parameter. Nonetheless, the results can still be considered representative for the fact that lower latitudes tend to be more favourable for the estimation of the RA.

The variability associated to the number of observations is visible for both the right ascension and declination, along the equator and the meridians with longitudes equal to 60 deg and 280 deg. Also for the pole position, the variability associated to the geographic distribution of the formal error is considerably smaller with respect to the improvement produced by the addition of one radio beacon to the mission architecture. If at mid-latitudes the error for the RA varies approximately in between $\sim 1.9 \times 10^{-5} - 3.0 \times 10^{-5}$ deg, and the error for the DE is bound to the range $\sim 2.0 \times 10^{-6} - 4.7 \times 10^{-5}$ deg, the analysis carried out in Section 3.3.2 shows that the variability ranges are within the variability of the configurations $1.Y.N$ in Figure 5.1.6, which is smaller than the reduction of about one order of magnitude provided by the addition of a radio beacon, as discussed in Section 5.1.

Moreover, for the gravity field, Figure 5.3.5 shows that the lander location has no major impact on the quality of the estimated gravity field coefficients of degree 2. Looking at the colorbar, it is possible to observe that the RMS varies in the range $\sim 2.38 \times 10^{-8} - 2.51 \times 10^{-8}$, whose amplitude is about 5% of the lower boundary value. Such a small variability might be due to the fact that the lander data are affected by a higher transponder noise, hence the lander and its location have a minor effect with respect to the contribution to the gravity signal given by the Earth tracking data, as discussed in Section 5.1. This phenomenon was observed also for the design space exploration in Figure 5.1.5, which showed that including one or more landers into the mission architecture does not improve significantly the accuracy of the estimated gravity field coefficients of degree 2.

Finally, with respect to the maximum estimatable degree of the gravity field, there is no variability with the lander location, hence it is not displayed in this section. In conclusion, given that also the estimated gravity field coefficients are negligibly affected by the location of the radio beacon, it can be inferred that the quality of the estimated gravity field coefficients is not a parameter to be considered for the selection of the location of the radio beacon.

5.3.2. Results associated to the K2 orbit

The analysis is performed also for the K_2 orbit. The relevant results are shown in Figure 5.3.7 to Figure 5.3.9. The additional plots not necessary for the discussion and thus not reported in this section can be found in Appendix H. In particular, the plot for the libration amplitude shows the same behaviour as in Figure 5.3.1 and the RMS of the formal error for the SH gravity coefficients of degree 2 does not add new information to the one already displayed in Section 5.3.1. Finally, the pole DE follows a similar pattern for the RA, and is provided in Appendix H.

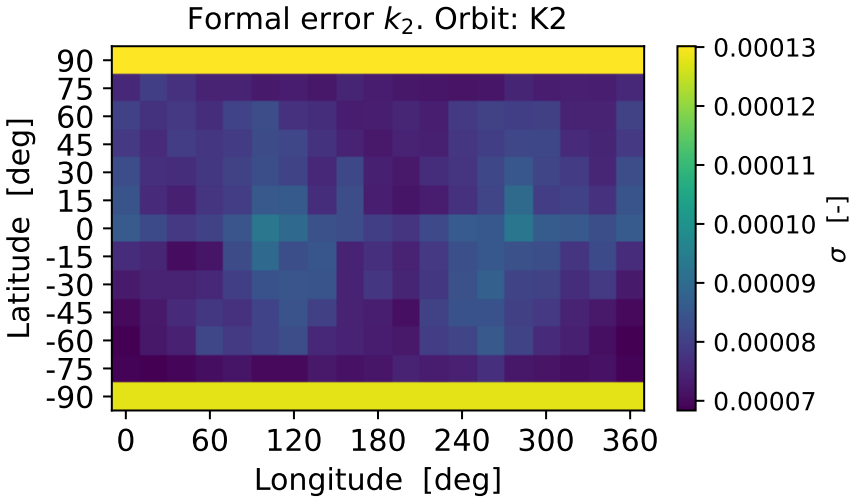

Figure 5.3.7.: Formal error for the k_2 Love number as a function of the lander location. The following quantity is plotted: $\sqrt{(\sigma(\Re(k_2)))^2 + (\sigma(\Im(k_2)))^2}$. Orbit solution: K_2.

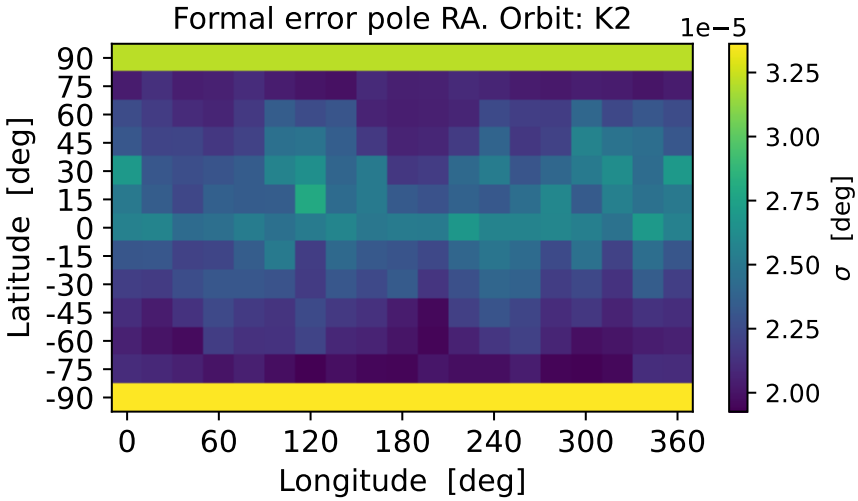

Figure 5.3.8.: Formal error for the rotation pole right ascension as a function of the lander location. Orbit solution: K_2.

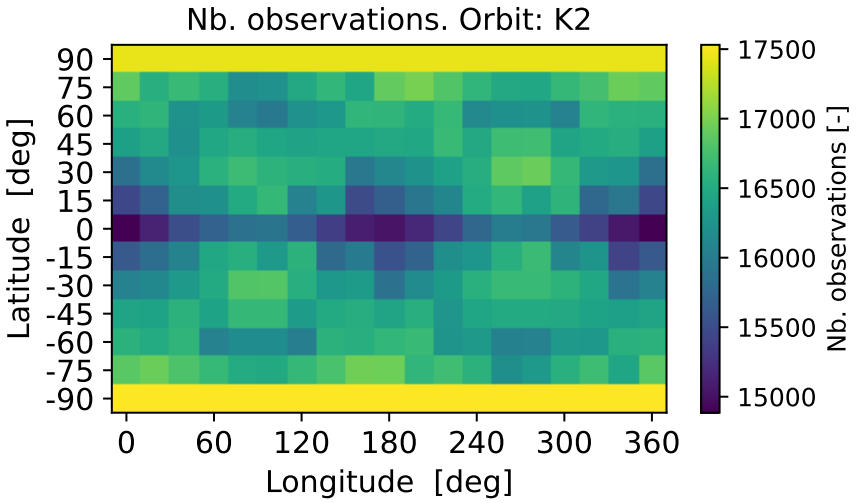

Figure 5.3.9.: Total number of observations as a function of the lander location. Orbit solution: K_2.

As for the other parameters, the results still show a dependency on the mission geometry, affecting the number of observations. In particular, it is possible to observe how the formal error associated to k_2 and to the constant pole position terms appears to be more homogenously spread with respect to the results for the K_1 orbit. A minor pattern at the equator is present, but no major inhomogeneous variability is present. This result agrees with Figure 5.3.9, which shows a stripe with a lower number of observations at the equator and a higher number at the poles, apart from which the number of observations seems homogeneous at mid-latitudes. Figure 5.3.6 shows a pattern with higher variability. Considering the orbit ground tracks displayed in Figure 3.1.1, it can be observed that the K_2 orbit solution covers more homogeneously Enceladus' surface with respect to K_1, leading to an improved distribution of the observations. As a result, at non-polar latitudes, the location of the lander has a minor impact on the science return, as Figure 5.3.7 to Figure H.1.2 show.

The level of formal uncertainty for the various estimation parameters is comparable for both the K_1 and K_2 cases, and the pattern related to the polar locations of the lander is still present.

5.3.3. Results associated to the K3 orbit

The results for the K_3 orbit solution are provided in Appendix H, since they confirm the considerations on the influence of the orbit ground track on the distribution of the results based on the location of the lander. There are no major discrepancies with respect to the plots produced for the K_2 orbit solution, except for a couple of outliers in both K_2 and K_3.

Given the discussion presented in Section 5.3.1 and Section 5.3.2, and given that the results for the K_3 orbit are in agreement with the previous ones, it can be concluded that if a radio beacon is included in the mission architecture, the design of the mission should focus first on the choice of the orbit, from which the distribution of the science parameters relies on. The choice of the orbit can then be followed by a more detailed analysis of the optimal location for the radio beacon, with an initial preliminary discretisation between polar mid and equatorial latitudes.

In order to investigate the higher number of observations when the lander is at mid-latitudes instead of the equator, the location of the S/C at the observation epochs is plotted. The investigation is carried out on the K_3 orbit, for which the distribution of the number of observation is plotted in Figure 5.3.10. The results are shown in Figure 5.3.11 for two landers at an equatorial and mid-latitude location. It can be observed that the higher the latitude, the denser the ground track. As a result, a lander located

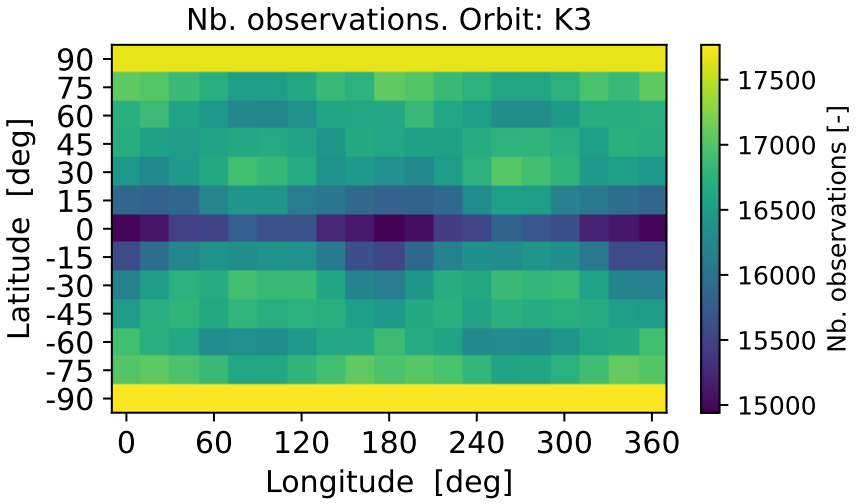

Figure 5.3.10.: Total number of observations as a function of the lander location. Orbit solution: K_3.

at mid-latitude can perform more observations with respect to an equatorial lander. In the proposed cases, the L_6 lander at a latitude of -60 deg generates about 900 more observations with respect to the equatorial L_3 lander.

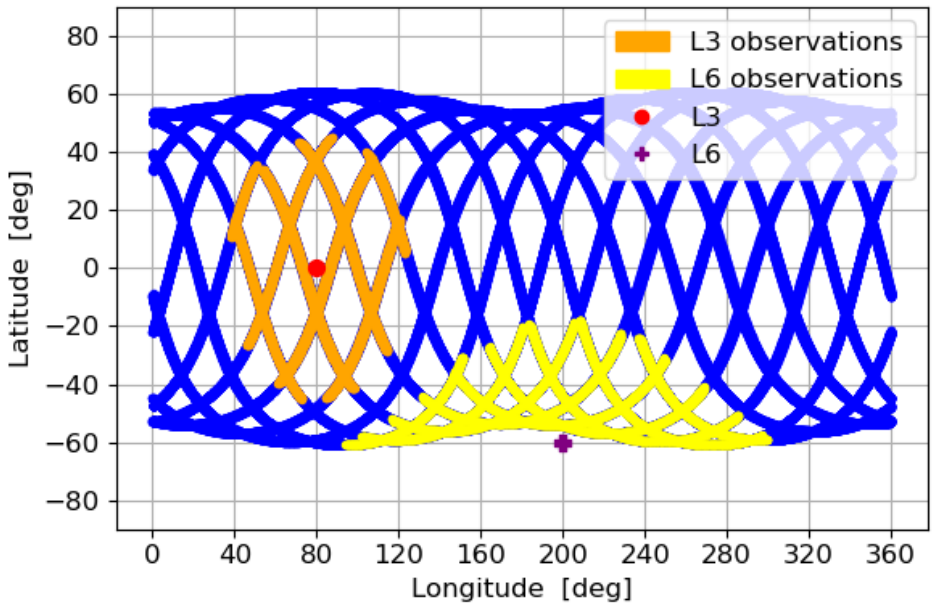

Figure 5.3.11.: Location of the S/C at the observation epochs of the L_3 and L_6 landers (coordinates available in Table 3.1.3). The landers are indicated with a red marker. The landers provide the following number of observations: 4808 for L_3 and 5705 for L_6. Orbit solution: K_3.

5.4. Preliminary one-at-a-time interior sensitivity analysis

As indicated in Figure 3.0.1, the covariance analysis (FC3) is followed by the analysis of the interior (FC4) with the final aim of answering the second research sub-question. The first step for the interior investigation is the one-at-a-time sensitivity analysis (FC4.1), whose output is the individual response of the observables to the interior parameters. The methodology followed in this step of the work is

laid out in Section 3.4.1. It is worth repeating here that the constraints on mass, MoI, and radius are not considered in this analysis, to avoid the degeneracy between the density and thickness of each layer that otherwise would arise and would make the interpretation of the one-at-a-time sensitivity more complex. Aware that the physical interactions between the parameters is lost, and that a body different from Enceladus is obtained when varying the density and thickness of the layers without applying the moon's physical constraints, a more rigorous approach is followed in the next section, as already mentioned in Section 3.4.1.

The dependence of the observables (reported in Table 3.4.2) on the single interior parameters (listed in Table 3.4.3) is shown in Figure 5.4.1 and Figure 5.4.2. It should be noted that the mechanical properties of the ocean are not considered in the analysis, as mentioned in the introduction of Section 3.4, since the ocean is assumed to be an incompressible and inviscid layer (Rovira-Navarro et al., 2024). With respect to the mechanical properties (i. e., shear modulus, viscosity, and bulk modulus) of both the core and ice shell, the Love numbers and shell libration amplitude do not show a particular sensitivity, except for the shear modulus of the ice shell, suggesting that it might be difficult to constrain the mechanical properties of Enceladus on the exclusive basis of the these observables.

Additionally, with respect to the radius and density of each layer, the results indicate that for the radius of the ocean and ice shell and the density of the ocean, there is a clear correlation with the real part of the Love numbers. A visible but less strong correlation with $\Re(k_2)$ and $\Re(h_2)$ characterises the radius and density of the core. These results suggest that the real part of the Love numbers might be helpful to constrain the interior of Enceladus.

On the other hand, with respect to the libration amplitude of the shell, Figure 5.4.2 shows a strong sensitivity to the radius (hence thickness) and density of each layer. The same applies to the shear modulus of the shell. The bulk modulus and viscosity appear to not be affected by the libration amplitude. It should be considered that varying the thickness of each layer leads to a body with a different diameter, since the physical constraints of Enceladus were not applied in this step. Hence, when applying the constraint of the total radius in Section 5.5 following a more rigorous approach, the correlation between the thickness of the layers and the libration amplitude might not be so strong. The same idea applies to the density and mass constraint. However, these results suggest that among the considered interior parameters, those that appear to be of greatest interest are the radius and density of each layer and the shear modulus of the ice shell.

As suggested by Rovira-Navarro et al. (2022) and Bagheri et al. (2025), to constrain the viscosity of the shell and core, the tidal dissipation, associated to the imaginary component of the k_2 Love number (see Section 2.1.6), is of most help. However, due to time limits, the analysis of the tidal dissipation is not included in this work, since more time was dedicated to the covariance analysis in the preceding sections.

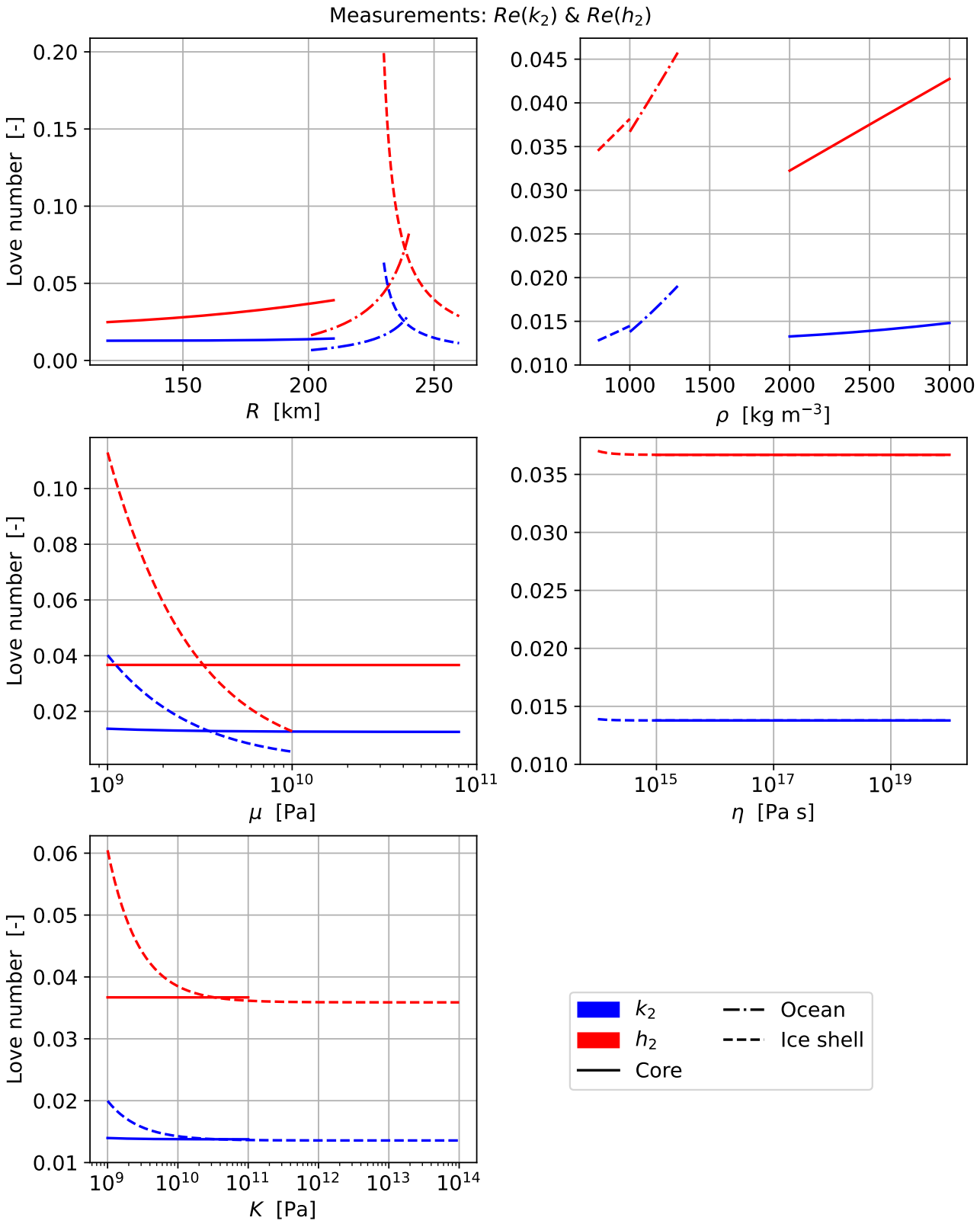

Figure 5.4.1.: One-at-a-time trends of the real component of the Love numbers with respect to the considered interior parameters of Enceladus (reported in Table 3.4.3).

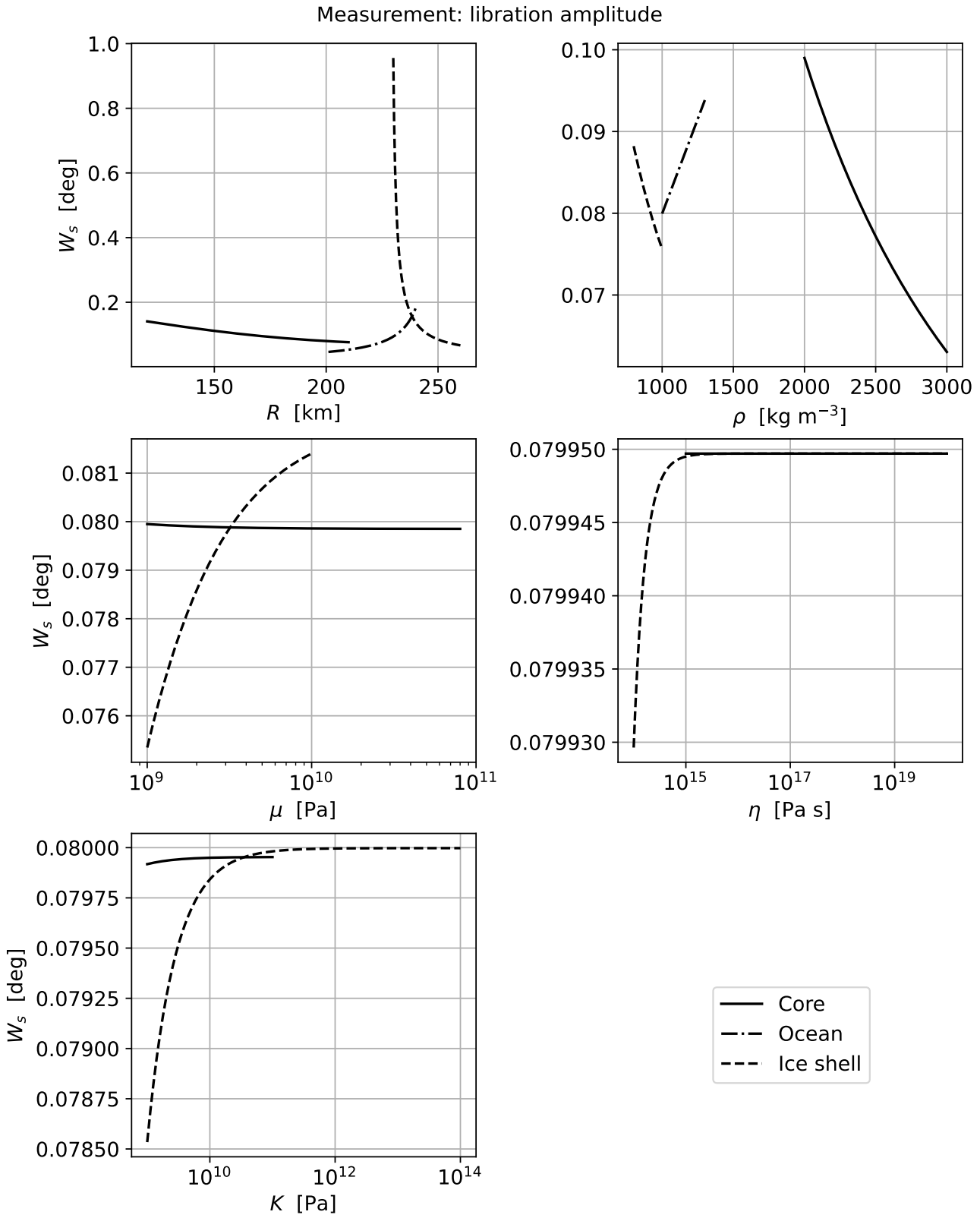

Figure 5.4.2.: One-at-a-time trends of the libration amplitude with respect to the considered interior parameters of Enceladus (reported in Table 3.4.3).

5.5. Preliminary full Monte Carlo analysis

The flow chart of Figure 3.0.1 shows that the preliminary one-at-a-time sensitivity analysis (FC4.1) is followed by a full MC analysis (FC4.2), whose results are displayed below. The methodology followed to produce the results is described in Section 3.4.2, which indicates the input parameters and relative range of interest in Table 3.4.4. The aim of this analysis is to study the full response of the observables to the interior properties, including the mutual interactions between the latter in producing the former. The physical constraints of mass, MoI, and radius of Enceladus are thus implemented. The associated values are reported in Table 3.4.5. As presented in Section 3.4.2 and summarised in Figure 3.4.1, the solutions of the preliminary full MC run are filtered for the density and ice shell thickness ranges provided in Table 3.4.6, and for the shell libration observations by Thomas et al. (2016) ($0.12 \pm 0.021\,\mathrm{deg}$).

Figure 5.5.1 to Figure 5.5.3 show the scatter plots for the h_2 Love number for each layer. The results for the k_2 Love number are not reported in this section due to the similarities with h_2; they can be viewed in Appendix I. Finally, Figure 5.5.4 to Figure 5.5.6 show the results for the libration amplitude.

From a general point of view, the results displayed in this section and in Appendix I confirm the trends observed in the one-at-a-time sensitivity analysis (Section 5.4). The panels associated to the mechanical properties in Figure 5.5.1 and Figure 5.5.3 show that there is no definite and clear trend between the observables and the mechanical properties of the core and ice shell, except for the shell shear modulus and bulk modulus. As already mentioned in Section 5.4, to constrain the viscosity of the core and shell, it appears necessary to include information on the tidal dissipation (Bagheri et al., 2025), related to the imaginary component of k_2 (discussed in Section 2.1.6).

With respect to the thickness and density of each layer, the real component of the Love numbers allows to find ranges in which the science parameters are most likely to lie, as shown in the first two panels of Figure 5.5.1 for the core, Figure 5.5.2 for the ocean, and Figure 5.5.3 for the shell. However, except for the shell thickness, there are no strong correlation trends, given that for a certain value of thickness or density, the samples span over a considerable range for the observables. This is most evident for the density of the three layers, as Figure 5.5.1 to Figure 5.5.3 show. With respect to the thickness of the layers, they appear to be more strongly correlated to the observables. For instance, Figure 5.5.2 shows that with increasing ocean thickness, $\Re(h_2)$ tends to span over a wider range of values, a trend that appears to be contrary to the thickness of the shell (Figure 5.5.3). This can be explained by considering that a thicker ocean, i. e., a thinner ice shell, leads to a higher response of the shell to the tidal forcing, in accordance with the results displayed by Bagheri et al. (2025, Figure 13). This trend is also visible for the libration amplitude, in Figure 5.5.5 and Figure 5.5.6. The core radius does not show a strong correlation to $\Re(h_2)$ (and $\Re(k_2)$), since the signal from the core contributes mostly to the static gravity and is not as involved in determining the dynamical response of the moon compared to the upper layers, as also discussed for the covariance analysis results in Section 3.3.2. It was found that the addition of a surface lander to the mission architecture greatly improves the results associated to the dynamical response of Enceladus, while it has a lesser impact on the static gravity coefficients, whose estimation relies more on the Earth radio tracking data, with lower noise and more sensitive to the stronger gravity signal of the deeper interior. Additionally, as the panels for the shear modulus in Figure 5.5.1 and Figure 5.5.3 suggest, the shear modulus of the shell is much more correlated to the tidal response of the moon compared to the core, suggesting that the deformation of the shell due to the forcing by Saturn is considerably more involved in producing the tidal response with respect to the core. This can be explained considering also that the shell is decoupled from the core due to the subsurface ocean, which allows the shell to respond to the forcing independently from the core (except for the gravitational coupling between the shell and core, which was not modelled (Rovira-Navarro et al., 2024)). Matsuyama et al. (2018) observed that for icy satellites with a subsurface ocean, the Love numbers at the bottom of the ocean are significantly smaller than those at the ocean top due to mechanical decoupling. Hence, the core plays a secondary role compared to the shell in producing the tidal response of the body.

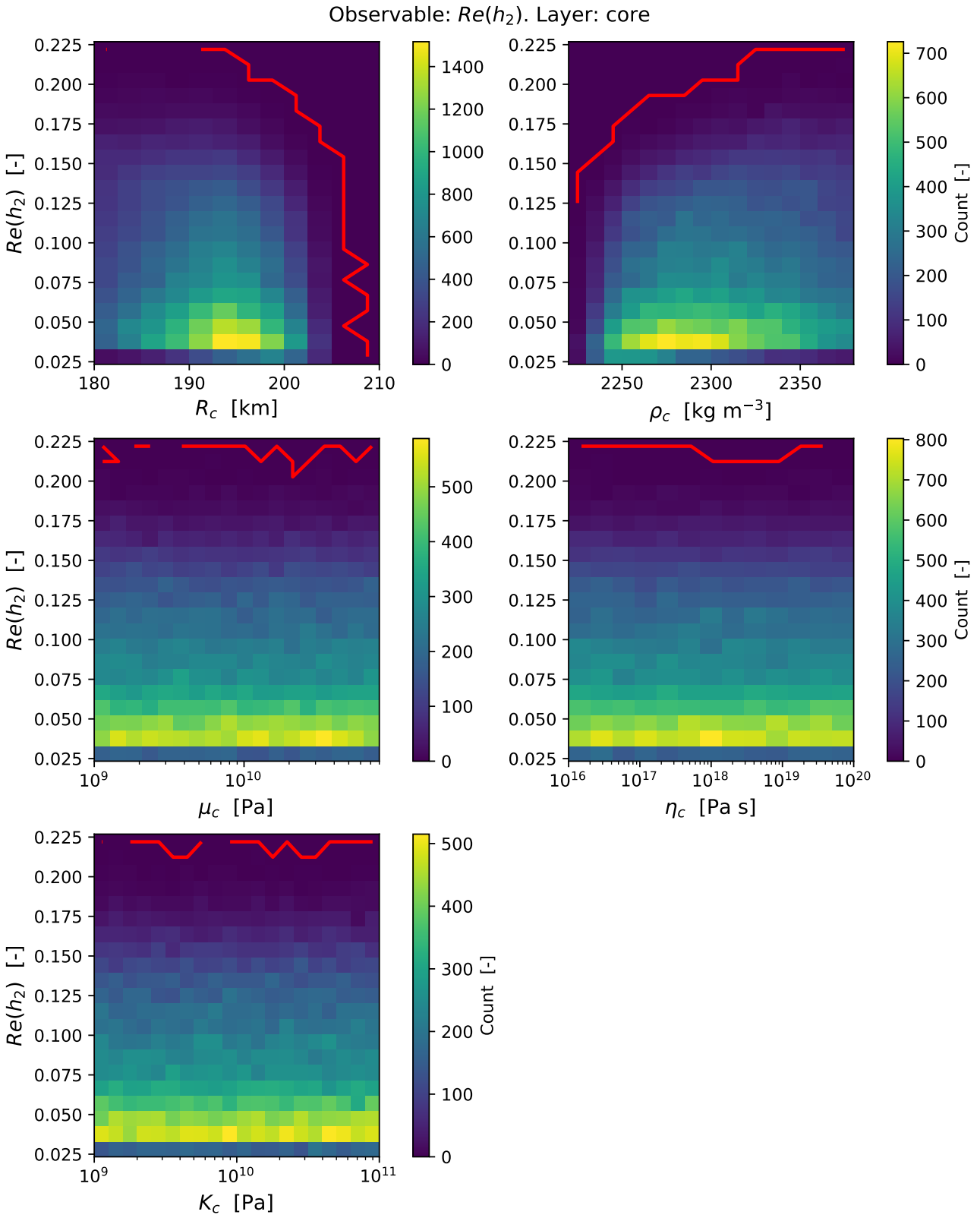

Figure 5.5.1.: Density plot of the preliminary full MC analysis, for the h_2 Love number and core parameters. The plotted samples are in agreement with the libration observations by Thomas et al. (2016) and with the density ranges reported in Table 3.4.6. The red lines are zero-level contours.

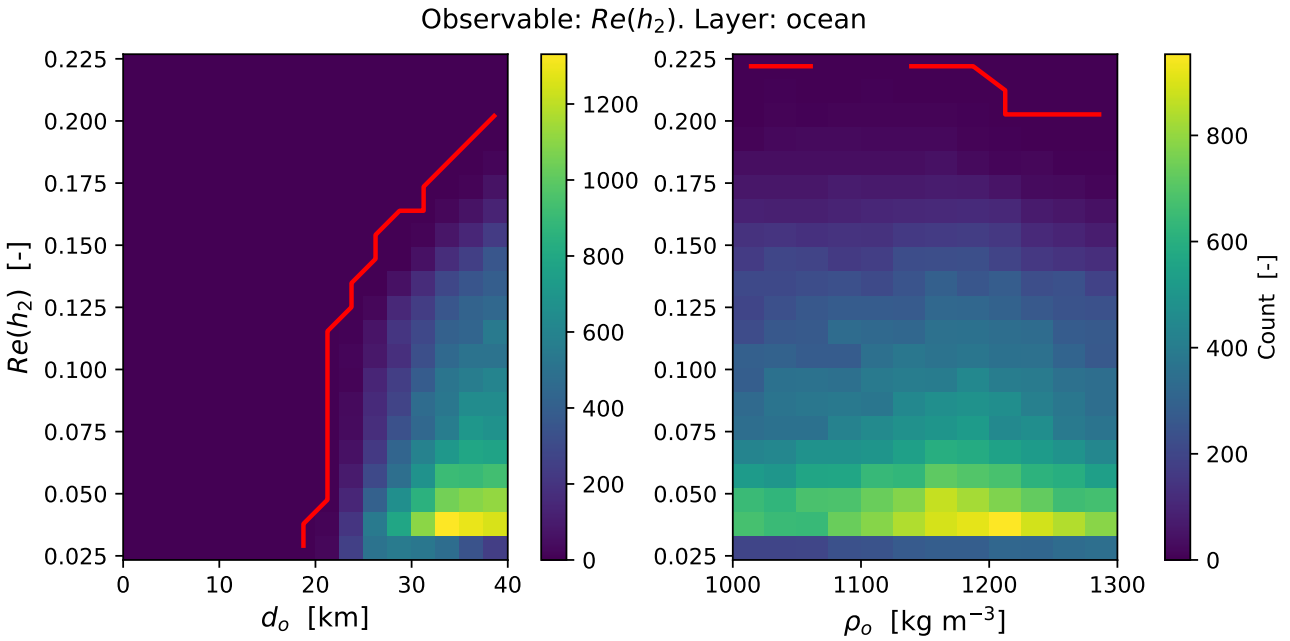

Figure 5.5.2.: Scatter plots of the preliminary full MC analysis, for the h_2 Love number and ocean parameters. The plotted samples are in agreement with the libration observations by Thomas et al. (2016) and with the ranges reported in Table 3.4.6. The red lines are zero-level contours.

With respect to the bulk modulus of the shell, as indicated in Section 3.4.2, it was computed according to Equation 3.4.1, given the logarithmically uniform samples for the Poisson ratio and the shear modulus. Figure 5.5.1 shows an area of higher probability between $1 \times 10^{10} - 1 \times 10^{11}$ Pa at lower values of $\Re(h_2)$. Also the one-at-a-time sensitivity analysis showed (in Figure 5.4.1) a stronger correlation between the shear modulus for the range $1 \times 10^{9} - 1 \times 10^{11}$ Pa and the Love numbers. Referring to the formulation of Equation 3.4.1, it can be observed that the shear modulus is proportional to the bulk modulus. Given that for a value of the Poisson ratio in the range $0.3 - 0.5$ as considered in this work (Table 3.4.4), the ratio μ/K lies in the range $[0, 0.46]$, and that literature provides preferential Poisson values close to the lower boundary of 0.3 (e. g., Gioia et al. (2007), Souček et al. (2016), Behounkova et al. (2017)), and since the shear modulus of the shell is bound in the region $1 - 5$ GPa, a high probability region for the bulk modulus is expected around $10^{9} - 10^{10}$ Pa, in accordance with the obtained results.

Let us consider now the libration amplitude of the shell (Figure 5.5.4 to Figure 5.5.6). The thickness of the ocean and particularly the shell show a correlation. Figure 5.5.5 and Figure 5.5.6 show that for increasing ocean thickness, i. e., decreasing shell thickness, the shell libration amplitude tends to increase. In Figure 5.5.5, the region of higher probability for a small libration amplitude appears to be centred at 30 km, while for increasing amplitude more samples are concentrated towards 40 km. For the shell thickness, the correlation appears to be even stronger. As discussed by e. g., Bagheri et al. (2025) and Hoolst et al. (2016), the libration amplitude of Enceladus' shell is strongly sensitive to its thickness. As also determined by Hoolst et al. (2016), the shell thickness is expected to be well constrained by the libration amplitude. Moreover, the panels for the ocean and shell density in Figure 5.5.5 and Figure 5.5.6 show a certain degree of correlation with the libration amplitude: the region of higher probability moves towards lower values of shell density for increasing libration amplitude, and there is an area with a larger number of samples around 1200 kg m^{-3}. With respect to the core properties, for a given value of libration amplitude, a wide range of thicknesses and densities is spanned. There are areas of higher probability, but it should be considered that these might be due to the constraints on mass, MoI, and radius, relating the higher probability areas of the density and thickness of the upper layers to those of the core. Given the decoupling of the shell and core, libration is not particularly

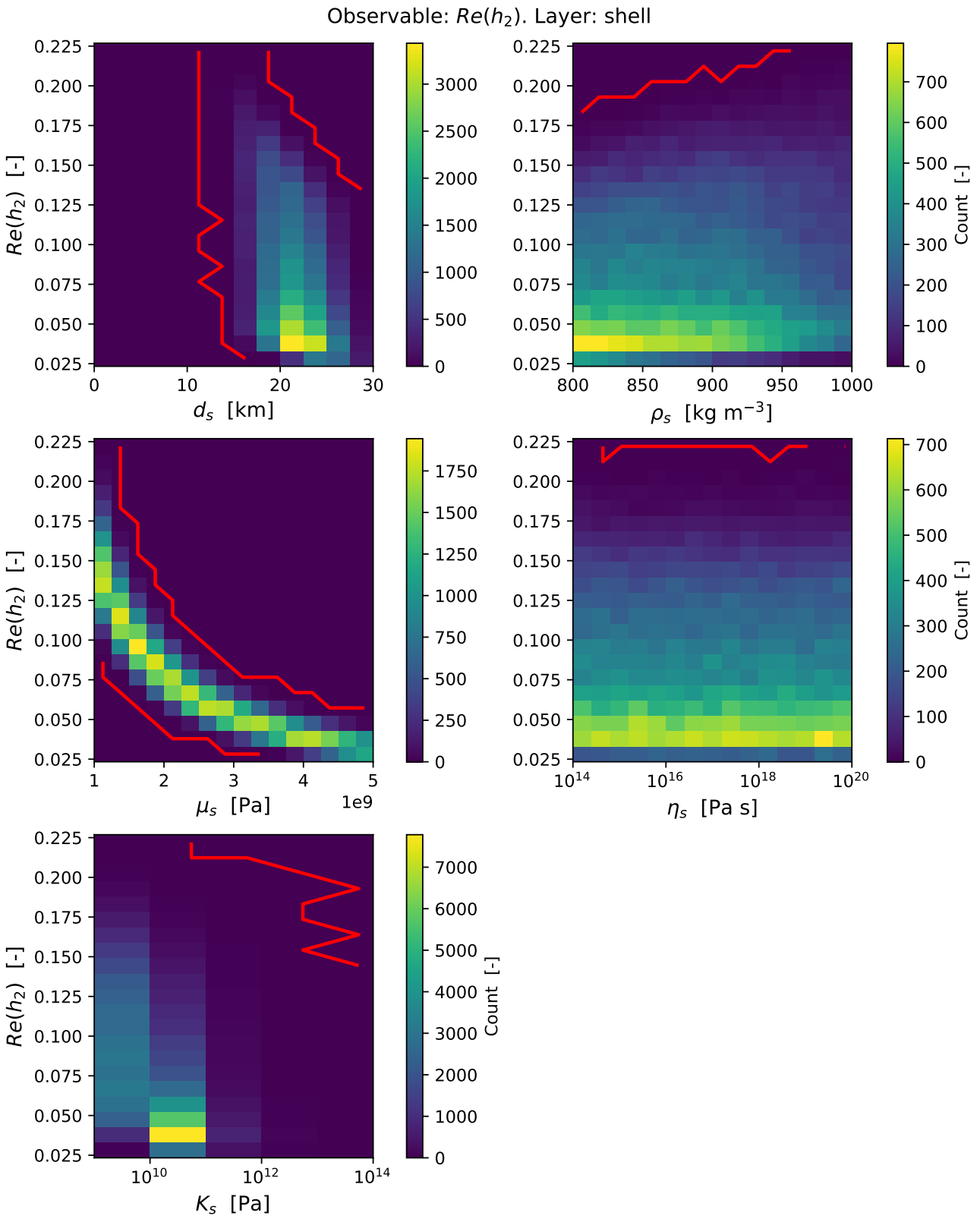

Figure 5.5.3.: Scatter plots of the preliminary full MC analysis, for the h_2 Love number and ice shell parameters. The plotted samples are in agreement with the libration observations by Thomas et al. (2016) and with the ranges reported in Table 3.4.6. The red lines are zero-level contours.

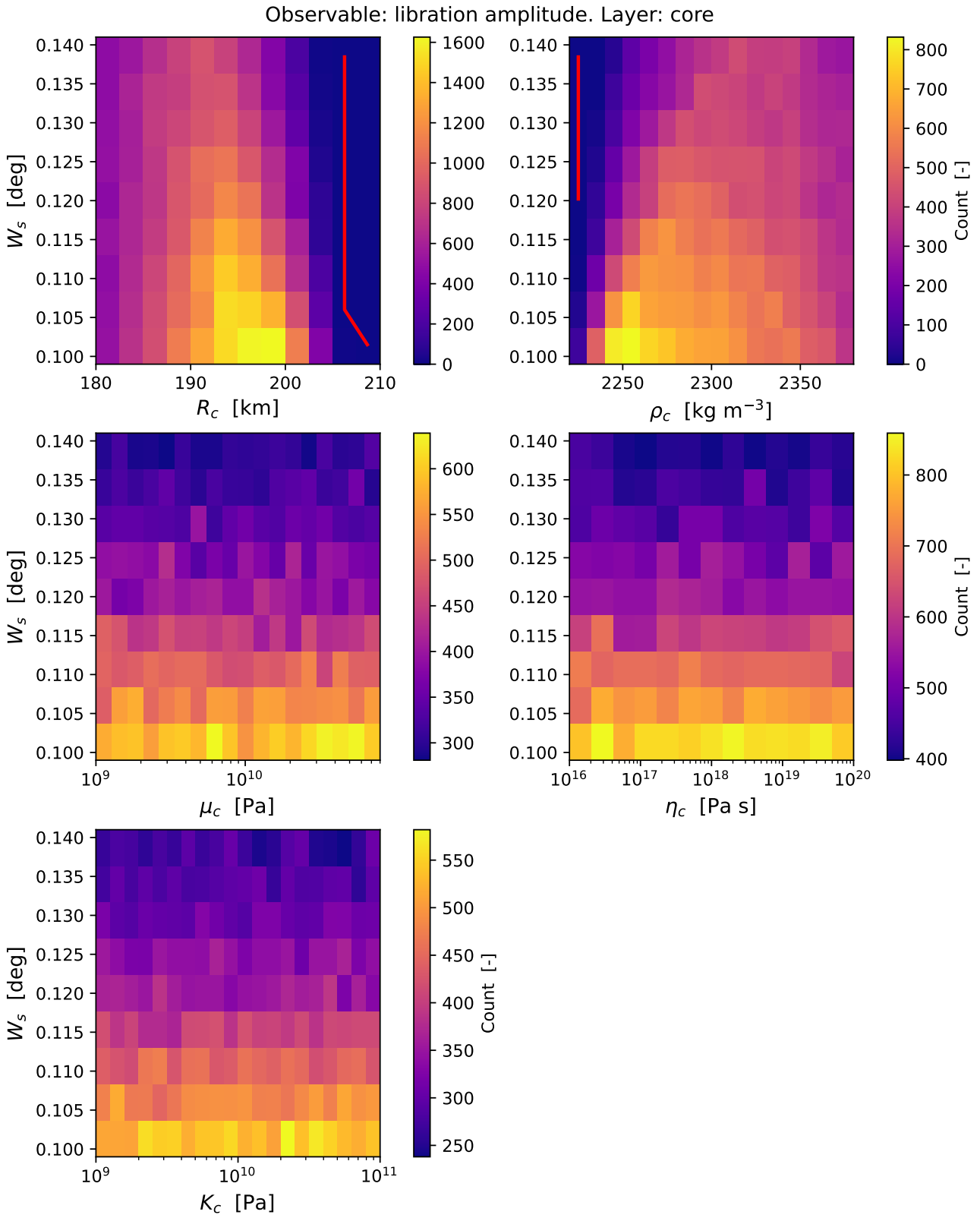

Figure 5.5.4.: Density plots of the preliminary full MC analysis, for the shell libration amplitude and core parameters. The plotted samples are in agreement with the libration observations by Thomas et al. (2016) and with the ranges reported in Table 3.4.6. The red lines are zero-level contours.

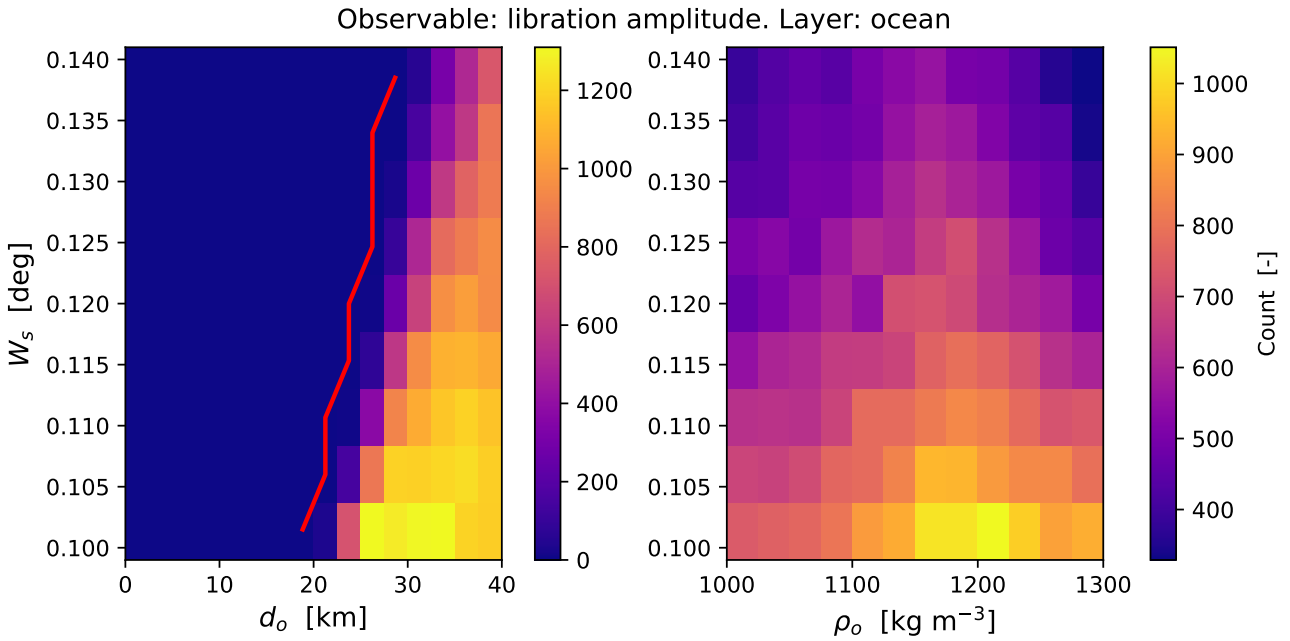

Figure 5.5.5.: Density plots of the preliminary full MC analysis, for the shell libration amplitude and ocean parameters. The plotted samples are in agreement with the libration observations by Thomas et al. (2016) and with the ranges reported in Table 3.4.6. The red lines are zero-level contours.

sensitive to the core parameters. This is due to the fact that the only effect from the core is through the gravitational perturbations caused by the core's tidal deformation on the shell (Bagheri et al., 2025), which typically is small and not implemented in this model (Rovira-Navarro et al., 2024).

Compared to the results of the full MC analysis, the one-at-a-time sensitivity analysis in Figure 5.4.1 and Figure 5.4.2 shows a stronger correlation for the density and thickness of the core and ocean, and for the density of the ice shell. As mentioned in Section 3.4.1, the constraints on mass, MoI, and radius were not applied, for avoiding the degeneracy between layer thickness and density. When the constraints are applied and the degeneracy between these parameters is introduced, the results have a less direct and clear pattern, due to the interaction between the interior properties in producing the observables.

The distribution of the interior parameters that satisfy the acceptable density and thickness ranges provided in Table 3.4.6 and the libration amplitude values by Thomas et al. (2016) (according to the methodology described in Section 3.4.2 and outlined in Figure 3.4.1) is showed in Figure 5.5.7 to Figure 5.5.9. For the core, the plots for the mechanical properties (in Figure 5.5.1 and Figure 5.5.4) do not add useful information and are thus not shown. For the other parameters, some tend to be centred around the expected values from literature. For instance, the ice shell thickness has a mean of about $\sim 21\,\text{km}$ and the distribution is in the range $\sim 15 - 30\,\text{km}$, in accordance with the range $15 - 40\,\text{km}$ determined by Bagheri et al. (2025). Additionally, for the core radius, Figure 5.5.7 shows a distribution centred around $\sim 192\,\text{km}$, in the range $180 - 205\,\text{km}$, in line with the *a posteriori* MCMC results provided by Bagheri et al. (2025, Table 6) using synthetic future measurements. Also the core density matches the results from Bagheri et al. (2025, Table 6).

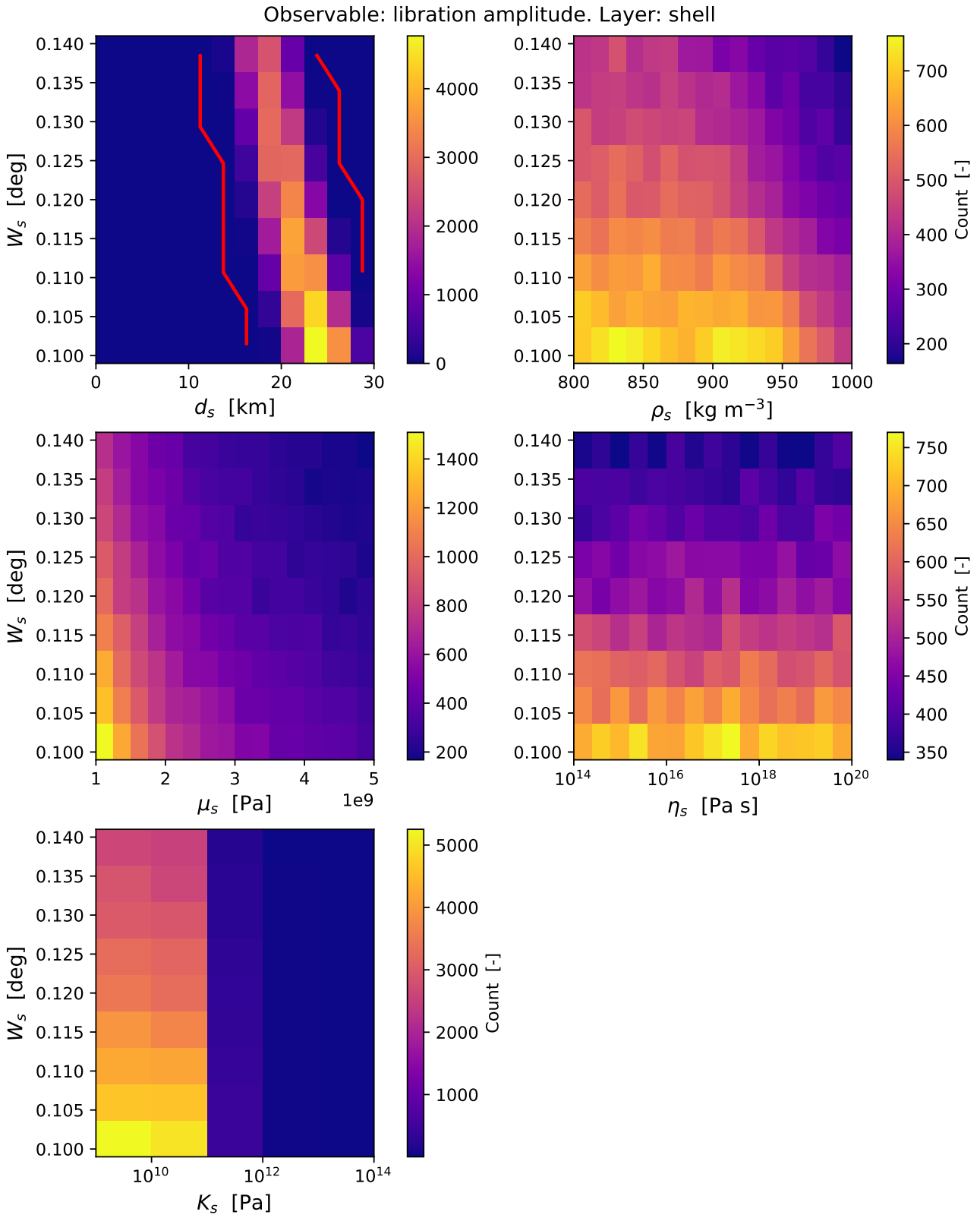

Figure 5.5.6.: Density plots of the preliminary full MC analysis, for the ice shell libration amplitude and shell parameters. The plotted samples are in agreement with the libration observations by Thomas et al. (2016) and with the ranges reported in Table 3.4.6. The red lines are zero-level contours.

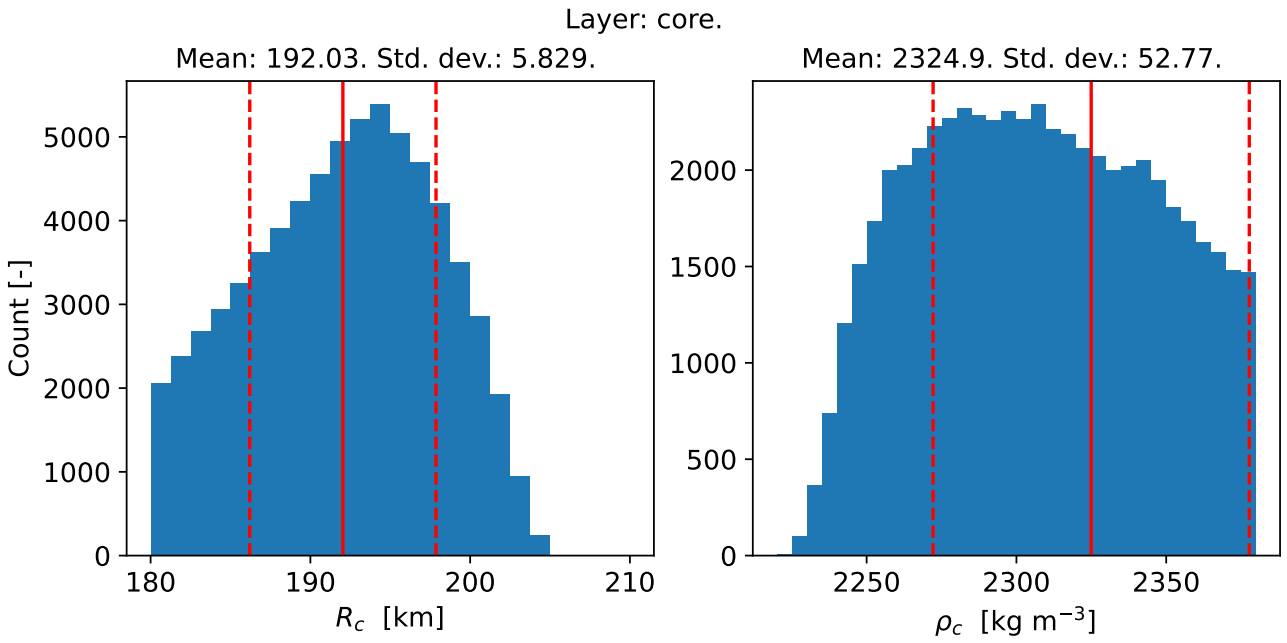

Figure 5.5.7.: Distribution of the core radius and density for the preliminary full MC analysis. The considered samples are in agreement with the libration observations by Thomas et al. (2016) and with the ranges reported in Table 3.4.6.

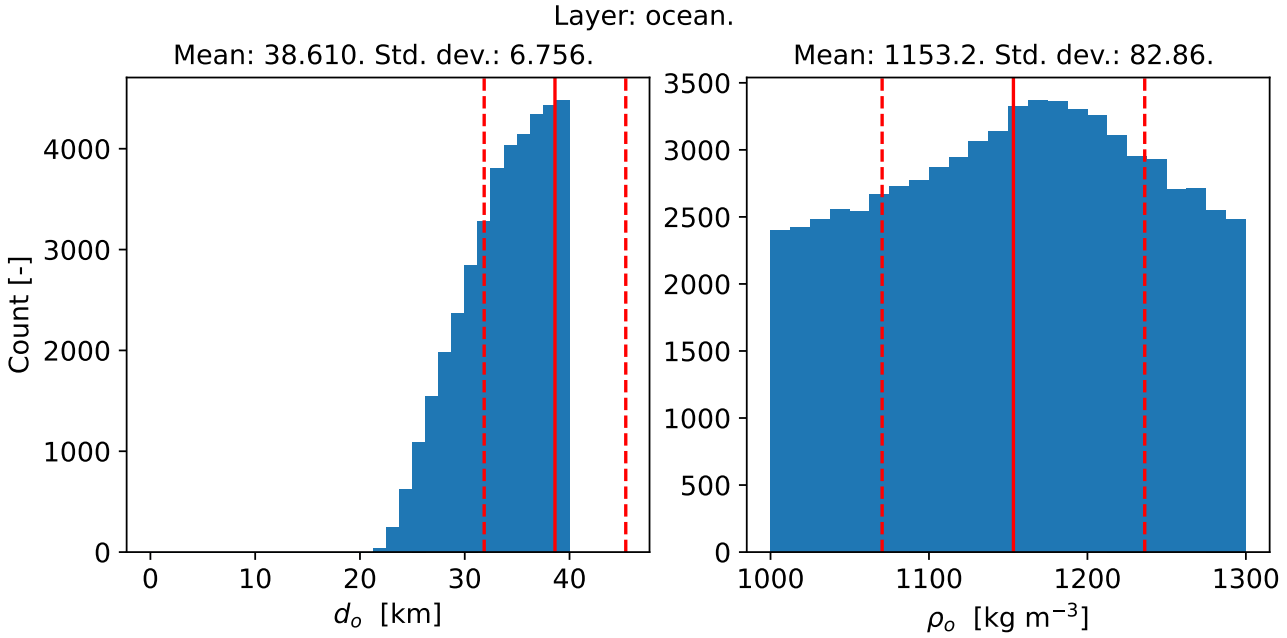

Figure 5.5.8.: Distribution of the ocean radius and density for the preliminary full MC analysis. The considered samples are in agreement with the libration observations by Thomas et al. (2016) and with the ranges reported in Table 3.4.6.

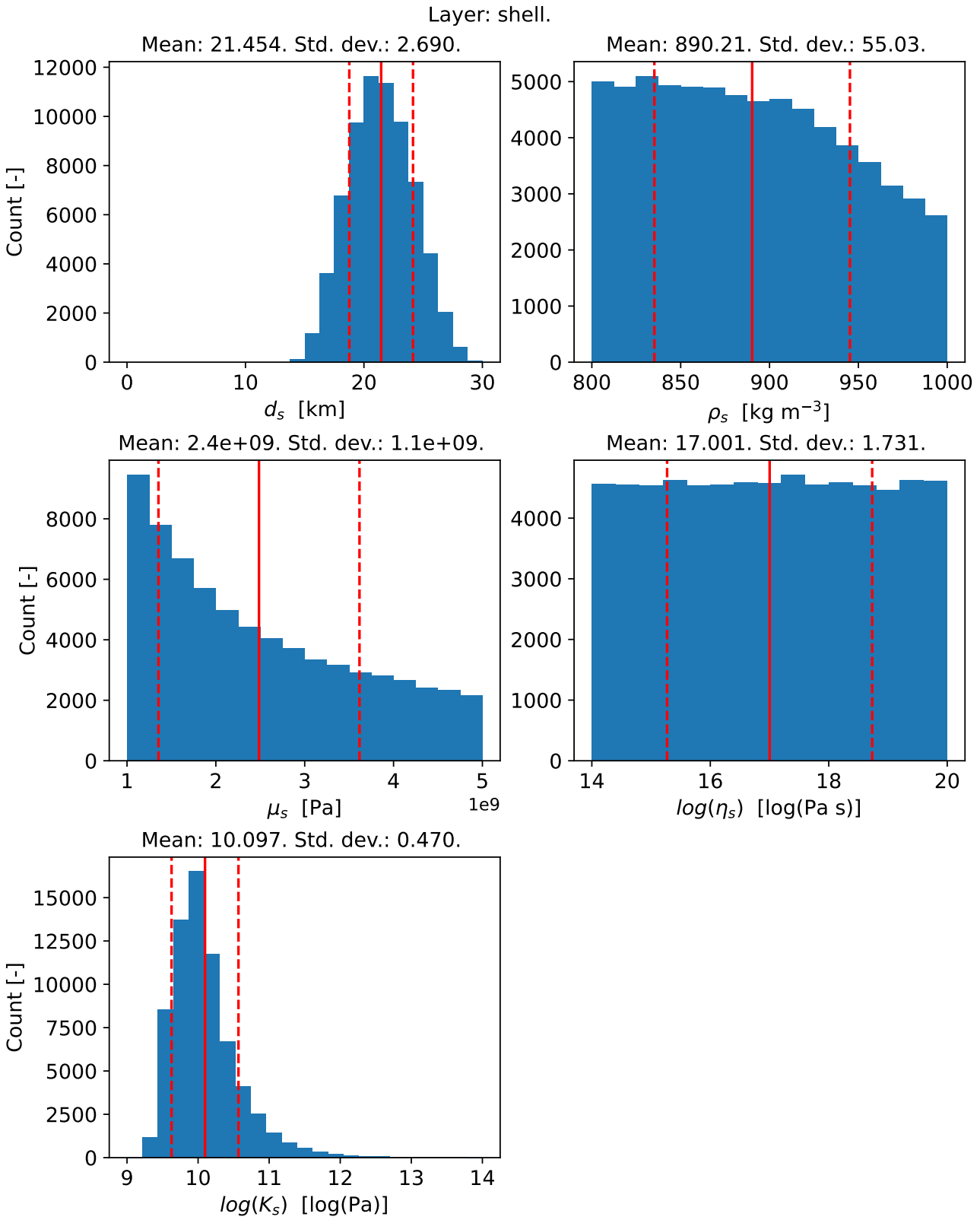

Figure 5.5.9.: Distribution of the shell parameters for the preliminary full MC analysis. The considered samples are in agreement with the libration observations by Thomas et al. (2016) and with the ranges reported in Table 3.4.6.

5.6. Constraining the interior with the available estimated uncertainties

The flow chart of Figure 3.0.1 shows that the work on the preliminary full MC analysis (FC4.2) is followed by two subsequent analysis steps (FC4.3 and FC4.4), aimed to translate the reference formal error values obtained in Section 5.2 for a few nominal scenarios, to uncertainties for those interior parameters that can be constrained with the considered observables. The goal of this section is to evaluate how the proposed mission scenario could enhance our understanding of Enceladus' interior. The considered reference formal errors for the observables listed in Table 3.4.2 are provided in Table 5.6.1. The values for the formal errors σ were taken so that they would be representative of the results computed in Section 5.2 for the three orbit scenarios (K_1, K_2, K_3, provided in Table 3.1.5) with only the L_3 lander (coordinates available in Table 3.1.3) included in the mission architecture, and an estimation arc length of 1 day. These scenarios are summarised in Figure 5.2.1 and detailed in Appendix G. It should be noted that for the libration amplitude, a value increased of three orders of magnitude is used: due to the filtering power of this constraint, too few interior models satisfied the tight range with $\sigma \approx 10^{-6}$ deg. Hence, a larger value was used to perform the analysis.

Table 5.6.1.: Considered constraints on the observables, used to filtered the physically feasible interior models, according to the methodology laid out in Section 3.4.3. For the formal errors of the Love numbers, the reference values displayed in Section 5.2 are representative of the nominal results for the three mission scenarios with an estimation arc length of 1 day and with only the L_3 lander included in the mission architecture. For the libration amplitude, a value increased of 3 orders of magnitude is considered, in order to have enough interior models in agreement with the constraint for performing the analysis.

Observable	Unit	Mean	Formal error (σ)
$\Re(h_2)$	–	7.9708×10^{-2}	7×10^{-4}
$\Re(k_2)$	–	3.1910×10^{-2}	6×10^{-5}
W_s	deg	1.1737×10^{-1}	1×10^{-3}

The first step taken to translate the formal errors of Table 5.6.1 into uncertainty values for the interior properties is the reduced full MC analysis (FC4.3 in Figure 3.0.1). As already described in Section 3.4.3, to generate enough samples in the ranges of interest, the $\pm 2\sigma$ interval of the distributions reported in Section 5.5 is considered for performing the second refined MC run. The models generated by this reduced MC analysis are filtered based on the core and ocean density, the ice shell thickness (see Table 3.4.6), and the libration amplitude provided by Thomas et al. (2016) (0.12 ± 0.021 deg).

As described in Section 3.4.3, in a first step, only the constraints on the real component of the Love numbers (provided in Table 5.6.1) are used to filter out the interior models. The $\pm 3\sigma$ interval around the mean value of the computed distribution of the physically feasible solutions is considered. When only the constraints on the real component of the Love numbers is applied according to Table 5.6.1, the distribution produced in Figure 5.6.1 to Figure 5.6.3 is computed. Only the parameters that in Section 5.5 were found to be sensitive to the observables are displayed.

The results discussed hereby on the effect of the $\Re(h_2)$ and $\Re(k_2)$ constraints are summarised for ease of understanding in Table 5.6.2. Figure 5.6.2 to Figure 5.6.3 show that with only the real components of the Love numbers and the uncertainties reported in Table 5.6.1, it is possible to constrain both the core and ocean density to an uncertainty of about $\sim 42\,\mathrm{kg\,m^{-3}}$, starting from a previous uncertainty of ~ 50 and $\sim 83\,\mathrm{kg\,m^{-3}}$ respectively. The reduction of the uncertainty for the ocean density of about 49% is in agreement with the results by Mitri et al. (2014), Jara-Orué and Vermeersen (2016), and Baland et al. (2014), who showed that the tidal Love numbers of Titan and Ganymede are strongly sensitive to the ocean density. Moreover, from Figure 5.6.3, it appears that the shell density cannot be constrained with just the real component of the tidal Love numbers, since the standard deviation

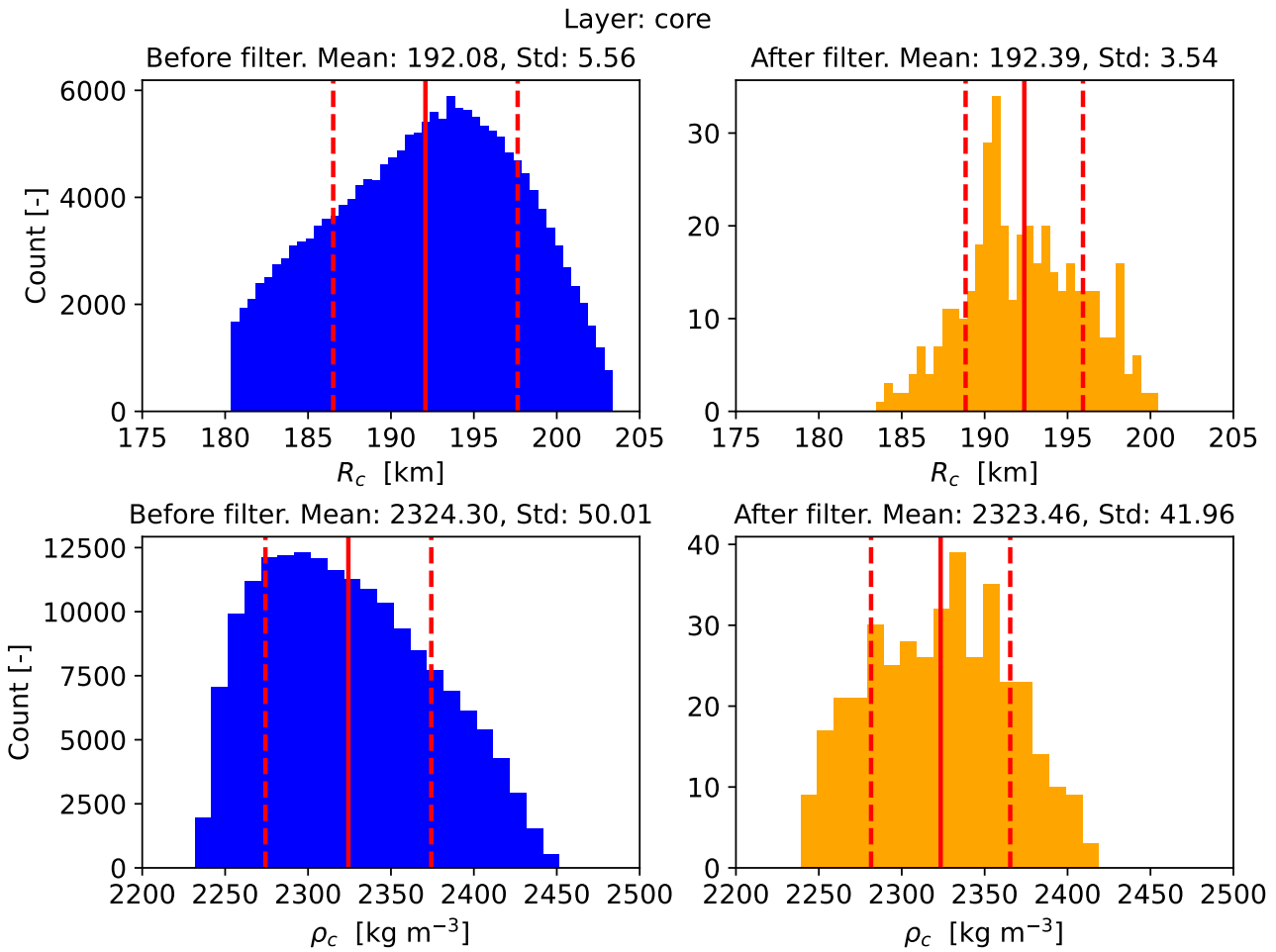

Figure 5.6.1.: Distribution of the relevant core parameters before (in blue) and after (in orange) filtering the interior models based on the constraints on $\Re(h_2)$ and $\Re(k_2)$, reported in Table 5.6.1.

changes of only 4.6%, as detailed in Table 5.6.2 . This result is in agreement with the studies by Jara-Orué and Vermeersen (2016) and Baland et al. (2016), who found that for Ganymede and Titan the dependence of the Love numbers on the density of the ice shell is weak.

Table 5.6.2.: Improvement of the uncertainty of the relevant interior parameters after filtering of the interior models based on the constraints on $\Re(h_2)$ and $\Re(k_2)$.

Parameter	Unit	Std. dev. before filtering	Std. dev. after filtering	Relative difference
R_c	km	5.56	3.54	−36.3%
ρ_c	kg m^{-3}	50.01	41.96	−16.1%
d_o	km	6.34	5.55	−12.5.0%
ρ_o	kg m^{-3}	82.74	42.18	−49.0%
d_s	km	2.633	2.634	+0.04%
ρ_s	kg m^{-3}	54.03	56.65	+4.6%
μ_s	Pa	1.13×10^9	2.68×10^8	−76.3%
$\log(K_\mathrm{s})$	log (Pa)	0.469	0.399	−14.9%

In terms of the layers' thickness, the improvement of the uncertainty is equal to about 36% for the core radius (Figure 5.6.1), 12% for the ocean thickness (Figure 5.6.2), while no improvement is made for the shell thickness (Figure 5.6.3). The shell thickness might not be affected by the constraints on $\Re(k_2)$ and $\Re(h_2)$ due to the fact that the dataset was already filtered with the libration observations by Thomas

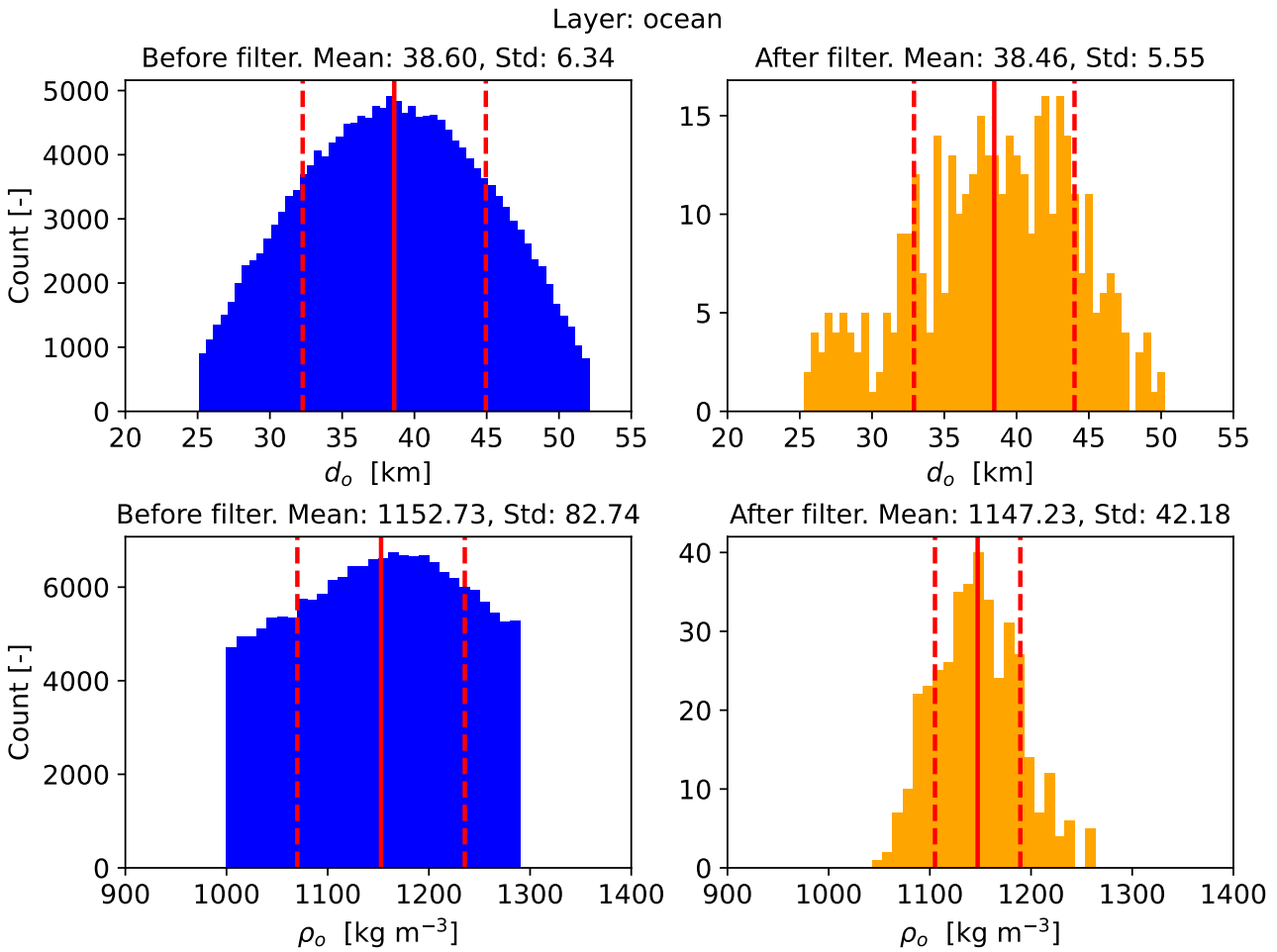

Figure 5.6.2.: Distribution of the relevant ocean parameters before (in blue) and after (in orange) filtering the interior models based on the constraints on $\Re(h_2)$ and $\Re(k_2)$, reported in Table 5.6.1.

et al. (2016) (see Section 3.4.3) and the resulting uncertainty of $\sim 2.63\,\mathrm{km}$ is already reasonably small. Thus, the shell thickness already varies in a small range, which thanks to the degeneracy with other parameters results feasible. Wahr et al. (2006) shows that the quantity $1 + k_2 - h_2$ is linearly dependent on the product between shell thickness and shear modulus. Additionally, Beuthe (2018) showed that for a thin ice shell floating on a subsurface ocean, the tidal response is controlled by the bending rigidity $D = 2\,(1 + \bar{\nu}_\mathrm{s})\,\mu_\mathrm{s} d_\mathrm{s}$. This implies that the variation of the shell thickness in a restricted feasible range can be absorbed by the variation of the shear modulus to a good extent and still satisfy the formal errors of the Love numbers, until the rigidity of the shell is too large or too small for the resulting Love numbers to satisfy the imposed constraint. Figure 5.6.4 shows that given a certain value for $\Re(h_2)$, the same value can be achieved at any shell thickness in the range by tuning the shell rigidity: for a thicker ice shell, the model retains the same radial displacement response with a lower rigidity. Hence, despite the trend observed in Figure 5.5.3, the shell thickness cannot be constrained further with only the Love numbers, and information on the formal error for the strongly correlated libration amplitude (see Figure 5.5.6) is needed.

If the shell thickness cannot be constrained further with only the tidal Love numbers, the shear modulus of the shell shows a reduction of about 1 order of magnitude of the associated uncertainty, from $\sim 1.1 \times 10^9\,\mathrm{Pa}$ to $\sim 2.7 \times 10^8\,\mathrm{Pa}$, an improvement of $\sim 76\%$ (refer to Figure 5.5.6 and Table 5.6.2). Also for the case of Ganymede, Jara-Orué and Vermeersen (2016) determined that the tidal Love numbers are strongly sensitive to the rigidity of the shell. Finally, the shell bulk modulus shows reduction of the uncertainty in logarithmic scale, with a preference around $10^{10}\,\mathrm{Pa}$, in agreement with the preliminary full MC results plotted in Figure 5.5.3 and Figure 5.5.6.

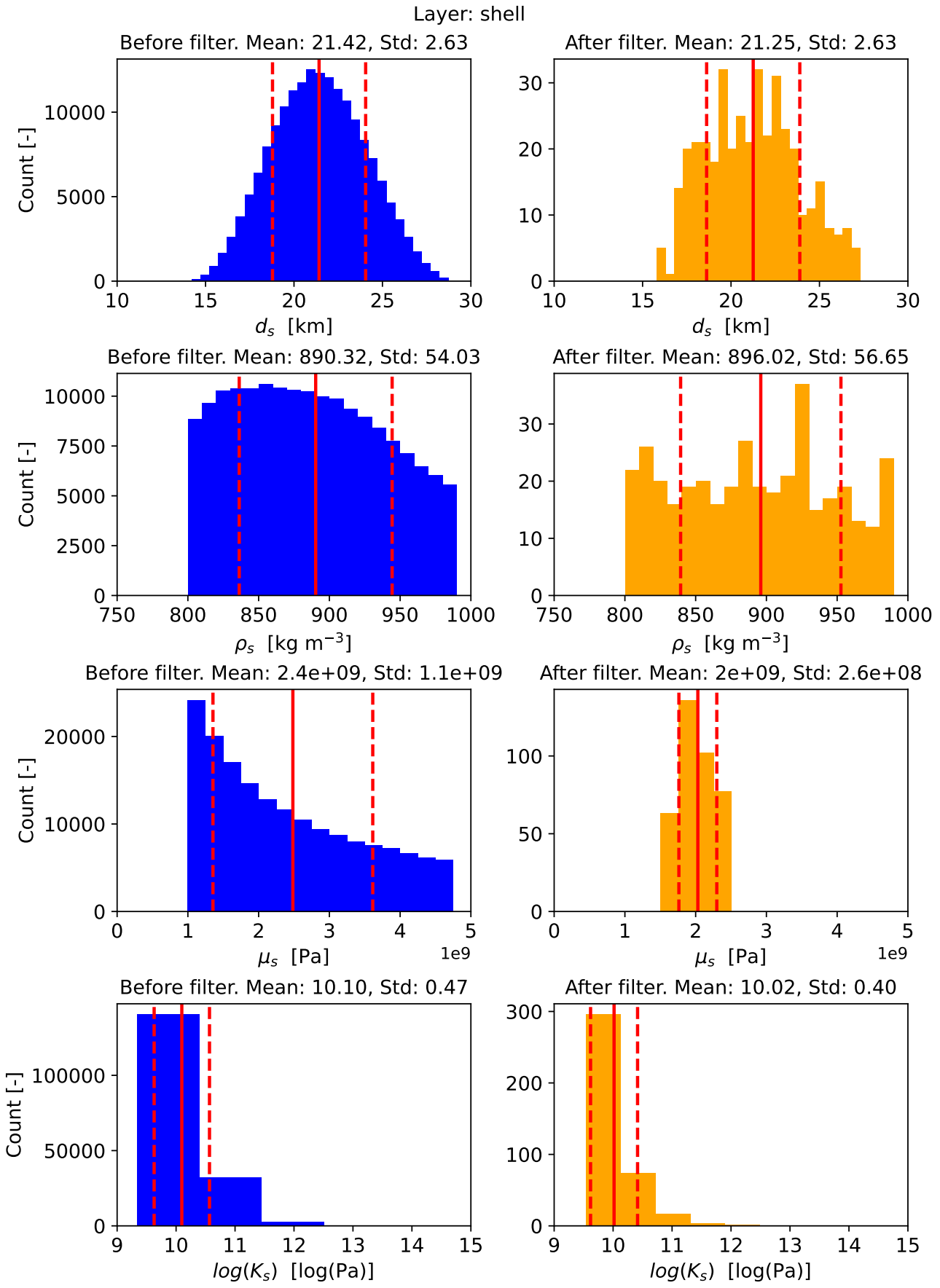

Figure 5.6.3.: Distribution of the relevant shell parameters before (in blue) and after (in orange) filtering the interior models based on the constraints on $\Re(h_2)$ and $\Re(k_2)$, reported in Table 5.6.1.

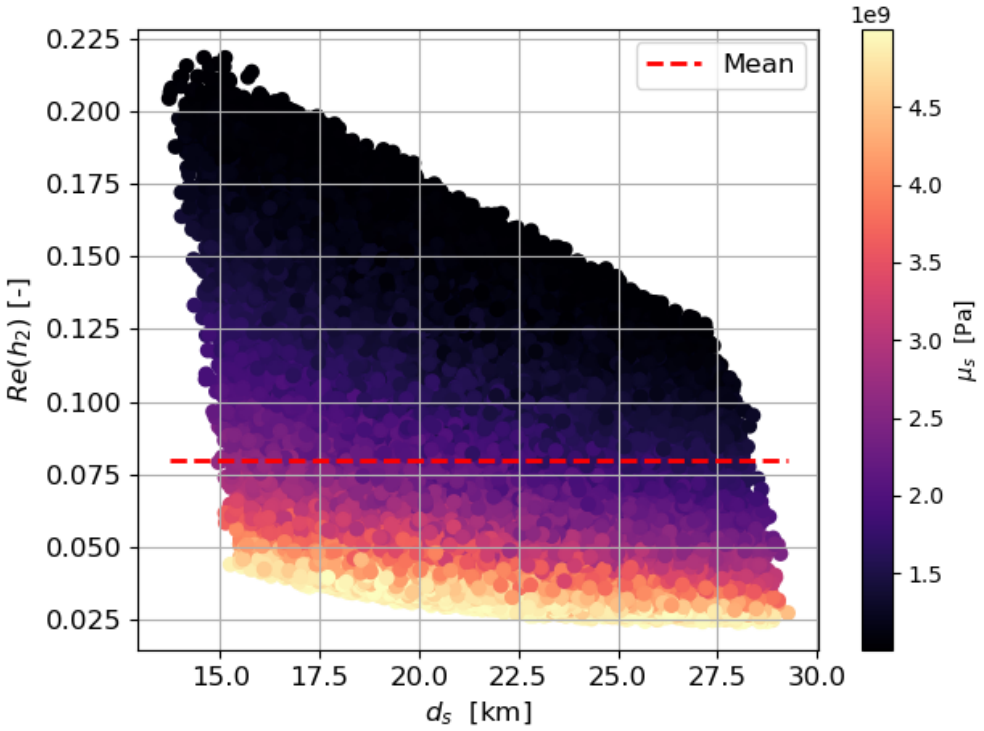

Figure 5.6.4.: Real component of the radial displacement Love number against the shell thickness and rigidity. The red dashed line indicates the mean value of the distribution. The plotted samples are produced with the second reduced MC analysis described in Section 3.4.3. All the samples satisfy the libration observation by Thomas et al. (2016) and the feasibility ranges in Table 3.4.6.

In a second step, the constraint on the libration amplitude is combined to the one on the Love numbers (refer to Table 5.6.1). Due to the need of preserving a sufficient number of solutions after filtering of the dataset, the uncertainty associated to the libration amplitude is increased of about three orders of magnitude to 1×10^{-3} deg. The results are summarised in Table 5.6.3.

Table 5.6.3.: Improvement of the uncertainty of the relevant interior parameters after filtering of the interior models based on the constraints on $\Re(h_2)$, $\Re(k_2)$, W_s.

Parameter	Unit	Std. dev. before filtering	Std. dev. after filtering	Relative difference
R_c	km	5.56	2.94	−47.1%
ρ_c	$\mathrm{kg\,m^{-3}}$	50.01	35.63	−28.8%
d_o	km	6.34	4.12	−35.0%
ρ_o	$\mathrm{kg\,m^{-3}}$	82.74	39.74	−52.0%
d_s	km	2.63	1.45	−44.9%
ρ_s	$\mathrm{kg\,m^{-3}}$	54.03	53.58	−0.8%
μ_s	Pa	1.13×10^9	1.44×10^8	−87.3%
$\log(K_\mathrm{s})$	log (Pa)	0.469	0.465	−0.8%

After applying the constraint on the libration amplitude in addition to the Love numbers according to Table 5.6.1, the number of available solutions decreases from the original 175,949, available after the filtering with feasibility ranges for the core and ocean density and shell thickness (Table 3.4.6) and for the libration observations by Thomas et al. (2016), to 42. If the original libration uncertainty of 1×10^{-6} deg was kept, less than 10 solutions would have been available. By comparing Table 5.6.2 and Table 5.6.3, it can be observed that the introduction of the constraint on the libration amplitude leads

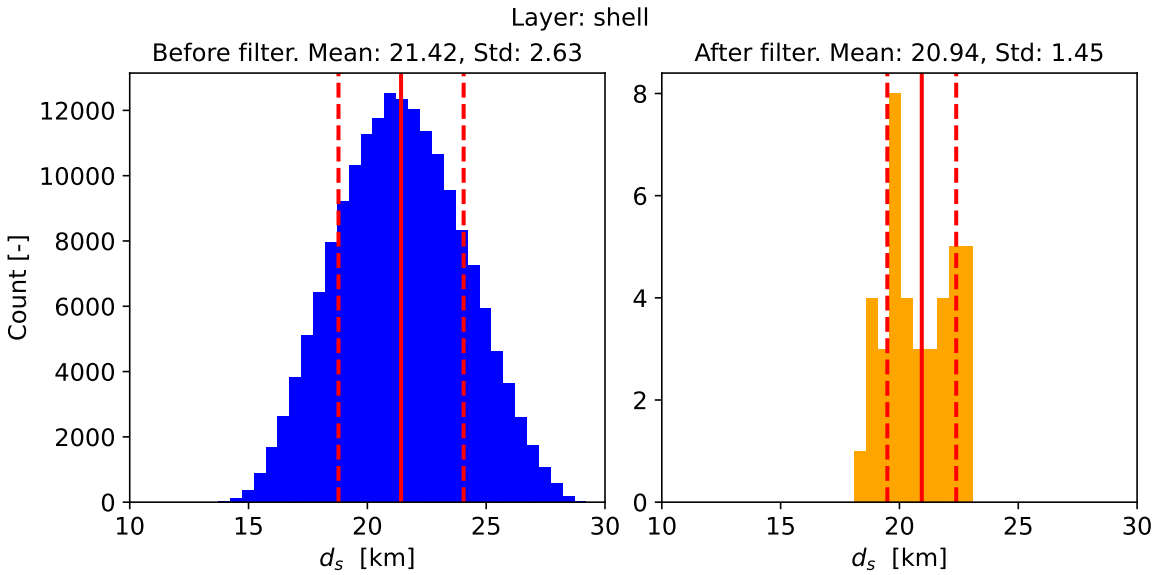

Figure 5.6.5.: Distribution of the relevant shell parameters before (in blue) and after (in orange) filtering the interior models based on the constraints on $\Re(h_2)$, $\Re(k_2)$, and W_s, reported in Table 5.6.1.

to a further decrease of the uncertainty associated to the layers thickness and density, compared to the case in which only $\Re(h_2)$ and $\Re(k_2)$ are used. For instance, the standard deviation improvement associated to the ocean thickness increases from 12.5% to 35%; for the core radius, the increase is from 36.5% to 47.1%, while the core density improvement is raised from 16.1% to 28.8%. The libration amplitude constraint leads also to a further decrease of the uncertainty associated to the shear modulus of the shell. However, the most significant contribution from the libration amplitude is on the constraint of the shell thickness. With respect to the case in which no constraints are applied, the standard deviation associated to the shell thickness decreases of about 45% (shown in Figure 5.6.5 and summarised in Table 5.6.3), while earlier no improvement was recorded. The resulting uncertainty is about $\sim 1.45\,\mathrm{km}$. This is in line with the results by Bagheri et al. (2025) and Hoolst et al. (2016), who determined that the shell thickness can be well constrained given the libration observations. On the contrary, the shell density still shows no further reduction of its uncertainty, and lies in the interval $800 - 990\,\mathrm{kg\,m^{-3}}$ in agreement with the results by Bagheri et al. (2025), who include information also on the phase lags of the Love numbers and on the tidal dissipation.

In conclusion, the following main results can be summarised:

1. The real component of the tidal gravitational and radial displacement Love numbers with their small uncertainties (Table 3.4.6) can provide an improvement of the uncertainty on the following parameters (☾ indicates those parameters that are best constrained):
   - Core radius
   - Core density
   - Ocean thickness
   - Ocean density (☾)
   - Shell shear modulus (☾)
   - Shell bulk modulus
2. The shell thickness appears to not be well constrained by only the tidal Love numbers, due to the degeneracy with the shear modulus. While the shear modulus can be well constrained, the resulting feasibility range of the shell thickness is such that variations of the shell thickness can be absorbed by the shear modulus, via the bending rigidity $2\,(1+\bar{\nu}_s)\,\mu_s d_s$.

3. The libration amplitude with the uncertainties estimated in Section 5.2 is a constraining observable for the interior models, especially for the shell thickness. Considering that the literature (e. g., X. Wu et al. (2001), Van Hoolst et al. (2009), Baland and Van Hoolst (2010), Van Hoolst et al. (2013), Thomas et al. (2016)) confirms that the libration amplitude is useful to constrain the ice shell thickness; considering that the results show that an uncertainty of 1×10^{-3} deg can lead to a standard deviation of 1.45 km, and considering that when adding the libration amplitude the number of viable models decreased from 393 to 42, by about an order 2, it is expected that a tight constraint on the libration amplitude such as the one computed in Section 5.2 will lead to a narrow uncertainty range for the shell thickness, beyond the $\sigma = 1.45$ km value obtained in this work.

5.7. Validation

The validation of the results of the covariance analysis algorithm is performed by comparing the a reference example from the representative scenarios discussed in Section 5.2 with the results obtained by Genova et al. (2024) for a comparable mission design.

As already mentioned in Section 5.2, Genova et al. (2024) investigated the interior of Enceladus through a New Frontiers-class mission composed of a S/C on a quasi-circular near-polar orbit, with altitudes between 100 km and 150 km, comparable to this work. Table 5.7.1 provides a comparison between the results produced by Genova et al. (2024) and those generated in Section 5.2 considering exclusively radio tracking data.

Table 5.7.1.: Comparison between the estimation results provided by Genova et al. (2024, Table 1) and the scenarios produced in Table 5.2.1 with no landers and 1-day long arcs. The characteristics of the mission architecture considered in this work and by Genova et al. (2024) were already detailed in Table 5.2.2, with the only difference that for the results presented here no lander was considered.

Parameter	Unit	Genova et al. (2024)	Scenario K_1	Scenario K_2	Scenario K_3
$\sigma(C_{2,0})$	–	1.95×10^{-8}	1.28×10^{-8}	1.05×10^{-8}	8.20×10^{-9}
$\sigma(C_{2,2})$	–	7.41×10^{-9}	1.17×10^{-8}	1.12×10^{-8}	9.11×10^{-9}
$\sigma(C_{3,0})$	–	2.39×10^{-8}	2.33×10^{-8}	2.02×10^{-8}	1.71×10^{-8}
$\sigma(\alpha_0)$	deg	2.4×10^{-3}	9.03×10^{-4}	1.22×10^{-3}	2.29×10^{-4}
$\sigma(\delta_0)$	deg	1.5×10^{-4}	1.15×10^{-4}	1.80×10^{-4}	3.37×10^{-5}
$\sigma(\Re(k_2))$	–	1.2×10^{-4}	1.94×10^{-4}	2.92×10^{-4}	2.50×10^{-4}
$\sigma(\Im(k_2))$	–	1.7×10^{-4}	1.27×10^{-4}	2.01×10^{-4}	1.74×10^{-4}

The table shows that the order of magnitude of the two sets of results is quite in agreement. The covariance analysis study can thus be considered validated.

6. Conclusions

This work aimed to show how an orbiter mission to Enceladus with surface landers could help constrain its interior structure, by means of estimating accurate geophysical measurements. A set of different scenarios were considered, in which the mission parameters and the a priori knowledge on science quantities were varied to show through covariance analysis to which level of estimated accuracy geophysical parameters of interest (e. g., SH gravity field coefficients, tidal Love numbers, libration amplitude, pole position and rate) can be measured. Nominal reference values were proposed out of all the explored cases. The work showed that in case one lander is included in the mission architecture, for a mission length of 28 days and 1-day long estimation arcs, the shell libration amplitude can be estimated with an accuracy of $\sim 3 \times 10^{-6}$ deg, while for the real component of the k_2 Love number the uncertainty is $\sim 6 \times 10^{-5}$. Moreover, the h_2 Love number can be estimated with an uncertainty of $\sim 7 \times 10^{-4}$ (see Section 5.2 and Appendix G).

By comparison with the optical measurements simulated by Genova et al. (2024) (see Table 5.2.2), these results show that a landers setup as the one considered in this work leads to an improvement of about two orders of magnitude for the accuracy of the libration, pole position, and pole rate measurements, and facilitates the determination of h_2. Moreover, the uncertainty associated to the imaginary part of the gravitational Love number shows a reduction of one order of magnitude.

Additionally, this work showed that the effect on the estimated uncertainty is significantly influenced by the number of landers included in the mission architecture. In particular, the higher the number of surface radio beacons, the smaller the amplitude of the variability introduced by other parameters, such as the length of the estimation arc, the mission duration, or the a priori knowledge on the gravity field. Furthermore, the impact on the formal errors of adding one lander to the orbiter mission with no radio beacons is larger than the impact of using nine landers compared to one. For instance, the uncertainty associated to the pole position is reduced of two orders of magnitude when one lander is added to the no-landers configuration. However, when using nine homogenously distributed radio beacons instead of one, the improvement is less than one order of magnitude (see the results displayed in Section 5.1 and Appendix G). Thus, the inclusion of only one lander in the mission architecture is considered optimal, given the increase of mission costs and spacecraft design complexity for carrying and deploying nine landers instead of one. Thus, a one-month long orbiter mission with one lander on the surface of Enceladus is expected to improve significantly our knowledge of the gravity field, tidal response, libration, and obliquity.

The effect of the location of a single surface lander on the estimated uncertainty for geophysical parameters of interest was assessed, considering three different stable orbits with repeating ground track, retrieved from Auer Wilkins et al. (2025). The results (see Section 5.3) show that both the orbit and the location of the radio beacon have an important effect on the number of lander observations, which in turn determines the quality of the estimation. This work showed that an orbit with a ground track homogeneously spread on the surface of the moon leads to a reduced geographic variability of the formal errors. Additionally, in terms of the location of the lander, it appears that the mid-latitudes are the most favourable with an orbit of inclination ~ 50 deg.

In terms of the study of Enceladus' interior, this work considered the real component of the h_2 and k_2 Love numbers, and the shell libration amplitude. A Monte Carlo analysis was performed in order to study the response of the observables to the structural and mechanical interior properties of Enceladus. The results produced by the Monte Carlo analysis were used to map the formal errors estimated in the covariance analysis work to uncertainty values for the interior parameters, assessing how the proposed mission could help constrain Enceladus' interior. It was shown that the mechanical properties

of the interior (shear modulus, viscosity, bulk modulus) cannot be constrained with the considered observables, except for the shear modulus of the shell, which appeared to be strongly correlated to the real component of the Love numbers. Furthermore, the uncertainty associated to the density of the three layers, the core radius, and the ocean thickness showed that it can be improved of $\sim 12 - 76\%$ with only the real component of the Love numbers. In addition, in accordance with e. g., Baland and Van Hoolst (2010), Hoolst et al. (2016), Bagheri et al. (2025), when the libration amplitude is included among the observables, also the shell thickness can be well constrained, with an improvement of the associated standard deviation of $\approx 45\%$. The libration amplitude appeared to be a highly constraining parameter on the solutions of the Monte Carlo analysis, suggesting that accurate measurements as those simulated in this work might lead to tight constraints on the layers thickness and density, especially the shell thickness. As for the shell density, it appears that with the selected observations it is not possible for it to be constrained further. The addition of information on tidal dissipation might allow to put a constraint on the shell density, given the work by Bagheri et al. (2025). The inclusion of the imaginary component of the Love numbers would also allow to constrain the viscosity of the layers.

As recommended by Bagheri et al. (2025), tight constraints by a future mission on the static gravity field, libration, tidal Love numbers, and tidal dissipation are needed to investigate further the interior of Enceladus, with an accent on the thermal state of the body. This work showed that an orbiter and lander mission to Enceladus is able to provide tight constraints on the tidal Love numbers, libration, and pole position, better than those that can be achieved with an on-board imager (Genova et al., 2024).

7. Recommendations for future work

In terms of the covariance analysis, future work could focus on the distinction of the core's libration from the shell's libration. In Section 3.3.2 it was mentioned that when no landers are included in the mission architecture, the formal error for the libration is affected by a component for the libration of the core and the one of the shell. When the landers are included in the mission, the signal is expected to be mostly referred to the libration of the shell, given the direct sensitivity of the surface radio beacons to movements of the ice layer. A future work could investigate the distinction between the libration of the core and shell, especially when at least one lander is part of the mission architecture. The core libration is expected to be estimated mostly through the gravitational influence of the core on the S/C orbit.

Moreover, in case topography measurements are included through a simulated altimeter, it is possible to infer an independent constraint on the MoI, through the admittance computed with the topography and gravity measurements, as described in Section 2.1.5. It is then possible to include the MoI among the observables (Genova et al., 2024).

In addition, as it was observed in Section 3.3.1, the state of Enceladus and Saturn was not included among the parameters to estimated, since refinement of the ephemerides was out of the scope. However, in a future work, inclusion of the state of the two bodies might allow to assess the impact of the knowledge of the ephemerides on the geophysical measurements. In this case, the spin of Enceladus ought to be included among the solve-for parameters, given that its rotation model is tied to the considered ephemerides, as observed in Section 3.2.2 in reference to the work by Park et al. (2024).

Also the impact of the lander location on the radial displacement Love number could be assessed. It was not included in this work for time management reasons, as mentioned in Section 3.3.4

In terms of the study of Enceladus' interior model, as presented in Section 3.4, this work focused on a two-steps MC analysis. Nowadays, an emerging and more commonly used approach for the investigation of planetary interiors is the MCMC (e. g., Bagheri et al. (2025), Filice et al. (2025), Genova et al. (2024), Petricca et al. (2023)). This analysis was not performed due to technical and time constraints. As described in Section 2.3, the MCMC allows to map the uncertainty of the observables to the uncertainty of the parameters of interest. This work showed which parameters can be constrained with the selected observables and provided reference values on how the uncertainty on the observables can constrain the interior properties. An MCMC approach would allow to bring this investigation further, by exploring the design space in order to find those interior models which lead to a minimum mismatch with respect to the observables.

Furthermore, as mentioned in Section 5.6, in order to investigate the mechanical properties of Enceladus, it is necessary to include among the observables information on the tidal dissipation. The formal error associated to the imaginary component of the gravitational Love number was computed. It could thus be included in a future work to investigate the rheology of the moon. Other observables could be included in a future analysis, such as $C_{3,0}$, related to the interior structure through the gravity/topography admittance (Genova et al., 2024).

A. Project plan

A.1. Work packages and project timeline

The work for this research project has been divided in the following Work Package(s) (WP):

WP0 Research definition. Expected time: 1 week.

- **WP0.1** Definition of the research question.
- **WP0.2** Definition of the general outline for the simulation of the science mission.

WP1 Literature study. Expected time: 5 weeks.

- **WP1.1** Study of the relevant parameters of interest for the investigation of planetary interiors from radio-tracking observations.
- **WP1.2** Study of the estimation framework for interplanetary applications.
- **WP1.3** Study of the methods available to infer interior properties of a body from geophysical measurements.

WP2 Covariance analysis for the estimation of geophysical measurements of interest of Enceladus. Expected time: 10 weeks.

- **WP2.1** Setup of the necessary code to perform the propagation of the science orbits about Enceladus: propagator, and dynamical and environment models.
- **WP2.2** Setup of the code to perform the covariance analysis for a single scenario (implementation of Tudat functionalities if necessary).
- **WP2.3** Exploration of the design space for the covariance analysis.
- **WP2.4** Selection of representative study cases and associated analysis.
- **WP2.5** Investigation of the impact of lander location on the results.

WP3 Interior structure analysis. Expected time: 10 weeks.

- **WP3.1** Preliminary sensitivity analysis of the observables to the interior parameters of interest.
- **WP3.2** Translation of the formal errors obtained in WP2 into a reference uncertainty for the interior parameters, through the methods investigated in WP1.3.

WP4 Finalisation of the report. Expected time: 2 weeks.

A brief description of the WPs is given below.

WP0 The objective of this WP is the definition of a clear and motivated research question, accompanied by the overview of the mission architecture. The mission architecture is based on the work by Auer Wilkins et al. (2025). Collaboration with them led to the definition of the mission concept, composed of an orbit and a series of landers, as detailed in Chapter 1. In addition, the scientific relevance of the plan is explored, based on the current interest of the scientific community.

WP1 In this WP, the aim is to lay the theoretical foundations for the work. Thus, the theoretical concepts not yet known or sufficiently understood are investigated. The methods and models to be applied to the project are studied, by referring to recent works on the investigation of planetary interiors from radio-tracking observations.

Thus, given the nature of the project as outlined in Chapter 1, WP1 comprises both aspects of radio-tracking science and planetary interiors. This requires the understanding of how an orbiter mission can help to study geophysical parameters of interest, and which kind of knowledge is useful for the investigation of the interior structure. In parallel to this information, WP1 comprises also the investigation of the methods that allow the study of geophysical parameters of interest given the outlined mission architecture. Finally, the investigation of the methods available to constrain the interior given a set of observables is required.

WP2 This WP constitutes the first research phase. The aim of WP2 is to obtain reliable and representative results for the estimation of geophysical parameters of interest of Enceladus.

The WP comprises an exploration of the relevant tuning settings that could affect the results, such as mission architecture parameters (e. g., mission duration, location of the landers, length of tracking arcs from Earth, etc.) or science parameters (e. g., a priori knowledge on the SH gravity field coefficients, a priori knowledge of unmodelled perturbing accelerations, etc.). Verification of the implemented models and validation of the results is included in the various sub-tasks, to ensure a setup of the code and analysis of the results as smooth as possible. When setting up the code for the covariance analysis, the solve-for parameters ought to be added one at a time, to ensure a gradual increase of the complexity of the problem, and the possibility to spot and solve issues related to the algorithm that might arise in the process.

WP3 The WP represents the second research phase. The aim of WP3 is to investigate how the uncertainty of Enceladus' geophysical parameters of interest translates to knowledge of the interior structure.

WP3 entails a sensitivity analysis to understand how the interior parameters relate to the selected observables, followed by the translation of the formal errors produced in WP2 into a reference uncertainty for the relevant interior structure parameters, through the methods found in WP1.

WP4 The finalisation of the report is expected to require the rearrangement of the sections, completion of chapters, and development of the analysis and conclusions.

After an extension of three weeks, the total time available for the execution of the work packages before the submission of the green-light deliverable was equal to 29 weeks. The planned milestones are presented in Table A.1.1.

Table A.1.1.: Planned milestones of the research project.

Milestone	Date
Kick-off meeting	3 March 2025
Research Proposal Review	7 April 2025
Midterm Review	19 June 2025
Green Light Review	26 September 2025
Thesis Defence	28 October 2025

A.2. Necessary rearrangements of the plan

A rearrangement of the time plan was required during the execution of WP2. At the time of the Midterm Review, the results until then produced were shown to the Planetary Exploration section of the Space Engineering department. During the presentation, a series of interesting questions were

asked, showing that it would be interesting to investigate more deeply some aspects of the work, in order to provide a complete answer to the first research question (see Section 1.2). Thus, it was decided to extend the number of weeks assigned to WP2 and dedicate more time to the study of the influence of the lander position on the formal errors. More time was also assigned to the production of a set of results for nominal reference mission scenarios, so that the work could provide a more refined answer to the research question, by showing exemplary results and comparing them with literature (see Section 5.2). These reference results were also used for WP3.

A rearrangement of the work was required for WP3. The initial idea for investigating the interior of Enceladus was based on the MCMC method studied in the literature review phase (Section 2.3). Before executing the MCMC, however, it was necessary to study how strongly the geophysical observables are correlated to the interior properties of Enceladus and how the interior properties interact with each other to produce the observables. For this purpose, a MC analysis was necessary. After setting up a first preliminary one-at-a-time sensitivity analysis, followed by a full MC run, the time left for performing the interior model inversion was not enough: technical issues associated to the working machine arose and the MCMC code was not robustly set up yet. As a result, aware of the limitations in case no MCMC was performed, and considering that the second research objective (see Section 1.2) could still be answered without the MCMC, even if not as exhaustively as desired, it was chosen to not pursue the MCMC analysis. This was substituted by a second MC run following the first exploratory one already performed (see Section 3.4.3). This second, refined MC analysis had the objective of translating the formal errors of some parameters from the covariance analysis into indicative uncertainty values for interior properties. Also in this case, it was chosen to limit the analysis to three observables, excluding the imaginary components of the Love numbers, conscious that some interior properties might remain unconstrained, as it was indeed shown in Section 5.6. The choice of limiting the number of observables was taken again for time management reasons, since it was chosen to dedicate more time to the core of the work, i. e., the covariance analysis. The inclusion of more observables would have required more time for the analysis and the discussion of the results. Nonetheless, the expected impact of the inclusion of the not considered observables was discussed in Section 5.6 and mentioned in Chapter 6 and chapter 7.

B. Gravity field

Considering the discussion in Wieczorek (2015, Section 10.05.2.1), the gravitational acceleration $\mathbf{g}$ at the position $\mathbf{r}$ can be expressed as the gradient of a scalar potential U:

$$\mathbf{g}(\mathbf{r}) = \nabla U(\mathbf{r}) \tag{B.0.1}$$

where the gradient operator in spherical coordinates is

$$\nabla = \hat{r}\frac{\partial}{\partial r} + \hat{\theta}\frac{1}{r}\frac{\partial}{\partial \theta} + \hat{\varphi}\frac{1}{r\sin\theta}\frac{\partial}{\partial \varphi} \tag{B.0.2}$$

In (B.0.2), r indicates the radial component of the position vector $\mathbf{r}$, while θ and φ are the planetocentric colatitude and longitude respectively.

Outside the mass distribution, the potential satisfies Laplace's equation

$$\nabla^2 U(\mathbf{r}) = 0 \tag{B.0.3}$$

Hence, the potential U exterior to the mass distribution can be written as a sum of spherical harmonics functions:

$$U(\mathbf{r}) = \frac{GM}{r}\sum_{l=0}^{\infty}\sum_{m=-l}^{l}\left(\frac{R_0}{r}\right)^l C_{lm}Y_{lm}(\theta,\varphi) \tag{B.0.4}$$

In (B.0.4), G is the gravitational constant, M is the total mass of the body, and R_0 is the reference radius at which the spherical harmonic coefficients C_{lm} are considered.

The coefficients with $m = 0$ are referred to as zonal coefficients; those with $l = |m|$ are the sectoral coefficients; the rest are called tesseral. It should be noted that often the zonal coefficients C_{l0} are often written as $-J_l$.

The spherical harmonic functions $Y_{lm}(\theta,\varphi)$ are defined as

$$Y_{lm}(\theta,\varphi) = \begin{cases} \bar{P}_{lm}(\cos\theta)\cos m\varphi & \text{if } m \geq 0 \\ \bar{P}_{l|m|}(\cos\theta)\sin|m|\varphi & \text{if } m < 0 \end{cases} \tag{B.0.5}$$

where the normalized associated Legendre functions are given by

$$\bar{P}_{lm}(\mu) = \sqrt{(2-\delta_{0m})(2l+1)\frac{(l-m)!}{(l+m)!}}P_{lm}(\mu) \tag{B.0.6}$$

and where δ_{ij} is the Kronecker delta function. The unnormalized Legendre functions in (B.0.6) are defined as

$$P_{lm}(\mu) = \left(1-\mu^2\right)^{m/2}\frac{d^m}{d\mu^m}P_l(\mu) \tag{B.0.7}$$

$$P_l(\mu) = \frac{1}{2^l l!}\frac{d^l}{d\mu^l}\left(\mu^2-1\right)^l \tag{B.0.8}$$

The normalized Legendre functions are orthogonal for a given value of m:

$$\int_{-l}^{l}\bar{P}_{lm}(\mu)\,\bar{P}_{l'm}(\mu)\,d\mu = 2(2-\delta_{0m})\,\delta_{ll'} \tag{B.0.9}$$

while the spherical harmonics are orthogonal over both l and m with the normalization

$$\int_{\Omega} Y_{lm}(\theta,\phi)\, Y_{l'm'}(\theta,\varphi)\, d\Omega = 4\pi\delta_{ll'}\delta_{mm'} \tag{B.0.10}$$

where $d\Omega = \sin\theta d\theta d\varphi$.

For a given harmonic degree l, the equivalent Cartesian wavelength λ can be introduced (Wieczorek, 2015, Section 10.05.2.1):

$$\lambda \approx \frac{2\pi R}{\sqrt{l(l+1)}} \tag{B.0.11}$$

where R is the mean planetary radius. Such equation is named Jeans relation.

Now, using the orthogonality properties of the spherical harmonic functions, it can be verified that the total power of a real square-integrable function f is related to its spectral coefficients through the equation:

$$\frac{1}{4\pi}\int_{\Omega} f^2(\theta,\varphi)\, d\Omega = \sum_{l=0}^{\infty} S_{ff}(l) \tag{B.0.12}$$

where

$$S_{ff}(l) = \sum_{m=-l}^{l} f_{lm}^2. \tag{B.0.13}$$

In (B.0.13), $S_{ff}(l)$ is referred to as the power spectrum of the function f.

Furthermore, the cross power of two functions f and g is given by

$$\frac{1}{4\pi}\int_{\Omega} f(\theta,\phi)\, g(\theta,\phi)\, d\Omega = \sum_{l=0}^{\infty} S_{fg}(l) \tag{B.0.14}$$

where

$$S_{fg}(l) = \sum_{m=-l}^{l} f_{lm} g_{lm} \tag{B.0.15}$$

is the cross power spectrum.

Up until now, only the potential U due to the gravitational attraction of the body has been considered. If the body is rotating, an additional non-gravitational force must be considered for the potential at the surface of the body. In the reference frame rotating with the body, the correction can be performed by adding a pseudo-potential term (Wieczorek, 2015, Section 10.05.2.2). This term is produced by the centrifugal force. Such rotational pseudo-potential is given by

$$U^{\text{rot}} = \frac{\omega^2 r^2 \sin^2\theta}{2} = \omega^2 r^2 \left(\frac{1}{3}Y_{00} - \frac{1}{3\sqrt{5}}Y_{20}\right) \tag{B.0.16}$$

where ω is the angular velocity of the body.

Additionally, in case the body is subjected to deformation due to tides exerted by another body, it is necessary to include the tidal potential of the parent body in the total potential. For a synchronously locked satellite on a circular orbit, the combined tidal and rotational potential is given by (Wieczorek, 2015, Section 10.05.2.2)

$$U^{\text{tide+rot}} \simeq \omega^2 r^2 \left(\frac{1}{3}Y_{00} - \frac{\sqrt{5}}{6}Y_{20} + \frac{1}{4}\sqrt{\frac{12}{5}}Y_{22}\right). \tag{B.0.17}$$

C. Topography

As presented by Nimmo et al. (2011, Section 3), the topography function h of a planetary object can be expressed as the summation of spherical harmonics coefficients

$$h(\theta, \phi) = R_0 \sum_{l=0}^{\infty} \sum_{m=-l}^{l} H_{lm} Y_{lm}(\theta, \phi) \tag{C.0.1}$$

Wieczorek (2015, Section 10.05.2.2) introduces the relationship between the gravitational field and topography in the spectral domain. For this, the following relation between the radial gravity g_{lm} and topography h_{lm} is presented:

$$g_{lm} = Q_{lm} h_{lm} + I_{lm} \tag{C.0.2}$$

In (C.0.2), Q_{lm} is a linear non-isotropic transfer function and I_{lm} stands for the portion of the gravitational field that is not predicted by the model. Furthermore, g_{lm} and h_{lm} are the spherical harmonic coefficients of the gravitational potential and topography function. In case that I_{lm} is a random variable independent of the surface topography, the expectation of the observed gravitational power spectrum is

$$S_{gg}^{\text{obs}}(l) = S_{gg}(l) + S_{II}(l) \tag{C.0.3}$$

where S_{gg} is the power spectrum predicted exclusively by the model Q_{lm} ans S_{II} is the expectation of the power spectrum of I_{lm}. Hence, the gravitational power spectrum is biased by the gravitational measurement noise.

A useful quantity introduced by Wieczorek (2015, Section 10.05.2.2) for describing the relationship between the gravitational power spectrum and topography is the *admittance*, defined by the cross power spectrum of gravity and topography, divided by the power spectrum of topography:

$$Z(l) = \frac{S_{hg}(l)}{S_{hh}(l)} \tag{C.0.4}$$

The power spectrum is defined in (B.0.13), while the cross power spectrum is given in (B.0.15). This function is not biased by the presence of noise.

Another quantity that relates the power spectra of gravity and topography is the *correlation*:

$$\gamma(l) = \frac{S_{hg}(l)}{\sqrt{S_{hh}(l)\, S_{gg}(l)}} \tag{C.0.5}$$

While the admittance is not affected by the noise in the radial gravity measurements, the bias feeds into the correlation, leading to smaller values due to the gravitational power spectrum at the denominator of (C.0.5).

D. Iterative numerical procedure for computing the gravitational harmonic hydrostatic coefficients

As discussed in Section 2.1.4, for a body in non-hydrostatic equilibrium, the observed degree-2 coefficients for gravity $\left({J_2}^{\text{obs}}, C_{22}^{\text{obs}}\right)$ and topography $\left(H_{20}^{\text{obs}}, H_{22}^{\text{obs}}\right)$ can be computed through the linear sum of the hydrostatic and non-hydrostatic parts (Genova et al., 2024), with the assumption that the non-hydrostatic parts are small with respect to the hydrostatic ones (Genova et al., 2024, Section 3.1):

$$\begin{aligned} {J_2}^{\text{obs}} &= {J_2}^{\text{hyd}} + {J_2}^{\text{nh}} \\ C_{22}^{\text{obs}} &= C_{22}^{\text{hyd}} + C_{22}^{\text{nh}} \\ H_{20}^{\text{obs}} &= H_{20}^{\text{hyd}} + H_{20}^{\text{nh}} \\ H_{22}^{\text{obs}} &= H_{22}^{\text{hyd}} + H_{22}^{\text{nh}} \end{aligned} \tag{D.0.1}$$

With respect to the harmonic gravity coefficients ${J_2}^{\text{hyd}}$ and C_{22}^{hyd}, the hydrostatic component can be computed through the numerical approach presented by Tricarico (2014). The method considers the total potential U_{tot} of a two-layer triaxial ellipsoid:

$$U_{\text{tot}} = \frac{x^2+y^2}{2}\dot{\Omega}^2 + \frac{2x^2-y^2-z^2}{2}\omega^2 + \sum_{i=1}^{N}\frac{\rho_i-\rho_{i-1}}{\rho_i}U_i \tag{D.0.2}$$

In the equation, the first term is the rotational pseudo-potential acting on a particle due to the centrifugal acceleration generated by the rotation of the body. The rotation axis is aligned with the z-axis of the body. Additionally, the second term is the tidal potential, while the third term is the potential produced by the single contribution U_i of each layer.

The potential U_i of each layer is given by Tricarico (2014, Appendix A)

$$\begin{aligned} \frac{U}{\pi G\rho} =& \frac{2abc}{\sqrt{a^2-c^2}}\left[1-\frac{x^2}{a^2-b^2}+\frac{y^2}{a^2-b^2}\right]F\left(\psi, e_{\text{q}}^2/e_{\text{p}}^2\right) \\ &+ \frac{2abc}{\sqrt{a^2-c^2}}\left[\frac{x^2}{a^2-b^2}-\frac{\left(a^2-c^2\right)y^2}{\left(a^2-b^2\right)\left(b^2-c^2\right)}+\frac{z^2}{\left(b^2-c^2\right)}\right]E\left(\psi, e_{\text{q}}^2/e_{\text{p}}^2\right) \\ &+ \frac{2abc}{\sqrt{\left(a^2+\kappa\right)\left(b^2+\kappa\right)\left(c^2+\kappa\right)}}\left[\frac{c^2+\kappa}{b^2-c^2}y^2-\frac{b^2+\kappa}{b^2-c^2}z^2\right] \end{aligned} \tag{D.0.3}$$

where ψ is such that

$$\sin^2\psi = \frac{a^2-c^2}{a^2+\kappa} \tag{D.0.4}$$

and where F and E are the elliptic integral functions of the first and second kind, respectively:

$$F\left(\psi, e_{\text{q}}^2/e_{\text{p}}^2\right) \coloneqq \int_0^{\psi}\frac{d\theta}{\sqrt{1-\left(e_{\text{q}}^2/e_{\text{p}}^2\right)^2\sin^2\theta}} \tag{D.0.5}$$

$$E\left(\psi, e_{\text{q}}^2/e_{\text{p}}^2\right) \coloneqq \int_0^{\psi}\sqrt{1-\left(e_{\text{q}}^2/e_{\text{p}}^2\right)^2\sin^2\theta}d\theta \tag{D.0.6}$$

Finally, the variable κ is the positive root of the equation

$$\frac{x^2}{a^2+\kappa}+\frac{y^2}{b^2+\kappa}+\frac{z^2}{c^2+\kappa}=1 \tag{D.0.7}$$

for points (x, y, z) outside the ellipsoid. Inside the ellipsoid, $\kappa = 0$.

Once U_{tot} is defined, the condition for equipotential surfaces is imposed:

$$U_{\text{tot}}\left(a_i, 0, 0\right) = U_{\text{tot}}\left(0, b_i, 0\right) = U_{\text{tot}}\left(0, 0, c_i\right) \tag{D.0.8}$$

The solution is found by numerical minimization of Δ^2:

$$\Delta^2 = \sum_{k=1}^{N}\left[U_{\text{tot}}\left(0, b_i, 0\right) - U_{\text{tot}}\left(a_i, 0, 0\right)\right]^2 + \sum_{k=1}^{N}\left[U_{\text{tot}}\left(0, 0, c_i\right) - U_{\text{tot}}\left(a_i, 0, 0\right)\right]^2 \tag{D.0.9}$$

using as decision variables of the optimization problem the polar and equatorial eccentricities $e_{\text{p},i}$ and $e_{\text{q},i}$. The initial values of $e_{\text{p},i}$ and $e_{\text{q},i}$ are to be chosen between 0 and 1, or can be seeded as described in Tricarico (2014).

Once the polar and equatorial eccentricities $e_{\text{p},1}$, $e_{\text{q},1}$, $e_{\text{p},2}$, and $e_{\text{q},2}$ are computed, it is possible to determine the hydrostatic harmonic coefficients for the gravity quadrupole (Tricarico, 2014, Appendix C):

$$\begin{aligned} J_{2_i}^{\text{hyd}} &= -C_{20,i}^{\text{hyd}} = -\frac{\left(e_{\text{q},i}^2 - 2e_{\text{q},i}^2\right)}{10} \\ C_{22,i}^{\text{hyd}} &= \frac{e_{\text{q},i}^2}{20} \end{aligned} \tag{D.0.10}$$

E. Acceleration and integrator settings selection

The selection of the acceleration and integrator settings is performed first by selecting the integrator settings and considering the same dynamical model (see Table 3.1.4) with which the refined solutions reported in Table 3.1.5 were produced. Afterwards, with the given integrator settings, the acceleration model for the S/C propagation is selected to obtain a reasonably small physical model error.

The outlined analysis is performed for the K_1 orbit solution. For the K_2 and K_3 solutions, figures of merit for the physical model and integrator errors are reported, to show that the considered settings are valid across all three available initial states.

E.1. Integrator settings

The integrator settings are analysed by assuming the dynamical model reported in Table 3.1.4. Furthermore, the Cowell propagator is chosen, due to its intuitive formulation and ease of interpretation. The Cowell formulation of the EoM defines the state as composed of the position vector and its derivative, for which the state derivative is composed of the velocity and the accelerations acting on the considered body.

A set of Runge-Kutta (RK), RKF, and Dormand-Prince (RKDP) fixed-step integrators is analysed. Variable step integrators are not considered since adaptation of the step size based on the required integration error for the single step is not necessary, given that the studied orbits are near-circular and low-altitude. Hence, the dynamics along the orbit is not fast changing, as opposed to a fly-by science mission. Thus a fixed step integrator is expected to work well, with no correction of the step size during the orbit integration. Additionally, a fixed-step integrator allows to obtain the state and other variables of interest at a constant cadence, avoiding the need of an interpolator for assessing the integration error, hence avoiding the inclusion of interpolation error in the integration one. For each integrator, a set of various time steps is selected. The integrators and associated time steps are reported in Table E.1.1.

Table E.1.1.: Set of integrators and fixed time steps considered for the selection of the integrator settings for the observations simulation.

Integrator	Fixed time steps [s]
RK4	2.5; 5; 10; 15; 20; 25; 30; 40
RKF4(5)	2.5; 5; 10; 15; 20; 25; 30; 40
RKF5(6)	2.5; 5; 10; 15; 20; 25; 30; 40
RKF7(8)	2.5; 5; 10; 15; 20; 25; 30; 40
RKF8(9)	2.5; 5; 10; 15; 20; 25; 30; 40
RKDP8(7)	2.5; 5; 10; 15; 20; 25; 30; 40

In order to compute an estimate of the integration error for every combination of integrator and time step Δt, a benchmark is generated with the same integrator and time step $\Delta t' = \frac{\Delta t}{4}$. At every integration epoch of the solution, the state difference between the solution and the benchmark computed. The norm of the position difference is thus computed and plotted over time. As an example, the integration error of the RK4 integrator with a time step of 20 s is computed through the difference of the state history with the benchmark, obtained with an RK4 integrator and a time step of 5 s.

The assumption that allows this method to be valid is the truncation error being dominant. Indeed, if truncation error is dominant, a reduction by a factor 2 of the time step leads to an expected reduction of 2^n of the integration error, where n is the order of the integrator. Hence, in case truncation error is dominant, the benchmark can be considered a good approximation of the true solution for estimating the integration error of the selected integrator settings. For the considered RK4 integrator with a time step of 5 s, Figure E.1.1 (upper left panel) shows that the final integration error is about 10^{-4} m. When the time step is doubled to 10 s, the final integration error is of the order of 10^{-3} m, in agreement with the expected improvement of $2^4 = 16$ times. The RK4 integrator with a time step of 5 s is thus considered as the benchmark.

The results for all the combinations of Table E.1.1 are reported in Figure E.1.1. The associated computational time is presented in Figure E.1.2. The higher order integrators are typically used for problems with a fast changing dynamics. It can be observed that the considered higher order integrators (RKF7(8), RKF8(9), RKDP8(7)) do not show the expected reduction of about 2^n. Hence, such integrators show a behaviour typical of rounding error, which is random. For analysing their behaviour in the region where truncation error is dominant, it would be necessary to increase the step size above at least 40 s, as displayed in Figure E.1.1. However, considering that reasonably larger step sizes would raise the problem of interpolation error in between the integrated epochs, and considering that a similar accuracy can be reached with lower-order integrators, which show a behaviour typical of truncation error being dominant, such higher-order integrators are discarded from the analysis.

With respect to the lower-order integrators, truncation error is dominant, hence for these combinations the integration error can be reliably estimated. Since there is no specific requirement on the integration error, the integrator settings are chosen so that they provide a reasonably small error of about $\sim 10^{-4}$ m, without requiring an excessive computational time. In case of the RK4 integrator, Figure E.1.1 shows that to achieve an error of about 10^{-4} m, a time step of 5 s would be required. However, in that region, rounding error appears to be dominant. Furthermore, such a time step would require a total computational time of about 20 s, as shown in the respective plot of Figure E.1.2. The other option would be a time step of 10 s, which would still lead to a small integration error of about $\sim 10^{-3}$ m and a computational time of 10 s. However, considering the other integrator methods, better options appear to be available. For instance, to achieve an integration error of $\sim 10^{-4}$ m after 28 days of integration, the RKF5(6) integrator requires a time step of 15 s, and takes about 12 s of computational time. Also the RKF4(5) with $\Delta t = 15$ s leads to an integration error of $\sim 10^{-4}$ m and a computational time of about 10 s. However, the RKF5(6) shows a smoother behaviour with the considered acceleration settings, including the gravitational acceleration due to the SH gravity field of Enceladus and Saturn (Table 3.1.4). Hence, the RKF5(6) integrator with a fixed time step of 15 s is selected for integrating the orbit and simulating the observations.

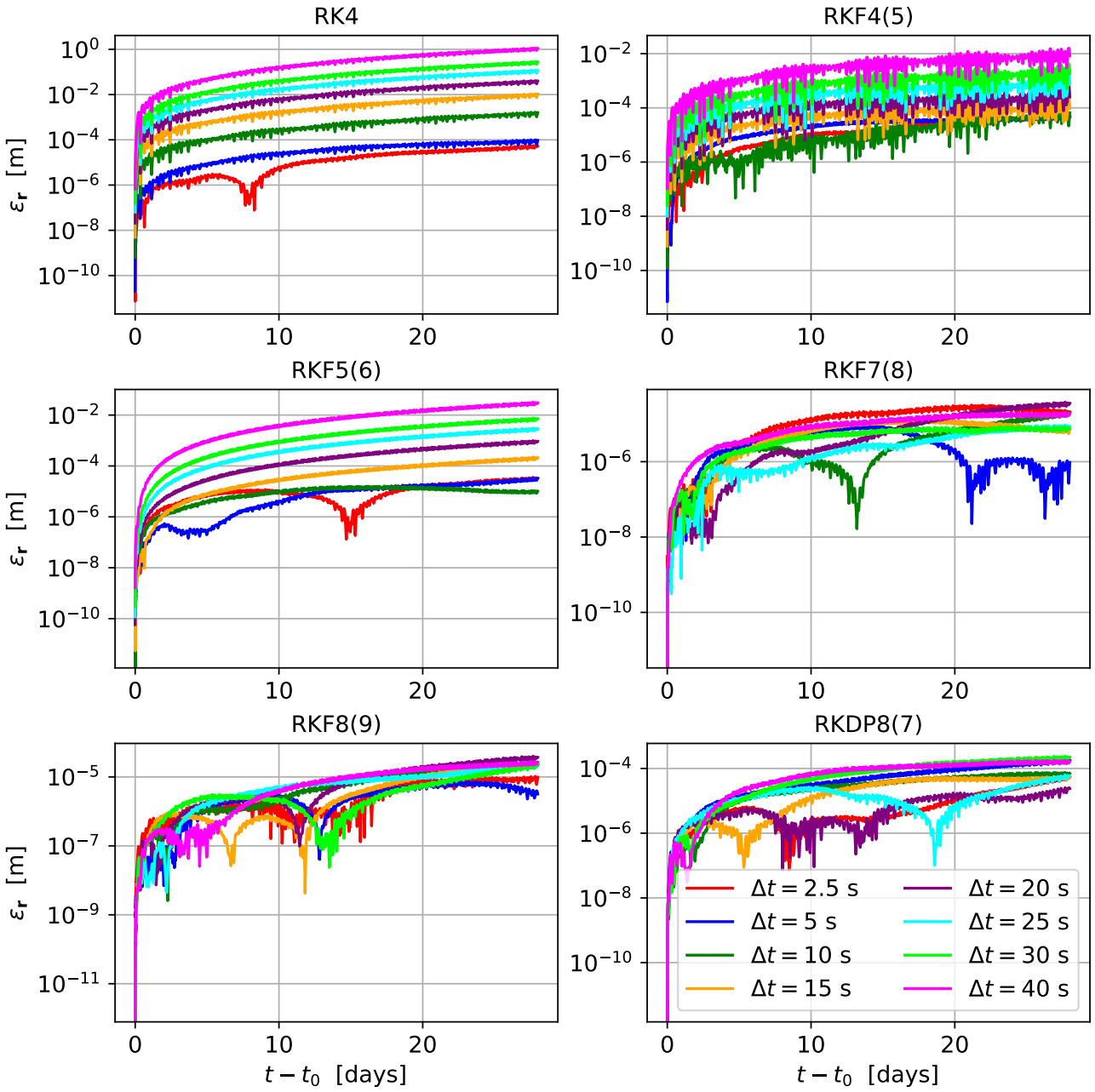

Figure E.1.1.: Integration error for all the integrator/time step combinations presented in Table E.1.1. Considered accelerations: Enceladus SH (3,0) grav. acceleration; Saturn SH (8,0) grav. acceleration. Considered initial state: K1.

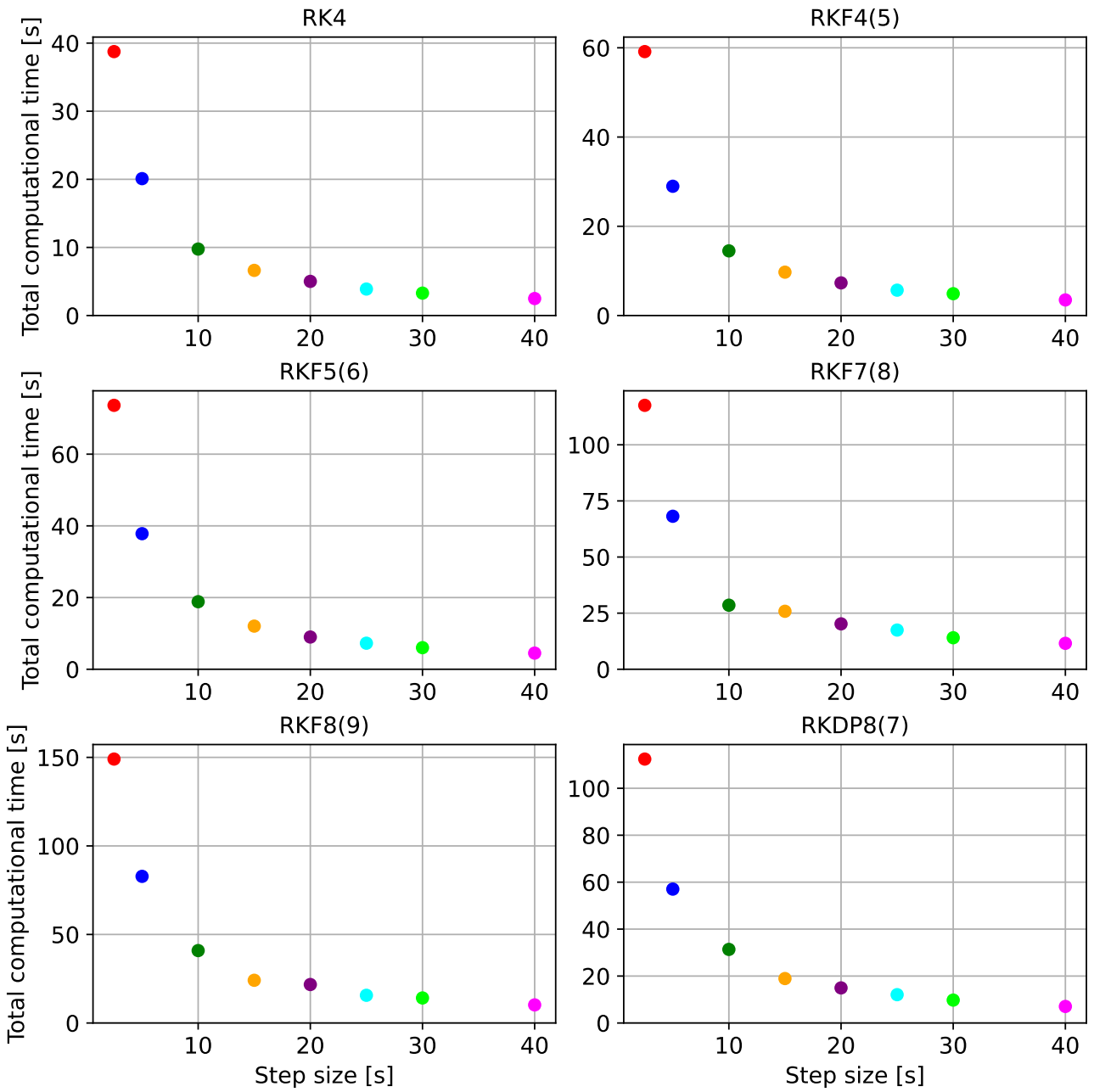

Figure E.1.2.: Total computational time for all the integrator/time step integrations presented in Table E.1.1. Considered accelerations: Enceladus SH (3,0) grav. acceleration; Saturn SH (8,0) grav. acceleration. Considered initial state: K1.

E.2. Acceleration settings

For selecting the acceleration settings to include in the dynamical model, the integrator settings chosen in the previous section are considered.

To study the error introduced by the dynamical model, the settings reported in Table 3.1.4 and applied also by Benedikter et al. (2022) are considered as base case. The base-case orbit is thus integrated.

A set of various accelerations is then considered for an improved model. They are reported in Table E.2.1. To assess the physical model error introduced by the accelerations, each acceleration is singularly added to the base case, and the norm of the position difference between the states of the improved and base-case model is computed for each integration epoch. Additionally, for each new acceleration setting, the magnitude of the additional acceleration acting on the vehicle is saved. The resulting plot for the K_1 orbit solution is shown in Figure E.2.1.

In terms of the accelerations magnitude, Figure E.2.1a shows a clear distinction between the magnitude of the gravitational acceleration of Enceladus and Saturn with respect to the rest of the perturbing accelerations. The fact that the magnitude of the acceleration of Saturn is just about one order of magnitude smaller than the one of Enceladus, while the other perturbing accelerations are at minimum 5 orders of magnitude lower, might explain why orbit design at Enceladus is challenging, with orbits that escape the moon or crash on its surface in a short period of time, as presented in Section 2.4.

Furthermore, Figure E.2.2 shows the position difference introduced by the perturbing accelerations. It can be observed that all the perturbing planets and planetary systems of the Solar System introduce a negligible error, of an order of magnitude about equal or smaller than the integration error ($\sim 10^{-4}$ m). On the other hand, the moons of the Saturnian system and the Sun introduce an error significantly larger than the integration error. Hence, they will be included in the dynamical model for the simulation of the observations, as reported in Table 3.2.2.

Body	Acceleration(s)	Environment settings
Sun	GM grav. acceleration; cannonball SRP	Default SPICE
Mimas	GM grav. acceleration	Default SPICE
Tethys	GM grav. acceleration	Default SPICE
Dione	GM grav. acceleration	Default SPICE
Rhea	GM grav. acceleration	Default SPICE
Titan	GM grav. acceleration	Default SPICE
Mercury	GM grav. acceleration	Default SPICE
Venus	GM grav. acceleration	Default SPICE
Earth Barycentre	GM grav. acceleration	Default SPICE
Mars Barycentre	GM grav. acceleration	Default SPICE
Jupiter Barycentre	GM grav. acceleration	Default SPICE
Uranus Barycentre	GM grav. acceleration	Default SPICE
Neptune Barycentre	GM grav. acceleration	Default SPICE

Table E.2.1.: Acceleration settings on the vehicle considered for the selection of the dynamical model for the observations simulation. The default settings for the considered bodies are retrieved from SPICE.

For a further analysis of the accelerations, the error introduced by the SH gravity coefficients of Saturn, which are included in the base dynamical model, is assessed. The orbit of the vehicle is propagated with only the gravitational acceleration by Enceladus and the point mass acceleration of Saturn, and is compared to the base-case run. The norm of the position and total acceleration difference is showed in Figure E.2.2. As it can be observed, including the SH coefficients up to degree 8 and order 0 is necessary to avoid an excessive error in the physical model. Such large position difference is caused by

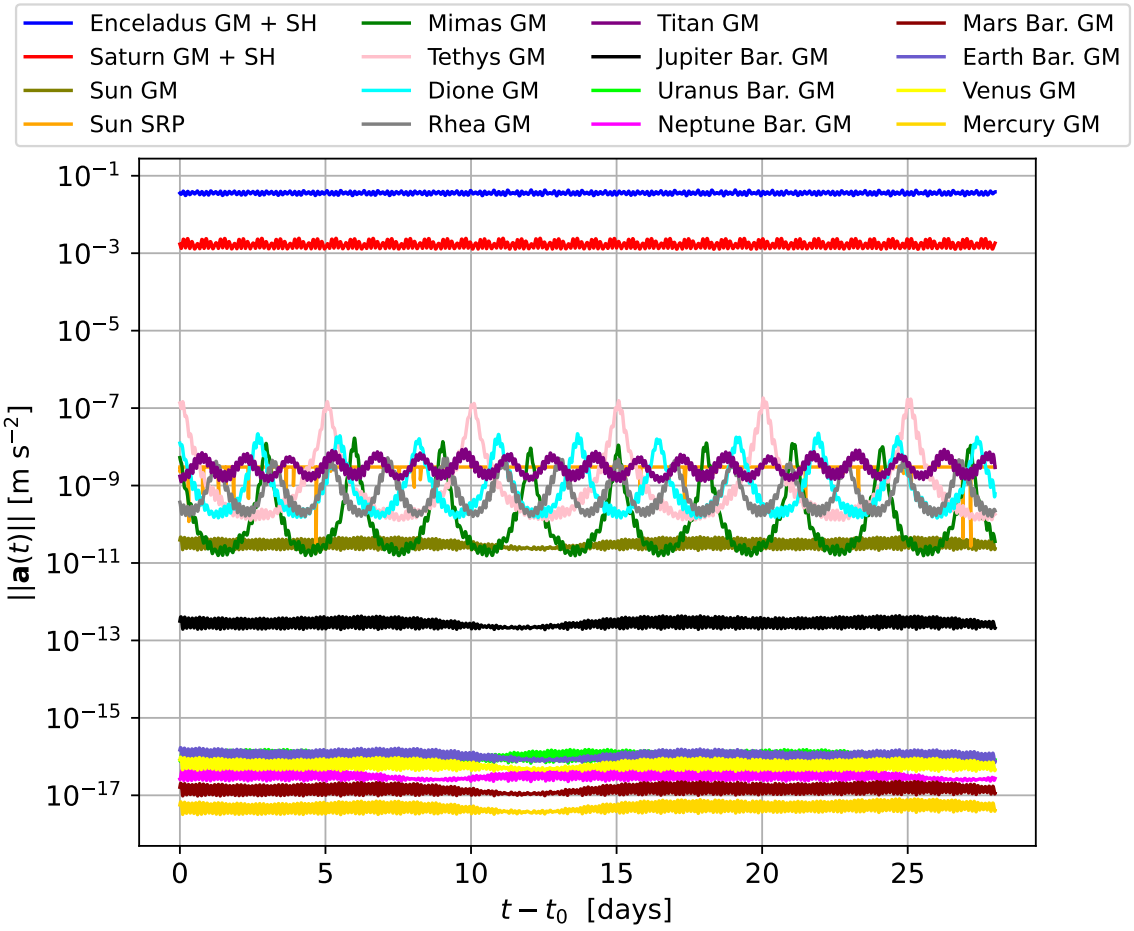

(a) Comparison of the magnitude of the perturbing accelerations with respect to the gravitational accelerations by Enceladus and Saturn of the base case.

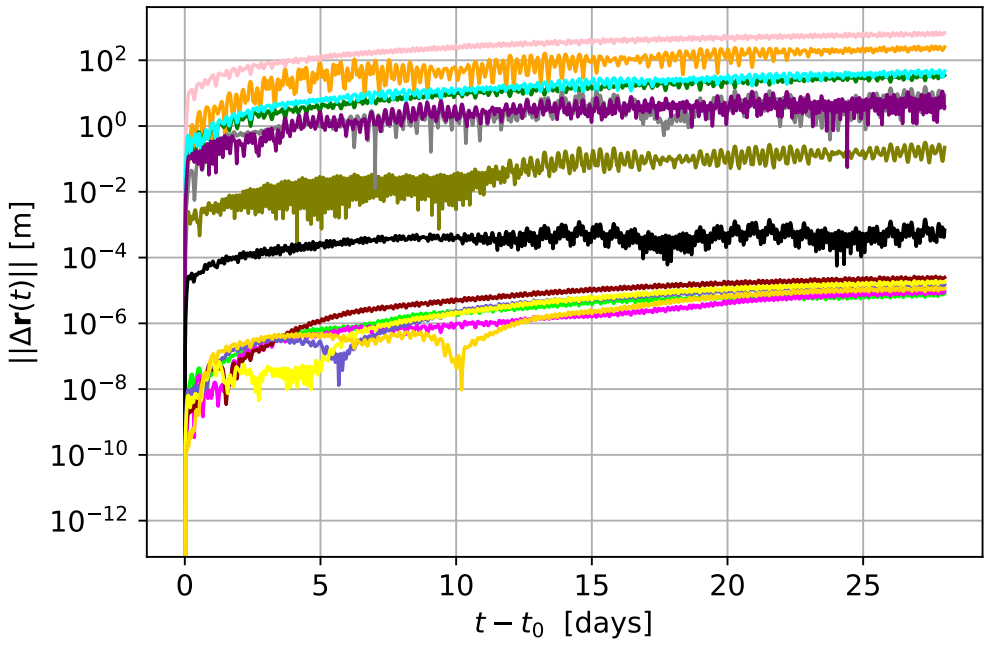

(b) Norm of position difference between the states integrated with the additional acceleration setting and the base case.

Figure E.2.1.: Perturbing accelerations analysis. Considered initial state: K1.

the fact that the magnitude of the acceleration difference, about $\sim 10^{-4}\,\mathrm{m\,s^{-2}}$ is just two orders of magnitude lower than the total gravitational acceleration by Enceladus, of about $\sim 10^{-2}\,\mathrm{m\,s^{-2}}$, as shown by Figure E.2.1a.

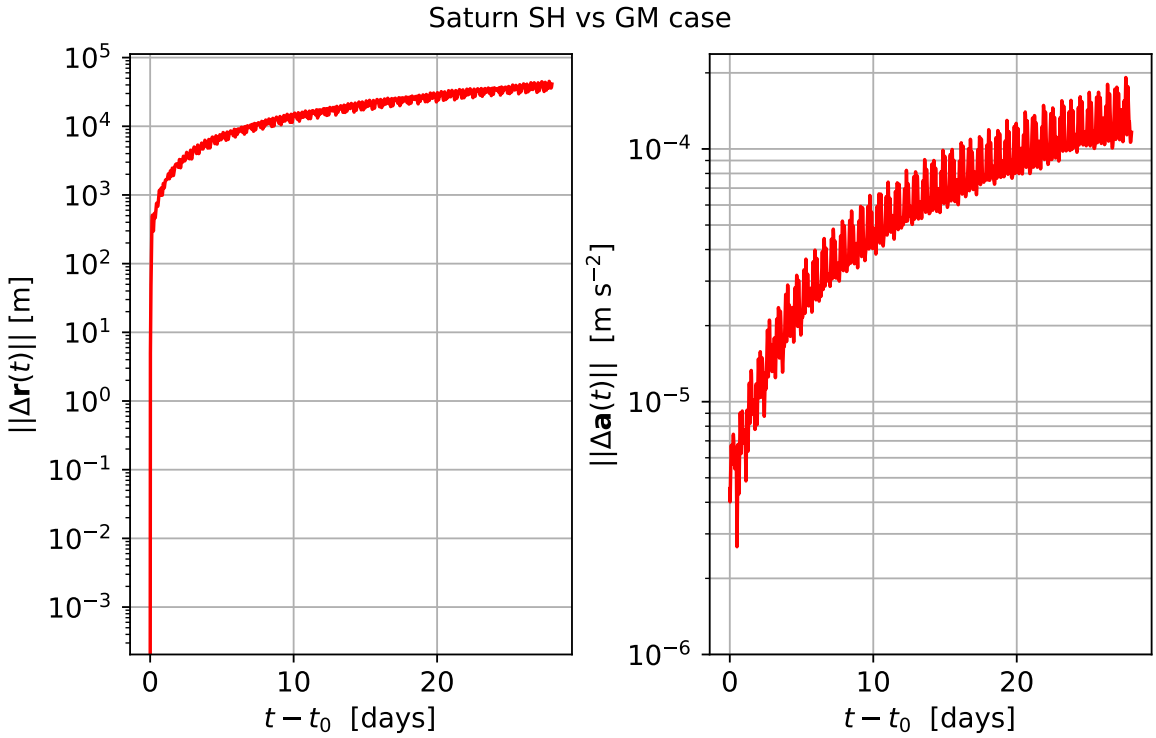

Figure E.2.2.: Norm of position and acceleration difference between the orbits propagated with the SH $(8, 0)$ gravity field and the point mass gravity field of Saturn. Considered initial state: K1.

E.2.1. Verification of the integrator settings with the updated dynamical model

Given the selection of the dynamical model, reported in Table 3.2.2, the analysis of the integrator settings is performed including the perturbing accelerations, to make sure that the chosen integrator settings (Table 3.2.1) still ensure that the integrated orbit is representative of the mission scenario.

The integration error for the RKF5(6) integrator with the same set of fixed step sizes considered in Appendix E.1 and the dynamical model from Table 3.2.2 is plotted in Figure E.2.3. Figure E.2.3a shows that with the complete dynamical model, the solution with $\Delta t = 15\,\mathrm{s}$ is affected by rounding error in all three orbit solutions. Furthermore, in all three cases, the final integration error after 28 days is of the order of magnitude of $10^{-2}\,\mathrm{m}$, two orders of magnitude higher with respect to the case without the additional perturbing accelerations. Figure E.2.3b shows that when the SRP acceleration is removed from the acceleration settings described in Table 3.2.2, the behaviour of the integrator improves significantly, and the integration error of the RKF5(6) integrator with $\Delta t = 15\,\mathrm{s}$ is $10^{-4}\,\mathrm{m}$, in line with the results shown in Appendix E.1. The fact that the SRP degrades the integration error might be due to the eclipses not being properly captured due to the given fixed time step.

Now, considering Figure E.2.3a, $\Delta t = 2.5\,\mathrm{s}$ might seem a better choice for the smaller integration, of about $10^{-4}\,\mathrm{m}$. However, considering that for all three orbits the integration with $\Delta t = 2.5\,\mathrm{s}$ takes about 130 s of machine time instead of the 21.5 s required for an integration with $\Delta t = 15\,\mathrm{s}$, and considering that the integrated orbit is still representative of the problem at hand (refer to Section 4.1), even with an integration error of $10^{-2}\,\mathrm{m}$, the integrator settings selected in Appendix E.1 are kept. The reduced machine time allows to reduce the time needed to perform the design space exploration for the covariance analysis and still provide results that are representative for the problem at hand.

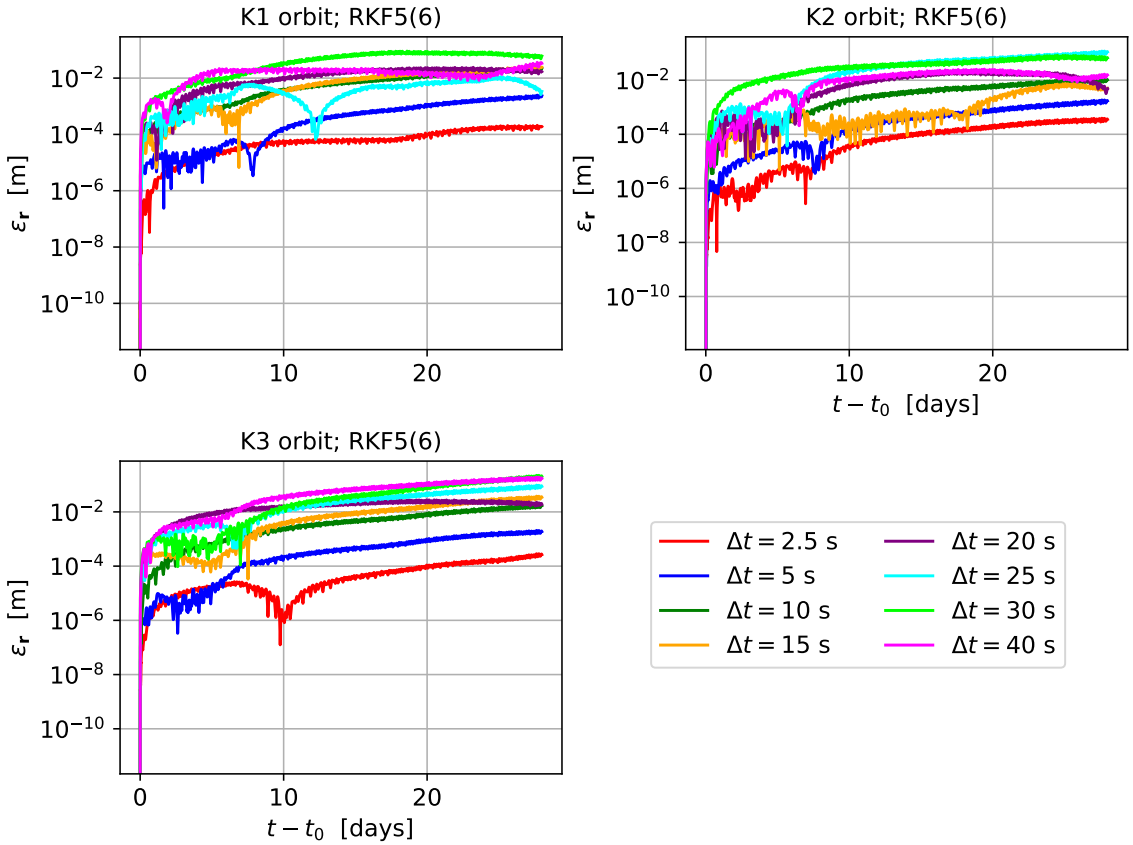

(a) Integration error with the SRP included in the dynamical model.

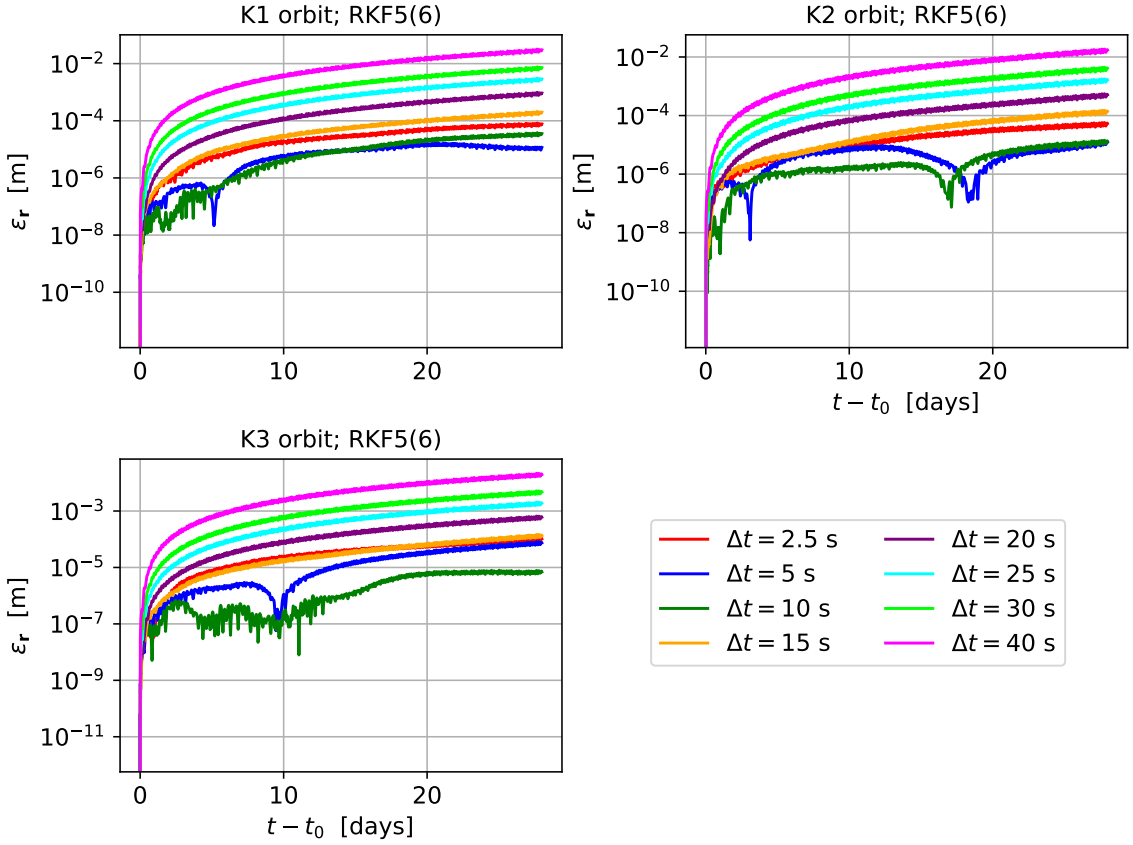

(b) Integration error with the SRP excluded from the dynamical model.

Figure E.2.3.: Integration error for the RKF5(6) integrator with the same sweep of time steps considered in Appendix E.1. The acceleration settings presented in Table 3.2.2 were considered in the dynamical model. The case with and without SRP are presented. An SRP coefficient equal to 1.2 is assumed (refer to Table 3.1.2).

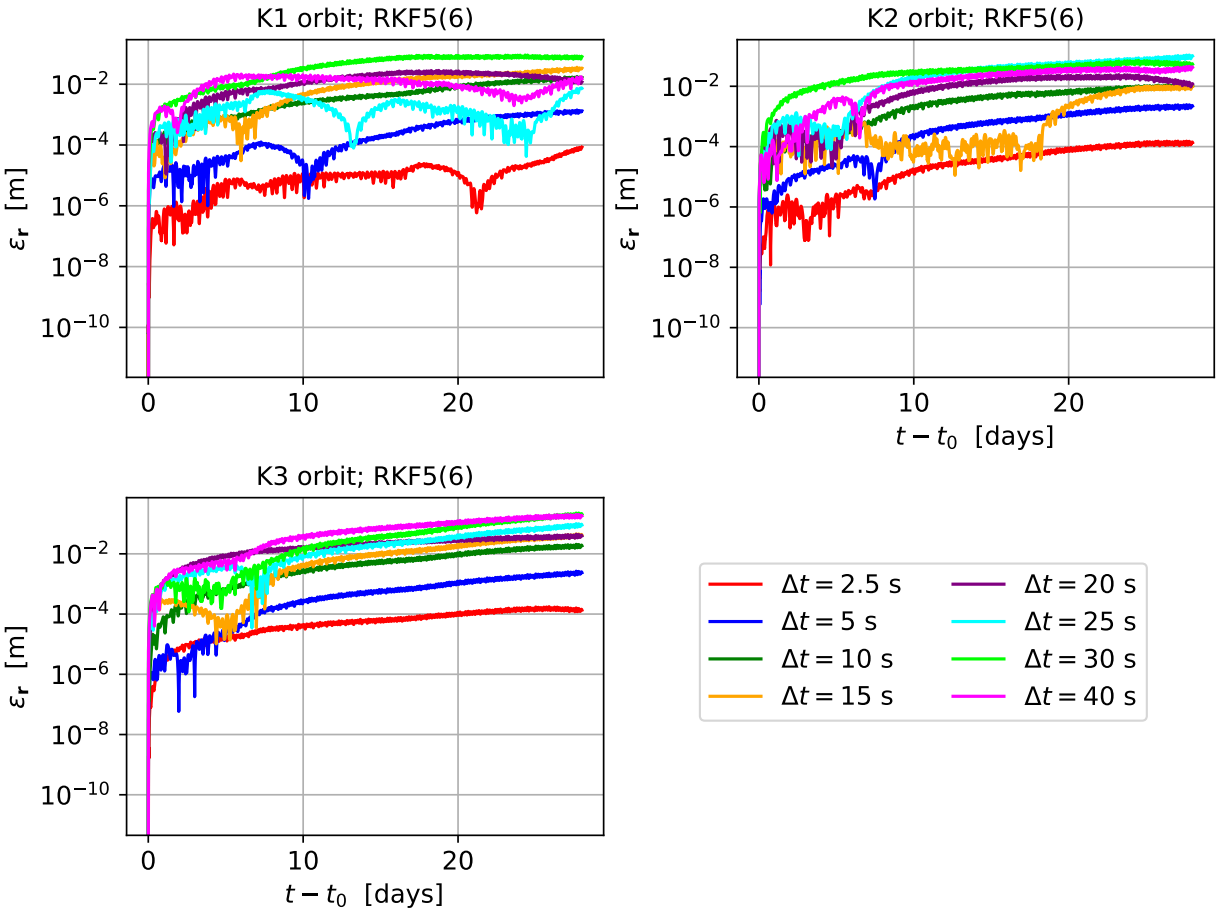

Figure E.2.4.: Integration error for the RKF5(6) integrator with the same sweep of time steps considered in Appendix E.1. The acceleration settings presented in Table 3.2.2 were considered in the dynamical model. The DE438 and SAT427 ephemerides were used.

F. Results for the perturbed K2 and K3 orbits for the verification of their feasibility and stability

To show that the selection of the dynamical model is valid also for the K_2 and K_3 solutions, which have similar Keplerian elements to K_1 (see Table 3.1.5), the multi-arc analysis described in Section 4.1 is performed also for these solutions.

The norm of the position difference and of the velocity correction for the K_2 and K_3 initial states is reported in Figure F.0.1 and Figure F.0.2 respectively. As it can be observed in Figure F.0.1, both for the K_2 and K_3 orbits, the selected perturbing accelerations from Table 3.2.2 lead to a position difference of less than 100 m after 1 day, with an accelerations difference of the same order of magnitude as for the K_1 solution. Furthermore, Figure F.0.1 shows that in order to correct for such position difference, an impulsive manoeuvre of an order of magnitude of maximum $10^{-3}\ \mathrm{m\,s^{-1}}$ is required, as for the K_1 orbit. Hence, with the selected perturbing accelerations reported in Table 3.2.2, also the K_2 and K_3 solutions are still representative of a science orbit around Enceladus, and they allow to answer to the first research sub-question in a representative way.

Finally, as observed for the K_1 orbit, Figure F.0.3 shows that the perturbed K_2 and K_3 are stable and do not crash on Enceladus nor escape it.

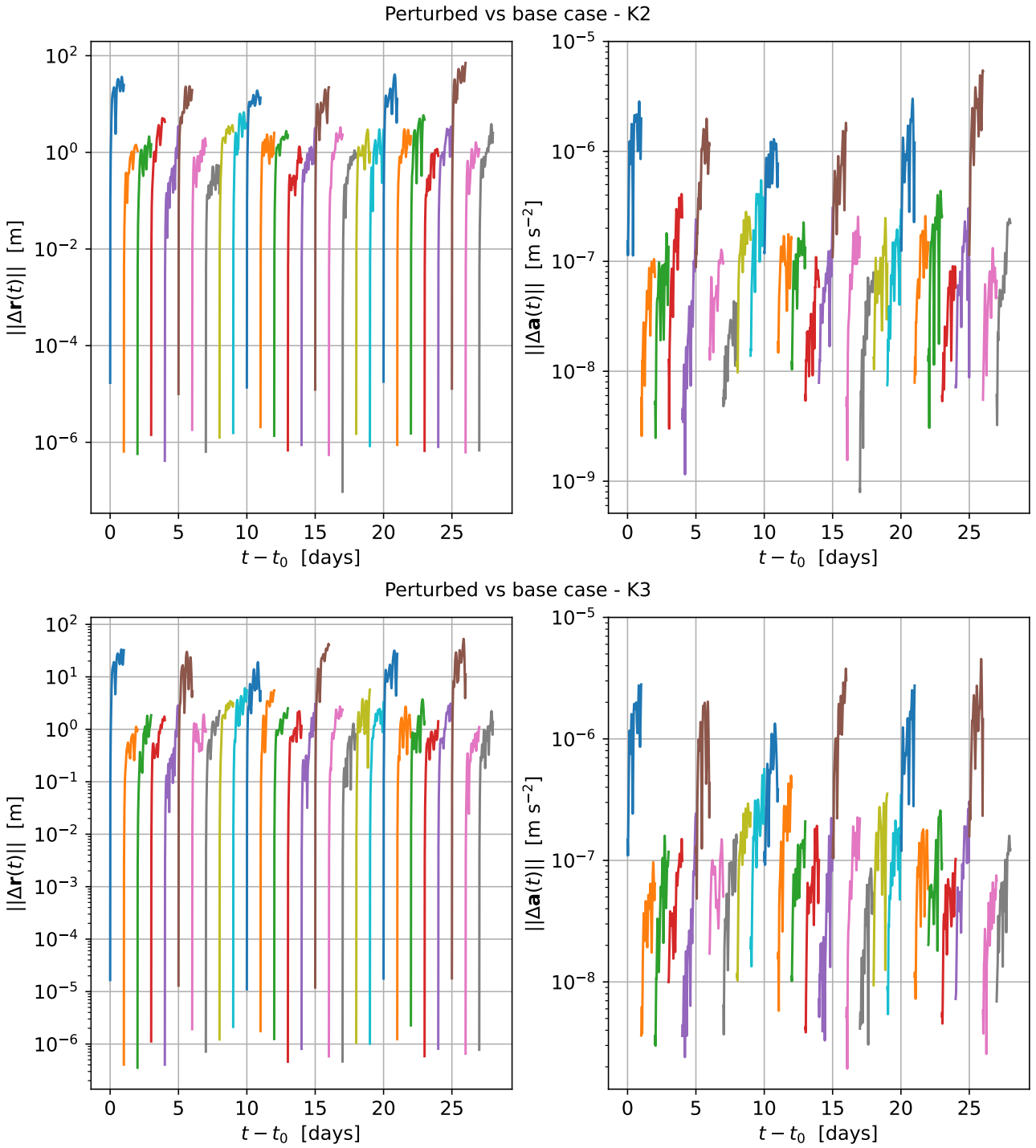

Figure F.0.1.: Arc-wise position and acceleration difference between the perturbed case with the additional acceleration settings from Table 3.2.2. Considered initial states: K2, K3.

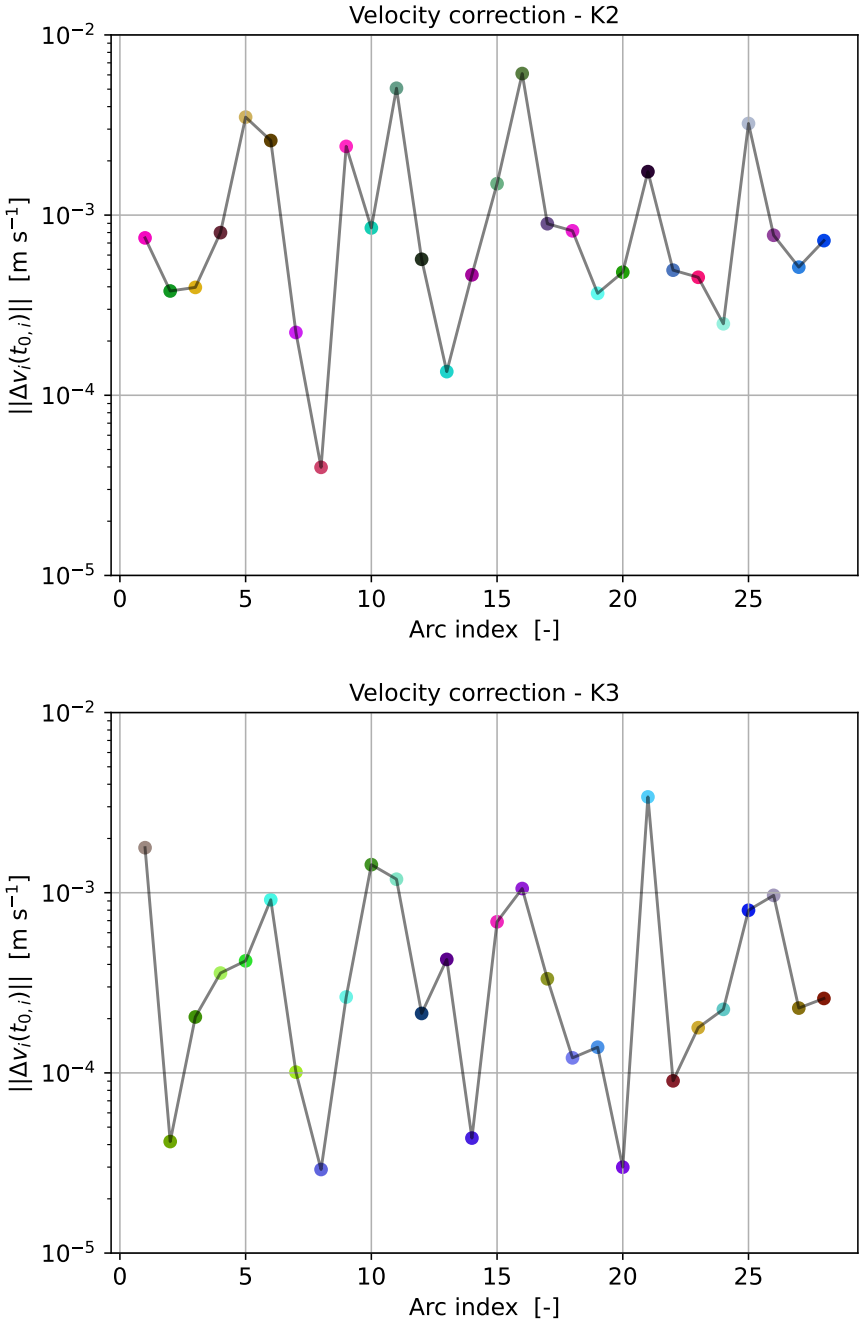

Figure F.0.2.: Norm of initial velocity correction at the start of each single arc for the K_2 and K_3 solutions.

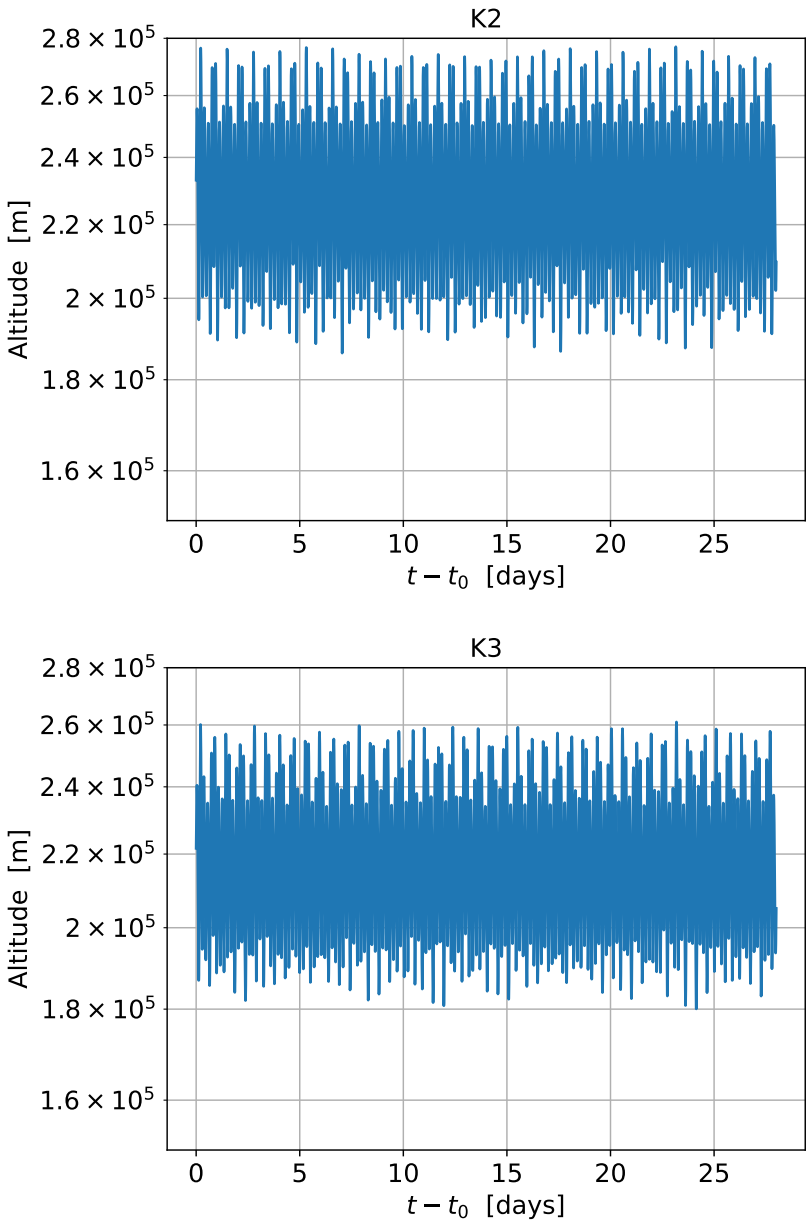

Figure F.0.3.: Altitude history for the perturbed science orbits K_2 and K_3. The acceleration settings from Table 3.2.2 are applied.

G. Detailed results of the nominal cases covariance analysis

Table G.0.1.: Detailed results of the nominal representative covariance analysis cases for the K3 orbit. The table summarises the results displayed in Figure 5.2.1.

Orbit	Arc length [days]	Nb. landers	$RMS\,(\sigma)$ deg. 2 cos & sin [–]	Max. deg. gravity [–]	σ $(\Re(k_2); \Im(k_2))$ [–]	$\sigma\,(\phi)$ [deg]	$\sigma\,(h_2)$ [–]	$\sigma\,(\alpha; \delta)$ [deg]	$\sigma\left(\dot{\alpha}; \dot{\delta}\right)$ [deg s^{-1}]	Nb. observations [–]
K_3	1	0	2.42×10^{-8}; 9.85×10^{-9}	15	$(2.50; 1.74) \times 10^{-4}$	2.51×10^{-4}	–	1.09×10^{-3}; 1.32×10^{-4}	9.60×10^{-11}; 1.06×10^{-10}	10,979
K_3	1	1	2.29×10^{-8};7.27×10^{-9}	15	$(6.52; 6.73) \times 10^{-5}$	2.81×10^{-6}	6.69×10^{-4}	2.51×10^{-5}; 3.25×10^{-6}	$(2.39; 2.33) \times 10^{-12}$	15,787
K_3	1	9	2.07×10^{-8}; 5.00×10^{-9}	15	$(2.04; 1.80) \times 10^{-5}$	6.14×10^{-7}	1.27×10^{-4}	6.97×10^{-6}; 7.50×10^{-7}	$(5.95; 5.30) \times 10^{-13}$	60,433
K_3	7	0	2.12×10^{-8}; 6.62×10^{-9}	15	$(8.60; 3.79) \times 10^{-5}$	8.26×10^{-5}	–	2.29×10^{-4}; 3.37×10^{-5}	$(3.31; 2.46) \times 10^{-11}$	10,991
K_3	7	1	2.08×10^{-8}; 5.69×10^{-9}	15	$(2.64; 2.79) \times 10^{-5}$	1.94×10^{-6}	4.64×10^{-4}	1.33×10^{-5}; 2.03×10^{-6}	$(1.66; 1.50) \times 10^{-12}$	15,801
K_3	7	9	1.99×10^{-8}; 4.58×10^{-9}	16	$(1.45; 1.45) \times 10^{-5}$	5.63×10^{-7}	1.21×10^{-4}	5.09×10^{-6}; 6.46×10^{-7}	$(5.27; 4.63) \times 10^{-13}$	60,518

Table G.0.3.: Detailed results of the nominal representative covariance analysis cases for the K1 and K2 orbits. The table summarises the results displayed in Figure 5.2.1.

Orbit	Arc length [days]	Nb. landers	$RMS\,(\sigma)$ deg. 2 cos & sin [−]	Max. deg. gravity [−]	σ $(\Re(k_2);\Im(k_2))$ [−]	$\sigma\,(\phi)$ [deg]	$\sigma\,(h_2)$ [−]	$\sigma\,(\alpha;\delta)$ [deg]	$\sigma\left(\dot{\alpha};\dot{\delta}\right)$ [deg s^{-1}]	Nb. observations [−]
K_1	1	0	$(2.58;1.44)\times 10^{-8}$	15	$(1.94;1.27)\times 10^{-4}$	1.82×10^{-4}	–	$(9.03;1.15)\times 10^{-4}$	$(7.88;9.84)\times 10^{-11}$	10,541
K_1	1	1	$(2.40;1.00)\times 10^{-8}$	15	$(5.78;5.02)\times 10^{-5}$	3.04×10^{-6}	6.52×10^{-4}	2.56×10^{-5}; 4.57×10^{-6}	$(3.13;3.10)\times 10^{-12}$	14,552
K_1	1	9	2.40×10^{-8}; 6.17×10^{-9}	15	$(1.75;1.76)\times 10^{-5}$	5.39×10^{-7}	1.17×10^{-4}	7.12×10^{-6} 7.08×10^{-7}	$(5.51;5.06)\times 10^{-13}$	57,924
K_1	7	0	2.23×10^{-8}; 8.08×10^{-9}	15	$(5.47;2.96)\times 10^{-5}$	4.78×10^{-5}	–	1.91×10^{-4}; 2.34×10^{-5}	$(2.50;1.98)\times 10^{-11}$	10,528
K_1	7	1	2.20×10^{-8}; 7.40×10^{-9}	15	$(2.56;2.27)\times 10^{-5}$	2.05×10^{-6}	4.82×10^{-4}	1.26×10^{-5}; 2.59×10^{-6}	$(2.05;1.90)\times 10^{-12}$	14,524
K_1	7	9	2.15×10^{-8}; 5.84×10^{-9}	15	$(1.39;1.36)\times 10^{-5}$	4.78×10^{-7}	1.13×10^{-4}	4.84×10^{-6}; 5.99×10^{-7}	$(4.77;4.26)\times 10^{-13}$	57,891
K_2	1	0	$(2.78;1.03)\times 10^{-8}$	14	$(2.92;2.01)\times 10^{-4}$	2.95×10^{-4}	–	1.22×10^{-3}; 1.80×10^{-4}	$(1.67;1.42)\times 10^{-10}$	10,690
K_2	1	1	2.36×10^{-8};8.09×10^{-9}	14	$(5.89;5.85)\times 10^{-5}$	2.59×10^{-6}	6.39×10^{-4}	2.42×10^{-5}; 3.19×10^{-6}	$(2.38;2.12)\times 10^{-12}$	15,879
K_2	1	9	2.16×10^{-8}; 5.45×10^{-9}	15	$(1.88;1.99)\times 10^{-5}$	6.29×10^{-7}	1.31×10^{-4}	6.96×10^{-6}; 7.80×10^{-7}	$(6.10;5.58)\times 10^{-13}$	61,917
K_2	7	0	2.20×10^{-8}; 6.22×10^{-9}	14	$(6.25;3.08)\times 10^{-5}$	6.41×10^{-5}	–	2.55×10^{-4}; 3.26×10^{-5}	$(3.18;2.61)\times 10^{-11}$	10,688
K_2	7	1	2.16×10^{-8}; 5.33×10^{-9}	14	$(1.96;2.10)\times 10^{-5}$	1.89×10^{-6}	4.53×10^{-4}	1.32×10^{-5}; 2.05×10^{-6}	$(1.83;1.51)\times 10^{-12}$	15,882
K_2	7	9	2.12×10^{-8}; 4.60×10^{-9}	15	$(1.09;1.14)\times 10^{-5}$	9.54×10^{-9}	1.27×10^{-4}	4.98×10^{-6}; 6.39×10^{-7}	$(5.45;4.59)\times 10^{-13}$	61,956

H. Additional results of lander location covariance analysis

This chapter provides the results of the investigation of the impact of the location of a single lander (FC3.3 in Figure 3.0.1) on the figures of merit listed in Section 3.3.2. The methodology followed to produce the results is described in Section 3.3.4, while the discussion of the results is provided in Section 5.3. The results reported in this section for the K_2 and K_3 orbits (refer to Table 3.1.5 for the details of the orbit solutions) follow the trends discussed in Section 5.3.

H.1. K2 orbit solution

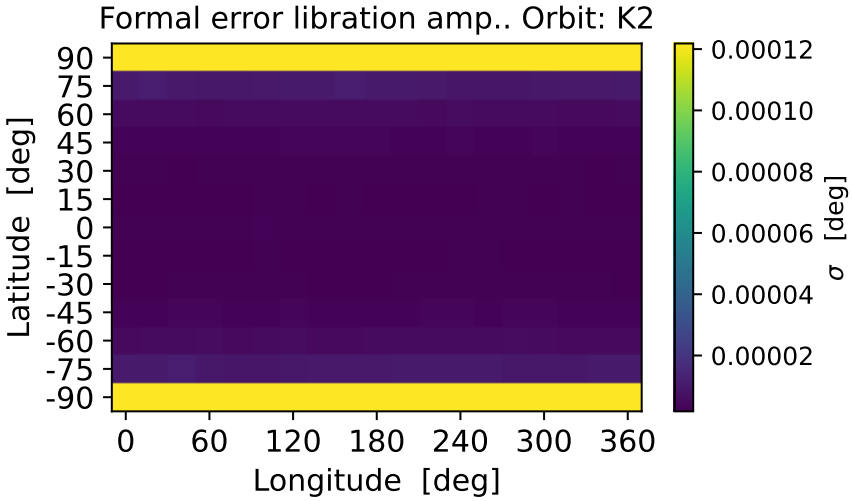

Figure H.1.1.: Formal error for the libration amplitude as a function of the lander location. Orbit solution: K_2.

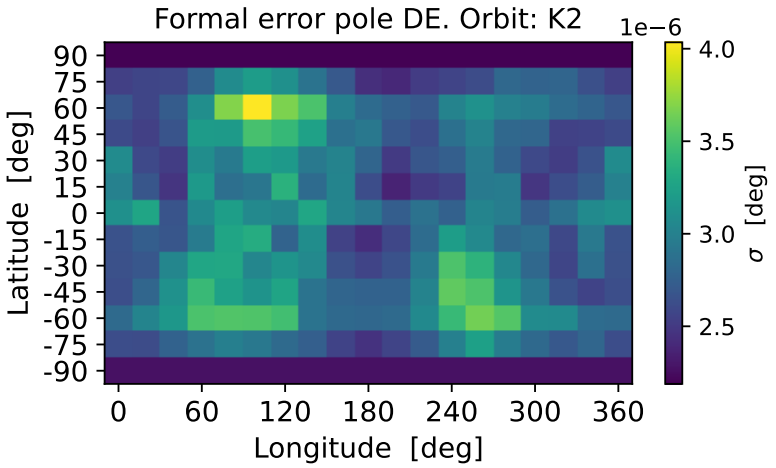

Figure H.1.2.: Formal error for the rotation pole declination as a function of the lander location. Orbit solution: K_2.

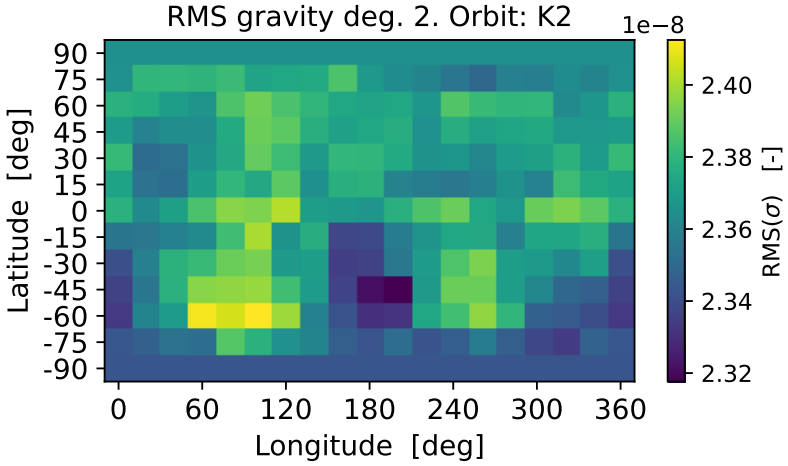

Figure H.1.3.: RMS of the formal error for the degree 2 gravity coefficients as a function of the lander location. Orbit solution: K_2.

H.2. K3 orbit solution

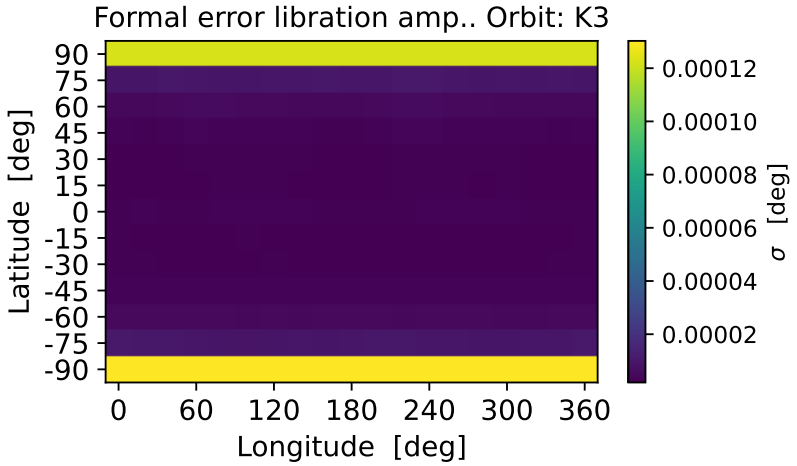

Figure H.2.1.: Formal error for the libration amplitude as a function of the lander location. Orbit solution: K_3.

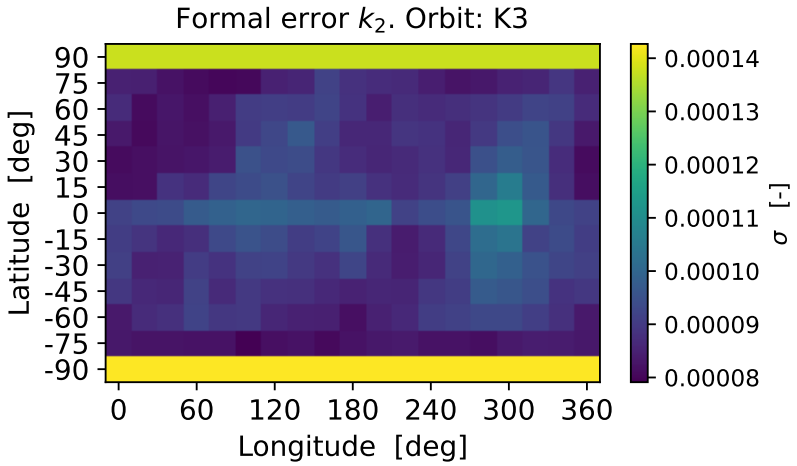

Figure H.2.2.: Formal error for the k_2 Love number as a function of the lander location. The following quantity is plotted: $\sqrt{(\sigma(\Re(k_2)))^2 + (\sigma(\Im(k_2)))^2}$. Orbit solution: K_3.

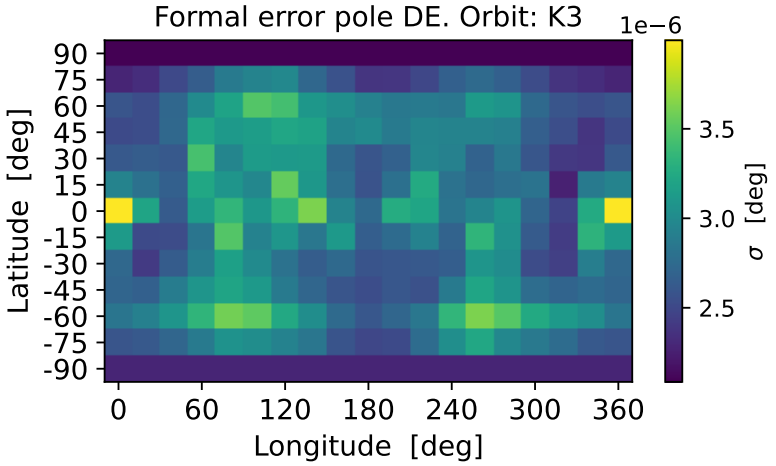

Figure H.2.3.: Formal error for the rotation pole declination as function of the lander location. Orbit solution: K_3.

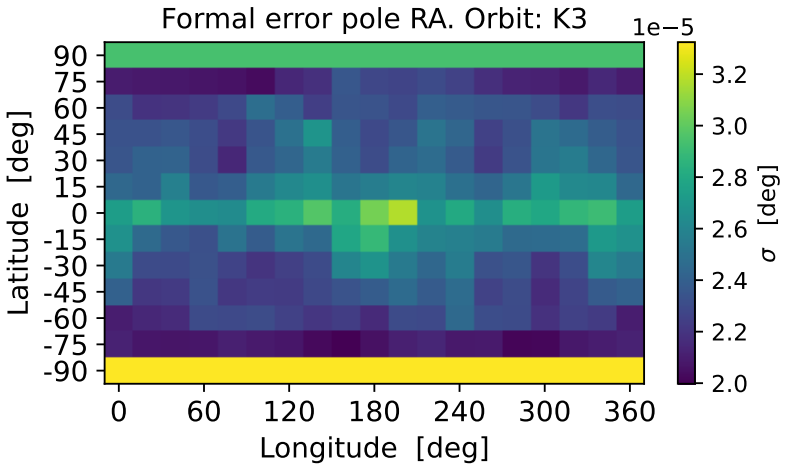

Figure H.2.4.: Formal error for the rotation pole right ascension as a function of the lander location. Orbit solution: K_3.

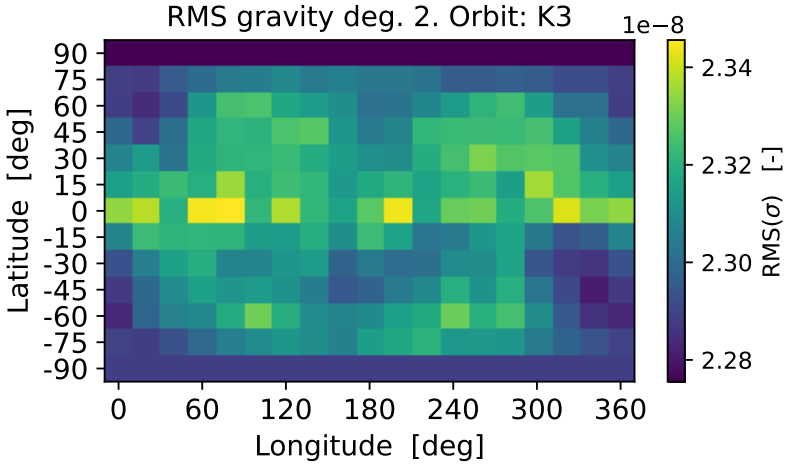

Figure H.2.5.: RMS of the formal error for the degree 2 gravity coefficients as a function of the lander location. Orbit solution: K_3.

I. Additional results of the interior parameters analysis

This chapter provides the results produced in Section 5.5 for the preliminary full MC analysis (FC4.2 in the flow chart of Figure 3.0.1), regarding the real component of the gravitational Love number. The methodology followed to produce these results is described in Section 3.4.2. The results displayed here show the similar trends to those discussed in Section 5.5 for the real component of the h_2 Love number.

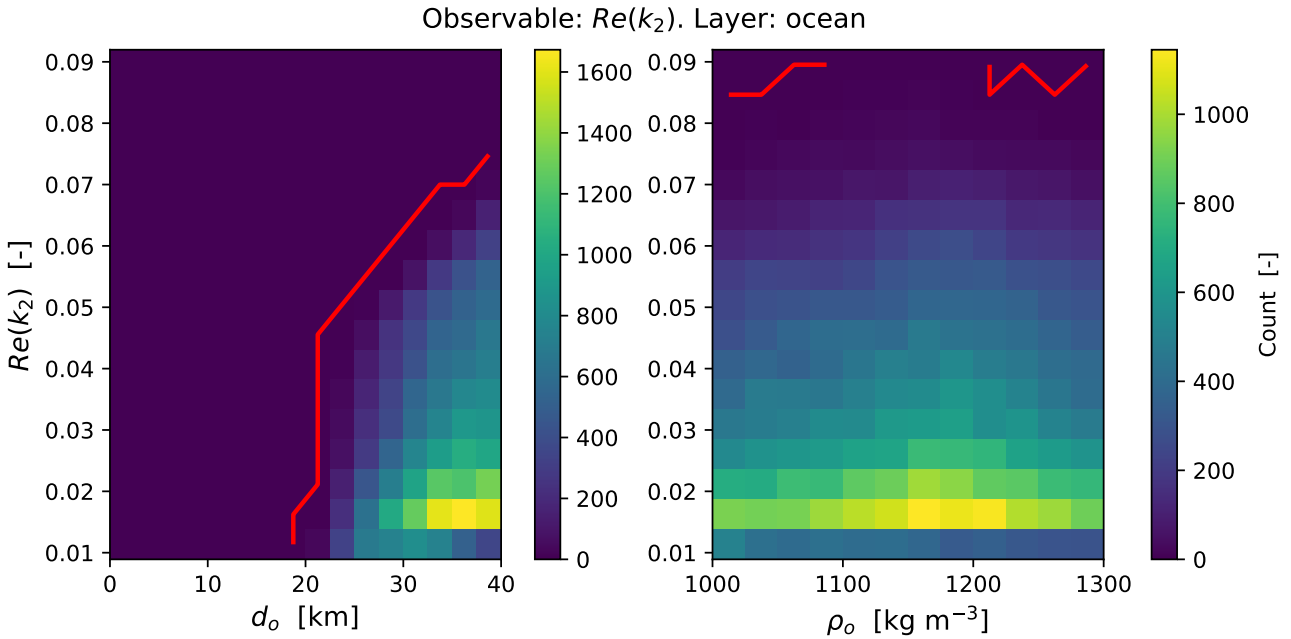

Figure I.0.1.: Scatter plots of the preliminary full MC analysis, for the k_2 Love number and ocean parameters. The plotted samples are in agreement with the libration observations by Thomas et al. (2016) and with the ranges reported in Table 3.4.6.

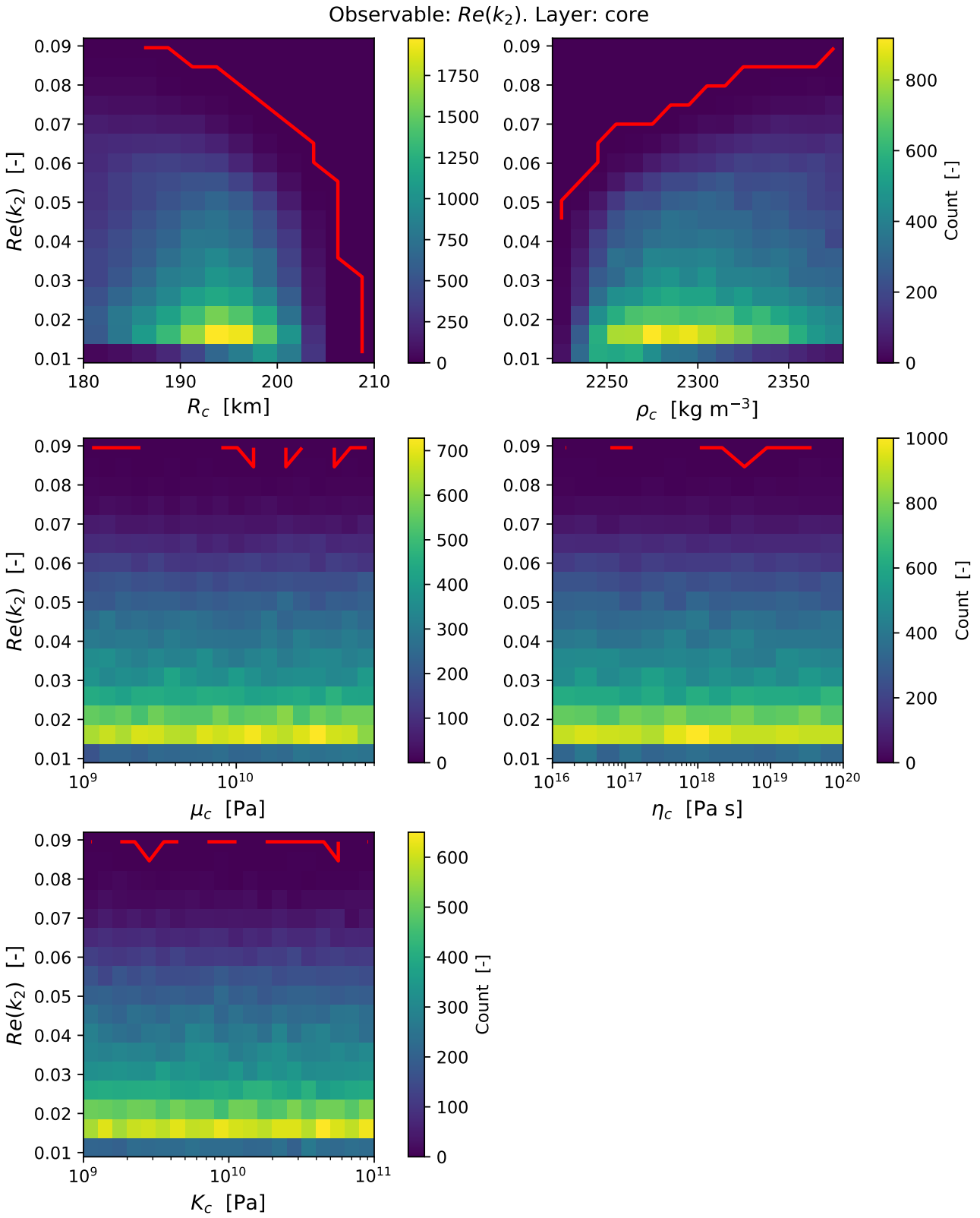

Figure I.0.2.: Density plot of the preliminary full MC analysis, for the k_2 Love number and core parameters. The plotted samples are in agreement with the libration observations by Thomas et al. (2016) and with the density ranges reported in Table 3.4.6.

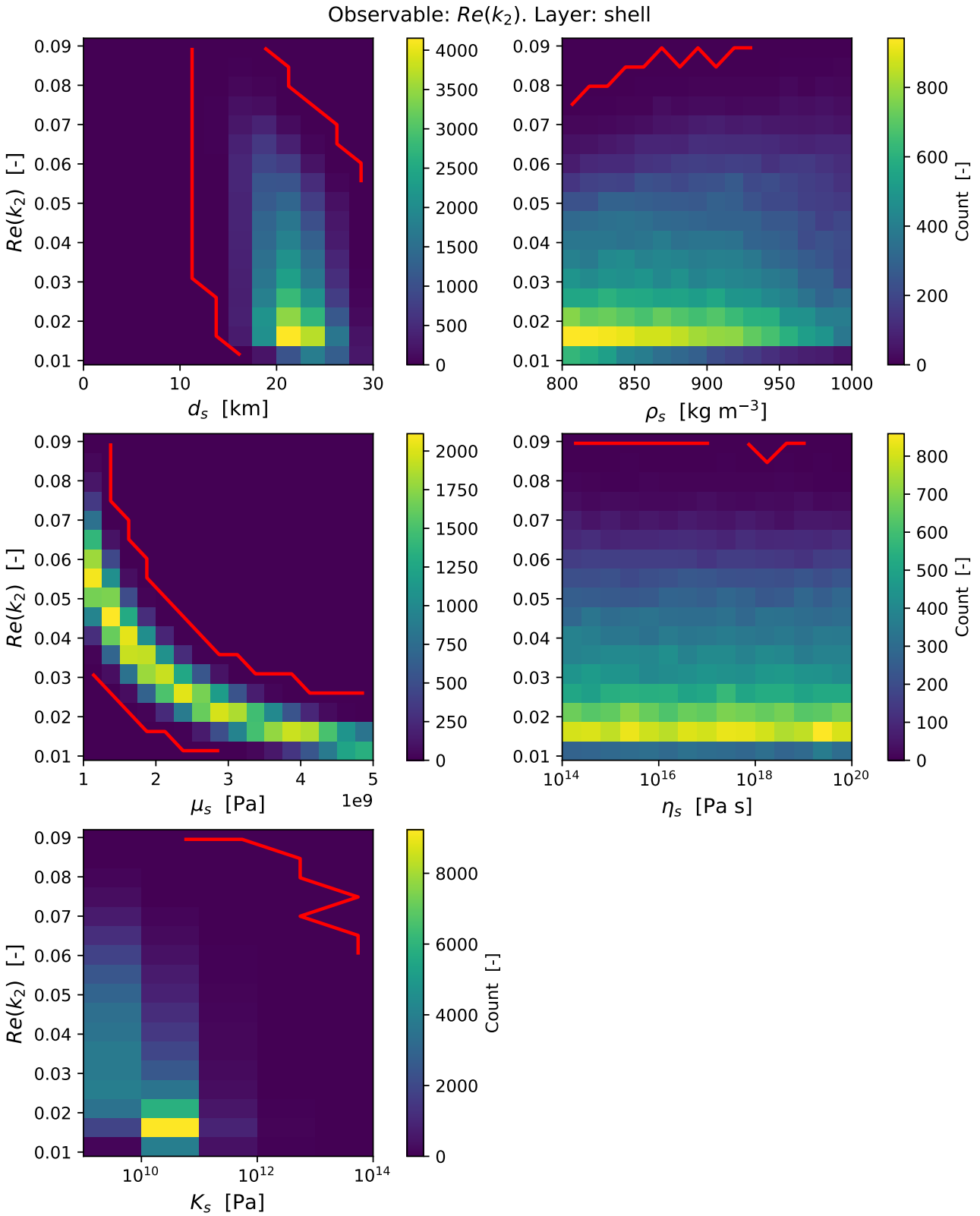

Figure I.0.3.: Scatter plots of the preliminary full MC analysis, for the k_2 Love number and ice shell parameters. The plotted samples are in agreement with the libration observations by Thomas et al. (2016) and with the ranges reported in Table 3.4.6.

Bibliography

Archinal, B. A., Acton, C. H., A'Hearn, M. F., Conrad, A., Consolmagno, G. J., Duxbury, T., Hestroffer, D., Hilton, J. L., Kirk, R. L., Klioner, S. A., McCarthy, D., Meech, K., Oberst, J., Ping, J., Seidelmann, P. K., Tholen, D. J., Thomas, P. C., & Williams, I. P. (2018). Report of the IAU Working Group on Cartographic Coordinates and Rotational Elements: 2015. *Celestial Mechanics and Dynamical Astronomy*, *130*(3). https://doi.org/10.1007/s10569-017-9805-5

Armstrong, J. W., Estabrook, F. B., Asmar, S. W., Iess, L., & Tortora, P. (2008). Reducing antenna mechanical noise in precision spacecraft tracking. *Radio Science*, *43*(3). https://doi.org/10.1029/2007RS003766

Asmar, S. W., Armstrong, J. W., Iess, L., & Tortora, P. (2005). Spacecraft Doppler tracking: Noise budget and accuracy achievable in precision radio science observations. *Radio Science*, *40*(2). https://doi.org/10.1029/2004RS003101

Asmar, S. W. (2022). *Radio Science Techniques for Deep Space Exploration*. https://doi.org/10.1002/9781119734178

Auer Wilkins, S., Oberst, J., Stark, A., Hussmann, H., Benedikter, A., & Neumann, W. (2025). Search for Stable Orbits around Saturn's Moon Enceladus using Numerical Modeling. *EPSC-DPS Joint Meeting 2025*. https://doi.org/10.5194/epsc-dps2025-1966

Bagheri, A., Simons, M., Park, R. S., Berne, A., Vance, S. D., & Daswani, M. M. (2025). Geodetic Exploration of the Interior Structure of Enceladus. http://arxiv.org/abs/2505.14743

Baland, R. M., Tobie, G., Lefèvre, A., & Van Hoolst, T. (2014). Titan's internal structure inferred from its gravity field, shape, and rotation state. *Icarus*, *237*, 29–41. https://doi.org/10.1016/j.icarus.2014.04.007

Baland, R. M., & Van Hoolst, T. (2010). Librations of the Galilean satellites: The influence of global internal liquid layers. *Icarus*, *209*(2), 651–664. https://doi.org/10.1016/j.icarus.2010.04.004

Baland, R. M., Yseboodt, M., & Van Hoolst, T. (2016). The obliquity of Enceladus. *Icarus*, *268*, 12–31. https://doi.org/10.1016/j.icarus.2015.11.039

Behounkova, M., Soucek, O., Hron, J., & Cadec, O. (2017). Plume activity and tidal deformation on enceladus influenced by faults and variable ice shell thickness. *Astrobiology*, *17*(9), 941–954. https://doi.org/10.1089/ast.2016.1629

Bellerose, J., Roth, D., & Wagner, S. (2018). The cassini mission: Reconstructing thirteen years of the most complex gravity-assist trajectory flown to date. *15th International Conference on Space Operations, 2018*. https://doi.org/10.2514/6.2018-2646

Benedikter, A., Wickhusen, K., Hussmann, H., Stark, A., Damme, F., Rodriguez-Cassola, M., & Krieger, G. (2022). Periodic orbits for interferometric and tomographic radar imaging of Saturn's moon Enceladus. *Acta Astronautica*, *191*, 326–345. https://doi.org/10.1016/j.actaastro.2021.10.041

Berne, A., Simons, M., Keane, J. T., & Park, R. S. (2023). Inferring the Mean Thickness of the Outer Ice Shell of Enceladus From Diurnal Crustal Deformation. *Journal of Geophysical Research: Planets*, *128*(6). https://doi.org/10.1029/2022JE007712

Bertone, S., Le Poncin-Lafitte, C., Rosenblatt, P., Lainey, V., Marty, J. C., & Angonin, M. C. (2018). Impact analysis of the transponder time delay on radio-tracking observables. *Advances in Space Research*, *61*(1), 89–96. https://doi.org/10.1016/j.asr.2017.09.003

Bertotti, B., Comoretto, G., & Iess, L. (1992). Doppler tracking of spacecraft with multi frequency links. *Astronomy and Astrophysics*, *269*, 608–616.

Bertotti, B., Iess, L., & Tortora, P. (2003). A test of general relativity using radio links with the Cassini spacecraft. *Nature*, *425*(6956), 374–376. https://doi.org/10.1038/nature01997

Beuthe, M. (2018). Enceladus's crust as a non-uniform thin shell: I tidal deformations. *Icarus*, *302*, 145–174. https://doi.org/10.1016/j.icarus.2017.11.009

Beuthe, M., Rivoldini, A., & Trinh, A. (2016). Enceladus's and Dione's floating ice shells supported by minimum stress isostasy. *Geophysical Research Letters*, *43*(19), 088–10. https://doi.org/10.1002/2016GL070650

Bierman, G. (1977). *Factorization Methods for Discrete Sequential Estimation*.

Bills, B. G., & Scott, B. R. (2022). Rotation models for the Galilean satellites. *Planetary and Space Science*, *219*. https://doi.org/10.1016/j.pss.2022.105474

Bunce, E., Grasset, O., Hamp, R., Jones, G., Le Gall, A., Lucchetti, A., Postberg, F., Prieto-Ballesteros, O., Roth, L., Tortora, P., & Vorburger, A. (2024, Mar.). *Report of the Expert Committee for the Large-class mission in ESA's Voyage 2050 plan covering the science theme "Moons of the Giant Planets"* (tech. rep.). European Space Agency. https://www.cosmos.esa.int/web/voyage-2050/updates

Čadek, O., Tobie, G., Van Hoolst, T., Massé, M., Choblet, G., Lefèvre, A., Mitri, G., Baland, R. M., Běhounková, M., Bourgeois, O., & Trinh, A. (2016, June). Enceladus's internal ocean and ice shell constrained from Cassini gravity, shape, and libration data. https://doi.org/10.1002/2016GL068634

Chib, S. (2001). Handbook of Econometrics.

Comstock, R. L., & Bills, B. G. (2003). A solar system survey of forced librations in longitude. *Journal of Geophysical Research: Planets*, *108*(9). https://doi.org/10.1029/2003je002100

Correia, A. C. (2015). Stellar and planetary Cassini states. *Astronomy and Astrophysics*, *582*. https://doi.org/10.1051/0004-6361/201525939

De Tiberis, F., Simone, L., Gelfusa, D., Simone, P., Viola, R., Santoni, A., Cocciolillo, O., Ziarelli, M., Barletta, F., Salerno, N., Maffei, M., & Nanni, V. (2011). The X/X/KA-band deep space transponder for the BepiColombo mission to mercury. *Acta Astronautica*, *68*(5-6), 591–598. https://doi.org/10.1016/j.actaastro.2010.01.023

Di Benedetto, M., Cappuccio, P., Molli, S., Federici, L., & Zavoli, A. (2021). *Analysis of 3GM Callisto Gravity Experiment of the JUICE Mission* (tech. rep.).

Dirkx, D., Vermeersen, L. L., Noomen, R., & Visser, P. N. (2014). Phobos laser ranging: Numerical Geodesy experiments for Martian system science. *Planetary and Space Science*, *99*, 84–102. https://doi.org/10.1016/j.pss.2014.03.022

Dirkx, D., Fayolle, M., Garrett, G., Avillez, M., Cowan, K., Cowan, S., Encarnacao, J., Lombrana, C. F., Gaffarel, J., Hener, J., et al. (2022). The open-source astrodynamics tudatpy software–overview for planetary mission design and science analysis. *EPSC2022*, (EPSC2022-253).

Dirkx, D., Prochazka, I., Bauer, S., Visser, P., Noomen, R., Gurvits, L. I., & Vermeersen, B. (2019). Laser and radio tracking for planetary science missions—a comparison. *Journal of Geodesy*, *93*(11), 2405–2420. https://doi.org/10.1007/s00190-018-1171-x

Drilleau, M., Samuel, H., Rivoldini, A., Panning, M., & Lognonné, P. (2021). Bayesian inversion of the Martian structure using geodynamic constraints. *Geophysical Journal International*, *226*(3), 1615–1644. https://doi.org/10.1093/gji/ggab105

Durante, D., Parisi, M., Serra, D., Zannoni, M., Notaro, V., Racioppa, P., Buccino, D. R., Lari, G., Gomez Casajus, L., Iess, L., Folkner, W. M., Tommei, G., Tortora, P., & Bolton, S. J. (2020). Jupiter's Gravity Field Halfway Through the Juno Mission. *Geophysical Research Letters*, *47*(4). https://doi.org/10.1029/2019GL086572

Durante, D., Mastrogiuseppe, M., Carli, E., Poggiali, V., Di Ruscio, A., Notaro, V., & Iess, L. (2024). Analysis of Cassini Altimetric Crossovers on Titan. *Remote Sensing*, *16*(12). https://doi.org/10.3390/rs16122209

Efroimsky, M., & Makarov, V. V. (2013). Tidal friction and tidal lagging. Applicability limitations of a popular formula for the tidal torque. *Astrophysical Journal*, *764*(1). https://doi.org/10.1088/0004-637X/764/1/26

Ermakov, A. I., Park, R. S., & Bills, B. G. (2018). Power Laws of Topography and Gravity Spectra of the Solar System Bodies. *Journal of Geophysical Research: Planets*, *123*(8), 2038–2064. https://doi.org/10.1029/2018JE005562

Ermakov, A. I., Park, R. S., Roa, J., Castillo-Rogez, J. C., Keane, J. T., Nimmo, F., Kite, E. S., Sotin, C., Lazio, T. J. W., Steinbrügge, G., Howell, S. M., Bills, B. G., Hemingway, D. J., Viswanathan, V., Tobie, G., & Lainey, V. (2021). A Recipe for the Geophysical Exploration of Enceladus. *Planetary Science Journal*, *2*(4). https://doi.org/10.3847/PSJ/ac06d2

Estefan, J. A., & Sovers, O. J. (1994, Oct.). *A Comparative Survey of Current and Proposed Tropospheric Refraction-Delay Models for DSN Radio Metric Data Calibration* (tech. rep.). Jet Propulsion Laboratory. Pasadena.

Fayolle, M., Dirkx, D., Lainey, V., Gurvits, L. I., & Visser, P. N. (2022). Decoupled and coupled moons' ephemerides estimation strategies application to the JUICE mission. *Planetary and Space Science*, *219*. https://doi.org/10.1016/j.pss.2022.105531

Fayolle, M., Magnanini, A., Lainey, V., Dirkx, D., Zannoni, M., & Tortora, P. (2023). Combining astrometry and JUICE-Europa Clipper radio science to improve the ephemerides of the Galilean moons. *Astronomy and Astrophysics*, *677*. https://doi.org/10.1051/0004-6361/202347065

Fayolle, S. (2025). *Natural satellites ephemerides: The Galilean moons' dynamics in the JUICE-Europa Clipper era* [Doctoral dissertation, Delft University of Technology]. https://doi.org/10.4233/uuid:667192b7-5555-49df-b2c6-2479942fc5f2

Filice, V., Cascioli, G., Le Maistre, S., Baland, R. M., Trinh, A., Mazarico, E., & Goossens, S. (2025). Informed Design of a Gravity Science Experiment for the Future Geophysical Investigation of the Uranian Moons. *Planetary Science Journal*, *6*(2). https://doi.org/10.3847/PSJ/ada7ef

Flandes, A., Mirón-Enríquez, P. E., & Ramírez-Cabañas, A. K. (2024). Geysers' Dust Dynamics Inside the Hill Sphere of Enceladus. *Geophysical Research Letters*, *51*(1). https://doi.org/10.1029/2023GL105298

Gammon, P. H., Kiefte, H., Clouter, M. J., & Denner, W. W. (1983). Elastic Constants of Artificial and Natural Ice Samples by Brillouin Spectroscopy. *Journal of Glaciology*, *29*(103), 433–460. https://doi.org/10.3189/s0022143000030355

Genova, A., Goossens, S., Mazarico, E., Lemoine, F. G., Neumann, G. A., Kuang, W., Sabaka, T. J., Hauck, S. A., Smith, D. E., Solomon, S. C., & Zuber, M. T. (2019). Geodetic Evidence That Mercury Has A Solid Inner Core. *Geophysical Research Letters*, *46*(7), 3625–3633. https://doi.org/10.1029/2018GL081135

Genova, A., Parisi, M., Gargiulo, A. M., Petricca, F., Andolfo, S., Torrini, T., Del Vecchio, E., Glein, C. R., Cable, M. L., Phillips, C. B., Bradley, N. E., Restrepo, R. L., Mages, D. M., Babuscia, A., & Lunine, J. I. (2024). Gravity Investigation to Characterize Enceladus's Ocean and Interior. *Planetary Science Journal*, *5*(2). https://doi.org/10.3847/PSJ/ad16df

Genova, A., & Petricca, F. (2021). Deep-space navigation with intersatellite radio tracking. https://doi.org/10.2514/1.G005610

Gioia, G., Chakraborty, P., Marshak, S., & Kieffer, S. W. (2007). *Unified model of tectonics and heat transport in a frigid Enceladus* (tech. rep.). www.pnas.orgcgidoi10.1073pnas.0706018104

Gomez Casajus, L., Ermakov, A. I., Zannoni, M., Keane, J. T., Stevenson, D., Buccino, D. R., Durante, D., Parisi, M., Park, R. S., Tortora, P., & Bolton, S. J. (2022). Gravity Field of Ganymede After the Juno Extended Mission. *Geophysical Research Letters*, *49*(24). https://doi.org/10.1029/2022GL099475

Goossens, S., Sabaka, T. J., Wieczorek, M. A., Neumann, G. A., Mazarico, E., Lemoine, F. G., Nicholas, J. B., Smith, D. E., & Zuber, M. T. (2020). High-Resolution Gravity Field Models from GRAIL Data and Implications for Models of the Density Structure of the Moon's Crust. *Journal of Geophysical Research: Planets*, *125*(2). https://doi.org/10.1029/2019JE006086

Hemingway, Iess, L., Tadjeddine, R., & Tobie, G. (2018). The Interior of Enceladus. In *Enceladus and the icy moons of saturn* (pp. 57–77). The University of Arizona Press. https://doi.org/10.2458/azu{_}uapress{_}9780816537075-ch004

Hemingway & Mittal, T. (2019). Enceladus's ice shell structure as a window on internal heat production. *Icarus*, *332*, 111–131. https://doi.org/10.1016/j.icarus.2019.03.011

Hoolst, T. V., Baland, R. M., & Trinh, A. (2016). The diurnal libration and interior structure of Enceladus. *Icarus*, *277*, 311–318. https://doi.org/10.1016/j.icarus.2016.05.025

Hussmann, H., Shoji, D., Steinbrügge, G., Stark, A., & Sohl, F. (2016). Constraints on dissipation in the deep interiors of Ganymede and Europa from tidal phase-lags. *Celestial Mechanics and Dynamical Astronomy*, *126*(1-3), 131–144. https://doi.org/10.1007/s10569-016-9721-0

Iess, L., Militzer, B., Kaspi, Y., Nicholson, P., Durante, D., Racioppa, P., Anabtawi, A., Galanti, E., Hubbard, W., Mariani, M. J., Tortora, P., Wahl, S., & Zannoni, M. (2019). Measurement and implications of Saturn's gravity field and ring mass. *Science*, *364*(6445). https://doi.org/10.1126/science.aat2965

Iess, L., Stevenson, D. J., Parisi, M., Hemingway, D., Jacobson, R. A., Lunine, J. I., Nimmo, F., Armstrong, J. W., Asmar, S. W., Ducci, M., & Tortora, P. (2014a). Supplementary Material for The gravity field and interior structure of Enceladus. *Science*, *344*(6179), 78–80. https://doi.org/10.1126/science.1250551

Iess, L., Stevenson, D. J., Parisi, M., Hemingway, D., Jacobson, R. A., Lunine, J. I., Nimmo, F., Armstrong, J. W., Asmar, S. W., Ducci, M., & Tortora, P. (2014b). The Gravity Field and Interior Structure of Enceladus. *Science*, *344*(6179), 78–80. https://doi.org/10.1126/science.1250808

Iess, L., Di Benedetto, M., James, N., Mercolino, M., Simone, L., & Tortora, P. (2014). Astra: Interdisciplinary study on enhancement of the end-to-end accuracy for spacecraft tracking techniques. *Acta Astronautica*, *94*(2), 699–707. https://doi.org/10.1016/j.actaastro.2013.06.011

Jacobson, R. A. (2010). THE ORBITS AND MASSES OF THE MARTIAN SATELLITES AND THE LIBRATION OF PHOBOS. *The Astronomical Journal*, *139*(2), 668. https://doi.org/10.1088/0004-6256/139/2/668

Jacobson, R. A. (2022). The Orbits of the Main Saturnian Satellites, the Saturnian System Gravity Field, and the Orientation of Saturn's Pole*. *The Astronomical Journal*, *164*(5), 199. https://doi.org/10.3847/1538-3881/ac90c9

Jacobson, R. A., Brozović, M., Mastrodemos, N., Riedel, J. E., & Sheppard, S. S. (2022). Ephemerides of the Irregular Saturnian Satellites from Earth-based Astrometry and Cassini Imaging*. *The Astronomical Journal*, *164*(6), 240. https://doi.org/10.3847/1538-3881/AC98C7

Jara-Orué, H., & Vermeersen, B. (2016). Tides on Jupiter's moon Ganymede and their relation to its internal structure. *Netherlands Journal of Geosciences*, *95 (2)*, 191–201. https://doi.org/https://doi.org/10.1017/njg.2015.23

Kinman, P. W., & Berner, J. B. (2003). Two-Way Ranging During Early Mission Phase. *IEEE Aerospace Conference proceedings*, *3-1441*. https://doi.org/10.1109/AERO.2003.1235263

Lainey, V., Noyelles, B., Cooper, N., Rambaux, N., Murray, C., & Park, R. S. (2019). Interior properties of the inner Saturnian moons from space astrometry data. *Icarus*, *326*, 48–62. https://doi.org/10.1016/j.icarus.2019.01.026

Lasagni Manghi, R., Bernacchia, D., Gomez Casajus, L., Zannoni, M., Tortora, P., Martellucci, A., De Vicente, J., Villalvilla, J., Maschwitz, G., Cappuccio, P., & Iess, L. (2023). Tropospheric Delay Calibration System Performance During the First Two BepiColombo Solar Conjunctions. *Radio Science*, *58*(2). https://doi.org/10.1029/2022RS007614

Le Maistre, S., Rosenblatt, P., Rambaux, N., Castillo-Rogez, J. C., Dehant, V., & Marty, J. C. (2013). Phobos interior from librations determination using Doppler and star tracker measurements. *Planetary and Space Science*, *85*, 106–122. https://doi.org/10.1016/j.pss.2013.06.015

Le Maistre, S., Rosenblatt, P., Rivoldini, A., Dehant, V., Marty, J. C., & Karatekin, O. (2012). Lander radio science experiment with a direct link between Mars and the Earth. *Planetary and Space Science*, *68*(1), 105–122. https://doi.org/10.1016/j.pss.2011.12.020

Lee, A. Y., Wang, E. K., Pilinski, E. B., MacAla, G. A., & Feldman, A. W. (2013). Estimation and modeling of Enceladus plume jet density using Cassini flight data. *Journal of Spacecraft and Rockets*, *50*(2), 317–325. https://doi.org/10.2514/1.A32344

Leinen, S., Becker, M., Dow, ; J., Feltens, J., & Sauermann, K. (2007). Geodetic Determination of Radio Telescope Antenna Reference Point and Rotation Axis Parameters. *Journal of Surveying Engineering*, *133*(2), 41–51. https://doi.org/10.1061/ASCE0733-94532007133:241

Lemoine, F. G., Goossens, S., Sabaka, T. J., Nicholas, J. B., Mazarico, E., Rowlands, D. D., Loomis, B. D., Chinn, D. S., Caprette, D. S., Neumann, G. A., Smith, D. E., & Zuber, M. T. (2013). High-degree gravity models from GRAIL primary mission data. *Journal of Geophysical Research: Planets*, *118*(8), 1676–1698. https://doi.org/10.1002/jgre.20118

Lorenz, R. D., & Burk, T. A. (2018). Enceladus plume density from Cassini spacecraft attitude control data. *Icarus*, *300*, 200–202. https://doi.org/10.1016/j.icarus.2017.09.003

Magnanini, A., Zannoni, M., Casajus, L. G., Tortora, P., Lainey, V., Mazarico, E., Park, R. S., & Iess, L. (2024). Joint analysis of JUICE and Europa Clipper tracking data to study the Jovian system ephemerides and dissipative parameters. *Astronomy and Astrophysics*, *687*. https://doi.org/10.1051/0004-6361/202347616

Matsuyama, I., Beuthe, M., Hay, H. C., Nimmo, F., & Kamata, S. (2018). Ocean tidal heating in icy satellites with solid shells. *Icarus*, *312*, 208–230. https://doi.org/10.1016/j.icarus.2018.04.013

McKinnon, W. B. (2013). The shape of Enceladus as explained by an irregular core: Implications for gravity, libration, and survival of its subsurface ocean. *Journal of Geophysical Research: Planets*, *118*(9), 1775–1788. https://doi.org/10.1002/jgre.20122

Mckinnon, W. B. (2015). Effect of Enceladus's rapid synchronous spin on interpretation of Cassini gravity. *Geophysical Research Letters*, *42*, 2137–2143. https://doi.org/10.1002/2015GL063384

Mitri, G., Meriggiola, R., Hayes, A., Lefevre, A., Tobie, G., Genova, A., Lunine, J. I., & Zebker, H. (2014). Shape, topography, gravity anomalies and tidal deformation of Titan. *Icarus*, *236*, 169–177. https://doi.org/10.1016/j.icarus.2014.03.018

Montenbruck, O., Gill, E., & Mahooti, M. (2000). *Satellite Orbits*.

Mott, P. H., Dorgan, J. R., & Roland, C. M. (2008). The bulk modulus and Poisson's ratio of "incompressible" materials. *Journal of Sound and Vibration*, *312*(4-5), 572–575. https://doi.org/10.1016/j.jsv.2008.01.026

Moyer, T. D. (1981). Transformation from proper time on Earth to coordinate time in Solar System barycentric space-time frame of reference. *Celestial Mechanics*, *23*, 33–56. https://doi.org/https://doi.org/10.1007/BF01228543

Moyer, T. D. (2000, Oct.). *Formulation for Observed and Computed Values of Deep Space Network Data Types for Navigation*.

Murray, C. D., & Dermott, S. F. (2000). *Solar system dynamics*. Cambridge University Press.

Nimmo, F., Bills, B. G., & Thomas, P. C. (2011). Geophysical implications of the long-wavelength topography of the Saturnian satellites. *Journal of Geophysical Research: Planets*, *116*(11). https://doi.org/10.1029/2011JE003835

Nimmo, F., Spencer, J. R., Pappalardo, R. T., & Mullen, M. E. (2007). Shear heating as the origin of the plumes and heat flux on Enceladus. *Nature*, *447*(7142), 289–291. https://doi.org/10.1038/nature05783

Oberst, J., Hussmann, H., Giese, B., Sohl, F., Shoji, D., Stark, A., Wickhusen, K., & Wählisch, M. (2017). Enceladus geodetic framework. *International Archives of the Photogrammetry, Remote Sensing and Spatial Information Sciences - ISPRS Archives*, *42*(3W1), 113–118. https://doi.org/10.5194/isprs-archives-XLII-3-W1-113-2017

Parisi, M., Iess, L., & Finocchiaro, S. (2014). *The gravity fields of Ganymede, Callisto and Europa: how well can JUICE do?* (Tech. rep.).

Park, R. S., Mastrodemos, N., Jacobson, R. A., Berne, A., Vaughan, A. T., Hemingway, D. J., Leonard, E. J., Castillo-Rogez, J. C., Cockell, C. S., Keane, J. T., Konopliv, A. S., Nimmo, F., Riedel, J. E., Simons, M., & Vance, S. (2024). The Global Shape, Gravity Field, and Libration of Enceladus. *Journal of Geophysical Research: Planets*, *129*(1). https://doi.org/10.1029/2023JE008054

Park, R. S., Folkner, W. M., Williams, J. G., & Boggs, D. H. (2021). The JPL Planetary and Lunar Ephemerides DE440 and DE441. *The Astronomical Journal*, *161*(3), 105. https://doi.org/10.3847/1538-3881/ABD414

Peale, S. J., & Cassen, P. (1978). Contribution of Tidal Dissipation to Lunar Thermal History. *Icarus*, *36*, 245–269.

Petit, G., & Luzum, B. (2010). *IERS Conventions (2010). IERS Technical Note No.36* (tech. rep.). http://www.iers.org/TN36/

Petricca, F., Genova, A., Castillo-Rogez, J. C., Styczinski, M. J., Cochrane, C. J., & Vance, S. D. (2023). Characterization of Icy Moon Hydrospheres Through Joint Inversion of Gravity and Magnetic Field Measurements. *Geophysical Research Letters*, *50*(17). https://doi.org/10.1029/2023GL104016

Porco, C. C., Helfenstein, P., Thomas, P. C., Ingersoll, A. P., Wisdom, J., West, R., Neukum, G., Denk, T., Wagner, R., Roatsch, T., Kieffer, S., Turtle, E., Mcewen, A., Johnson, T. V., Rathbun, J., Veverka, J., Wilson, D., Perry, J., Spitale, J., … Squyres, S. (2006). Cassini Observes the Active South Pole of Enceladus. *Science*, *311*, 1393–1401. https://www.science.org

Porco, C. C., West, R. A., Squyres, S., Mcewen, A., Thomas, P., Murray, C. D., Delgenio, A., Ingersoll, A. P., Johnson, T. V., Neukum, G., Veverka, J., Dones, L., Brahic, A., Burns, J. A., Haemmerle, V., Knowles, B., Dawson, D., Roatsch, T., Beurle, K., & Owen, W. (2004). *CASSINI IMAGING SCIENCE: INSTRUMENT CHARACTERISTICS AND ANTICIPATED SCIENTIFIC INVESTIGATIONS AT SATURN* (tech. rep.). Kluwer Academic Publishers.

Postberg, F., Kempf, S., Schmidt, J., Brilliantov, N., Beinsen, A., Abel, B., Buck, U., & Srama, R. (2009). Sodium salts in E-ring ice grains from an ocean below the surface of Enceladus. *Nature*, *459*(7250), 1098–1101. https://doi.org/10.1038/nature08046

Rambaux, N., Van Hoolst, T., & Karatekin, Ö. (2011). Librational response of Europa, Ganymede, and Callisto with an ocean for a non-Keplerian orbit. *Astronomy and Astrophysics*, *527*(15). https://doi.org/10.1051/0004-6361/201015304

Rambaux, N., Castillo-Rogez, J. C., Williams, J. G., & Karatekin, Ö. (2010). Librational response of enceladus. *Geophysical Research Letters*, *37*(4). https://doi.org/10.1029/2009GL041465

Rappaport, N. J., Iess, L., Tortora, P., Anabtawi, A., Asmar, S. W., Somenzi, L., & Zingoni, F. (2007). Mass and interior of Enceladus from Cassini data analysis. *Icarus*, *190*(1), 175–178. https://doi.org/10.1016/j.icarus.2007.03.025

Rhoden, A. R., Hurford, T. A., Spitale, J., Henning, W., Huff, E. M., Bland, M. T., & Sajous, S. (2020). The formation of Enceladus' Tiger Stripe Fractures from eccentricity tides. *Earth and Planetary Science Letters*, *544*. https://doi.org/10.1016/j.epsl.2020.116389

Rovira-Navarro, M. (2022). *Tidal Dynamics of Moons with Fluid Layers: From Ice to Lava Worlds* [Doctoral dissertation, Delft University of Technology]. https://doi.org/10.4233/uuid:c6d607fe-11d7-4c14-870e-97d1a9d6e0d5

Rovira-Navarro, M., Katz, R. F., Liao, Y., Wal, W. van der, & Nimmo, F. (2022). The Tides of Enceladus' Porous Core. *Journal of Geophysical Research: Planets*, *127*(5). https://doi.org/10.1029/2021JE007117

Rovira-Navarro, M., Matsuyama, I., & Berne, A. (2024). A Spectral Method to Compute the Tides of Laterally Heterogeneous Bodies. *Planetary Science Journal*, *5*(5). https://doi.org/10.3847/PSJ/ad381f

Russell, R. P., & Lara, M. (2009). On the design of an Enceladus science orbit. *Acta Astronautica*, *65*(1-2), 27–39. https://doi.org/10.1016/j.actaastro.2009.01.021

Sabadini, R., Vermeersen, B., & Cambiotti, G. (2016). *Global Dynamics of the Earth: Applications of Viscoelastic Relaxation Theory to Solid-Earth and Planetary Geophysics* (Second Edition). Springer. https://doi.org/10.1007/978-94-017-7552-6

Scheeres, D. J., Guman, M. D., & Villac, B. F. (2001). Stability analysis of planetary satellite orbiters: Application to the Europa orbiter. *Journal of Guidance, Control, and Dynamics*, *24*(4), 778–787. https://doi.org/10.2514/2.4778

Schubert, G., Anderson, J. D., Travis, B. J., & Palguta, J. (2007). Enceladus: Present internal structure and differentiation by early and long-term radiogenic heating. *Icarus*, *188*(2), 345–355. https://doi.org/10.1016/j.icarus.2006.12.012

Segatz, M., Spohn, T., Ross, M. N., & Schubert, G. (1988). Tidal Dissipation, Surface Heat Flow, and Figure of Viscoelastic Models of Io. *Icarus*, *7*, 187–206.

Sharma, S. (2017). Markov Chain Monte Carlo Methods for Bayesian Data Analysis in Astronomy. *Annual Review of Astronomy and Astrophysics*, *55*, 213–59. https://doi.org/10.1146/annurev-astro-082214

Souček, O., Hron, J., Běhounková, M., & Čadek, O. (2016). Effect of the tiger stripes on the deformation of Saturn's moon Enceladus. *Geophysical Research Letters*, *43*(14), 7417–7423. https://doi.org/10.1002/2016GL069415

Spencer, J. R., Barr, A. C., Esposito, L. W., Helfenstein, P., Ingersoll, A. P., Jaumann, R., McKay, C. P., Nimmo, F., & Waite, J. H. (2009). Enceladus: An active cryovolcanic satellite. In *Saturn from cassini-huygens* (pp. 683–724). Springer Netherlands. https://doi.org/10.1007/978-1-4020-9217-6{_}21

Spencer, J. R., & Nimmo, F. (2013). Enceladus: An active ice world in the saturn system. *Annual Review of Earth and Planetary Sciences*, *41*, 693–717. https://doi.org/10.1146/annurev-earth-050212-124025

Srinivasan, J. M., Barltrop, C., Berman, S., Bushman, S., Dickson, J., Drain, T., Engelbrecht, C., Fugett, D., Gruel, D., Hill, S., Horner, M., Jedrey, T., Kahn, B., Kang, B., Low, N., Lui, A., McMahon, E., Mora, M., Paris, T., … Tuszynski, M. (2025). Europa Clipper Flight System Overview. *Space Science Reviews*, *221*(1). https://doi.org/10.1007/s11214-025-01139-9

Steinbrügge, G., Schroeder, D. M., Haynes, M. S., Hussmann, H., Grima, C., & Blankenship, D. D. (2018). Assessing the potential for measuring Europa's tidal Love number h2 using radar sounder and topographic imager data. *Earth and Planetary Science Letters*, *482*, 334–341. https://doi.org/10.1016/j.epsl.2017.11.028

Sulaiman, A. H., Achilleos, N., Bertucci, C., Coates, A., Dougherty, M., Hadid, L., Holmberg, M., Hsu, H. W., Kimura, T., Kurth, W., Gall, A. L., McKevitt, J., Morooka, M., Murakami, G., Regoli, L., Roussos, E., Saur, J., Shebanits, O., Solomonidou, A., … Waite, J. H. (2022). Enceladus and Titan: emerging worlds of the Solar System. *Experimental Astronomy*, *54*(2-3), 849–876. https://doi.org/10.1007/s10686-021-09810-z

Thomas, P. C. (2010). Sizes, shapes, and derived properties of the saturnian satellites after the Cassini nominal mission. *Icarus*, *208*(1), 395–401. https://doi.org/10.1016/j.icarus.2010.01.025

Thomas, P. C., Tajeddine, R., Tiscareno, M. S., Burns, J. A., Joseph, J., Loredo, T. J., Helfenstein, P., & Porco, C. (2016). Enceladus's measured physical libration requires a global subsurface ocean. *Icarus*, *264*, 37–47. https://doi.org/10.1016/j.icarus.2015.08.037

Thornton, C. L., & Border, J. S. (2005, Feb.). *Radiometric Tracking Techniques for Deep-Space Navigation*.

Tricarico, P. (2014). MULTI-LAYER HYDROSTATIC EQUILIBRIUM OF PLANETS AND SYNCHRONOUS MOONS: THEORY AND APPLICATION TO CERES AND TO SOLAR SYSTEM MOONS. *The Astrophysical Journal*, *782*, 99. https://doi.org/10.1088/0004-637X/782/2/99

Van Hoolst, T., Rambaux, N., Karatekin, Ö., & Baland, R. M. (2009). The effect of gravitational and pressure torques on Titan's length-of-day variations. *Icarus*, *200*(1), 256–264. https://doi.org/10.1016/j.icarus.2008.11.009

Van Hoolst, T., Baland, R. M., & Trinh, A. (2013). On the librations and tides of large icy satellites. *Icarus*, *226*(1), 299–315. https://doi.org/10.1016/J.ICARUS.2013.05.036

Van Hoolst, T., Tobie, G., Vallat, C., Altobelli, N., Bruzzone, L., Cao, H., Dirkx, D., Genova, A., Hussmann, H., Iess, L., Kimura, J., Khurana, K., Lucchetti, A., Mitri, G., Moore, W., Saur, J., Stark, A., Vorburger, A., Wieczorek, M., … Witasse, O. (2024). Geophysical Characterization of the Interiors of Ganymede, Callisto and Europa by ESA's JUpiter ICy moons Explorer. *Space Science Reviews*, *220*(5). https://doi.org/10.1007/s11214-024-01085-y

Verma, A. (2014, Mar.). *Improvement of the planetary ephemerides using spacecraft navigation data and its application to fundamental physics* [Doctoral dissertation, Université de Franche-Comté]. http://arxiv.org/abs/1403.2817

Vienne A. & Duriez L. (1995). TASS1.6: Ephemerides of the major Saturnian satellites. *Astronomy and Astrophysics*, *297*, 588–605.

Wahr, J. M., Zuber, M. T., Smith, D. E., & Lunine, J. I. (2006). Tides on Europa, and the thickness of Europa's icy shell. *J. Geophys. Res*, *111*, 12005. https://doi.org/10.1029/2006JE002729

Wieczorek, M. A. (2015, Jan.). Gravity and Topography of the Terrestrial Planets. In *Treatise on geophysics: Second edition* (pp. 153–193, Vol. 10). Elsevier Inc. https://doi.org/10.1016/B978-0-444-53802-4.00169-X

Wu, X., Bar-Sever, Y. E., Folkner, W. M., Williams, J. G., & Zumberge, J. F. (2001). Probing Europa's hidden ocean from tidal effects on orbital dynamics. *Geophysical Research Letters*, *28*(11), 2245–2248. https://doi.org/10.1029/2000GL012814

Wu, Y. (2005). ORIGIN OF TIDAL DISSIPATION IN JUPITER. II. THE VALUE OF Q. *The Astrophysical Journal*, *635*, 688–710. https://doi.org/10.1086/497355

Zannoni, M., Hemingway, D., Gomez Casajus, L., & Tortora, P. (2020). The gravity field and interior structure of Dione. *Icarus*, *345*. https://doi.org/10.1016/j.icarus.2020.113713

Zannoni, M., Tommei, G., Modenini, D., Tortora, P., Mackenzie, R., Scoubeau, M., Herfort, U., & Carnelli, I. (2018). Radio science investigations with the Asteroid impact mission. *Advances in Space Research*, *62*(8), 2273–2289. https://doi.org/10.1016/j.asr.2017.12.003

Zannoni, M., & Tortora, P. (2013). Numerical error in interplanetary orbit determination software. *Journal of Guidance, Control, and Dynamics*, *36*(4), 1008–1018. https://doi.org/10.2514/1.59294

Zumberge, J. F., Border, J. S., Dehant, V., Folkner, W. M., Jones, D. L., Martin-Mur, T., Oberst, J., Williams, J. G., & Wu, X. (2009). Geodesy: Foundation for exploring the planets, the solar system and beyond. In H. .-. Plag & M. Pearlman (Eds.), *Global geodetic observing system*. Springer. https://doi.org/10.1007/978-3-642-02687-4